The Physics of Plasma-Driven Accelerators and Accelerator-Driven Fusion

The Proceedings of Norman Rostoker Memorial Symposium

Newport Beach, CA, USA
24-25 August 2015

Editors
Toshiki Tajima and Michl Binderbauer

Foreword

T. Tajima and M. Binderbauer

Editors

Professor Norman Rostoker served as a mentor and inspiration, incubating the burgeoning brains of more than 40 PhD students in his illutrious entire career at U. Toronto, Carnegie Tech, GA, UCSD, Cornell, and UCI. His fame as a physicist began to develope from originating a very sucessful geophysical prospecting method based on Green's functions. which he and others later applied to the fundamental mathematical technique for calculating the band structure in solids, widely known and celebrated as the KKR (Korringa-Kohn-Rostoker) method (1954). He then went on to contribute to the theoretical foundation of plasma physics utilizing a similar technique and also developed other profound and fundamental plasma physics tenets (early1960's). These accomplishments would have been enough to establish any physicist's rarefied stature. But he continued to innovate and established an even more impactful legacy thereafter.

Focusing only on his highly regarded success as a mathematical physicist would miss the incredible breath of his body of work and perhaps his most profound character traits. He was a man with a special sense of humor and perseverance – a rare combination, which he showcased, amongst others, through his strong willful recovery from cancer in the 1970's. He was the kind of guy who sang "Onward Christian Soldier" when we (TT and MB) visited him at his nursing home on Dec. 19, 2014 with his usual vigor and cracking jokes, 6 days before he was summoned to the Heavens. He was also a pragmatic and fundamental thinker while at the same time an entrepreneur. Aside from his abstract theoretical physics genius, with exceptional mathematical rigor in his work, he also displayed a deep and grounding intuitive awareness of what is possible in terms of practical implementations of his ideas and theories. It was this combination of traits that made his output so productive in driving towards applied solutions. Above all, Norman was a devoted husband, father, mentor and true humanist. He treated all around him with a selfless kindness, hospitality and generosity that made everybody feel embraced and welcome. It was this set of traits more than any other that made him such a prolific educator and allowed his students to excell and achieve to their fullest.

With regards to his work focused on fusion, Norman enlisted many of his students to explore the many facets and paths towards reactors by handing out his own as well as other's concepts and ideas as research and thesis topics. He also pursued every avenue to raise funding for these projects (DoE, DoD, foreign governments, private funds, etc.). He was equally broad in his pursuits beyond fusion. In fact, his entrance into collective accelerators and related radiation sources was as fundamental as the rest of his life's work and he made groundbreaking contributions by applying his vast plasma phsyics knowledge. Some of these early efforts led to medical and other societal applications (and provided his students broad opportunities and the widest possible career options). However, his foray into beam-driven fusion was possibly his greatest legacy. In particular, in retrospect, his early attempt of turning Don Kerst's betatron accelerator into a fusion reactor in the 1960's and 1970's may have given him lasting direction for the rest of his career. In those days he was, perhaps, considering betatrons as his prime candidate for both collective accelerators as well as fusion reactors.

While one of us (TT) picked up Norman's collective accelerator legacy by turning it into a new version of plasma accelerator, the wakefield accelerator, Norman went on to be facinated by beam-driven fusion. This was based on the notion that beams can readily achieve the high energies necessary for fusion. More importantly, Norman believed that the energetic beam particles' large orbits would considerably stabilize plasma instabilities on both the macro and micro scale. An early example of this fundamental line of thinking was his famous paper on finite larmor radius effects with Rosenbluth and Krall 1962. This paper eventually incubated what is now known as Norman's Conjecture among those that worked closely with him. He meandered into colliding beam fusion, eventually settling on field reversed configurations driven by beams. Meanwhile, his persistent efforts to seek supporters for his work continued. Broadening his outreach more and more beyond the DoE, he was creatively seeking other government support and ultimately focused on private capital. In the 1990's, Norman's conviction and perseverance of finding private support for his reactor concept converged with those supporters' asprirations and enthusiasm and ultimately led to the launch of Tri Alpha Energy, Inc. (TAE) in 1998.

The history of advanced fusion fuels (beyond D-T) stretches long (including Dawson, Lidzky, Momota, Monkhorst, et al.), but Norman was one of the most persistent. He was successful in assembling an exceptional group of visionary individuals with a broad spectrum of talents (*). These included Buzz Aldrin, Frank Braun, Andy Conrad, Harry Hamlin, Allen Puckett, Glenn Seaborg (Nobel Laureate in Chemistry), George Sealy, Jerry Simmons, as well as entrepreneurial seed investors such as Mike Buchanan, Dale Prouty, Art Samberg, and Jim Valentine, who launched TAE into orbit in early 2000. The steady and sometimes explosive progress of TAE is well documented in some of the articles in this Proceedings. Thus TAE has become the most identifiable legacy of the brilliance, vision, perseverance, kindness and humor of Norman Rostoker.

The Norman Rostoker Memorial Symposium was kindly initiated by Dean Ken Janda of the School of Physical Sciences at UCI with assistance of Ms. Audrey Kelaher and Ms. Tatiana Arizaga, and followed up by Department of Physics and Astronomy Chairman Peter Taborek with help from Ms. Jan Strudwick and Ms. Alison Lara of his Office. Jan and Alison's efforts were also supported by Ms. Debbie Margarit of TAE. Toegther they executed all the details and significantly contributed to making the Symposium the resounding success it became. Many of Norman Rostoker's family members, amongst them Rachel Uchizono, Stephen Rostoker, and Gordon Rostoker, were equally instrumental in forging this effort. In editing the Proceedings book, a debt of gratitude is due to the anonimous referees for their reviewing of the manuscripts. In addition, the dedications by Jan Strudwick, as well as Drs. N. Bolte, D. Fulton, E. Granstedt, A. Necas, and E. Trask in keeping track of and proofreading the final articles are deeply and greatfully appreciated. For the AIP publishers, we thank Lacie Clark and Ruth Levins for their depth of guidance and patience. Among all, your overwhelming participation in the Symposium and following contributions to these Proceedings have been most inspiring and moving, which we are sure has reached Norman's notice in the Heavens.

Feb. 15, 2016, the Editors at Irvine, CA

NB: (*) One of the Editors (TT) gratefully acknowledges his interview with Dr. Dale Prouty, CEO of TAE, for sharing his experience and stories on the cradle and most vulnerable times of the Company that Norman helped launch, which George Sealy, Dale, and Michl Binderbauer managed and incubated out of UCI. My respect to them.

Norman Rostoker and Strongly Correlated Plasmas

Setsuo Ichimaru

The University of Tokyo, Tokyo

Abstract. If Norman were alive and attended this symposium, he might have quipped: "Setsuo! What are you talking about! A plasma is, after all, a strongly correlated object, and there is nothing so special about it!""Yes, Norman, you are so correct! A statistical system consisting of mutually non-interacting and thus uncorrelated particles may be an "ideal-gas" system from a physics teacher's pedagogical point of view, but real systems do consist of mutually interacting and thus strongly correlated particles; a plasma is definitely one of them.Here, in the memory of Professor Rostoker's outstanding contributions to strongly correlated plasmas for the past 60 years, we wish to survey on "Scattering of Electromagnetic Waves by a Strongly Correlated Plasma" and "Multi-particle Correlation, Equations of State, and Phase Diagrams" in what follows.

1. SCATTERING OF ELECTROMAGNETIC WAVES BY A STRONGLY CORRELATED PLASMA

1.1 Dynamic Structure Factor

The scattering of electromagnetic waves by electron density fluctuations in a plasma is regulated by the dynamic structure factor, $S(\boldsymbol{k},\omega)$, the Fourier transform of the electron density-density correlation function [1,2]. It is defined by

$$S(\mathbf{k},\omega)=\frac{1}{2\pi V}\int_{-\infty}^{\infty}dt\left\langle\rho_{\mathbf{k}}(t'+t)\rho_{-\mathbf{k}}(t')\right\rangle\exp\left(i\omega t\right), \tag{1}$$

where

$$\rho_{\mathbf{k}}(t)=\int d\mathbf{r}\left\{\sum_{j=1}^{N}\delta[\mathbf{r}-\mathbf{r}_j(t)]-n\right\}\exp(-i\mathbf{k}\cdot\mathbf{r})=\sum_{j=1}^{N}\exp[-i\mathbf{k}\cdot\mathbf{r}_j(t)]-N\delta(\mathbf{k},0) \tag{2}$$

refers to the spatial Fourier components of the electron density fluctuations, and N is the total number of electrons in a volume V. In this expression, $\delta(\boldsymbol{k},\boldsymbol{k}')$ is the three-dimensional Kronecker's delta, n (= N/V) is the average number density, and $\mathbf{r}_j(t)$ describes the trajectory of j-th electron.

We designate incoming and outgoing waves by wave vector $\mathbf{k}$ and frequency ω as $(\mathbf{k}_1, \omega_1)$ and $(\mathbf{k}_2, \omega_2)$. The differential cross section, $d^2Q/do d\omega$, for scattering into a solid angle do and a frequency interval $d\omega$ is expressed in a form proportional to $S(\mathbf{k}, \omega)$ with $\mathbf{k} = \mathbf{k}_2 - \mathbf{k}_1$ and $\omega = \omega_2 - \omega_1$:

$$\frac{d^2Q}{do\,d\omega}=\frac{3V}{8\pi}\sigma_{\mathrm{T}}\left(1-\frac{1}{2}\sin^2\theta\right)S(\mathbf{k},\omega)\,. \tag{3}$$

Here, $\sigma_T = (8\pi/3)(e^2/mc^2)^2 = 6.533\times10^{-25}$ cm^2 is the cross section of Thomson scattering, θ is the angle between the incident and scattered waves, and we have averaged over directions of polarization of both waves. Scattering of electromagnetic waves thus offers a unique way of measuring strong correlations in a plasma.

1.2 Collective *vs*. Individual Particles Aspects of Fluctuations

In early 1950s, Bohm and Pines advanced a series of papers dealing with "a collective description of electron interactions," in which they explicitly stated [3]:

-- The density fluctuations may be split into two approximately independent components. The collective component, that is, the plasma oscillation, is present only for wavelengths greater than the Debye length. The individual particles component represents a collection of individual electrons surrounded by co-moving clouds of screening charges; collisions between them may be negligible under the random-phase approximation (RPA). --

Here, the plasma oscillation has a characteristic frequency,

$$\omega_p = (4\pi n e^2/m)^{1/2}; \tag{4}$$

the Debye length is the inverse of the Debye wave number,

$$k_D = (4\pi n e^2/k_B T)^{1/2}; \tag{5}$$

and k_B refers to Boltzmann constant.

The collective *vs*. individual particles aspects of fluctuations described above can be most succinctly expressed in terms of the dielectric response function, $\varepsilon(\mathbf{k},\omega)$. It is a linear response function of a plasma as an externally applied potential $F_{ext}(\mathbf{k}, \omega)$ may induce a potential $F_{ind}(\mathbf{k}, \omega)$; the resultant total potential field $F_{tot}(\mathbf{k}, \omega)$ $(= F_{ext}(\mathbf{k}, \omega) + F_{ind}(\mathbf{k}, \omega))$ may then be expressed as

$$F_{tot}(\mathbf{k}, \omega) = F_{ext}(\mathbf{k}, \omega)/\varepsilon(\mathbf{k}, \omega). \tag{6}$$

The zeros of the dielectric response function, determined from $\varepsilon(\mathbf{k}, \omega) = 0$ on the complex ω-plane, that is, $\omega = \omega_{\mathbf{k}} - i\gamma_{\mathbf{k}}$, give the frequency dispersions and the life-times of the collective mode. When density fluctuations of an individual electron moving in a trajectory, $\mathbf{r}_j(t) = \mathbf{r}_j + \mathbf{v}_j t$, are expressed as

$$\rho_j^{(0)}(\mathbf{k}, \omega) = 2\pi \exp(-i\mathbf{k}\cdot\mathbf{r}_j)\,\delta(\omega - \mathbf{k}\cdot\mathbf{v}_j);$$

those of the dressed electrons may then be given as

$$\rho_j^{(s)}(\mathbf{k}, \omega) = \rho_j^{(0)}(\mathbf{k}, \omega)/\varepsilon(\mathbf{k}, \omega). \tag{7}$$

In RPA, where collisions between dressed particles are negligible, the dynamic structure factor may be evaluated by superposition of the dressed test charges as [4-6]

$$S(\mathbf{k}, \omega) = S^{(0)}(\mathbf{k}, \omega)/|\varepsilon(\mathbf{k}, \omega)|^2, \tag{8}$$

where

$$S^{(0)}(\mathbf{k},\omega) = \int d\mathbf{p} F(\mathbf{p})\delta(\omega - \mathbf{k}\cdot\mathbf{v}) \tag{9a}$$

$$S^{(0)}(\mathbf{k}, \omega) = (n/k)(m/2\pi k_B T)^{1/2} \exp(-m\omega^2/2k_B T k^2). \tag{9b}$$

Eq. (9a) applies to a non-equilibrium situation such as a beam-plasma system with $F(\mathbf{p})$ denoting the single-particle momentum ($\mathbf{p} = m\mathbf{v}$) distribution; Eq. (9b) applies to a plasma in thermodynamic equilibrium at temperature T.

1.3 Radar Backscattering From the Ionospere

As a first example of scattering experiments demonstrating correlation effects, let us take up radar back-scattering measurements from the ionosphere [7], the experiment mentioned in the first paragraph of the Rosenbluth-Rostoker scattering paper [2].

Ionospheric F layer extends from 200 to 500 km in altitude; average number density is $10^5 - 10^6$ cm^{-3}; temperature is around 1,500 K.

Observation that Bowles of NBS made in 1958 utilizes radar pulses at frequency 42.92 MHz, pulse-width of 120 ms, repetition frequency of 25～40 per second, and peak power of 1 MW [7,8].

Since the radar frequency is far greater than the plasma frequency at 13 MHz, ionosphere is transparent to those radar pulses, and thereby backscatters them at strengths proportional to the local densities of electrons. The density profile so observed is shown in Fig. 1.

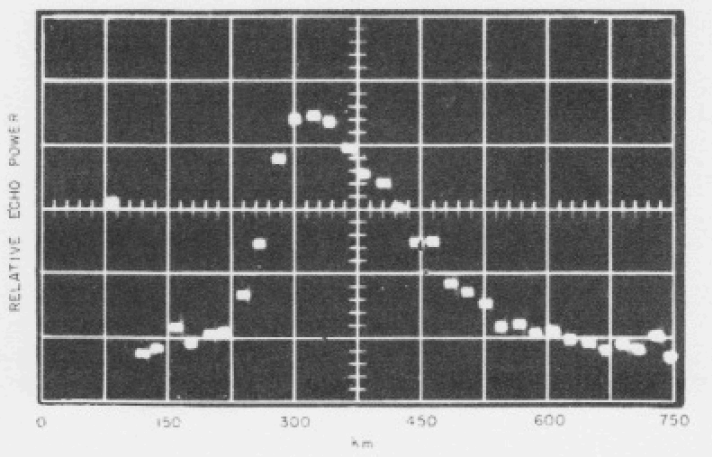

FIGURE 1. Radar-backscattering measurement of the ionospheric electron distribution as a function of the scattering altitude. [1959 Feb. 27, 7:40 pm - Illinois local time] After ref. 8

We expect the back-scattered waves would be broadened by the thermal motion of the electrons by a width of 82 kHz as in (9b), on top of a 9 kHz spread in the radar frequencies. To detect such a spectral distribution, the receiver's bandwidth was fixed at 9 kHz. When the central frequency of the receiver was set at the outgoing radar frequency, maximum signal strength was obtained. When the receiver's central frequency was shifted by 15 kHz relative to the radar, however, virtually no signals were observed. This casts an enigma, since it might mean no broadening caused by the scatterers.

To look into the features of broadening more closely, Pineo, et al. of MIT two years later performed analogous experiments, in which, however, the outgoing radar frequency was raised to 440 MHz [9]. Frequency spectrum of the back-scattered waves is now detected as in Fig. 2; we here find that the broadening actually takes place, correspondingly to thermal motion of the ions.

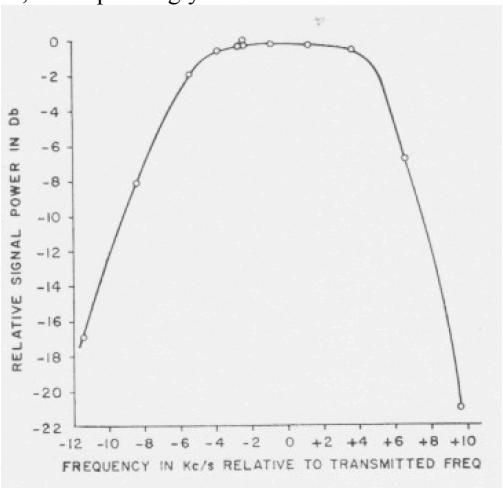

FIGURE 2. Spectral distribution of the backscattered wave from the ionosphere (～300 km in altitude) in the measurement of [9]

Now, in these experiments, we recognize that the wave number k relevant to scattering is much smaller than k_D of (5), meaning that we are in the collective regime where features of strongly correlated plasmas should be exhibited.

In the present case, notion of "dressed" ions should be remarked. Coulomb potential around an ion is screened by co-moving cloud of electrons at half a strength and the remaining half stems from repelled ions. The observed spectrum may be interpreted as coming from scattering by electrons co-moving with ions.

Another collective phenomenon to be noted here is a mild hump caused by ion-acoustic waves. These waves in the ionosphere, however, are strongly damped since temperature of the electrons is almost equal to that of the ions, or $T_e \simeq T_i$, hence a mild hump.

1.4 Plasma Critical Opalescence

If, however, $T_e >> T_i$, the ion-acoustic wave, $\omega_{\mathbf{k}} = sk$, becomes a well-defined collective mode for $k < k_D$. Here, $s \simeq V_i (T_e/T_i)^{1/2}$ is the ion-acoustic velocity with V_i denoting ionic thermal velocity.

Drift motion of the electrons relative to the ions acts to excite the ion-acoustic waves. If, then, the drift velocity V_d of electrons approaches the onset condition for the acoustic-wave instability, we may expect enhancement of scattering, analogous to critical opalescence near the critical point of the gas-liquid phase transition [1,10].

1.5 Static Structure Factor

In the scattering experiments, if we pay no attentions to frequencies, that is, if we collect the scattered waves at all frequencies, then differential cross-section of scattering may be given by

$$dQ/do = (3N/8\pi)\sigma_T(1 - \tfrac{1}{2} \sin^2 \theta)\, S(\mathbf{k}) \tag{10}$$

Here, the static structure factor $S(\mathbf{k})$ defined by

$$S(\mathbf{k}) = \frac{1}{N}\left\langle \left|\rho_{\mathbf{k}}(t)\right|^2 \right\rangle = \frac{1}{n}\int_{-\infty}^{\infty} d\omega S(\mathbf{k},\omega) \tag{11}$$

describes the spectral distribution of spatial density fluctuations or spatial configurations such as lattice structures. Short-ranged crystalline order at the nearest-neighbor separations may thus be approached by these scattering techniques.

In fact, von Laue observed such scattering patterns in 1914 by shining X-ray onto metal; father-and-son Braggs developed X-ray crystallography in 1915. Both works led to Nobel Prizes in the respective years.

1.6 Observation of Layered Structures and Laue Patterns in Coulomb Glasses

In these connections, let us now turn to observation of layered structures and Laue patterns in Coulomb glasses, created by Monte Carlo (MC) simulations.[11] In these simulations, acceptance probability of MC configurations generated by random displacements of particles is set at

$$P = \begin{cases} \exp\left(-\dfrac{\Delta E}{k_B T}\right), & \text{if } \Delta E > 0, \\ 1, & \text{if } \Delta E \le 0, \end{cases} \tag{12}$$

where ΔE denotes the energy increment created by the displacements. The probability (12) may lead the statistical system to approach a canonical distribution equilibrated at temperature T.

In the study, it is useful to introduce the Coulomb coupling parameter Γ for an OCP, that is, a one-component plasma immersed in an uniform background of opposite charges, via

$$\Gamma = (Ze)^2/ak_BT = 2.7\times10^{-5}\, Z^2\, [n/10^{12}\ cm^{-3}]^{1/3}\, [T/10^6\ K]^{-1}, \qquad (13)$$

with $a = (4\pi n/3)^{-1/3}$ referring to the ion-sphere radius; Z is the charge number of an ion. This Γ is the ratio of the Coulomb energy to the kinetic energy, inversely proportional to T; as we see here, Γ takes on extremely small values in ordinary gaseous plasmas.

When the temperature is lowered into $\Gamma > 180$, an OCP may undergo a Wigner crystallization into a bcc (body-centered cubic) crystal. If a rapid quench is applied, the resultant state might possibly be a Coulomb glass, a mixture of different crystalline structures and configurations.

We thus follow dynamic evolution of an OCP by MC simulations with 432 particles, starting with a fluid state at $\Gamma = 160$, leading to formation of Coulomb glasses at different quenches: (A) an application of a sudden quench to $\Gamma = 400$ at c = 0; (B) an application of a gradual quench stepwise with $\Delta\Gamma = 10$ from $\Gamma = 160$ at c = 0 to $\Gamma = 400$ at c = 23; (C) a sudden quench to $\Gamma = 300$ at c = 0. Here c denotes the sequential number of MC configurations measured in units of a million configurations; the sequential number corresponds to a MC time via $\omega_p t = 2.7\times10^2 c$, with ω_p referring to the plasma frequency (4).

To study the nature of interlayer correlations, we identify the particles in the three central layers and project their positions normally onto a plane. In Fig. 3, such projections are exhibited for the quenches (A) – (C), where open circles, closed circles and crosses denote projections of the particles on upper, middle and lower layer, respectively.

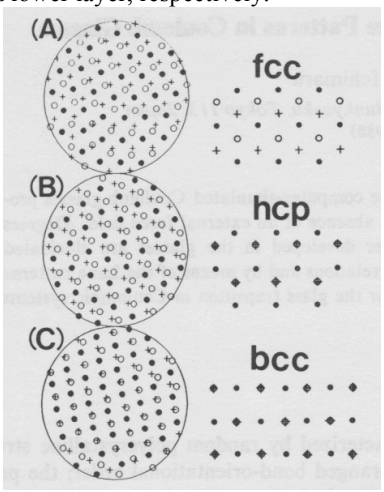

FIGURE 3. Normal projections of most closely packed layers: open circles, upper layer; closed circles, middle layer; crosses, lower layer. After ref. 11

For comparison, analogous projections are shown in Fig. 4 for the most closely packed layers in the fcc (face-centered cubic), hcp (hexagonal close-packed) and bcc crystals. We find here that the Coulomb glass with the quench (B) has developed an advanced state of polycrystalline nucleation predominantly with local fcc-hcp configurations over those with (A) and (C).

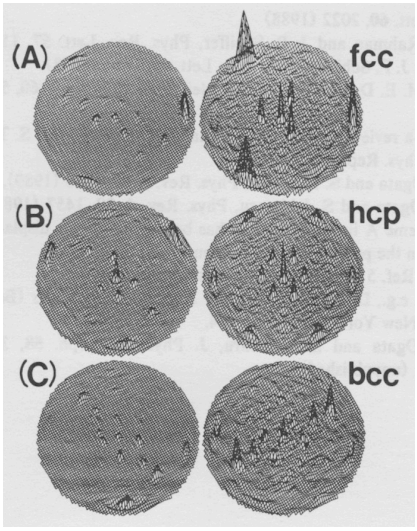

FIGURE 4. Laue patterns for the glasses (A) - (C) and for the fcc, hcp and bcc lattices of 432 particles. The polar coordinates consist of $0 \le (\pi - \chi)/2 \le 0.45\pi$ and $0 \le \phi \le 2\pi$; the origin corresponds to $\chi = \pi$. Here, χ is the scattering angle between incident and scattered waves; ϕ is the azimuthal angle around the incident wave. After ref. 11

Finally, we investigate the combined effects between the intralayer and interlayer correlations by a scattering method of Sec. 1.5. We thus inject plane waves with wave vector $\boldsymbol{k}_1$ to the glasses (A) – (C) in the direction normal to the layered structures, and measure the strength of scattered waves $\boldsymbol{k}_2$ in the directions specified by (χ,ϕ), where χ is the scattering angle between $\boldsymbol{k}_1$ and $\boldsymbol{k}_2$ and ϕ is the azimuthal angle around $\boldsymbol{k}_1$. The cross section (10) for coherent scattering is proportional to the static structure factor (11), where $\boldsymbol{k} = \boldsymbol{k}_2 - \boldsymbol{k}_1$. We assume that the incident wave numbers have a distribution proportional to $exp[-(k_1-k_0)^2/k^2]$ with $k_0 = 2\pi$ and $k = 0.24$. The scattering experiment is thus capable of detecting the coherence in the phases $4\pi\, sin(\chi/2)\boldsymbol{k} \cdot \boldsymbol{r}_j/k$ over those particles $\boldsymbol{r}_j$ contained in a slab of width $4.2/sin(\chi/2)$ in the direction of $\boldsymbol{k}$.

Fig. 4 displays the Laue patterns so obtained for the glass states (A) – (C), and compares them with those of the fcc, hcp and bcc lattices. We observe the existence of local hexagonal order in (B) and to a lesser extent in (A); a slight involvement of local bcc configurations is likewise detected for all the cases of (A) – (C).

2. MULTI-PARTICLE CORRELATION, EQUATIONS OF STATE, AND PHASE DIAGRAMS

We now proceed to the second subject in which equations of state and phase diagrams of a plasma are studied.

2.1 Radial Distribution Functions and Correlation Energies

The radial distribution function $g(\mathbf{r})$ is a joint probability density of finding two particles at a separation r; Fig. 5 shows $g(\mathbf{r})$ evaluated with the MC method of Sec. 1.6 for $\Gamma > 1$.

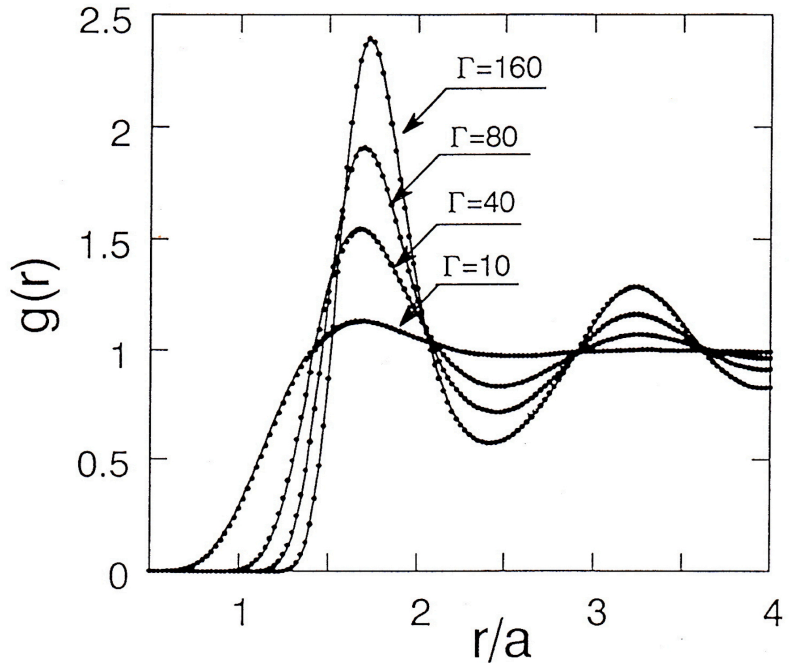

FIGURE 5. Radial distribution functions of OCP fluids obtained by MC methods with N = 1024 at various values of Γ. The number of the MC configurations generated for each run was $7x10^6$; g(r) was calculated with 200 bins in the range $0 \le r \le L/2$, a half of the cubic MC cell with size L = 26.2a. After ref. 17

The radial distribution function is related directly with the static structure factor (11) as

$$g(r) = 1 + \frac{1}{n}\int \frac{d\mathbf{k}}{(2\pi)^3}\left[S(\mathbf{k}) - 1\right]\exp\left(i\mathbf{k}\cdot\mathbf{r}\right). \tag{14}$$

The correlation energy U_{int} in a plasma can then be calculated, once either $S(\mathbf{k})$ or $g(\mathbf{r})$ is known, through the formula,

$$\begin{aligned} U_{\text{int}} &= 2\pi(Ze)^2 n\int \frac{d\mathbf{k}}{(2\pi)^3}\frac{1}{k^2}\left[S(k) - 1\right] \\ &= \frac{(Zen)^2}{2}\int d\mathbf{r}\frac{1}{r}\left[g(r) - 1\right]. \end{aligned} \tag{15}$$

Substituting the RPA structure factors (8) in (15) via (11), we obtain the RPA expression for the normalized correlation energy, $u_{ex} = U_{int}/nk_BT$, as

$$u_{\text{ex}}^{\text{DH}} = -\frac{\sqrt{3}}{2}\Gamma^{3/2}. \tag{16}$$

This is called the Debye-Hückel term.

2.2 Multi-particle Correlation and OCP Internal Energy

The correlation energy (16) takes account of binary correlation to the lowest order in Γ with RPA and thus is applicable to OCP for $\Gamma << 1$ only. The expression for correlation energies next order in the Γ expansion has been accurately obtained as

$$u_{\text{ex}}^{\text{ABE}} = -\frac{\sqrt{3}}{2}\Gamma^{3/2} - 3\Gamma^3\left[\frac{3}{8}\ln(3\Gamma) + \frac{\gamma}{2} - \frac{1}{3}\right] \quad (\Gamma < 0.1) \tag{17}$$

with γ = 0.57721… denoting Euler's constant.

Correlation energies beyond RPA require accurate assessments for the triple and more correlation effects. These may be approached by various theoretical methods, such as the giant cluster-expansion calculation [12], expansion in Γ of the BBGKY hierarchy [13], multi-particle correlation in the convolution approximation [14], and density-functional formulation of multi-particle correlations [15].

The use of Monte Carlo radial distribution functions (such as those in Fig. 5) in Eq. (15) yields the correlation energies in large Γ regime [16,17],

$$u_{\mathrm{ex}}^{\mathrm{OCP}} = -0.898004\Gamma + 0.96786\Gamma^{1/4} + 0.220703\Gamma^{-1/4} - 0.86097 \quad (1 < \Gamma < 180) \quad .(18)$$

The formula for OCP correlation energies covering all the parameter regimes accurately has been obtained by connecting Eqs. (17) and (18) as

$$u_{\mathrm{ex}}(\Gamma) = \frac{u_{\mathrm{ex}}^{\mathrm{ABE}}(\Gamma) + (3\times 10^3)\Gamma^{5.7} u_{\mathrm{ex}}^{\mathrm{OCP}}(\Gamma)}{1 + (3\times 10^3)\Gamma^{5.7}} \quad (\Gamma < 180) \quad . \tag{19}$$

The excess Helmholtz free energy, $f_{ex}(\Gamma)$, is then calculated with the coupling-constant integration of Eq. (19); the excess pressure may be evaluated by differentiation of $f_{ex}(\Gamma)$ with respect to volume at a constant temperature [18].

These procedures thus form the basis of assessing the equations of state for various plasmas.

2.3 Equations of State for Metallic Hydrogen

We now consider such equations of state for metallic hydrogen, distinguishing between fluid and solid states [19].

Metallic fluid hydrogen consists of itinerant electrons (fermions with spin ½) and itinerant protons (classical, or fermions with spin ½) with strong e-i coupling. Metallic solid hydrogen consists of itinerant electrons (fermions with spin ½) and a bcc array of protons (classical) with harmonic and anharmonic lattice vibrations with strong e-i coupling.

Fluid-solid transitions are described through comparison of Gibbs free energy, $G = F + PV$, at a constant pressure, $P = -(\partial F/\partial V)_T$.

On these and in what follows, we shall recall various thermodynamic relations.

2.4 Equations of State for the Insulator Phase of Hydrogen

States with molecular fluid and those with molecular solid are distinguished. Equations of state in the insulator phase consist in various elements, as enlisted below [19].

Molecular fluid consists in elements of an ideal Bose gas, short-range repulsive interaction between molecular cores, attractive (dipolar) van der Waals forces, molecular rotation (roton), intramolecular vibration (vibron), and the ground-state energy of a H2 molecule (E_{H2}).

Molecular solid consists in cohesive energy with a hcp structure, lattice vibration (phonon), roton, vibron, and the ground-state energy of a H2 molecule (E_{H2}).

In addition, we take into account contributions of atomic hydrogen to the equations of state, including the repulsive hard sphere, the attractive van der Waals, and the ground-state energy (E_{H}) of a H atom.

2.5 Equations of State for Hydrogen

We now express the Helmholtz free energy for hydrogen as a sum of molecular, atomic, metallic, and mixture contributions as [19]

$$
\begin{aligned}
f_{\mathrm{tot}}(n_{\mathrm{H}},T;\langle Z\rangle,\alpha_{\mathrm{d}}) &\equiv \frac{F}{N_{\mathrm{H}}k_{\mathrm{B}}T} \\
&= \frac{(1-\alpha_{\mathrm{d}})(1-\langle Z\rangle)}{2}\left(f_{\mathrm{m}}^{\mathrm{id}} + f_{\mathrm{vib}} + f_{\mathrm{rot}} + \frac{E_{\mathrm{H_2}}}{k_{\mathrm{B}}T}\right) \\
&+\alpha_{\mathrm{d}}(1-\langle Z\rangle)\left(f_{\mathrm{a}}^{\mathrm{id}} + \frac{E_{\mathrm{H}}}{k_{\mathrm{B}}T}\right) + \langle Z\rangle f_{\mathrm{met,fl}}(\overline{n},T) \\
&+\frac{(1-\alpha_{\mathrm{d}})(1-\langle Z\rangle)}{2}\left(f_{\mathrm{HS}} + f_{\mathrm{attr}}\right).
\end{aligned}
\tag{20}
$$

Here, $\langle Z\rangle$ denotes the degree of ionization; α_{d}, the degree of dissociation. Those parameters are determined through minimization of the free energy at constant density n_{H} of protons and temperature. A renormalized density, $n^* = n/(1-\eta)$, taking account of the total packing fraction, η, of hydrogen atoms and molecules.

2.6 Metal-Insulator Transitions in Hydrogen

Hydrogen, which we know as a light gaseous substance at ambient temperature and pressure, may exhibit extraordinary features pertinent to the strongly correlated plasmas when it is compressed to densities comparable to or greater than those of ordinary solids. Basically, hydrogen matter is a statistical ensemble consisting of electrons and protons. The protons, with the smallest atomic number (unity) among various chemical elements and thus with de Broglie wavelengths longer than those of other nuclear species, tend to interfere with each other quantum mechanically under such condensed circumstances.

Two sorts of phase transitions are of relevance in dense hydrogen.

Metal-insulator transitions [20] may take place between low-density and low-temperature insulator phase composed of molecular hydrogen and high-density and/or high-temperature metal phase composed of itinerant electrons and protons, the latter of which being either in a crystalline state or in a fluid state. When hydrogen in an insulator phase is compressed to a state of high density such that average interparticle spacing between protons becomes comparable to or less than the orbital radii of the bound electrons, which are on the order of the Bohr radius, electrons begin to assume *itinerant* states due to overlapping of wave functions between adjacent electrons; *pressure* ionization may thus result.

Analogous process of metallization may take place when the temperature is raised above the atomic or molecular binding energies of electrons; it is *thermal* ionization.

We may analyze those phase transitions on the basis of the equations of state (20), and thereby obtain in Fig. 6 the phase diagrams of hydrogen, describing metallization and solidification [19]. Solar interior [21], Jovian interior [21], shock compression [19,22] and diamond anvil cell [23] experiments are remarked on this phase diagram as well. (The "rock" shown here for the core of Jupiter is not hydrogen, however.)

In a higher density regime where quantum nature of protons becomes apparent, a ferromagnetic phase may arise. We shall consider such an issue in the next section.

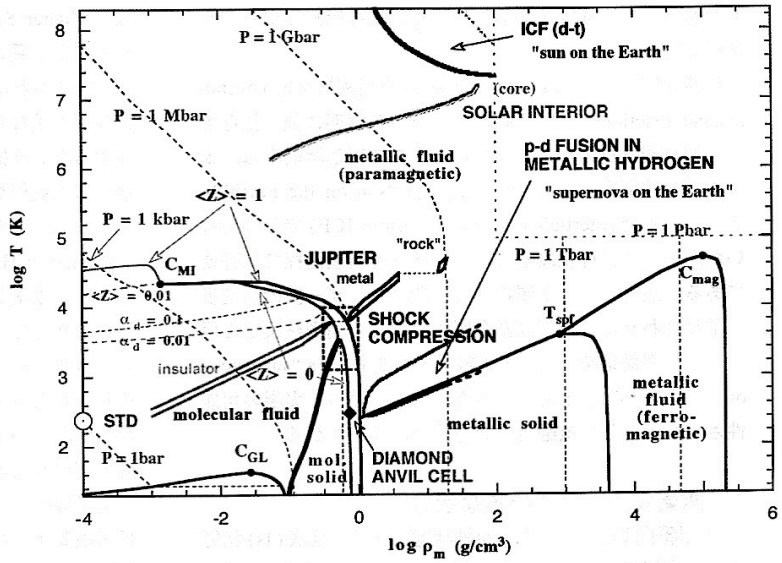

FIGURE 6. Phase diagrams of hydrogen, describing metallization and solidification. C_{MI} and C_{GL} are the critical points associated with metal-insulator and gas-liquid transitions. After ref. 19

2.7 Ferromagnetic and Freezing Transitions in Metallic Hydrogen

In addition to the metal-insulator transitions treated in the previous section, another class of phase transitions may be found for hydrogen in metallized states. As the cases with itinerant electrons or the electron liquids [24,25], the protons in metallic hydrogen may be in a paramagnetic or a ferromagnetic fluid state, or in a Wigner crystalline state. In this section, we consider the issues of ferromagnetic and/or freezing transitions and thereby elucidate the associated phase diagrams for metallic hydrogen [26].

Theoretical approaches to these issues begin with evaluations of the free energies as in Eq. (20). In the present case, the degrees of ionization and molecular dissociation are to be set at $\langle Z \rangle = 1$ and $\alpha_d = 0$; instead, the spin polarization, $\zeta = (n_\uparrow - n_\downarrow)/n$, with $n_\uparrow$ and $n_\downarrow$ denoting the partial number densities of spin up and down protons (where $n = n_\uparrow + n_\downarrow$) enters as a new parameter.

We thus consider the total free energy, $f_{tot}(n, T; \zeta)$, in place of Eq. (20). The degrees of spin polarization and the resultant magnetic states are determined through minimization of the total free energy with respect to the variation of ζ.

Phase diagrams of hydrogen describing magnetization and solidification of metallic hydrogen are obtained in Fig. 7 for higher density and finite temperature regime [26]. TABLE I lists the values of the physical parameters at the fluid-solid critical point (C_{FS}) and the magnetic critical point (M_C) in the phase diagrams of Fig. 7.

TABLE I. Physical parameters at the fluid-solid critical point (C_{FS}) and the magnetic critical point (M_C) in the phase diagrams of Fig. 7 for the liquid-metallic hydrogen. After ref 26.

	C_{FS}	M_C
ρ_m (g/cm^3)	4.0×10^3	1.4×10^6
T (K)	6.6×10^3	6.6×10^5
B_M (G)	2.6×10^5	8.0×10^6

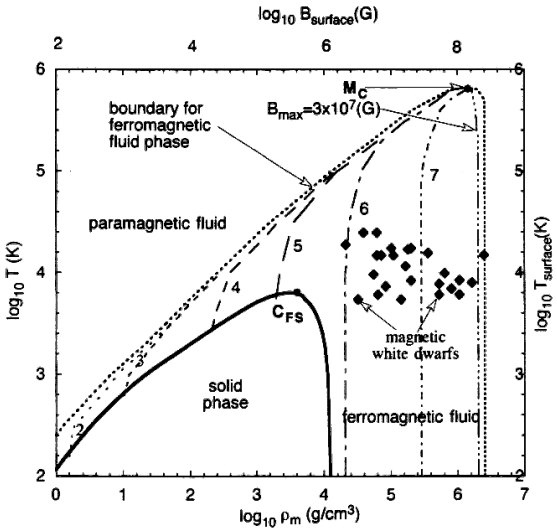

FIGURE 7. Phase diagrams of metallic hydrogen describing partial spin-ordering and Wigner crystallization. The thick solid curve depicts the phase boundary between fluid and solid, with C_{FS} designating the associated critical point. The dashed and chain curves describe the conditions at a constant strength magnetization, with the numerals denoting the decimal exponents of the field strength B_M in G; M_C designates the magnetic critical point. The diamond markers plot the observed surface-field strengths ($B_{surface}$) vs the effective surface temperatures ($T_{surface}$) for the magnetic white dwarfs. After ref. 26

2.8 Nuclear Ferromagnetism with the Magnetic White Dwarfs

The white dwarf represents a final stage of stellar evolution, corresponding to a star of about one solar mass compressed to a characteristic radius (R_{WD}) of approximately 5,000 km and an average density of some $10^6 - 10^7$ g/cm^3. Its interior consists of a multi-ionic condensed matter composed of C and O as the main elements and Ne, Mg, Si, …, Fe as trace elements. Observationally a class of white dwarfs (DA) is known to have hydrogen-rich atmosphere and envelopes.

Of all the isolated white dwarfs surveyed, only about 3% – 5% have observable magnetic fields that are in the range ~1 – 500 MG. The surface magnetic fluxes of these white dwarfs, $\sim BR_{WD}^2 = (10^{24} - 5\times10^{26})$ G cm^2, are regarded as similar in magnitude to those of the magnetic Ap stars, a spectroscopic type of stars that exhibit intense hydrogen lines. Such Ap stars may therefore be looked upon as probable progenitors of the magnetic white dwarfs [27,28].

The ferromagnetic transitions in dense metallic hydrogen as elucidated in Fig. 7 may offer an ingredient of physics relevant to the mechanisms for the origin of strong magnetization in the magnetic white dwarfs [24]. The magnetic critical point occurs at a temperature of 6.6×10^5 K and the strengths of induced magnetization may range as high as 3×10^7 G along the B_{max} line of Fig. 7. The plots in Fig. 7 of the magnetic-field strengths ($B_{surface}$) vs the effective blackbody temperatures ($T_{surface}$) on the surfaces of 25 magnetic white dwarfs observed[28] have shown that except for a few cases (with the field strengths exceeding the theoretical maximum by a factor of 1 – 15) the observed field strengths fall within the predicted range and that the surface temperatures are lower than the critical temperature by approximately two orders of magnitude.

The hydrogen densities (~$10^4 - 10^6$ g/cm^3) required for magnetization may be expected in an outer shell of a hydrogen-rich white dwarf at some 70% – 90% of the stellar radius, where the mass densities may take on values lower by three or more orders of magnitude than those in the core. Solidification of metallic hydrogen, on the other hand, may not take place in such a white dwarf, since all the $T_{surface}$ values exceed the temperature at C_{FS}.

For those white dwarfs with super-strong magnetic fields exceeding 3×10^7 G, a maximum field strength obtainable by the ferromagnetism alone in metallic hydrogen, a separate amplification mechanism such as a "dynamo" would have to be called for [27], where the nuclear ferromagnetism in Fig. 7 may provide "seed" fields for such an amplification.

The electric resistivity r_E calculated for the metallic hydrogen at the critical conditions (M_C) takes on the value, 6.0×10^{-12} W cm [29]. The magnetic Reynolds number associated with a rotating white dwarf is thus evaluated as

$$R_m = 4\pi R_{WD}^2 \omega_{WD}/\rho_E c^2 = 3.8\times10^{16}\ (\mathrm{R_{WD}}/5{,}000\ \mathrm{km})^2\ (\omega_{WD}/2\pi\ \mathrm{day}^{-1}), \qquad (21)$$

where ω_{WD} is the angular velocity of a white dwarf. Comparing this number with the corresponding estimates, $\sim1.2\times10^{12}$ and $\sim1.0\times10^{8}$, for Jovian and solar magnetic activities [24] (where the ferromagnetic seed fields are not available) respectively, we may conclude that considerable strengths of the magnetic fields may be sustained around a white dwarf by the presence of highly conductive, *ferromagnetic* hydrogen in the outer shell.

CONCLUDING REMARK

It is clear from what we have surveyed in the foregoing that Norman Rostoker made outstanding contributions to the advancement of the fundamental plasma physics.

REFERENCES

1. S. Ichimaru, D. Pines and N. Rostoker, Phys. Rev. Lett. **8**, 231 (1962).
2. M. N. Rosenbluth and N. Rostoker, Phys. Fluids **5**. 776 (1962).
3. D. Bohm and D. Pines, Phys. Rev. **92**, 609 (1953).
4. N. Rostoker, Nucl. Fusion **1**, 101 (1961).
5. N. Rostoker and M. N. Rosenbluth, Phys. Fluids **3**, 1 (1960).
6. S. Ichimaru, Ann. Phys. **20**, 78 (1962).
7. K. L. Bowles, Phys. Rev. Lett. **1**, 454 (1958).
8. K. L. Bowles, J. Res. N. B. S., **65D**, 1 (1961).
9. V. C. Pineo, L. G. Kraft and H. W. Briscoe, J. Geophys. Res. **65**, 2629 (1960).
10. L. D. Landau and E. M. Lifshitz, "Statistical Physics" p. 366 (Addison-Wesley, Reading, Mass., 1958).
11. S. Ogata and S. Ichimaru, Phys. Rev. Lett. **62**, 2293 (1989).
12. R. Abe, Prog. Theor. Phys. **22**, 213 (1959).
13. T. O'Neil and N. Rostoker, Phys. Fluids **8**, 1109 (1963).
14. H. Totsuji and S. Ichimaru, Prog. Theor. Phys. **50**, 753 (1973).
15. S. Ichimaru, H. Iyetomi and S. Tanaka, Phys. Rep. **149**, 92 (1987).
16. W. L. Slattery, G. D. Doolen and H. E. DeWitt, Phys. Rev. A **26**, 2255 (1982).
17. S. Ogata and S. Ichimaru, Phys. Rev. A **36**, 5451 (1987).
18. S. Ichimaru "Statistical Plasma Physics - Vol. II: Condensed Plasmas" p. 56 (Westview Press, Boulder, 2004).
19. H. Kitamura and S. Ichimaru, J. Phys. Soc. Jpn. **67**, 950 (1998).
20. E. Wigner and H. B. Huntington, J. Chem. Phys. **3**, 764 (1935).
21. H. M. Van Horn, Science **252**, 384 (1991).
22. S. T. Weir, A. C. Mitchell and W. J. Nellis, Phys. Rev. Lett. **76**, 860 (1996).
23. R. J. Hemley, H.-k. Mao, A. F. Goncharov, et al., Phys. Rev. Lett. **76**, 1667 (1996).
24. S. Ichimaru, Phys. Lett. A **235**, 83 (1997).
25. S. Ichimaru, Phys. Rev. Lett. **84**, 1842 (2000).
26. S. Ichimaru, Phys. Plasmas **8**, 48 (2001).
27. G. Chanmugam, Annu. Rev. Astron. Astrophys. **30**, 173 (1992).
28. J. Weisheit, in "Elementary Processes in Dense Plasmas: Proc. Oji International Seminar" edited by S. Ichimaru and S. Ogata, p. 61 (Addison-Wesley, Reading, MA, 1995).
29. H. Kitamura and S. Ichimaru, J. Phys. Soc. Jpn **65,** 1250 (1996).

Experiments with Nonneutral Plasmas

T. M. O'Neil

University of California San Diego, Physics Department 0319, La Jolla, CA92129-0319

Abstract. Selected experiments with nonneutral plasmas are discussed. These include the laser cooling of a pure ion plasma to a crystalline state, a measurement of the Salpeter enhancement factor for fusion in a strongly correlated plasma and the measurement of thermally excited plasma waves. Also, discussed are experiments that demonstrate Landau damping, trapping and plasma wave echoes in the 2D ***ExB*** drift flow of a pure electron plasma, which is isomorphic to the 2D ideal flow (incompressible and inviscid flow) of a neutral fluid.

INTRODUCTION

When I became Norman's first graduate student in the early days of UCSD, he was just finishing his beautiful body of work on correlations, fluctuations and collisions in weakly correlated, thermal equilibrium plasmas [1, 2, 3, 4], and the first problem that he asked me to work on was a calculation of the triple correlation function [5]. Today, I will discuss recent experiments with nonneutral plasmas (pure ion and pure electron plasmas), selecting examples that illustrate correlation and fluctuation physics. At the end of my talk, I will discuss an example that illustrates my thesis research [6] with Norman on the nonlinear saturation of Landau damping through the trapping of particles in wave troughs, but in a novel context. Landau damping and trapping are not limited to plasma waves that are excited in Vlasov plasmas, but also can occur when Kelvin waves are excited on a vortex in an ideal fluid, that is, an incompressible and inviscid fluid [7]. As we will see, a Kelvin wave analogue of plasma wave echoes also exists in such fluids [8]. The 2 D dynamics of an ideal fluid is well modeled by the 2D ***ExB*** drift dynamics of pure electron plasma.

Figure 1 illustrates the confinement of pure ion plasma in a Malmberg-Penning trap [9, 10]. A conducting cylinder is divided axially into three sections, with the central section grounded and the two end sections held at a positive potential. The plasma resides in the region of the central cylinder, with axial confinement provided by electric fields and radial confinement provided by a uniform axial magnetic field. Because the ion plasma is not neutralized, Gauss's law requires that there be a radial electric field, and the radial electric field and axial magnetic field together cause the plasma to undergo ***ExB*** drift rotation.

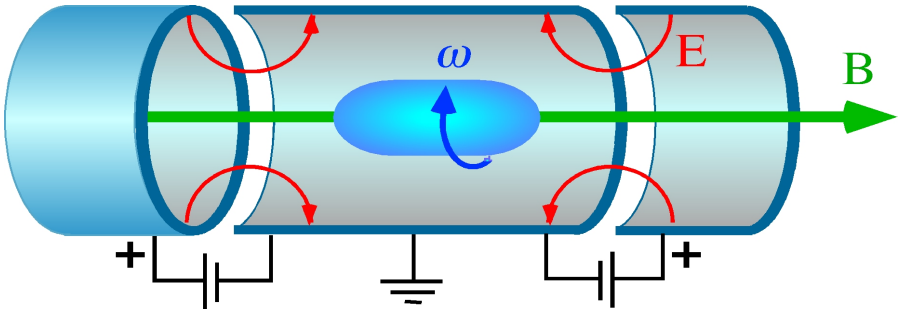

FIGURE 1. Schematic diagram of Malmberg-Penning trap for a pure ion plasma

An important property distinguishing these plasmas from neutral plasmas is that these plasmas can come to a state of thermal equilibrium while they are confined [11, 12]. As is well known, a neutral plasma cannot be confined by static electric and magnetic fields and also be in a state of thermal equilibrium [12]. When a neutral plasma is confined by such fields, there is always free energy, and the free energy tends to drive instabilities. That is why the confinement of neutral plasmas is notoriously difficult. In contrast, a plasma with a single sign of charge that is confined in a state of thermal equilibrium has no free energy and is guaranteed to be stable and quiescent.

For a cylindrically symmetric trap, both the total Hamiltonian and the total canonical angular momentum for the ions are constants of the motion, so the Boltzmann distribution takes the form [12]

$$f = C\exp[-(h-\omega p_\theta)/kT]\ , \tag{1}$$

where C is a constant, k is the Boltzmann constant, T is the plasma temperature, and ω is the plasma rotation frequency. The quantity $h = mv^2/2 + e\varphi(r,z)$ is the 1-particle Hamiltonian, where v is the particle velocity, and $e\varphi(r,z)$ is the potential energy. The quantity $p_\theta = mv_\theta r + eBr^2/2c$ is the 1-particle canonical angular momentum, where the first term is the usual mechanical contribution and the second term is the vector potential contribution. Here, (r,θ,z) is a cylindrical coordinate system with the z-axis coincident with the axis of the trap. The combination

$$h_{rot} = h - \omega p_\theta = m(\mathbf{v} - \omega r\hat{\theta})^2/2 + e\varphi(r,z) + m\omega(\Omega_c - \omega)r^2/2 \tag{2}$$

is the 1-particle Hamiltonian in a frame rotating with frequency ω. Here, $\Omega_c = eB/mc$ is the ion cyclotron frequency. From the first term in Eq. (2), one can see that the velocity dependence of the Boltzmann distribution is a Maxwellian in the rotating frame. The spatial dependence for the distribution is determined by the last two terms in Eq. (2), which together are the potential energy of an ion in the rotating frame. The last term is the correction to the potential energy due to rotation and consists of the centrifugal potential energy, $-m\omega^2 r^2/2$, plus the potential energy associated with the inward radial electric field that is induced by rotating through the magnetic field, that is, the quantity

$$-\int_0^r eE_r\,dr = \int_0^r e(\omega rB/c)dr = m\Omega_c\omega r^2/2 \tag{3}$$

.

To see that the Boltzmann distribution corresponds to a confined plasma, let us start at the center of the trap (i.e., $r=z=0$) and first move toward larger values of z. As z approaches the positively biased end cylinders, the second term in Eq. (2) becomes large and positive, forcing the distribution to become exponentially small. If one moves radially outward from the center and if $\Omega_c > \omega$, the third term becomes

large, again forcing the distribution to become exponentially small. The effective potential in the rotating frame is a potential well, and the plasma simply comes to thermal equilibrium in that well.

Another way to understand the thermal equilibrium state starts with the observation that the third term in Eq. (2), that is, the term that provide the correction due to rotation, is quadratic in r [12]. Suppose that the ion plasma were not confined by rotation through the magnetic field, but rather by an imaginary cylinder of uniform negative charge. Gauss's law implies that the cylinder would produce an inward radial electric field proportional to *r*, or equivalently, a radial potential that is a quadratic potential in *r*. By choosing the negative charge density to have a value determined by the relation $\omega_p^2 = \omega(\Omega_c - \omega)$, where $\omega_p^2 = 4\pi ne^2/m$ is the square of the plasma frequency and n is the density, the potential energy of an ion in the imaginary cylinder of uniform negative charge would be identical to the potential energy due to the third term in Eq. (2).

This is a useful way to think about the ion potential energy, since we know what will happen if we throw a bunch of ions into a potential well produced by the cylinder of uniform negative charge and the positively biased end cylinders. The ions will match their density to the density of the uniform negative charge filling the well up to some surface of revolution where the supply of ions is exhausted, and there the density will fall off on the scale of a Debye length. That is, for small Debye length, the plasma density is uniform out to the surface of revolution and there drops abruptly to zero. The temperature and rotation frequency also are uniform inside the thermal equilibrium plasma; if they were not, viscosity and heat conduction would produce entropy, and that is not possible for a state of maximum entropy.

Figure 2 shows a schematic diagram of a Malmberg-Penning trap that is used to confine Mg^+ ion plasmas at UCSD [13]. Provision is made for a laser beam directed along the magnetic field and for a laser beam transverse to the field. The beams are used to laser cool the plasma and to diagnose the plasma by measurement of the laser induced fluorescence at axial position *z*=0.

The thermal equilibrium state is predicated on the assumption of a cylindrically symmetric trap, and although care is taken to insure a high degree of cylindrical symmetry in the trap and fields, there inevitably remain small construction errors and field errors that break the cylindrical symmetry and exert a weak drag torque on the rotating plasma. This weak torque changes the total canonical angular momentum and produces a slow outward radial drift that leads to plasma loss over relatively long times, say, of order an hour. Of course, the ions of the rotating plasma are in thermal equilibrium with each other, but not with the stationary wall. To counteract the torque from the stationary field asymmetries and achieve arbitrarily long confinement, a field asymmetry that rotates slightly faster than the plasma is applied using the azimuthally sectored section of the wall labeled "rotating wall". The name derives from the notion that the rotating field asymmetry tricks the plasma into thinking that the wall is rotating.

In recent years, Norman and his collaborators have pursued such a rotating field scheme as a means of driving current in an FRC [14].

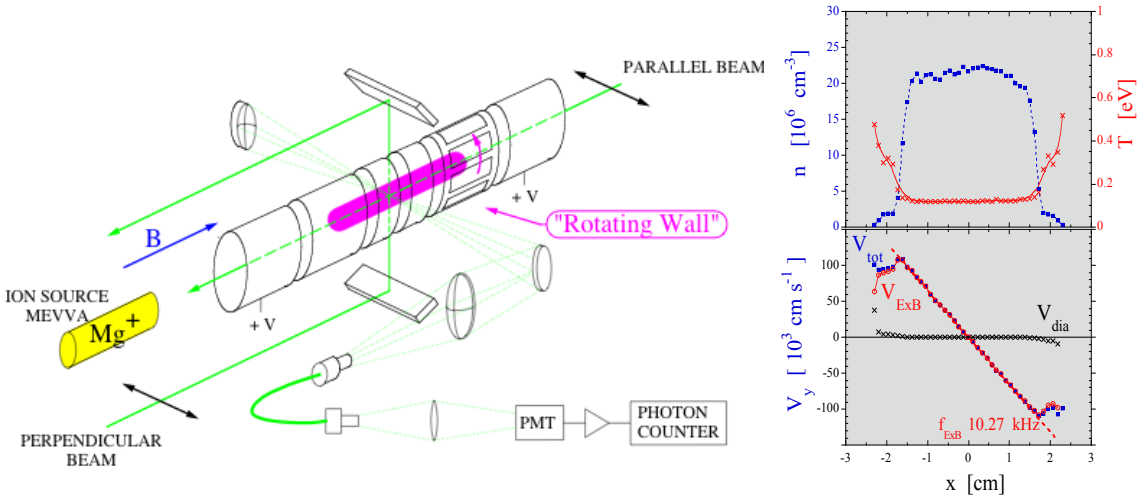

FIGURE 2. Schematic diagram of a Malmberg-Penning trap used to confine Mg^+ ions at UCSD.

The inset in Fig. 2 shows a plot of the density n, temperature T and azimuthal velocity V as a function of radius for an 18-hour-old plasma [13]. To see that the plasma is very near to thermal equilibrium, note that the density and temperature are essentially constant inside the plasma and that the mean azimuthal velocity is nearly a linear function of radius, implying near uniform rotation. The full velocity distribution is nearly Maxwellian in the rotating frame of the plasma. The macroscopic state of the thermal equilibrium plasma is well described by the Boltzmann distribution.

CORRELATION AND CRYSTALS

To understand the microscopic order, the Gibbs distribution is needed. This distribution is of the same form as the Boltzmann distribution, except that the 1-particle Hamiltonian h_{rot} is replaced by the N-particle Hamiltonian H_{rot}, including the ion-ion interactions. Using the same argument as used for the Boltzmann distribution, one can show that the Gibbs distribution for the magnetically confined ion plasma differs only by rotation from the Gibbs distribution for an ion plasma confined by a cylinder of uniform neutralizing negative charge [12]. All of the correlation properties are the same for the two systems.

A single species of point charges imbedded in a uniform neutralizing background charge is called a One Component Plasma (OCP) and has been a favorite theoretical model for the study of correlation effects [15]. All of the theory developed for correlations in a thermal equilibrium OCP can be taken over and applied to the magnetically confined pure ion plasma; indeed, the magnetically confined plasma is a simple laboratory model of an OCP.

For an OCP large enough that the bulk free energy dominates over surface free energy, the state of correlation is determined solely by the coupling parameter $\Gamma = e^2 / akT$, where $a = \sqrt[3]{3/4\pi n}$ is the Wigner-Seitz radius, essentially the inter-particle spacing [12]. For $\Gamma << 1$ theory predicts that the OCP is weakly correlated, for $\Gamma \sim 2$ stronger correlation and OCP begins to exhibit the local order characteristic of a liquid, and for $\Gamma = 178$ that there is a phase transition to a body-centered-cubic (bcc) crystal.

Figure 3. shows an experimental image of a Be^+ ion plasma that has been laser cooled to the bcc crystal state by John Bollinger and collaborators of the NIST ion storage group [16]. The plasma is a small spheroid with dimensions of order a millimeter, density of $n \simeq 4 \times 10^8 cm^{-3}$ and temperature $T < 10mK$, which corresponds to a coupling parameter $\Gamma > 200$. This value is well into the crystal regime. From the schematic diagram in the center of the figure, one can see that the NIST group orients the Malmberg-Penning trap vertically, rather than horizontally as was shown in Figs. 1 and 2. There is an axial laser cooling beam and a transverse laser cooling beam. In the image from the side view camera, one sees scattered light from both the axial and the transverse laser beams, with the latter being more intense. The strobed top view camera shows light largely from the transverse laser beam, and one can see that the ions are arranged in a crystal structure. A blow up of a small region shows the (100) plane of a bcc crystal with lattice spacing in close agreement with the theory prediction, based on the magnetic field strength and the rotation frequency. Interestingly, the light seen here is scattered by individual atoms, collected in synchronously strobed time windows over many rotations of the crystal structure.

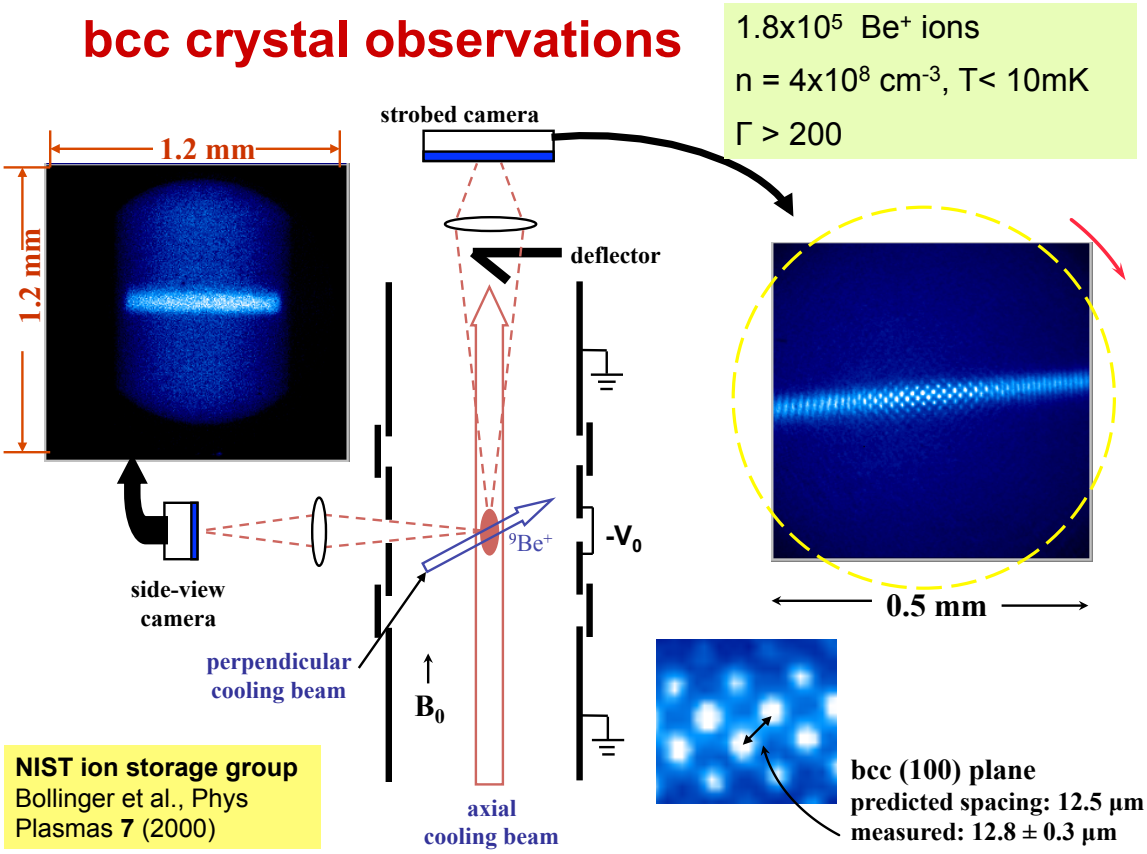

FIGURE 3. Schematic diagram of a Malmberg-Penning trap used by the NIST ion storage group to cool a Be^+ ion plasma to a bcc crystal state.

CORRELATION ENHANCEMENT OF CLOSE COLLISIONS

Norman often thought about correlation effects in terms of dressed test particles, where each particle is dressed in a Debye cloud [2,17]. Thinking along similar lines, Ed Salpeter predicted that Debye shielding, and more generally correlations, enhance the thermonuclear fusion rate, for example in stars [18]. The shielding reduces the Coulomb repulsion between two colliding ions, allowing the ions to approach one another more closely and increasing the probability of tunneling through to produce a fusion reaction. The enhancement of the fusion rate is approximately of the form $R_{enhanced} = R_0 e^{\Gamma}$, where $R_{enhanced}$ is the enhanced rate and R_0 is the rate neglecting shielding and correlation. The exponential enhancement factor assumes that Γ is not too large, and that restriction is satisfied for the experiments discussed here.

We want to measure this enhancement factor using the Mg^+ plasma described in Fig. (2). Since there aren't any fusion reactions in such a cryogenic ion plasma, we need a stand in for fusion reactions. When a plasma is strongly magnetized and has very low temperature, the cyclotron radius $r_c = \sqrt{kT/m}/\Omega_c$ can be smaller than the classical distance of closest approach $b = e^2/kT$. Then the cyclotron action is an adiabatic invariant that is nearly conserved in collisions [19]. The modifier "nearly" is used here since an adiabatic invariant is not an exact constant of the motion, but rather is changed by an exponentially small amount. Of course, close energetic collisions are most effective in changing the adiabatic invariant and liberating cyclotron energy. This sounds a lot like nuclear fusion, where it is the close energetic collisions that are

most effective in liberating the nuclear energy. In fact, Dan Dubin has shown that the analogy is quantitatively correct [20].

A measure of the rate of liberation of cyclotron energy is the collisional equipartition rate $\nu_{\perp\|}$, where $dT_\| / dt = \nu_{\perp\|}(T_\perp - T_\|)$. Here, $T_\|$ is the temperature associated with velocity components parallel to the magnetic field and $T_\perp$ is the temperature associated with velocity components perpendicular to the field. Dubin's enhanced equipartition rate [20] is given by $(\nu_{\perp\|})_{enhanced} = (\nu_{\perp\|})_0 e^\Gamma$, which is the same enhancement as that for the fusion rate. For the case of fusion, the exponentially small tunneling factor is averaged over a thermal distribution of collisions, and for the case of equipartition the exponentially small factor for breaking the adiabatic invariant is averaged over a thermal distribution of collisions.

Figure (4) shows measurements of the equipartition rate versus temperature for two values of the density [21]. The abscissa on the bottom is a logarithmic scale of temperature in electron volts, and the abscissa on the top is the corresponding ratio of r_c/b for the magnetic field strength 3 Tesla. The ordinate is a logarithmic scale of the equipartition rate.

For the lower density, $n = 1.2 \times 10^6 cm^{-3}$, the solid blue curve is the predicted equipartition rate neglecting the enhancement, and the dashed blue curve is the predicted rate including the enhancement. The points are the measurements. One can see that the rate follows the usual scaling $1/T^{3/2}$ for large T and falls of dramatically for sufficiently small T (i.e., $r_c/b < 1$), confirming the effect of the adiabatic invariant. For this value of density, the blue diagonal line in the lower left hand corner of the figure shows the value of Γ versus temperature. Since Γ is smaller than unity over the full range of measurements, the predicted enhancement is small, the solid and dashed blue curves are very close to each other, and the measurement points do not distinguish between the two curves.

The red curves and points are for the higher density, $n = 2 \times 10^7 cm^{-3}$, and for this density one sees that Γ values as large as 10 are accessed in the measurements. The points now favor the dashed curve, providing evidence of enhancement.

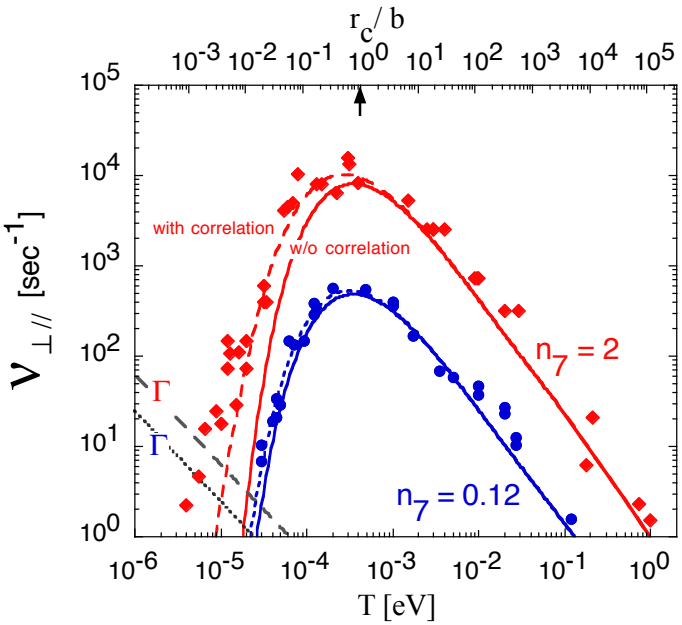

FIGURE 4. Predicted and measured equipartition rates versus temperature.

Figure (5) shows a log-log plot of the enhancement factor versus Γ. Again the points are measurements and the curves are e^Γ and three other more accurate predictions for the enhancement factor [22]. On this log-log plot, the curves are nearly indistinguishable. One sees a nine orders of magnitude enhancement of close energetic collisions.

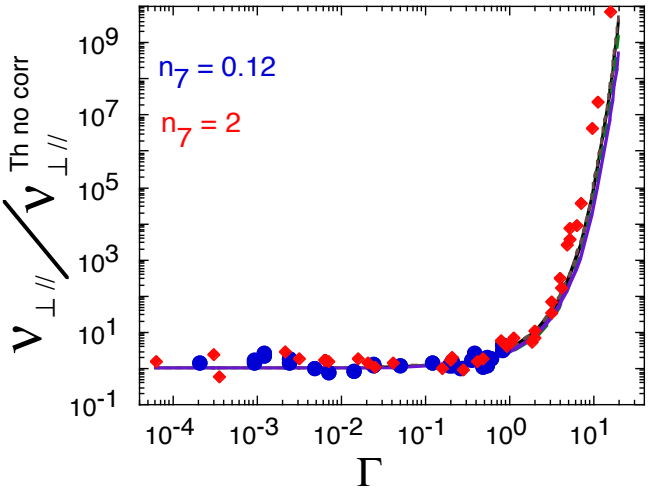

FIGURE 5. The measured enhancement factor versus Γ, compared to theoretical predictions for the enhancement factor.

THERMAL FLUCTUATIONS

Recent experiments have measured thermal level fluctuations of plasma modes, or more precisely Trivelpiece-Gould modes, in pure electron plasmas [23]. Figure 6 shows the result of a transmission experiment in which a sinusoidal voltage is applied to a driver electrode, and the response is measured on a well-separated receiver electrode. The driver frequency is swept, and when the frequency matches the frequency of a standing mode, the mode is excited and detected on the receiver electrode. The standing modes differ in the number of half wavelengths that fit in the length of the plasma column (i.e., $\lambda = L_p / 2m_z$). Figure 6 shows the received signal for three drive amplitudes, including zero amplitude. For zero drive amplitude, that is, thermal excitation, the modes m_z=1,3,4,5 are still received. The coupling to the m_z=2 mode is suppressed with this electrode geometry, and the resonance labeled RW is the signal from the "rotating wall" drive.

Figure 7 shows the received spectra of the thermally excited m_z=1 mode for four different plasma temperatures. The mode frequency increases with temperature according to the Bohm-Gross correction to the dispersion relation, so the four curves are displaced in frequency relative to one another. The width of each spectral peak is determined by the total damping rate for the mode, which is the sum of the intrinsic mode damping and the load damping, that is, the damping due to resistance in the measuring circuit. The intrinsic mode damping includes Landau damping, which becomes large as the temperature increases, substantially increasing the width of the resonance.

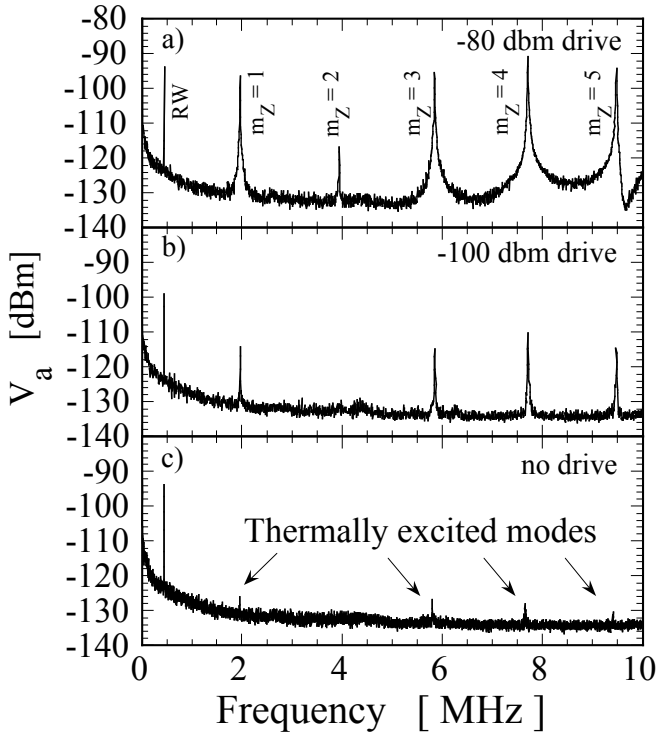

FIGURE 6. Spectrum of $m\theta$=0, m_z=1,2,…,5 Trivelpiece-Gould modes excited at three levels of drive amplitude, including zero drive, that is, thermally excitation.

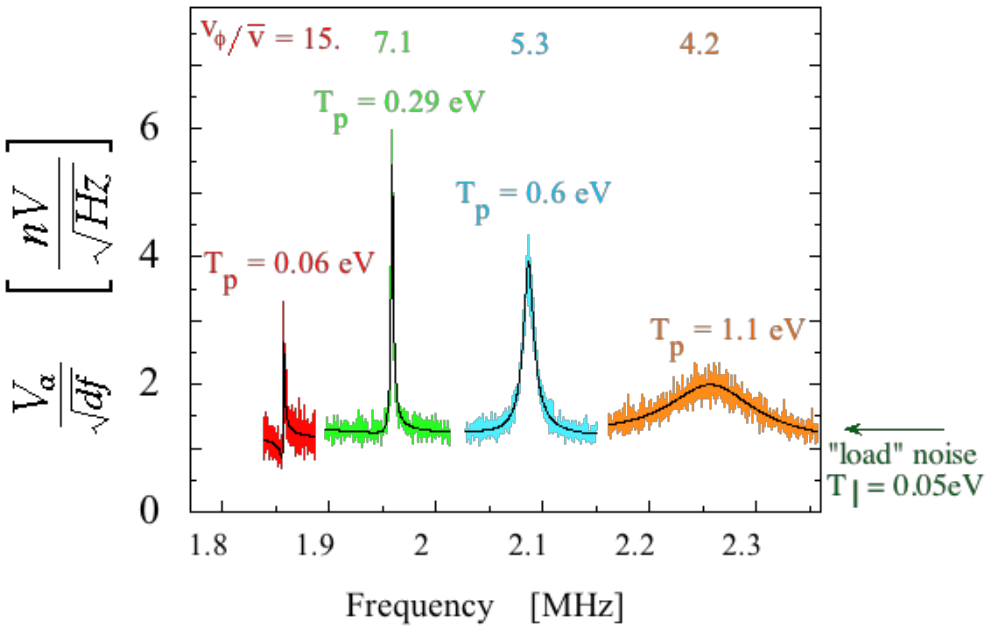

FIGURE 7. Thermal spectrum of the m_z=1 mode for 4 different plasma temperatures.

Norman's theoretical calculations of fluctuations in thermal equilibrium plasmas are not directly applicable to these experiments, because here the mode is coupled to a measuring circuit, characterized by

an impedance. The circuit resistance both damps the mode and excites the mode through thermal noise in the resistor.

Figure 8-a shows a schematic diagram of the plasma and measuring circuit (load), and Fig. 8-b shows an equivalent circuit, with the plasma impedance and load impedance in parallel between ground and the receiver electrode. From the equivalent circuit diagram, one obtains the generalized Nyquist formula

$$\frac{V_a^2(f)}{df} = 4kT_p Z_m^{\mathrm{Re}} \left| \frac{Z_l}{Z_m + Z_l} \right|^2 + 4kT_l Z_l^{\mathrm{Re}} \left| \frac{Z_m}{Z_m + Z_l} \right|^2 , \qquad (4)$$

where T_p is the plasma temperature and T_l is the load temperature. The quantity Z_m is the impedance of the plasma near the resonance of mode m, and Z_l is the load impedance. In Eq. (4) the sum of the squared voltages are added, since the shot noise in the plasma is uncorrelated with the noise in the load resistor. The first term in Eq. (4) is a Lorentzian resonance spectrum characterizing the mode, with slight shifts in the frequency and width due to interaction of the mode with the load. When the plasma temperature is much higher than the load temperature, the Lorentzian dominates the observed spectrum, as shown in Fig. 7 for the higher temperature measurements. At the lower temperature measurements (e.g.,kT_p=0.06 eV) the Lorentzian is distorted by the influence of the second term. Nevertheless, using the known impedance for the load and the shape of the measured spectrum, the plasma temperature T_p can be extracted. The black curves in Fig. 7 are the best fits to Eq. (4), determining T_p.

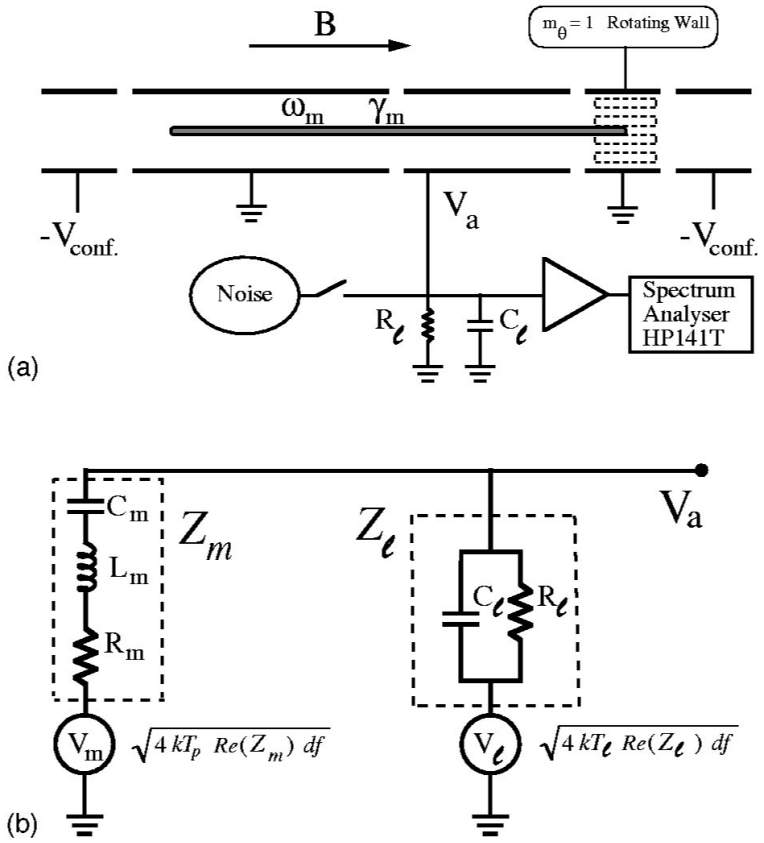

FIGURE 8. (a) Schematic diagram of Malmberg-Penning trap and measuring circuit. (b) Equivalent circuit for plasma mode and receiver

Figure 9 shows a comparison of the plasma temperature measured from the fluctuation spectra with the plasma temperature measured by dumping the plasma out axially along the field lines to a velocity analyzer. Of course, this latter measurement destroys the plasma. Since the agreement between the two

temperature measurements is good, the fluctuation measurements can be used as a non-destructive temperature measurement [23].

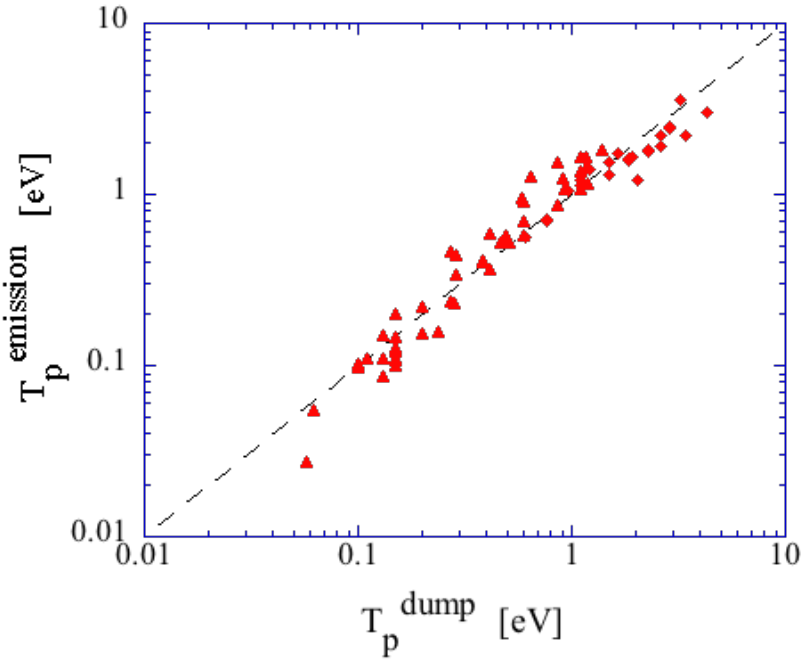

FIGURE 9. Comparison of plasma temperature measured from the thermal fluctuations with plasma temperature measured by dumping plasma to a velocity analyzer.

LANDAU DAMPING, TRAPPING, AND ECHOES IN IDEAL FLUIDS

Figure 10 shows a schematic diagram of a pure electron plasma experiment that can be used to model the ideal (incompressible and inviscid) flow of a neutral fluid [7]. The apparatus is operated in an inject-hold-dump sequence. Electrons from a hot filament are trapped and held long enough for interesting ***ExB*** drift flows to take place. The cylinder at the far end is then switched to ground, dumping the electrons out along the magnetic field lines to a phosphor screen, which is imaged by a CCD camera. In this way, the number of electrons along each field line is imaged.

In the experiments, frequencies are ordered as $\Omega_c >> \omega_B >> \omega_D$, where Ω_c is the cyclotron frequency, $\omega_B \approx \pi \bar{v} / L_p$ is the axial bounce frequency and ω_D is the frequency characterizing the ***ExB*** drift motion. With this ordering the cross-magnetic-field electron dynamics can be described as 2-D, bounce-averaged ***ExB*** drift dynamics. The density $n(r,\theta,t)$ evolves according to the coupled 2-D continuity equation and Poisson's equation, which are identical to Euler's equations for the flow of an ideal fluid [7]. In this equivalence, the electric potential corresponds to the stream function, the ***ExB*** drift velocity to the fluid velocity, and the electron density to the vorticity.

One advantage of the electron system is that the vorticity is imaged directly; one need not take the curl of measured flow velocities, which can include noise. Also, the effective viscosity is very low, allowing large Reynolds number ($R>10^5$), and the boundary condition at the wall is free-slip, so there are no boundary layers at the wall. Good shot to shot reproducibility enables movies of vorticity evolution, with subsequent frames in the movie imaged at successively later dump times. The system has been used for a wide variety of studies involving vortex dynamics and 2-D turbulence [24].

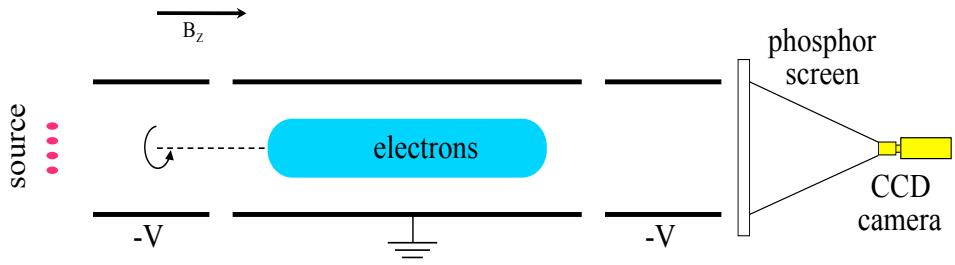

FIGURE 10. Schematic diagram of pure electron plasma experiment that is used to model the flow of an ideal fluid.

Figure 11 shows an experimental demonstration of the fluid equivalent of Landau damping and nonlinear saturation through trapping [7]. My thesis research with Norman, was a theoretical study of such saturation for the Landau damping of a plasma wave in a Vlasov plasma [5]. Of course, the Vlasov flow occurs in the phase space (x, v_x) and the ***ExB*** drift flow (and isomorphic ideal fluid flow) occur in (r,θ) space, but both flows are 2 D incompressible flows and nearly identical near the critical layer of the Landau resonance.

In the language of fluid dynamics, Fig. 11 (a) shows images of a vortex at three subsequent times. An m=2 Kelvin wave has been excited on this vortex; one can see a quadrupole distortion of the vortex in the T=0 image and cat's eye orbits at the resonant layer in the later images. The critical layer occurs at the radius where the Kelvin wave phase velocity matches the rotational flow velocity of the fluid in the vortex, and the resonant interaction between the wave and the fluid elements there gives rise to Landau damping of the wave. Figure 11 (b) shows the quadrupole moment of the vortex, effectively the amplitude of the m=2 wave, versus time. One sees an initial decay due to Landau damping followed by nonlinear saturation due to trapping.

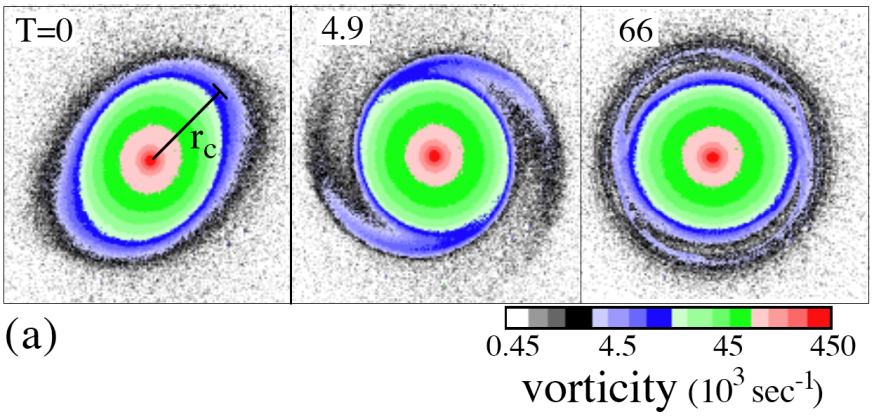

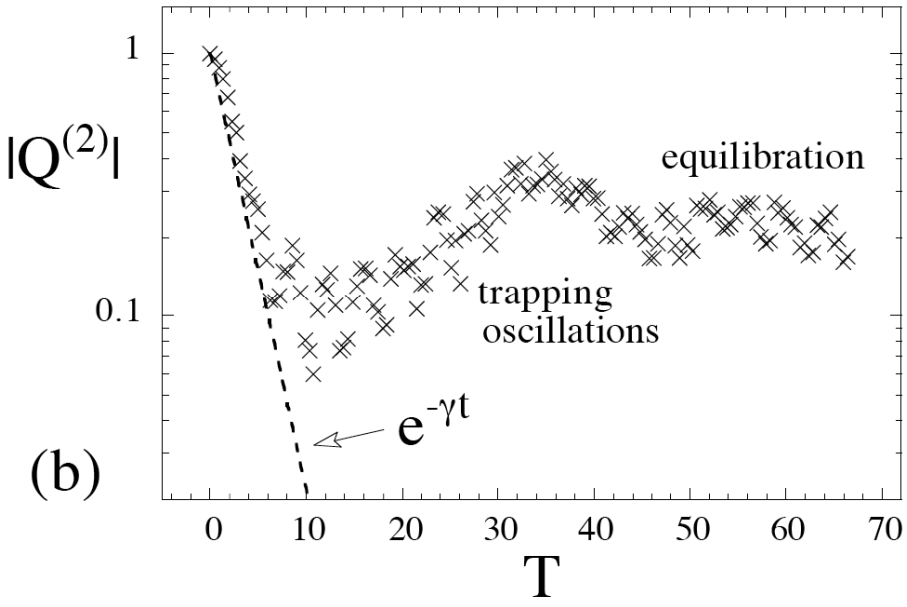

FIGURE 11. Experimental demonstration of the fluid equivalent of Landau damping and nonlinear saturation through trapping oscillations.

Figure 12 shows results from an experiment that demonstrates the existence of a fluid echo [8], a direct analogue of the plasma wave echo [25]. In this figure, the images (a) --- (f) are difference measurements, where the image of the unperturbed density is subtracted electronically from the image of the perturbed density, leaving only the perturbation. In image (a), one sees that an m=2 mode has been excited. Below the figures is a plot of the wave signal measured on a wall electrode, and one sees that the signal damps away as the m=2 perturbation phase mixes. One can think of Landau damping as resulting from such phase mixing. By the time of image (c), the perturbation is thoroughly phase mixed and the wall signal is nearly zero. Just before image (d), an m=4 mode is excited, rippling up the unperturbed density to form an l=4 density perturbation. This perturbation then phase mixes and the corresponding wall signal damps away. However, the m=4 field also ripples up the phase mixed ripple left over from the original m=2 mode, and a portion of this nonlinear m=2 ripple begins to un-phase mix causing an echo at the time of image (f). Of course, this reversal of phase mixing can be degraded by "non-ideal" flow effects. In these electron plasmas, the maximum coherence time for echoes is limited by extraneous rotational drifts associated with the end fields [8].

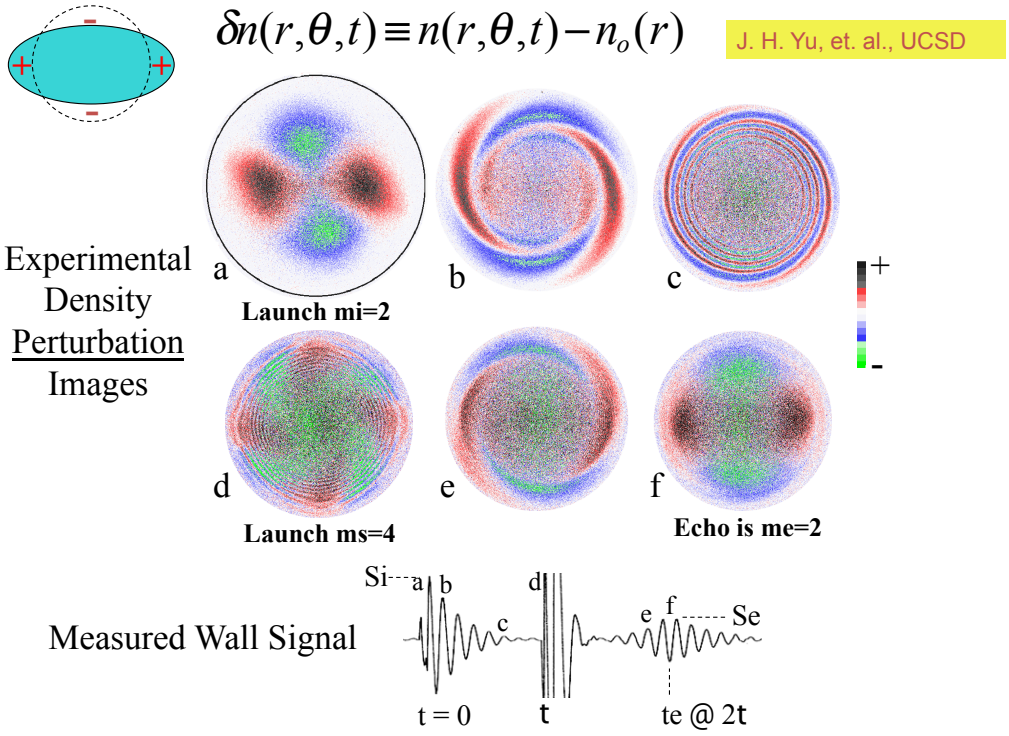

FIGURE 12. Experimental demonstration of the fluid echo.

ACKNOWLEDGEMENTS

As is apparent from the references, many people have contributed to the work that I have talked about today, and I want to give a special thanks to my long time collaborators at UCSD: Fred Driscoll, Dan Dubin, Cliff Surko, Francois Anderegg and Andrey Kabantsev. Also, special thanks goes to John Bollinger of the NIST ion storage group and to Roy Gould of Cal Tech with whom we have collaborated for many years. Over the years, research on nonneutral plasmas at UCSD has been supported by the NFS/DoE Partnership in Basic Plasma Science and Engineering and by the Office of Naval Research, where Chuck Roberson organized an ONR Research Initiative focused on the nonneutral plasmas.

REFERENCES

1. N. Rostoker and M. Rosenbluth, *Phys. Fluids* **3,** 1 (1960)
2. N. Rostoker, *Nucl. Fusion* **1**, 101 (1960)
3. N. Rostoker, *Phys. Fluids* **3,** 922 (1960)
4. M. Rosenbluth and N. Rostoker, *Phys. Fluids* **5,** 776 (1962)
5. T. O'Neil and N. Rostoker, *Phys. Fluids* **8,** 1109 1965)
6. T. M. O'Neil, *Phys. Fluids* **8**, 2255 (1965)

7. D. A. Schecter, D. H. E. Dubin, A. C. Cass, C. F. Driscoll, I. M. Lansky and T. M. O'Neil, *Phys. Fluids* **12,** 2397 (2000)
8. J. H. Yu, C. F. Driscoll and T. M. O'Neil, *Phys. Plasmas* **12,** 0055701: 1-8 (2005)
9. J. H. Malmberg, C. F. Driscoll, B. Beck, D. L. Eggleston, J. Fajans, K. S. Fine, X. P. Huang and A. W. Hyatt, *Non-neutral Plasma Physics* (C. W. Roberson and C. F, Driscoll, eds.) AIP Conf. Proc. **175** (1988)
10. T. M. O'Neil, *Physics Today* **52**, 24 (1999)
11. R. C. Davidson, *Physics of Nonneutral Plasmas* (Addison-Wesley, Redwood City, CA) (1990)
12. D. H. E. Dubin and T. M. O'Neil, *Rev. Mod. Phys.* **71**, 87 (1999)
13. Personal communication: F. Anderegg and C. F. Driscoll, UCSD
14. A. Kuley, Z. F. Wang, Z. Lin and F. Wessel, *Phys. Plasmas* **20**, 10(2013); A. Necas, *Electrostatic current drive for a field reversed configuration,* Phd. Thesis, University of California at Irvine, Department of Physics and Astronomy, (2007)
15. S. Ichimaru, *Rev. Mod. Phys.* **54**, 1017 (1982)
16. J. J. Bollinger, J. B. Mitchell, X. P. Huang, W. M. Itano, J. N. Tan, B. M. Jelenkovic and J. D. Wineland, *Phys. Plasmas* **7**, 7 (2000)
17. N. Rostoker, *Phys. Fluids* **7**, 479 (1964)
18. E. E. Salpeter, *Aust. J. Phys.* **7**, 373 (1954)
19. T. M. O'Neil and P. J. Hjorth, *Phys. Fluids* **28**, 3241 (1985); M. E. Glinsky, T. M. O'Neil, M. N. Rosenbluth, K. Tsuruta and I. Ichimaru, *Phys. Fluids B* **4**, 1156 (1992); B. R. Beck, J. Fajans and J. H. Malmberg, *Phys. Plasmas* **4**, 1250 (1996)
20. D. H. E. Dubin, *Phys. Rev. Lett.,* **94**, 025001 (2005)
21. F. Anderegg, D. H. E. Dubin, T. M. O'Neil and C. F. Driscoll, *Phys. Rev. Lett.* **102**, 185001 (2009); *Phys. Plasmas* **17**, 055702 (2010)
22. H. Dewitt and W. Slattery, *Contrib. Plasma Phys.* **39**, 97 (1999); A. Chugunov, H. E. Dewitt and D. G. Yakovlev, *Phys. Rev. D* **76**, 025028 (2007); S. Ogata, *Astrophys. J.* **481**, 883 (1997); S. Ogata, H. Iyetomi and S. Ichimaru, *ibid.* **372**, 259 (1991)
23. F. Anderegg, N. Shiga, D. H. E. Dubin, C. F. Driscoll and Roy Gould, *Phys. Plasmas* **10**, 1556 (2003)
24. C. F. Driscoll and K. S. Fine, *Phys. Fluids B* 2, 1359 (1990); T. B. Mitchell and C. F. Driscoll, *Phys. Fluids* **8**, 1828 (1996); A. A. Kabantsev and C. F. Driscoll, *IEEE Trans. On Plasma Science* **30**, 22 (2002); K. S. Fine, A. C. Cass, W. G. Flynn and C. F. Driscoll, *Phys. Rev. Lett.* **75**, 3277 (1995)
25. R. W. Gould, T. M. O'Neil and J.H. Malmberg, *Phys. Rev. Letters* **19**, 219 (1967); T. M. O'Neil and R. W. Gould, *Phys. Fluids* **11**, 134 (1968); J. H. Malmberg, C. B. Wharton, R.W. Gould and T. M. O'Neil, *Phys. Rev. Letters* **20**, 95 (1968)

Relevance of Advanced Nuclear Fusion Research: Breakthroughs and Obstructions*

Bruno Coppi[1, a)]

[1]*MIT Plasma Science and Fusion Center, 77 Massachusetts Avenue*
Cambridge, MA 02139-4307
[a)]Corresponding author: coppi@mit.edu

Abstract. An in depth understanding of the collective modes that can be excited in a wide range of high-energy plasmas is necessary to advance nuclear fusion research in parallel with other fields that include space and astrophysics in particular. Important achievements are shown to have resulted from implementing programs based on this reality, maintaining a tight connection with different areas of investigations. This involves the undertaking of a plurality of experimental approaches aimed at understanding the physics of fusion burning plasmas. At present, the most advanced among these is the Ignitor experiment involving international cooperation, that is designed to investigate burning plasma regimes near ignition for the first time.

*Sponsored in part by the U.S. Department of Energy.

INTRODUCTION

A puzzling question is why, after decades of research on nuclear fusion and highly significant advances made with it, an experiment capable of demonstrating the scientific feasibility of a self-sustained reactor has not been carried out. In fact, the often quoted promises of a fusion power producing reactor within 20 years were not made by scientists who had a sufficient in-depth knowledge of the importance of collective modes in determining the properties of fusion burning plasmas. The role of these modes has to be understood in order to conceive the construction of a significant fusion power station and proceed with it.

An aspect often overlooked is that the physics undertaking of the high pressure plasmas to be produced for fusion research is effectively transferable to other fields of physics and to high energy astrophysics in particular. Thus a special effort to maintain fusion research coupled to that of other relevant fields can be of mutual benefit and facilitate the advances of all fields involved. To outsiders, the coupling of research program motivated by two different needs, that of producing a novel source of energy and the other of attempting to understand the Universe, may seem extravagant but is well justified by our experience.

A parallel argument can be made for the wide spectrum of technologies developed in the past for fusion research and of those needed for further advancements. One of the best known cases is that of the LHC (particle accelerator) machine at CERN that employs super conducting magnets of the types developed earlier for fusion research.

The lack of understanding of these realities, and of the maturity of the field to proceed with experiments on fusion burning plasmas, by the entities in charge of fusion research in the richest countries of the world are the main reasons why this field has been kept from advancing at the rate and in the way that we had anticipated.

A SPECTRUM OF EXPERIMENTAL PROGRAMS

Given the state of fusion research and the options of its advancements that are available, it seems appropriate that a spectrum of experimental programs be undertaken as exemplified by the following:

1. A program aimed at identifying the collective modes in burning plasma close to ignition conditions. A program of this kind has to be based, in order to achieve its goals, on the high magnetic field technologies developed for the Alcator (MIT), Frascati Torus (ENEA) and Ignitor Programs. Ignitor is in fact the first machine designed with this objective.
2. A program on plasma confinement configurations sustained by the injection of high energy particle populations as pioneered by the GDT program Russia and the Tri Alpha Energy program in the US.
3. A program aimed at producing nearly steady state configurations such as that developed by the Tokamak Energy group of the U.K.
4. A program aimed at developing the technologies needed to achieve significant fusion burn conditions for D-^{3}He and pure D plasmas.
5. A continuation of the existing programs on tridimensional (stellarator type) confinement configurations.
6. A more coordinated program than the existing isolated efforts on fusion with polarized nuclei given the advantages that this would offer.
7. An effort to integrate the Iter project with the outlined portfolio of programs offering valuable contributions to the physics of large volume plasmas.

Clearly, all of these programs involve considerable risks of failure but the benefits of possible successes and of technology and physics advancements that they can generate can justify their costs.

NUCLEAR REACTIONS AND IGNITION CONDITIONS

The nuclear reactions that are considered for fusion research are as follows

- D-T
- D-^{3}He
- D-D
- p-^{11}B

Their properties are well known but the difficulties and advantages of employing them for fusion reactors are not equally well known. The DT reaction is the easiest to exploit in order to investigate the physics of fusion burning plasmas given its considerable reactivity at relatively low plasma temperatures. In reality the development of the high magnetic field technologies introduced in fusion research for the investigation of the fusion burn conditions of D-T plasmas can be extended to envisioned design experimental devices capable of exploring D-D and D-^{3}He burn conditions.

Referring to D-T plasmas, the reaction products are a neutron ($\varepsilon_n = 14.1\ MeV$) and an alpha particle ($\varepsilon_\alpha = 3.5\ MeV$). Ignition is defined as the condition under which energy associated with the produced α particles and deposited in the plasma can compensate all forms of energy loss. An important requirement for this is that the burning plasma be relatively free of impurities as they increase the rate of radiation energy loss and in addition can lead to the excitation of impurity driven modes that can degrade energy confinement.

The thermal energy balance at ignition can be written roughly (the appropriate averages would need to be specified) as

$$n_D n_T \alpha_F \varepsilon_\alpha < \sigma_F v >= n_e \left(T_e + T_i\right) \frac{1}{\tau_E}, \tag{1}$$

where α_F is the fraction of α particle energy deposited in the plasma column, $n_D = n_T = n_e/2$ indicate the particle densities, for the temperature of interest $\langle \sigma_F v \rangle \propto T_i^2$ and τ_E is a global thermal energy confinement. Thus Eq. (1) leads to consider a parameter of merit

$$P_M \equiv n\tau_E \frac{T_i^2}{\left(T_e + T_i\right)}, \tag{2}$$

that (with appropriate averages) can be used as criterion for advancement toward ignition. Unfortunately, this is often used without considering other important parameters such as the degree of purity $\left(1/Z_{eff}\right)$, the partial degree α particle containment, etc. to classify the results of advanced confinement experiments relative to the goal of ignition.

An important intermediate goal to be reached is that of the ideal ignition condition, defined as that where α particle heating is sufficient to compensate the (unavoidable) bremsstrahlung radiation losses. This, for $T_e = T_i$, and $\alpha_F = 1$ corresponds to

$$n^2 < \sigma_F v > \cong \alpha_B n^2 T^{1/2}, \tag{3}$$

and, for a homogenous plasma, leads to a temperature of about 4.5 keV. After this condition is reached, the density with which a plasma column is heated can be raised without encountering a bremsstrahlung barrier. It is paradoxical that no experimental program before Ignitor was proposed had been undertaken to reach the limited goal of ideal ignition.

Now we must note that in a toroidal magnetically confined plasma, the maximum plasma pressure is related to the value of the parameter

$$\beta_p = \frac{8\pi n\left(T_e + T_i\right)}{B_p^2}, \tag{4}$$

where B_p is the poloidal component of the magnetic field. Then the reactivity $\boldsymbol{R}$ scales as

$$R \equiv n^2 < \sigma_F v > \propto n^2 T_i^2 \propto B_p^4 \beta_p^2, \tag{5}$$

showing how important it is to devise experiments capable of sustaining relatively high poloidal fields. Likewise, the parameter of merit $\boldsymbol{P_M}$ scales as

$$P_M \propto \beta_p B_p^2 \tau_E. \tag{6}$$

By considering the results of a variety of significant experiments we may take

$$\tau_E \propto I_p n^{\alpha_1} B^{\alpha_2} / T^{\alpha_3}, \tag{7}$$

where $\boldsymbol{I_p}$ is the plasma current producing the field $\boldsymbol{B_p}$ and $\boldsymbol{B}$ is the toroidal magnetic field, and obtain

$$P_M \propto \beta_p I_p B_p^2 n^{\alpha_1} B^{\alpha_2} / T^{\alpha_3}, \tag{8}$$

where $\alpha_1, \alpha_2 \; and \; \alpha_3$ are positive numerical coefficients smaller than unity, pointing to a desirable direction that involves a combination of high currents and high poloidal fields [1].

As is well known there are stability considerations that link the maximum poloidal field to the toroidal field, the torus aspect ratio and other geometrical characteristics. The so-called "Iter Precipice" curve derived by various authors is an illustration of the scaling indicated by Eq. (5) as the poloidal field $B_p \propto I_p/\bar{a}$, $\bar{a}$ being a mean minor radius of the considered toroidal configuration. This curve shows that a decrease of the produced plasma current $\boldsymbol{I_p}$, relative to that corresponding to the assumed minimal stability safety factor, results in a steep decrease of the generated fusion power. Clearly Eq. (8) does not point to the necessity of constructing large scale devices in order to advance the physics of fusion burning plasmas contrary to widespread information supplied to the public opinion.

Finally we note that, if ignition can be achieved, it becomes possible to investigate the onset and development of the so-called "thermonuclear instability" related to the fact that $\langle \sigma_F v \rangle \propto T_i^2$. In fact, it has been shown that, as a result of the large values of the longitudinal to the transverse thermal conductivities, this instability can develop as a helical snake in a toroidal configuration [2].

HIGH ENERGY ASTROPHYSICS AND THE ALCATOR EXPERIMENTAL PROGRAM

One of the main motivations for starting and developing the Alcator program in 1969 was that of producing and investigating plasmas with parameters close to those inferred for the plasmas surrounding the very few X-ray stars known at that time. In particular, the objective was to create low density plasmas characterized by non-thermal spectra, such as that of the Crab Nebula, and plasmas with very high densities, such as those associated with Cygnus X-1 the first X-ray object discovered (besides the Sun) and the resulting thermal spectra. In fact, Cygnus X-1 inferred densities were in the range 10^{15}-10^{16} cm^{-3}, values that had never been produced earlier in a well-confined plasma.

To achieve these goals a toroidal machine featuring relatively high values of the ratio ***B/R***, ***B*** being the toroidal field and ***R*** the major radius had to be devised. The solution for the high toroidal field was introduction of a toroidal magnet made of copper Bitter-plates alternated with steel plates by B. Montgomery.

However, the most difficult problem was that of inventing a completely new poloidal field system that would fit in a compact configuration and induce and sustain relatively high currents. In fact, the Russian tokamak solution was not appropriate for this purpose. Thus the "air-core poloidal field system" of the type represented in Fig.1 was invented [B. Coppi and B. Montgomery, 1969].

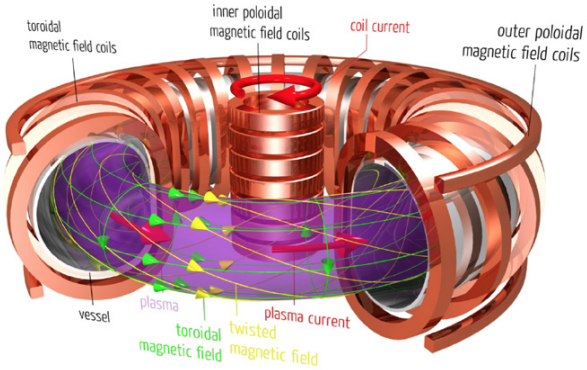

FIGURE 1. Magnetic coil and current configuration of a Tokamak

By now this system is adopted in all advanced toroidal confinement machines with an axisymmetric configuration including the largest machine under construction, Iter, Fig. 2.

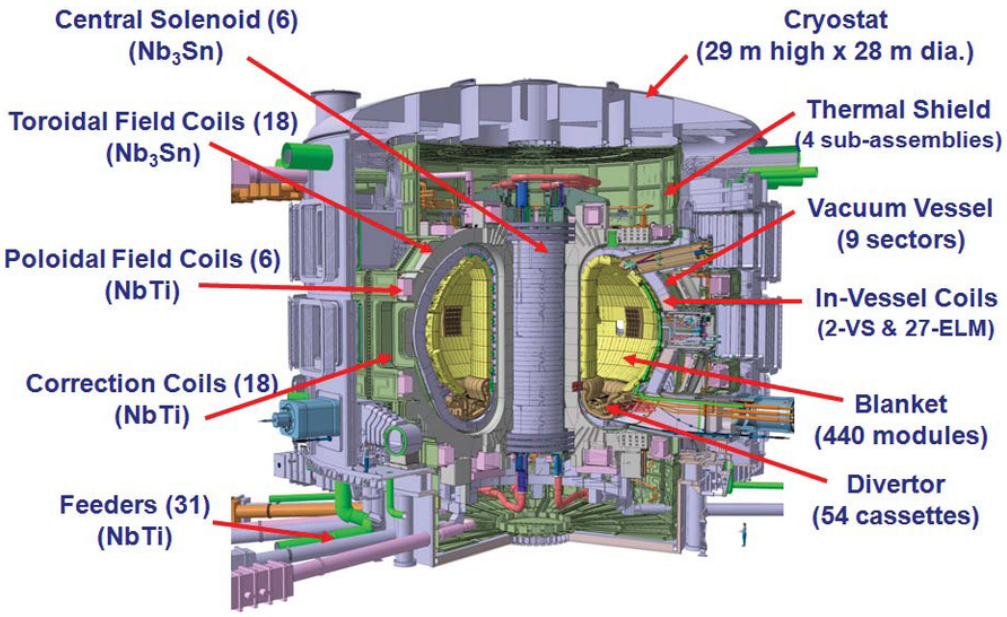

FIGURE 2. Schematic diagram of the components of the ITER tokamak

The first class of plasmas, non-thermal, were the first to be produced as they involved very low densities, in the 10^{12}-10^{13} cm^{-3} range. Then a new regime was discovered and analyzed consisting of a thermal and super-thermal electron populations created by the applied electric field $E_{//}$ along the toroidal direction. In this regime [3], called "slide-away" two types of mode were found to be present: i) an electron scattering mode that would produce a pitch angle scattering converting electron parallel (to the magnetic field) energy into perpendicular energy; ii) a lower hybrid mode producing a non-thermal ion populations to which longitudinal electron energy is transferred.

The second mode was later used to interpret the formation of ion-conics distributions in the auroral ionosphere [4]. The first mode had in fact been identified independently by V. Ginzburg in the context of cosmic ray physics. The analysis of the slide-away regime led to propose the first current drive process, called "slide-away regime in reverse" [5] whereby a lower hybrid mode is injected in a well-confined plasma producing a current carrying super-thermal electron population. The current drive process for toroidal plasmas had later received extensive attention theoretically and has motivated a considerably large experimental effort.

The second class of plasmas required a considerable more effort to produce them. In the case of the Alcator-A machine the density could be raised to peak values around 10^{15} cm^{-3} by the gas valve technique which led to identify a new particle transport equation [6] that is not of the diffusive type. Later this led to identify a similar equation for the angular momentum transport that has been verified repeatedly by dedicated experiments [7] and is relevant to astrophysics [8].

The discovery of the high density regime [9] carried two surprises: one, that the relevant plasmas had a high degree of purity as realized first by S. Mirnov; the other that the energy confinement time was relatively high and it increased with density. These observations, led to the idea that a high field compact experiment could be devised in order to achieve ignition condition and initiated the Ignitor program. Clearly, the original motivations to produce plasmas with densities $n \sim 10^{15}$ cm^{-3} came from Astrophysics but the end results turned out to be relevant to fusion research as well.

It may be worth mentioning the initial reactions that the idea of a compact ignition experiment derived from a small machine built in a university environment elicited (need a word here). The large research outfits reacted with evident unease. The most benign comment was by an outstanding member (B.B. Kadomtsev) of the major Russian Institute active in fusion research who remarked that the idea was "worth a Nobel Prize but would not be of practical use". A fusion manager of the European Commission in Brussels felt that his career and retirement

would be threatened by either a failure or a success of the experiment. Instead, the international academic community around the World reacted most favorably.

THE IGNITOR PROGRAM

As indicated earlier, the main objective of the Ignitor Program is to explore the ignition conditions of magnetically confined D-T plasmas while producing significant amounts of fusion power (up to about 100 MW). For this, a (necessarily) compact, high field device has been designed that advances the line of high field experiments which began with the Alcator program at MIT and was later also developed in Italy with the FT (Frascati Torus) program.

A short description and analysis of the machine core (see Figs. 1, 3, and 4) has been given in Ref. [1]. A detailed design of all the main machine components has been carried out and its results and drawings are now ready to be transferred to the industrial groups that have been identified as capable of constructing all the components of the machine core.

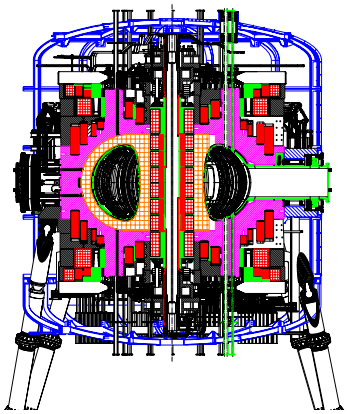

FIGURE 3. Vertical cross section of the Ignitor machine as presently designed.

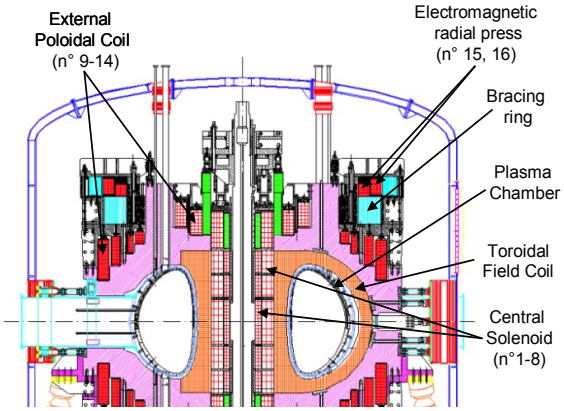

FIGURE 4. Sketch of the vertical cross section of the Ignitor machine where the main components are indicated.

The Ignitor facility is expected to be operated at the Troitsk (Moscow) site of Rosatom and managed by the IGNIR collaboration between Italy and Russia. At this time the Ignitor Program is the only one that has retained the objective of investigating the approach and the access to ignition conditions thanks to the regular updates of the machine design that have followed relevant advances in physics, technology and materials (See Table 1.)

TABLE 1. Main Design Parameters

Toroidal plasma current I_p (MA)	11
Toroidal field B_T (T)	13
Major radius R_0 (m)	1.32
Minor radius $a \times b$ (m^2)	0.47 × 0.86
Elongation κ	1.83
Triangularity δ	0.4
Plasma volume V_0 (m^3)	10
Edge safety factor $q_* = q_*(a)$	3.5
ICRF power P_{ICRH} (MW)	6.4→12.8
Poloidal plasma current (MA)	≅8.4
ICRH Pulse length (s)	4

A major effort in the machine design has been that of producing a plasma column in which a high mean poloidal field $B_p \cong \sqrt{10}T$ can be reached together with plasma currents $I \cong 10 - 11\,MA$ while maintaining reasonable safety factors against the onset of macroscopic instabilities (i.e. $q(\Psi_a) \cong 3.6$.)

Sophisticated numerical simulations of the plasmas that Ignitor is expected to produce have been carried out by 1+1/2 D transport codes [1, 10]. An example of a set of plasma parameters obtained by these simulations is given in Table 2.

TABLE 2. Example of Plasma Parameters Obtained with Modest ICRH Power (JETTO codes [10])

Toroidal plasma current I_p (MA)	10
Toroidal field B_T (T)	13
Major radius R_0 (m)	1.35
Minor radius $a \times b$ (m^2)	0.46 × 0.80
Elongation k	1.74
Triangularity δ	0.44
Plasma volume V_0 (m^3)	8.7
Edge safety factor $q_* = q_*(a)$	3.5
Central electron temperature T_{e0} (keV)	15.8
Central ion temperature T_{i0} (keV)	13.6
Central electron density n_{e0} (m^{-3})	8.7×10^{20}
Alpha density parameter n^*_α (m^{-3})	2.3×10^{18}
Fusion alpha power P_α (MW)	19.8
Plasma stored energy W (MJ)	11.5
OH power P_{0H} (MW)	3.5
Bremsstrahlung power loss P_{brem} (MW)	2.3
Poloidal beta $\langle\beta_p\rangle$	0.22
Toroidal beta $\langle\beta_T\rangle$ (%)	1.2
Bootstrap current I_{bs} (MA)	1.1
Energy confinement time τ_E (s)	0.58
Alpha slowing-down time $\tau_{\alpha,sd}$ (s)	0.09
ICRF power P_{ICRH} (MW)	2.2
Poloidal plasma current (MA)	7.9
ICRH Pulse length (s)	1.3

In this connection we observe that well confined plasmas with maximum densities close to 10^{15} cm^{-3} have been obtained repeatedly by the Alcator line of experiments and, with lower temperatures, by the Large Helical Device machine of Japan. To facilitate the attainment of these densities, the adoption, as in the case of the Alcator C experiments, of a pellet injector is planned. In the case of Ignitor, however, the required pellet speeds are considerably higher and further advances (expected to be possible) in the technology of these injectors are needed.

An important additional criterion that has driven the Ignitor design process is that of having a strong Ohmic heating that would persist up to temperatures where α particle heating can take over. Thus the need for an auxiliary heating system (ICRH is the only feasible option) is minimized together with the deterioration of the energy confinement time that has to be dealt with when Ohmic heating ceases to be significant. Assuming that the loop voltage is about constant, as has been observed experimentally until now, the best criterion to be followed in order to have a strong Ohmic heating rate is to have a major radius with the lowest possible values.

An essential requirement to achieve ignition condition is the degree of plasma purity that has to be high as discussed in Ref. [1]. This restricts the spectrum of plasma regimes with which Ignitor has to operate in order to fulfill its main objectives. Therefore while following the progress made in analyzing various transport regimes the main attention remains devoted to the very high density so-called L-regime discovered originally by Alcator that can be reliably obtained and to the so-called I-regime that continues to be the subject of a series of investigations whose results are promising. In both regimes the observed degrees of purity are well within the limits required for ignition. Ignitor graced the cover of a recent edition of Nuclear Fusion, Fig. 5.

FIGURE 5. View from above the core of the Ignitor machine. Reprinted on the cover of a recent volume of Nuclear fusion. "High Field Superconducting Magnet Technology, Second Stability Region and 'Advanced' Fusion Reactions"

Starting from a presentation on the Ignitor Program made at the 2002 Snowman meeting on the future of fusion research, the Program undertook the task of introducing high field superconducting magnet technology involving relatively large volumes into fusion research. The motivation is twofold. One is that a recently discovered superconducting material, Magnesium Diboride, has allowed the design of large size superconducting magnets operating at temperatures around 10 K. The development of these magnets has reached the point where they have substituted the two large vertical field copper coils in the design of the Ignitor machine. In addition, the bus bars for the LHC machine of CERN are made of this material and manufactured by the same company, Columbus of Genoa working on Ignitor. A pioneering toroidal machine involving high field superconductors had been constructed and operated earlier by S. Itoh at Kyshu University.

The other motivation is of a longer range nature. The limitation of using superconducting magnet in the Ignitor only for the large vertical field superconductors of large volume has not progressed sufficiently to warrant their substitution to super cooled (30 K) copper magnets. Looking into future experiments where long pulses are required a solution that has been found promising is that of hybrid magnets. These consist of a MgB_2 magnet

external component producing fields up to 10 T. The internal component that involves a smaller volume is envisioned to be "high" temperature superconducting magnet such as one made of REBCO with a configuration of the type suggested in Refs. [11, 2]. Clearly, when envisioning possible fusion power stations the development of high field superconducting magnets gives new and appealing perspectives. The structural solutions to deal with the relatively high stresses associated with high magnetic fields for present day experiments are expected to be suitable for more advanced experiments and, in case of success, of future power stations. In particular, the main structural solution adopted for the Ignitor machine is sketched in Fig. 6.

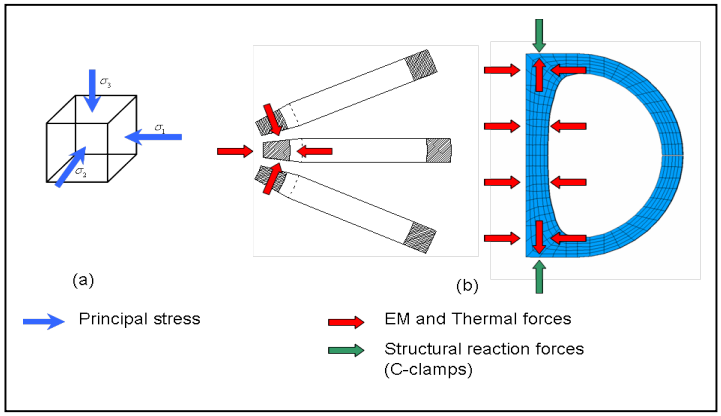

FIGURE 6. "Bucking, Wedging and Bracing" structural solution for the toroidial magnet. The objective is to minimize the unbalance between the principal stress components

Plasma axisymmetric configurations of the type that can be produced with existing technology were found to have the possibility, through proper choice of their characteristic parameters, to enter the so-called "second stability region" [12]. In this region the confined plasma can reach finite values of $\beta \equiv 8\pi n(T_e + T_i)/B^2$ without exciting known macroscopic instabilities the best known of which is the "ballooning instability" [13] driven by the plasma pressure gradient. By combining this result with the perspectives opened by advancements in high field magnet technologies it became possible to identify for the first time [14] ignition conditions for D-^{3}He and D-D burning plasmas with realistic parameters for which a serious program of investigations can be conceived. Thereafter G. Miley analyzed envisioned scenarios of power producing systems involving D-D and D-^{3}He burning reactors that continues to deserve attention.

CONCLUSIONS

Fusion research has to deal with the reality (and responsibility) of not having yet investigated the physical properties of meaningful fusion burning plasmas. The relevant knowledge is necessary in order to proceed with conceiving and constructing realistic power producing fusion reactors. On the other hand the field (fusion research) is ripe with the developments of new technologies and new related ideas to justify a faster rate of progress than the one we are witnessing, with a more committed support and a deeper understanding by both the public and the private sector.

ACKNOWLEDGEMENTS

This paper is based on a presentation made at the opening of the symposium to honor the memory of Professor N. Rostoker held by the University of California at Irvine. Professor Rostoker in addition to being a brilliant and creative scientist had been a generous friend to me as well as a source of inspiration and encouragement that sustained me through my professional life. The presented work was sponsored in part by the U.S. Department of Energy.

REFERENCES

1. B. Coppi, *et al*., *Nucl. Fus*. **53**, (2013) 104013.
2. B. Coppi, *et al., Nucl*. Fus. **55**, (2015) 053011.
3. B. Coppi, F. Pegoraro, R. Pozzoli, G. Rewoldt, *Nucl. Fus.* **16**, (1976) 2: 309-328.
4. T. Chang and B. Coppi, *Geophys. Res. Lett*. **8**, (1981) 1253.
5. B. Basu and B. Coppi, MIT/RLE Report PRR-76/4 (1976).
6. B. Copp and C. Spight, *Phys. Rev. Lett*. **41**, (1978) 551.
7. K. Nagashima, Y. Koide, H. Shirai, *Nucl. Fusion* **34**, (1994) 449.
8. B. Coppi, *Plasma Phys. Control Fus.* **36** (1994) B107.
9. E. Apgar, B. Coppi, *et al*. *Plasma Physics and C.N.F. Research* **1**, (1976) 247.
10. A. Airoldi, G. Cenacchi, *Nucl. Fus*. **37**, (1997) 1117.
11. B. Coppi and L. Lanzavecchia, *Comments Plasma Phys. Control. Fusion* **47**, (1987) 11.
12. B. Coppi, J. Ramos, A. Ferreira, *Phys. Rev. Lett*. **44**, (1979) 990.
13. B. Coppi, M.N. Rosenbluth, S. Yoshikawa, *Phys. Rev. Lett*. **20**, (1967) 190.
14. B. Coppi, *Physica Scripta*, T2/2, (1982) 590.

Early Days with Norman

Russell M. Kulsrud[1,a)]

[1]*Princeton University*

[a)]Corresponding author: rkulsrud@pppl.gov

I first met Norman in 1957, long before anyone else in the audience, and before most of you were born. I was a brash young fusion physicist working at Project Matterhorn in Princeton with a group of equally brash young physicists. At the time we had no idea that most of us were involved in a lifetime effort. I noticed that the secret meetings on fusion were filled with experimentalists, and I thought that the theorists should have their own meeting. I organized it, and limited it to at most 40 participants. When it got to 40, I noticed that Harold Furth was missing. I tried to hold the line, but Marshall Rosenbluth persuaded me to include him.

Marshall brought a person comparatively unknown to fusion physics named Norman Rostoker. Norman presented a very general kinetic theory, which developed everything from a systematic expansion in a single parameter. I went over to compliment him on this beautiful theory and, being Norman, he brushed off me and my compliments. In spite of this, we became fast friends. He was somewhat senior and older than me, and I was happy to be guided by his advice. Even though it had a touch of cynicism about it, it was very valuable.

We next met, with our wives, in Uppsala and had a lot of fun mostly laughing at the Swedes and their customs. For example, we arrived ten minutes late to a Smorgasbord and everything was gone. At dinner the soup had sugar in it and Norman was greatly offended by both things. When we left Sweden on the same airline, Norman literally ran to the plane to be the first one on. After the Smorgasbord fiasco he didn't want to be left behind. His wife, who was a great shopper, had bought a lot of pots and pans, and I remember that the Swedes were alarmed by the clacking of her pans as she ran with Norman.

As you may know, Norman was a terrible driver, in that he was always getting lost. Norman was driving us to a charming little baroque theater, called the Drottningholm, or the Queen's theater, and we got terribly lost. We stopped to ask directions from a Swede who did not speak any English. Norman tried to show him where we wanted to go on our road map, and he became enthralled with it. He stuck his head in the window and wouldn't let go of it. I still remember him saying "you are harr and you want to go thar". We finally wrested the map away from him and continued on our feckless search. Finally, we got there. Norman was not too impressed with the opera. But ever afterward when I would see him, he would say "We are harr and we want to go thar".

Norman had this idea that everybody, including the Swedes, should behave as though they were in California, and he simply couldn't tolerate any deviation. In 1960 Norman tried to get me to join him at General Atomics. I had impressed Creutz, the assistant director of GA, because when he came to Project Matterhorn he found me working in the control room, not realizing I was there because it was the only air-conditioned room at the laboratory. GA was very attractive to me with its swimming pools, tennis courts, its general *laisser faire* attitude, and the fact that there was a wealth of first class scientists working there. Norman got me an excellent offer from Creutz, but my attachment to Princeton was too strong, and I returned home.

Norman was not only one of the top scientists at GA, but he was also the chief entertainment officer for distinguished and not so distinguished visitors. For entertainment he would drive them over the border to Tijuana to see the strip joints and raunchy shows. On the spur of the moment, we took Velikov along. He had not brought any papers to justify his crossing the border, so on the way back we had to get him to lie down on the floor of the car, to get back across the border again. We could not figure out how Norman could get away with all his shenanigans, until one time (the story goes) he and Marshall and their wives were walking down the streets of Tijuana, and suddenly a very sexy dame rushes up to Norman, throws her arms around him and says 'Marshall' ! He had been using a false name.

I never sat down to work directly with Norman on any papers, but when we were at the same meetings we would have dinner together and tell each other jokes about our colleagues. Actually, his wife Helen told the better jokes.

Our longest encounter was at the Nick Christofilos Memorial Symposium on the Greek island of Spetsis in 1977. I believe that it was at this meeting that Norman developed his real passion for tennis.

My wife and I had a really tough time at this meeting because Ravi and Dipu Sudan were night persons and we would stay up to all hours in a taverna to watch the Greeks throw dishes at a wall, (a Greek form of recreation). On the other hand, Norman was a morning person, and Laney and I, would get up early to play tennis with Helen and him.

The Spetsis tennis courts were some of the worst courts in the world. They were full of pot holes. This did not phase Norman. He would get up early to survey the positions of all these pot holes. Then during our game he would aim the ball towards them. You may be aware that Norman does not like to lose and will do anything to avoid it. After the conference was over Norman stayed on for a week on the mainland and took intensive training in tennis. Some of you may have suffered from this.

Norman had a vendetta against DOE because they kept turning down his proposal for a proton-boron fusion reactor. He eventually decided to go at it without DOE.

The prelude to this was somewhat due to Bogdan Maglich and his Migma machine. His laboratory was in Princeton at that time. Maglich was originally a high energy physicist. (He actually found the Omega meson.) Suddenly, he became sick of high energy physics, and turned to fusion. He wanted to do something for humanity. On the basis of his total ignorance of plasmas he developed the Migma machine which, the way he went at it, was actually a horrible idea. He felt that if he could do high energy physics, plasma physics would be a snap. He planned to simply concentrate high energy beams through a center where the density would be large enough to make practical fusion energy.

He was working for an Advanced Projects center of DOE and getting nowhere, so DOE called for a review panel to evaluate the Migma idea. Norman, I, and also Herb Berk were put on the committee. Herb and I showed that synchrotron radiation would kill his idea, and Norman agreed, so we voted the idea down. (This did not stop Maglich who had many prominent friends from high energy physics who strongly supported him; people like Murray Gell-Mann and Glen Seaborg.) Well, our vote did not kill Migma, However, when I afterward spoke to Norman and asked him wasn't that a terrible idea, Norman said maybe there was something to what Maglich was doing. He was not referring to Maglich's physical idea itself, but to his idea of collecting support from a lot of important people, whether they understood the plasma physics or not.

At first, Norman teamed up with Maglich, but after a year or two they split up. By then Norman, with the invaluable help of Michael Binderbauer, had refined the colliding beam idea in a much more plausible direction. He also had collected a number of influential people to support him. He was still not able to sway DOE, but somehow his idea prevailed, TRI ALPHA emerged, and here we are.

FIGURE 1. Norman in Princeton in 1964, relaxing with three of his colleagues. Left to right they are: Russell Kulsrud, Martin Kruskal, Norman himself, and Carl Oberman.

Norman was a wonderful person to be friends with. His sense of humor always dominated him, and made him great fun to be with. His pulse power work was well beyond me, but his enthusiasm was not. I once got him mad at me when I said "Norman your sense of humor is ruining your career". He did not understand or appreciate this remark at all, but I think there was some truth to it. Norman was very profound and published much significant and important work, but he would often times rub people the wrong way just to put over a joke. Without this quality I think he could have been an even more prominent scientist, but then where would TRI ALPHA ENERGY be!

Formation and Sustainment of Field Reversed Configuration (FRC) Plasmas by Spheromak Merging and Neutral Beam Injection

Masaaki Yamada

Princeton Plasma Physics Laboratory, Princeton University
Princeton, New Jersey

Abstract.This paper briefly reviews a compact toroid reactor concept that addresses critical issues for forming, stabilizing and sustaining a field reversed configuration (FRC) with the use of plasma merging, plasma shaping, conducting shells, neutral beam injection (NBI). In this concept, an FRC plasma is generated by the merging of counter-helicity spheromaks produced by inductive discharges and sustained by the use of neutral beam injection (NBI). Plasma shaping, conducting shells, and the NBI would provide stabilization to global MHD modes. Although a specific FRC *reactor* design is outside the scope of the present paper, an example of a promising FRC reactor program is summarized based on the previously developed SPIRIT (Self-organized Plasmas by Induction, Reconnection and Injection Techniques) concept in order to connect this concept to the recently achieved the High Performance FRC plasmas obtained by Tri Alpha Energy [Binderbauer et al, Phys. Plasmas 22,056110, (2015)]. This paper includes a brief summary of the previous concept paper by M. Yamada et al, Plasma Fusion Res. 2, 004 (2007) and the recent experimental results from MRX.

THE STABILITY OF FRCS AND THE EFFECTS OF FINITE ION GYRO-RADIUS

In the past half century, compact toroid plasma configurations, such as field-reversed configurations (FRCs), have been extensively studied in the search for a cost-effective, high-power-density fusion energy reactor concept [1-4]. Since FRC's have the highest achievable beta among magnetic fusion configurations, they offer the possibility of an advanced-fuel reactor, provided the confinement and stability is sufficiently favorable. In this paper, we describe a recent development of a generic compact reactor plasma concept by addressing critical issues for forming, stabilizing and sustaining a compact toroid plasma with the use of plasma merging, plasma shaping, conducting shells, as well as neutral beam injection (NBI).

A significant progress in the theoretical understanding of FRC stability properties has been made in the past decade regarding the stability with respect to low-n (toroidal mode number) magnetohydrodynamic (MHD) modes, which is one of the most important scientific issues in field-reversed configuration (FRC) research. According to an empirical scaling relation [5] based on experimental data, a stability criterion of FRCs of various shape against global MHD modes is written as

$$S^*E < 3\text{-}4, \qquad (1)$$

where E is the separatrix elongation factor, and the kinetic parameter $S^*=R_s/d_i$, is the ratio of the separatrix radius to the ion skin depth d_i. S^* is also approximately equal to s, the ratio of the separatrix radius to the ion gyroradius ρ_i in the external magnetic field (since $\rho_i \sim \lambda_i$ for $\beta \sim 1$). Since S^* is a key factor for stabilizing effects of finite ion Larmor

radius effects (FLR effects), several recent theoretical studies have considered the stabilizing effects of finite ion FLR effects together with the effects of the Hall term and those of sheared ion flow on the n=1 tilt mode in prolate FRC configurations [6-11]. These studies have resulted in significant advances in the basic understanding of FRC stability properties in comparison with simpler rigid rotation models. In these studies, (a) the role of ion FLR effects in affecting FRC stability properties has been clarified showing stability of FRC for finite gyro-radius effects; (b) resonant particle effects have been demonstrated to be responsible for the instability drive in cases where FLR effects and the Hall term stabilize the MHD-unstable modes [10]; (c) modern relaxation theory and the properties of two-fluid flowing equilibria have been studied; (d) and the nonlinear saturation of the n=1 tilt instability has been discovered in low-S^* configurations [11]. The recent simulations demonstrate for variety of equilibria that the normalized tilt mode growth rate is a function only of the parameter S^*/E [8]. This supports the empirical stability scaling obtained earlier with the parameter S^*/E [5] shown in Eq. (1). Very recently in the high performance FRC plasma, the above relationship was also experimentally verified by Binderbauer et al.[30]. Figure 1 demonstrates a relationship between evolution of the C-2 discharges and the value of S^*/E. As the time progression from right to left, the stable discharge (solid squares) stays well below the boundary for $S^*/E < 3$, while two unstable shots (solid and open circles and triangles) closely approaches or cross the boundary.

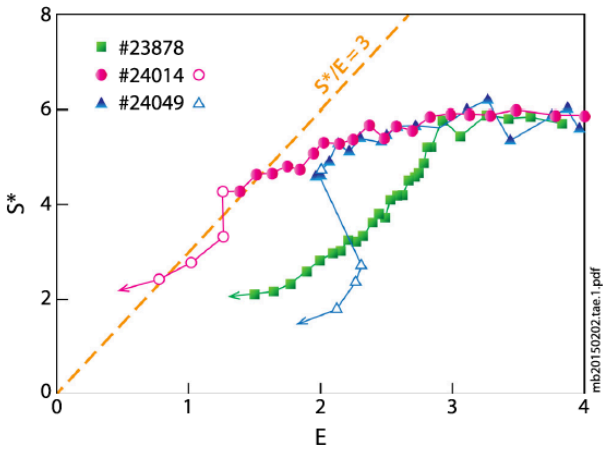

FIGURE 1. Global stability diagram for FRC and recent C-2 results. Evolution of S*/E parameters for stable (solid squares) and unstable (circles and triangles) discharges. Also shown is the nominal tilt stability boundary at S*/E = 3. Open symbols indicate the further progression of the discharge after onset of instability. From Binderbauer et al [30].

Effects of energetic beam ions: Thermal ion kinetic effects play a major role in stabilization of global MHD modes in low-S^* prolate FRC experiments [6-11]. Injection of energetic beam ions can provide an additional stabilizing mechanism in both prolate and oblate FRCs, provided that the beam ions carry a significant fraction of the total plasma current [12-14]. In addition, the injection of energetic beam ions is expected to contribute to plasma heating and sustainment of the FRC configuration. The low-frequency stability properties of a hybrid system in which field reversal is created by both plasma currents and by a low-density energetic component of large-orbit ions, have been studied previously in theory by means of a generalized energy principle and by using 3D numerical simulations. It has been shown for the low-n co-interchange (kink) modes that the energetic ion beam contribution is stabilizing provided the condition $n|\Omega| > \omega_\beta$ is satisfied [14], where Ω is the ion toroidal rotation frequency, ω_β is betatron frequency, and $\omega << \Omega$ is assumed. Numerical simulations of the tilt instability including the effects of the energetic beam ions have been performed [11]. In some of the cases considered, stabilization of the tilt instability was obtained for normalized beam ion density $n_b/n_e < 2\%$, and large beam ion velocities $V_b \geq 10V_A$, where the Alfven speed $V_A = B_Z/\sqrt{\mu_0 nm}$ is defined in term of the peak density and edge field strength. Furthermore it was found that the beam particles tend to coalesce near the mid-plane, which reduces the efficiency of stabilization by energetic ions. Linearized simulations have shown that these resonances (particularly the one with l=2, m=0) can contribute significantly to stabilization or destabilization of the low-n kink modes depending on the beam parameters and the mode polarization. More importantly, nonlinear hybrid simulations have demonstrated that the beam-driven instabilities are not dangerous, because they saturate nonlinearly at low amplitudes by changes in the beam ion distribution function [9-11]. Additional stabilizing effects are expected even after the beam ions are slowed down but remain hot due to the large ion-ion collision time, by effectively reducing the parameters S^* through ion gyro-viscosity.

Oblate FRC Stability Properties with Conducting Shell: The global stability properties of oblate (small elongation, E<1) FRC configurations have been investigated numerically using both 3D MHD and hybrid simulations [9, 11]. It is found that the n=1 tilt mode becomes an external mode when E<1, and that this mode can be effectively stabilized by a close-fitting conducting shell, even in the small-gyro-radius (MHD) regime. Interchange mode stability properties are strongly profile dependent, and all n≥1 interchange modes can be stabilized for a class of pressure profiles with a separatrix beta larger than 0.035. The simulation results show that all n=1 modes can be stabilized in the MHD regime, but additional means of stabilizing the n>1 co-interchange modes are thought to be required.

FORMATION OF FRC BY SPHEROMAK MERGING:

An FRC can be formed by merging two spheromaks of opposite helicity, i.e, with the same toroidal currents and opposite toroidal fluxes. Spheromak merging was first studied on the TS-3 device at the University of Tokyo in the late 1980's and then further developed on the MRX device in 1990's [15-22]. These TS-3 and MRX experiments demonstrated that the plasma merging formation scheme could successfully produce both spheromaks and FRCs. These experiments also revealed a violent plasma acceleration and strong ion heating during the spheromak merging process [17]. These effects were observed in both merging configurations, but they were particularly strong in the counter-helicity case. This formation scheme has significant advantages over the conventional theta pinch formation schemes, since it does not require uncontrollable shock heating, nor electrodes. Since spheromak plasmas are inductively formed in much slower time scale than the Alfven time, a large amount of magnetic flux can be generated resulting in a large FRC target plasma before injecting high energy ion beams. In the counter-helicity merging, a violent plasma acceleration was observed through a slingshot effect in the toroidal direction [17] as the field lines contracted after the merging of two toroidal plasmas of the opposite helicities [Fig.2]. This acceleration mechanism and direction is significantly different from that conjectured in the typical 2-D models. In the 2-D picture, plasma acceleration occurs perpendicular to the neutral line. But in the 3-D picture, plasma acceleration can occur parallel to the neutral line. Initially, the merging plasmas formed the Bt profile shown in color in Fig. 2, positive on the left side and negative on the right side. As reconnection progressed, the value of Bt decreased, as expected, but then the Bt profile flipped (changed its polarity) between t = 18 and 22 msec [19]. An energy transfer from magnetic to plasma thermal energy was anticipated in this dynamic reconnection process of toroidal field annihilation. Strong ion heating up to Ti = 200 eV has been measured during reconnection, as shown in Fig. 2.

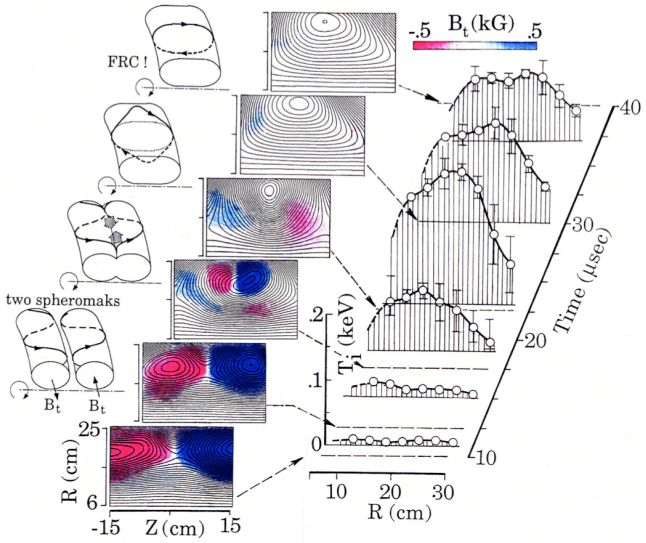

FIGURE 2. Time evolution of the flux contours, toroidal field (red for negative values and blue for positive values), and ion temperature during the formation of an FRC plasma by merging counter-helicity spheromaks [17].

Many experimental campaigns were carried out to study plasma formation more in detail by spheromak merging. The University of Tokyo program was expanded with the construction of the larger TS-4 merging device that contains both flux cores and coaxial magnetized guns. Another facility, the Swarthmore Spheromak Experiment (SSX), was constructed in the late 1990's to study merging with simply-connected spheromaks [21].

In counter-helicity merging experiments [18], relative values of the helicity of the two merging spheromaks were varied. The results indicated that the FRC equilibrium was almost as robust as the Taylor-state spheromak. When the difference of helicity in two spheromaks is smaller than a threshold value, i.e., $(|K1| - |K2|)/(|K1| + |K2|) < 0.2$, the resulting plasma relaxes to a FRC configuration. When the difference was larger than the threshold value, the

resulting plasma relaxed to a Taylor-type spheromak. An important difference between FRC relaxation and Taylor-type spheromak relaxation is that a significant portion of annihilated toroidal magnetic field energy, as much as 70%, was converted to the kinetic energy of ions in FRC formation, while no such energy was available for ion heating in the co-helicity merging case.

Among several previous experimental campaigns, first in the mid-1990's [22] and later from 2004-2008 [Gerhardt '07, '08, '09], were conducted to study merging on MRX. The two axi-symmetric flux cores create spheromaks that pinch-off and then merge in the center of the MRX device. In the 2004-2008 campaign, counter-helicity merging was employed to the study of formation, stability, and sustainment of oblate FRCs. It was demonstrated that a central Ohmic heating (OH) solenoid like those used in tokamaks could be used to induce toroidal currents in the FRC in order to sustain it for longer than the resistive decay time. In addition, shaping field coils were used to control the FRC boundary shape and elongation. This permitted a study of the effect of these shaping fields on stability. It was experimentally demonstrated that the n=1 tilt mode (and the n=1 radial mode) are stabilized in an oblate shape FRC. Also, the growth rate of n=2 modes slowed with favorable shaping. Finally, instability to n=2 co-interchange (not rotational) modes was observed for the first time, even in FRCs that were stable to the aforementioned n=1 modes. These results constituted important advances in the understanding of FRC physics. In addition to these stability and sustainment results, significant ion heating was again observed in counter-helicity merging experiments. A co-helicity merging of two spheromaks generated less heating but sufficiently high-beta plasmas (beta ~ 0.2-0.3).

SPIRIT CONCEPT

This section describes a promising FRC reactor program based on SPIRIT (Self-organized Plasmas by Induction, Reconnection and Injection Techniques) concept developed late 1990's at PPPL [22,23]. Three critical issues were discussed regarding plasma formation, sustainment of plasma with the use of plasma shaping, conducting shells, neutral beam injection (NBI) and a current transformer. In the SPIRIT program, compact toroid plasmas would be generated by the merging of co- and counter-helicity spheromaks produced by inductive discharges utilizing flux cores, and the plasmas would be sustained by the use of neutral beam injection (NBI) [23]. Plasma shaping, conducting shells, and the NBI would provide stabilization to MHD modes. This generic idea has been verified in C-2 experiment carried out recently at Tri Alpha Energy Company [30]. Although promising FRC reactor concepts have been developed in the past [4], a reactor design is outside the scope of the present paper,

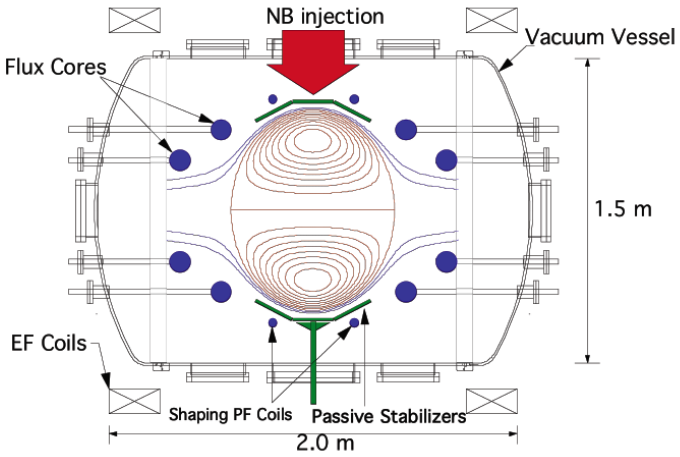

FIGURE 3. Schematics of a proposed SPIRIT experimental device, including plasma forming flux cores, passive stabilizers, shaping coils, and neutral beam injection.

The physics basis for the SPIRIT concept has been verified in numerical calculations [6-13], as well as oblate FRC experiments. Some numerical studies have found an operation regime in an oblate FRC which is stable against all global modes. This configuration utilizes a stabilizing shell and neutral beam injection with a practically broad velocity distribution [10]. Slow formation of an FRC plasma by the merging of spheromak plasmas has been successfully demonstrated in a number of experiments as described above [15-21]. The experimental observation of the co-interchange instability in MRX [24] yields further motivation for the NBI system included in the SPIRIT concept. Many of these techniques unique to the SPIRIT concept are illustrated in Fig. 3. Spheromaks are formed by a method utilizing a pair of flux-cores on each end of the device. These spheromaks, which have oppositely directed toroidal fields, are allowed to merge in the center of the machine, producing the FRC as is illustrated. The combination of the equilibrium field (EF) coils, flux-core windings, and shaping field coils is used to control the plasma shape. To stabilize n=1 tilt/shift modes, passively stabilizing shells are utilized. It was considered and studied that a 25kV, 60A neutral beam is injected into this target plasma. The kinetic effects associated with these beam particles aids the stabilization of tilt and co-interchange modes, as well as helping to sustain the plasma pressure, and hence the diamagnetic toroidal current of the FRC. Other components of the SPIRIT concept, such as possible inductive transformers [can be inserted from the both ends] and quadrupole stabilizers for the n=2 rotational mode are not illustrated in this figure.

A key element of the SPIRIT program was NBI stabilization of the plasma via finite Larmor radius (FLR) effects [23]; the target plasma must have sufficient orbit confinement of these high energy particles for this scheme to be successful. In order to generate plasmas with proper flux levels and shaping for neutral beam injection, FRC plasmas would be generated by the counter-helicity merging of inductively formed spheromaks. This flux-core based inductive formation scheme, which uses neither conventional fast shock heating nor electrode discharges, has significant advantages for the development of a compact reactor core. A large amount of magnetic flux can be generated in this scheme. A series of successful spheromak merging experiments have been carried out on the devices in which FRC configurations are formed by the merging of two toroidal plasmas with opposing toroidal fields. These experiments have established the technical feasibility of this approach.

PLASMA MERGING EXPERIMENTS ON MRX AND MEASUREMENT OF ION HEATING

Important progress has been made on the MRX device in three important areas regarding; formation by plasma merging, stability study, and current drive and sustainment of compact toroids. A systematic study of oblate FRC equilibrium and stability, including detailed comparisons with theoretical and numerical results has been performed in MRX [24] with the apparatus shown in Fig.4. It should be noted that the two inductive solenoids are inserted from the both sides of major axis. They could be removed if necessary. Ability to form oblate FRC by spheromak merging and to modify the FRC shape in a controlled manner through the use of equilibrium field shaping, have been demonstrated; the n=1 tilt and shift modes stabilization by central conductor and strong shaping fields; and unstable n>1 co-interchange modes studied experimentally, and these modes were shown to be reduced in very oblate plasmas [24-26]. To generate large ion radius which induce more FLR stabilization, Argon gas was used. Oblate FRCs have been sustained for longer period than 15 magnetic diffusion times by use of an inductive solenoid.

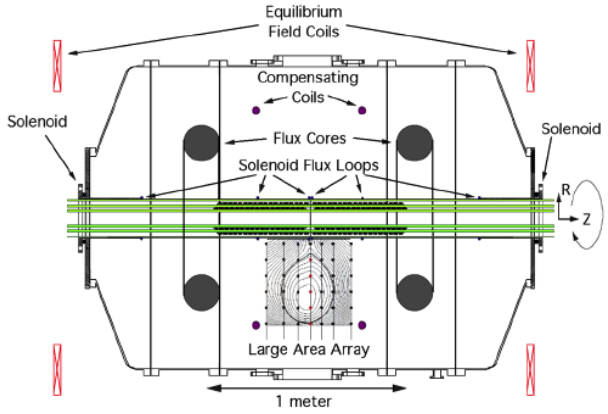

FIGURE 4. MRX set-up for FRC/SPIRIT stability study. The two inductive solenoids can be separated or removed.

It was again found on MRX the spheromak merging experiments [26, 27] that a significant amount of magnetic energy is converted to ion thermal energy during plasma merging and that the energy conversion rate is much larger than the value expected from classical dissipation mechanisms. The reconnection speed was factor of 10 faster than the Sweet-Parker time. The plasmas are made to merge to induce reconnection by controlling external coil current. Through time evolution of the poloidal flux contours derived experimentally from internal probe arrays, it was found that merging of spheromaks of opposite helicity occurs faster than merging of the same helicity. The evolution of poloidal and toroidal flux carried by plasmas showed complete annihilation of toroidal flux through reconnection for

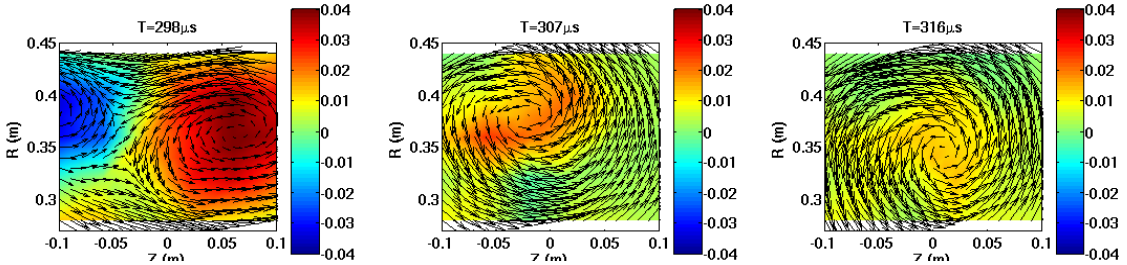

FIGURE 5. Measurements of formation process of FRC plasmas in MRX through snap-shots of the magnetic field at three times during the merging process in MRX. The poloidal magnetic field is represented by arrows, and the toroidal magnetic field by colors. The toroidal field scale on the right of each figure is in units of Tesla.

counter-helicity merging as shown in Fig.5.

We measured the dynamics of the plasma merging using a two-dimensional array of magnetic pickup coils centered on the merging region. This array measures all three components of the magnetic field at each location, providing detailed information on the magnetic structure. In Fig.5, the merging sequence for a helium discharge is illustrated at three times. The flux cores are located at Z=±0.4m, outside the range of the measurement. At t=298μs, the two spheromaks have pinched off from the flux cores and are approaching each other. At t=307μs, the poloidal fields of the two spheromaks have reconnected, but the toroidal fields are still present and finite. At t=316μs, the toroidal fields have settled to a small final value [maximum $(B_T/B_p)<20\%$], and the FRC plasmas is formed. The FRC plasma then decays away, possibly due to an instability.

STRONG ION HEATING DURING RECONNECTION

This merging process can lead to significant ion heating, in agreement with previous results [17]. The ion temperature evolution is shown in Fig.6, for helium discharges. The shaping field coils are used to compress the

spheromaks before merging in this case, leading to large values of the reconnecting fields. The ion temperature is measured using a spectroscopic probe [27] located at (R,Z)=(0.375,0) meters. The ion temperature before merging is about 10 eV. During the merging process, the temperature increases to 30 eV, significantly exceeding the electron temperature (measured by a triple Langmuir probe). This reconnection-driven ion heating may provide an important pathway to establishing kinetic FRCs. These initial experimental results provide considerable confidence that the proposed experimental manifestation of the SPIRIT concept can indeed be carried out in more fusion-reactor-relevant plasma conditions.

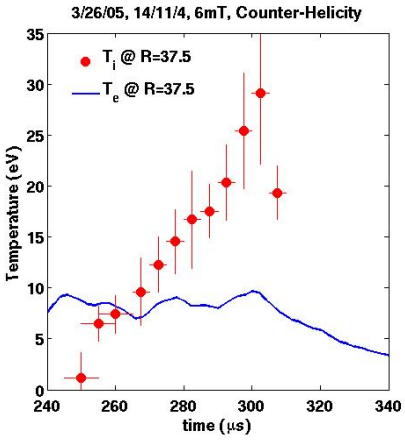

FIGURE 6. Ion temperature rise during merging of Helium-plasma spheromaks. The ion temperature vastly exceeds the electron temperature, illustrating the heating inherent in merging plasmas.

Without passive stabilizer shells, the tilt instability often leads to the immediate disruption of the plasma discharge, while the shift mode is observed to be relatively benign in the MRX geometry. Co-interchange modes with n≥2, which often terminate the plasma, remained after passive stabilization; their amplitude can be reduced by proper shaping of the external field, leading to plasmas with significantly improved stability. This improved stability was understood from a rigid-body model, which indicates that the specific external field configuration and plasma shape in MRX are responsible for this improvement in stability [11]. These experiments demonstrated for the first time the role of both passive stabilization and plasma shape in improving oblate FRC stability in the MHD regime, are the first experimental identification of the co-interchange mode [26].

SUSTAINMENT OF FRC ON MRX

At the formation stage of two merging spheromaks, extra magnetic fluxes can be injected by inserting inductive coils at the major axis at the both sides of the SPIRIT device as shown in Fig. 4. FRCs can have their poloidal flux sustained or increased, depending on the timing and strength of the induction.

Current drive with a transformer at the major axis of an FRC was experimentally demonstrated in the MRX experiments. In Fig. 7 a typical evolution of poloidal flux configuration is shown to be sustained for a substantially long time.

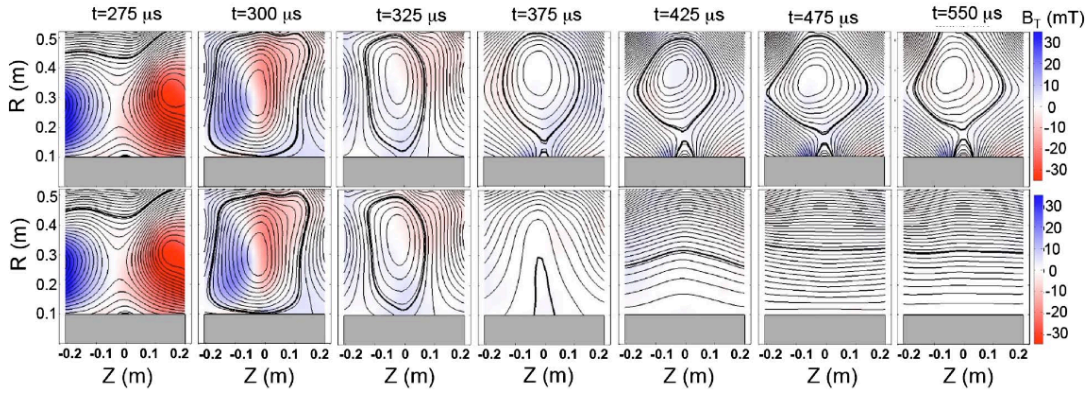

FIGURE 7. The poloidal flux contours and toroidal field colors for inductively sustained (top row) and unsustained (bottom row) argon FRC discharges. Note the non-uniform timing of the figures.

When an Ohmic transformer is turned on, it generates a one-turn inductive voltage in the azimuthal direction, thus creating an electric field in the azimuthal direction. This electric field induces a current as well as an inward plasma motion at the plasma surface through the Ohm's law,

$$E_\theta + V_r \times B_p = \eta_\perp j_\theta \qquad (2)$$

where $\eta_\perp$ is the perpendicular resistivity. With an external driving field, E_θ would compress the plasma by the Vr×Bp force, thus inducing a stronger pressure gradient and increasing the (diamagnetic) plasma current. Under quasi-steady-state conditions, a continuous inflow of poloidal flux should be balanced by the dissipative loss of current inside the plasma. This mechanism is recognized as similar to Ohmic current maintenance in tokamaks except for the fact the current flows perpendicular to magnetic field in FRC plasmas. In tokamak operation, the inductive drive would increase current much more efficiently.

Oblate FRCs were sustained for a notable duration time, 350 ms, or 15 magnetic diffusion times, through the use of an inductive solenoid [Fig. 7] [24-26]. An inward pinch is observed during sustainment, leading to a peaking of the pressure profile and maintenance of the FRC equilibrium. The stability in argon and krypton is attributed to a combination of external field shaping, magnetic diffusion, and finite-Larmor radius effects. This observation support Norman Rostoker's concept [28] that the presence of large gyro-radius ions greatly helps the stability of FRC.

SUSTAINMENT OF AN FRC BY NEUTRAL BEAM INJECTION

An essence of the SPIRIT research program is to scientifically test the idea of steady-state sustainment and kinetic stabilization of FRC plasmas by neutral beam injection. Our initial goal was to inject a 20-30 keV neutral beam with a 'current' of ~ 60A into the FRC plasma made in MRX, in order to sustain the configuration for at least a millisecond. It was expected that this neutral beam injection would induce the plasma to spin with a high velocity of the order of VA, which would in turn help stabilize the global MHD modes. Neutral beam injection should also decrease

THE VALUE OF THE KINETIC PARAMETER S*.

A theoretical scoping study was carried out based on the expected target plasma parameters of MRX. Neutral beam deposition was calculated using a Monte Carlo algorithm to select rays with a Gaussian distribution representative of the beam spot size. The path integral for ionization of the incoming neutral hydrogen atoms along each ray was calculated, and the ionization locations were obtained by sampling from a decaying exponential distribution. Ionization due to charge exchange dominates, but ionization from proton and electron impact was also included. The radial excursion of fast ion orbits (and their motion out of the midplane) was fully modeled, using a source distribution calculated in the manner described above.

Full-orbit test particle simulations of the confinement of the neutral-beam-injected ions in an FRC configuration, as shown in Fig. 8, showed that, for injection energy of Eb=25keV and B=1kG, the relative number of particles

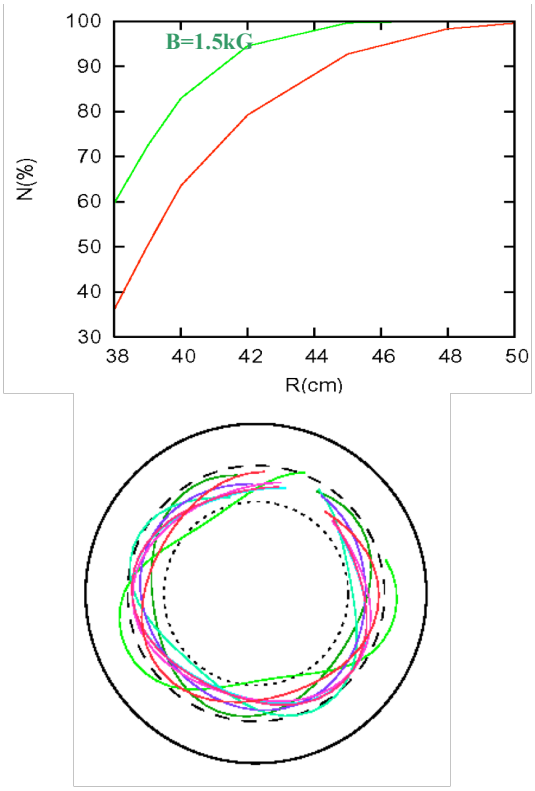

FIGURE 8. (top) Number of confined NBI ions versus radial position of conducting shell for R_{tang} =34cm and E_b=25keV. The edge magnetic field is B=1kG (red curve) and B=1.5kG (green curve). (bottom) Typical orbits of NBI ions for R_{tang} =34cm, E_b=25keV, and B=1kG; dashed line shows the separatrix position.

lost by direct losses (collision with conducting shell) depends strongly on tangential radius of injection [Fig.8 (top)]. The initial deposition profiles for the different Rtang have been calculated by the method mentioned above, and these were used as initial conditions for simulation runs. Results are shown in Fig.8, where the number of confined particles is plotted versus the conducting shell radius for Rtang =34cm (separatrix radius Rs =40cm). The direct losses of the neutral-beam-injected ions are smaller for larger Rtang due to the smaller initial radial velocity of the NBI particles, and therefore the smaller radial extent of the orbit. For larger field (B=1.5kG), good confinement of the beam ions is achieved for a range of the injection radii as also shown in Fig.8 (top). If we can demonstrate and verify a steady state sustainment of an FRC by neutral beam injection, it would constitute a major advance in plasma physics. More extensive orbit calculations would illustrate that for experimentally achievable values of poloidal flux of a intermediate size machine, the confinement of high energy ions from NBI should be quite feasible

SUMMARY

This paper briefly reviewed scientific foundations of the SPIRIT concept, a promising, physics-based path for progress towards an attractive FRC reactor. Unique features of the SPIRIT concept is that a large-flux (> 30 mW) oblate shape (elongation factor <1) FRC can be generated by the merging of two spheromaks of opposite helicities that are created by the flux-core induction scheme. This formation scheme has a major advantage of generating an FRC in a slow time scale without using electrodes. Because of the efficiency of spheromak merging, a large flux can be generated converting more than 60 % of the toroidal energy to the plasma's kinetic energy. In some cases, through flux conversion process, the poloidal flux can be amplified. The poloidal flux of a formed FRC can be as large as 50 mW for the size of R_s< 60 cm with the aid of current transformers at spheromak generator at the both ends of the system.

Our theoretical scoping studies of the SPIRIT concept developed a regime where the combination of oblate shape, conducting shells, and NBI lead to a sustained FRC stable to all global MHD modes. Preliminary experimental scoping studies have demonstrated the feasibility of this concept using the MRX facility.

A good portion of the SPIRIT concept has recently been verified by the C-2 experiments whose project was independently conceptualized and carried out [29, 30]. They first created a hot FRC by supersonic merging of two high beta FRC plasmas. This way of merging of FRCs is another method for increasing magnetic flux, heating the plasmas by shock heating and prolonging its life time. In this experiment a part of the kinetic energy was converted into thermal energy leading to a plasma with ion temperature of the order of 0.5 keV. To my knowledge this is the first experimental observation of such a conversion process. Although the lifetime exceeded 1 msec in the earlier stage of their research, they found that it was limited by global MHD instabilities, of the n=2 mode [29]. They injected a high current of 20 keV neutral beams and found they could effectively stabilize these modes and extend the FRC lifetime from 1 to 4 msec. These experiments were a confirmation of the Norman Rostoker's concept as well as that of the SPIRIT, that finite gyration radius effects should stabilize global instabilities of FRCs. More recently, by careful tuning the NBI beams, by controlling the radial electric field in the edge by plasma guns, and by introducing a divertor, they further optimized the plasma conditions to a well-confined, reproducible, macroscoptically stable hot FRC. The ion temperature approached near 1 keV and they achieved a still longer life time of 10 msec. [30].

It is a author's hope that a formation of high flux target plasmas proposed here by the SPIRIT program, can contribute to further advances of the experimental program at Tri Alpha Energy.

ACKNOWLEDGEMENTS

I appreciate my long time association with the late Norman Rostoker who has given me much inspiration, scientific advices and warm friendship. His forward looking visions for fusion science have always given me much encouragement to carry out my experimental plasma physics research. I thank Russell Kulsrud for his helpful technical discussions and advice and his careful reading of this manuscript.

REFERENCES

1. "Compact Toroids," Special Issue, Fusion Tech. 9 (1986).
2. M. Tuszewski, "Field Reversed Configurations," Nucl. Fusion 28 (1988) 2033.
3. L.C. Steinhauer, *et al.*, "FRC 2001: A White Paper on FRC Development in the Next Five Years," Fusion Tech. 30 (1996) 116.
4. H. Momota, A. Ishida, Y. Kohzaki, G.H. Miley, S. Ohi, M. Ohnishi, K. Yoskikawa, K. Sato, L.C. Steinhauer, Y. Tomita, and M. Tuszewski, "Conceptual design of the D-^{3}He reactor Artemis," Fusion Technol. 21, 2307 (1992)
5. M. Tuszewski, D. C. Barnes, R. E. Chrien, J. W. Cobb, D. J. Rej, R. E. Siemon, D. P. Taggart, B. L. Wright, "Observations of Tilt Instabilities in Field-Reversed Configurations of a Confined Plasma," Phys. Rev. Lett. 66, 711 (1991).
6. E. V. Belova, S. C. Jardin, H. Ji, M. Yamada and R. Kulsrud, "Numerical study of tilt stability of prolate field-reversed configurations", Phys. Plasmas," Phys. Plasmas 7, 4996 (2000).
7. E. V. Belova, S. C. Jardin, H. Ji, M. Yamada and R. Kulsrud, "Numerical study of global stability of oblate field-reversed configurations", Phys. Plasmas 8, 1267 (2001).
8. E. V. Belova, R. C. Davidson, H. Ji and M. Yamada, "Kinetic effects on the stability properties of field-reversed configurations. I. Linear stability", Phys. Plasmas 10, 2361 (2003).
9. E. V. Belova, R. C. Davidson, H. Ji and M. Yamada, "Kinetic effects on the stability properties of field-reversed configurations. II. Nonlinear evolution," Phys. Plasma 11, 2523 (2004).
10. E.V. Belova, R. C. Davidson, H. Ji, M. Yamada, C. D. Cothran, M. R. Brown, M. J. Schaffer, "Numerical study of the formation, ion spin-up and nonlinear stability properties of field-reversed configurations", Nuclear Fusion 46, 162 (2006).
11. E. V. Belova, R. C. Davidson, H. Ji, M. Yamada, "Advances in the numerical modeling of field-reversed configurations", Phys. Plasmas 13, 056115 (2006).
12. D. C. Barnes, and R. D. Milroy, "Stabilization of the field-reversed configuration (FRC) tilt instability with energetic ion beams," Phys. Fluids B 3, 2609 (1991).
13. R. N. Sudan, and M. N. Rosenbluth, "Stability of axisymmetric field-reversed equilibria of arbitrary ion gyroradius," Phys. Fluids 22, 282 (1979).
14. R. V. Lovelace, "Low-frequency stability of high-current particle rings," Phys. Fluids 19, 723 (1976).
15. M. Yamada, Y. Ono, A. Hayakawa, M. Katsurai, F.W. Perkins, "Magnetic Reconnection of Plasma Toroids with Co-helicity and Counter-helicity," Phys. Rev. Lett. 65 (1990) 721.
16. Y. Ono, A. Morita, T. Itagaki, and M. Katsurai, "Merging of Two Spheromaks and Its Application to Slow Formation of a Field Reversed Configuration," in *Plasma Physics and Controlled Nuclear Fusion Research 1992* (Proc. 14th Int. Conf., Würzburg, Germany, 1992), Vol. 2 (International Atomic Energy Agency, Vienna, 1993) 619.
17. Y. Ono, M. Yamada, T. Akao, T. Tajima, and R. Matsumoto, "Ion Acceleration and Direct Ion Heating in Three-component Magnetic Reconnection," Phys. Rev. Lett. 76 (1996) 3328.
18. Y. Ono, M. Inomoto, Y. Ueda, T. Matsuyama, and T. Okazaki, "New relaxation of merging spheromaks to a field reversed configuration," Nucl. Fusion 39, 2001 (1999);
19. E. Kawamori & Y. Ono, "Effect of Ion Skin Depth on relaxation of Merging Spheromaks to a Field-Reversed Configuration," Phys. Rev. Lett. 95, 085003 (2005).
20. E. Kawamori, Y. Murata, K. Umeda, D. Hirota, T. Ogawa, T. Sumikawa, T. Iwama, K. Ishii, T. Kado, T. Itagaki, M. Katsurai, A. Balandin, and Y. Ono, "Ion kinetic effect on bifurcated relaxation to a field-reversed configuration in TS-4 CT experiment," Nucl. Fusion 45, 843 (2005).
21. C.D. Cothran, A. Falk, A. Fefferman, M. Landreman, M.R. Brown, and M.J. Shaffer, "Spheromak merging and field reversed configuration formation at the Swarthmore Spheromak Experiment," Phys. Plasmas 10, 1748(2003).
22. M. Yamada, H. Ji, T.A. Carter, S.C. Hsu, R.M. Kulsrud, N.L. Bretz, F.C. Jobes, Y. Ono, M. Katsurai, T.-H. Watanabe, T. Sato, T. Hayashi, "Comparative Study of Compact Toroid Plasmas Formed by Induction and Reconnection," in *Fusion Energy 1996* (Proc. 16th Int. Conf., Montreal, Canada, 1996), Paper IAEA-CN-64/CP-19.
23. M. Yamada, H. Ji, S. Gerhardt, E. Belova, R. Davidson, D. Mikkelsen, A Self-Organize Plasma with Induction, Reconnection, and Injection Techniques: the SPIRIT Concept for Field Reversed Configuration Research, Plasma Fusion Res. 2, 004 (2007)

24. S.P. Gerhardt, M. Inomoto, E. Belova, M. Yamada, and Y. Ren, “Experimental Demonstration of Improved Stability Oblate Field Reversed Configurations through Passive Stabilization and Plasma Shaping “ Submitted to Phys. Rev. Lett., 2006
25. S. Gerhardt, E. Belova, M. Inomoto, M. Yamada, H. Ji, Y. Ren, A. Kuritsyn, "Equilibrium and stability studies of oblate field-reversed configurations in the Magnetic Reconnection Experiment", Physics of Plasmas 13, 112508 (2006)
26. S. Gerhardt, E. Belova, M. Yamada, H. Ji, M. Inomoto, C, Jacobson, R. Maqueda, B. McGeehan, Y. Ren, "Inductive sustainment of oblate field-reversed configurations with the assistance of magnetic diffusion, shaping, and finite-Larmor radius stabilization", Physics of Plasmas 15, 022503 (2008)
27. G. Fiksel, D.J. Den Hartog, and P.W. Fontana, “An optical probe for local measurements of fast plasma ion dynamics”, Rev. Sci. Instrum. 69, 2024 (1998)
28. N. Rostoker, M. W. Binderbauer, H. J. Monkhorst, “Colliding Beam Fusion Reactor”, Science 278, 1419 (1997).
29. M.W. Binderbauer et al, “Dynamic Formation of a Hot Field Reversed Configuration with Improved Confinement by Supersonic Merging of Two Colliding High-β Compact Toroids” Phys. Rev. Lett. 105, 045003 (2010)
30. M.W. Binderbauer et al, “A high performance field reversed configuration”, Phys. Plasmas 22, 056110 (2015).

Robustness of Waves with a High Phase Velocity

T. Tajima[1,2,a)] and A. Necas[2,b)]

[1]*Department of Physics and Astronomy, University of California at Irvine, Irvine, CA, 92697 USA*
[2]*Tri Alpha Energy, Inc., P.O. Box 7010, Rancho Santa Margarita, CA 92688, USA*

[a)]Corresponding author: ttajima@uci.edu
[b)]anecas@trialphaenergy.com

Abstract. Norman Rostoker pioneered research of (1) plasma-driven accelerators and (2) beam-driven fusion reactors. The collective acceleration, coined by Veksler, advocates to drive above-ionization plasma waves by an electron beam to accelerate ions. The research on this, among others, by the Rostoker group incubated the idea that eventually led to the birth of the laser wakefield acceleration (LWFA), by which a large and robust accelerating collective fields may be generated in plasma in which plasma remains robust and undisrupted. Besides the emergence of LWFA, the Rostoker research spawned our lessons learned on the importance of adiabatic acceleration of ions in collective accelerators, including the recent rebirth in laser-driven ion acceleration efforts in a smooth adiabatic fashion by a variety of ingenious methods. Following Rostoker's research in (2), the beam-driven Field Reversed Configuration (FRC) has accomplished breakthroughs in recent years. The beam-driven kinetic plasma instabilities have been found to drive the reactivity of deuteron-deuteron fusion beyond the thermonuclear yield in C-2U plasma that Rostoker started. This remarkable result in FRCs as well as the above mentioned LWFA may be understood with the aid of the newly introduced idea of the "robustness hypothesis of waves with a high phase velocity". It posits that when the wave driven by a particle beam (or laser pulse) has a high phase velocity, its amplitude is high without disrupting the supporting bulk plasma. This hypothesis may guide us into more robust and efficient fusion reactors and more compact accelerators.

INTRODUCTION

The word plasma arose from the blood plasma that is an amorphous and liquid organic material, as ionized gas is also as amorphous and fluid as the blood plasma. Over many years of research the plasma physicist has discovered that plasma is so unstable that large volumes of literatures have been written such as [1]. Often plasma instabilities either destroy the intended magnetic bottle that tries to contain plasma or enhance the plasma escape path (often called the plasma anomalous confinement). Because of this plasma penchant for instabilities, it is often believed that the utility of plasma for useful functions such as fusion reactors or as an accelerator medium is limited. Sometimes it would be said that if there is free energy available, the plasma would go unstable. So it is of great merit to advance research in either confirming the above point or perhaps to find methods by which the plasma's inclination to go unstable may be curbed or avoided.

Norman Rostoker was a pioneer in pushing the frontier of beam-driven plasma fusion reactor research (accelerator-driven plasma) as well as leading the collective plasma acceleration in which plasma is marshaled as a central driving component of an accelerator (plasma-driven accelerator). He was one of rare species of scientists who bridged over two distinct fields of plasma fusion research and accelerator physics (Incidentally, he was not only one of the greatest integrators of the accelerator science and fusion plasma science, but he brought fields such as exploratory geophysics, solid state physics (see Professor Kohn's article [2] in this proceedings), and a broad genre of scientists (see Professor Mackey's article [3] in this proceedings). In the occasion of the Norman Rostoker Memorial Symposium, commemorating the visions and accomplishments of Norman, we would like to make an attempt to carve out unique properties of beam-plasma interactions in which we can expect robust behavior of the plasma, rather than the fragile and chaotic outcome of plasma. Our working hypothesis here is what we term as the robustness of waves with a high phase velocity. This is in addition to the now famous "Norman's Conjecture",

which states that large orbits of energetic particles (that might be formed by injection of a beam of accelerated particles) have a tendency to stabilize instabilities whose wavelengths may be averaged out by the largeness of the orbit size and that perhaps as a consequence plasma confinement may be improved [4]. Such a conjecture was based on the paper of finite Larmor radius (FLR) stabilization [5] that Dr. Rostoker co-authored with flash of mathematical brilliance. Dawson and collaborators [6] found a computer simulation of drift waves which may be stabilized with large FLR effects. Such effects are fully adopted as a central guiding principle of the beam-driven Field Reversed Configuration (FRC) and its recent research is underscoring Norman's Conjecture [7, 8]. Further confirmation of Norman's conjecture is found in [9] of this Proceedings.

In the plasma-based accelerators Tajima and Dawson suggested the laser-driven wakefield accelerator method (LWFA) to drive electrons (and other particles) that are trapped in the wake [10]. In later renditions, the laser may be replaced by an electron beam [11] or by an ion beam [12]. In the wake of the laser pulse (or charged particle bunch), a large amplitude plasma wave is excited, whose amplitude may be relativistically large. The relativistic amplitude means that the amplitude of the wave is so large that particles may be driven to relativistic energies in just one oscillation, i.e. $E = mc\omega_p / e$, where ω_p is the plasma frequency [10] (In the case of the laser being also relativistic (we will discuss on this later) the field expression takes a slight modification). When such a theoretical (and computational) proposal was made, there were some opinions that plasma would become unstable and unable to support such waves. Over the years (particularly after 2004 [13-15] since the first LWFA experiment [16],) large and robust plasma waves excited with a phase velocity nearly equal to the speed of light c have been observed (Downer's group could even "see" the wakefield by holographic method [17]). These experiments supported the idea that the plasma waves are robust, stable, intense, and almost rigid, the last of which is referred to as the relativistic coherence [18]. Why is this? The ponderomotive force of the laser (corresponding to the motorboat in Fig.1 (a)) is moving with the group velocity of the laser ($\sim c$) and has the resonant length l_b with the plasma wavelength λ_p ($l_b = \frac{1}{2} \lambda_p$). It excites and feeds the plasma eigenmode with the high phase velocity of $\sim c$. Such a wave cannot trap thermal electrons of plasma, since the wave phase velocity sits far from the thermal velocities of particles that are around zero. This remains the case until the wave amplitude reaches the relativistic amplitude $eE/m\omega_p \sim c$, when the wave growth saturates. This is similar to the fast wake wave of the motorboat that only bobs the floating swimmer behind the boat (Fig.1(a)). The tsunami wave offshore does not carry stationary ships and the ships escape wreckage. However, the tsunami wave that slows down to near zero velocity on shore can deliver devastating wave energy to the onshore ships, surfers, or the coastline (see Fig.1(b)).

In addition to the above reasons for the wave with a high phase velocity staying robust and intact, there is an additional mechanism why LWFA remains sturdy; the relativistic coherence [18]. When the wave amplitude grows, the wave form steepens and further steepening goes over to break the wave (see Fig.2(b)) [19]. However, relativistic wave steepening dynamics is quite different from the nonrelativistic wave steepening (Fig.2(a)) when the wake wave is propagating with the relativistic speed (Fig.2(a)). Since the wave moves near at the speed of light, electrons cannot pass over the steepened wave and thus are hard to tip over and to break the wave and by doing so, electrons cohere to form a steep sheet (a cusp singularity). This is the manifestation of relativistic coherence.

In this paper we will focus on the robustness of the wave dynamics with a high phase velocity, including the original LWFA but also extending its reach to other applications. We also touch on the issue that if we do not fulfill this high phase velocity condition, what kind of inconvenience we encounter. An example for this was encountered in the early research of collective accelerators. This issue now has a new added importance in the recent laser-driven ion acceleration research. This will be reviewed in Sec.II. The lesson learned in Sec.II has led us to introduce the high phase velocity concept of LWFA. An additional learned lesson is applied to increase the adiabaticity in laser-driven ion acceleration. This is discussed in Sec.III. In Sec. IV we will expand the utility of the high phase velocity hypothesis on the wave robustness to a plasma fusion reactor research. In this we step out of nonmagnetized plasma with the waves of the electron branch modes at the phase velocity $\sim c$ and to extend the concept to magnetized plasma with the waves of the ion branch modes driven by an ion beam at the phase velocity near the beam velocity.

COLLECTIVE ACCELERATORS

Veksler introduced the concept of collective acceleration in 1956 [20]. His vision consisted of two elements. The first element is the introduction of plasma as the accelerating medium. In the conventional acceleration method when we increase the accelerating electric field in a vacuum surrounded by a metallic tube, the electric field on the surface of the metallic wall increases and eventually the surface begins to spark, yielding electron breakdown of the metal. As is necessary in most accelerator structures, waveguides are formed with a slow wave structure. Such a

structure is accompanied by periodically protruded surface metallic structures, which makes the local electric field even greater. In addition most materials contain impurities within its material structure, such as f-centers. These in combination make the metallic breakdown field far greater than the typical gradient that shifts the electronic

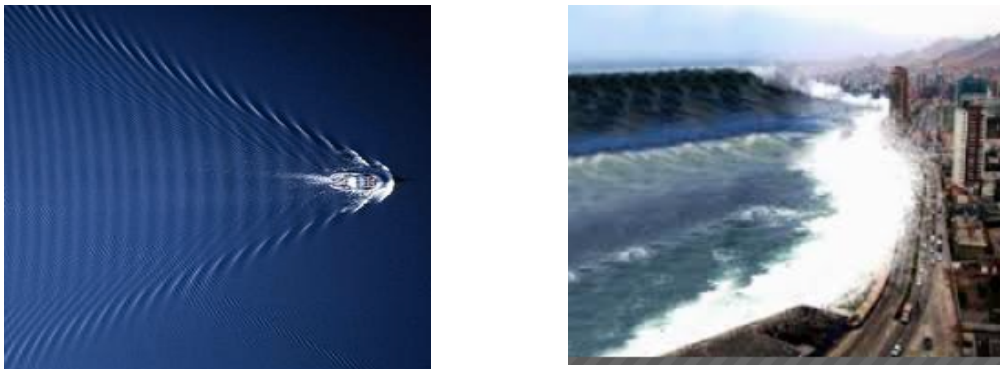

(a) (b)

FIGURE 1. Wake wave vs. tsunami wave. (a) The wake wave propagates in the medium with a high phase velocity by maintaining its integrity of a coherent motion of the organized wave. Its phase velocity is so large that most of the constituent particles (except the trapped particles or surfers) do not move with the wave. (b) The tsunami wave can propagate intact, just like the wake wave of the left does off shore. Tsunami can propagate many thousands of kilometers from the seismic center across the ocean. Ships on the ocean are hardly affected by tsunami. On the other hand when the tsunami approaches the shore and slows down in its phase velocity on shore, the phase velocity in this case is nearly zero so that the tsunami wave interacts with the coast strongly to cause the tsunami damages. In other words the tsunami phase velocity begins to resonate with the "bulk motion" (in this case the seashore coast structure, which is sitting with no moving velocity).

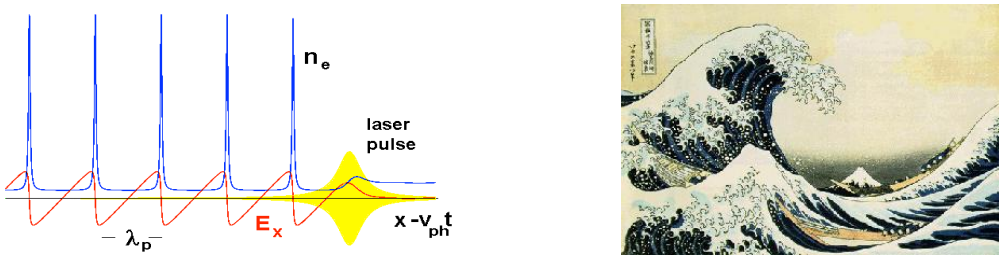

(a) (b)

FIGURE 2. Large-amplitude robust wave dynamics. (a) The nonlinear wakefield (left is our 1D computer simulation, not a cartoon) driven by laser has a group velocity which is close to the speed of light and the phase velocity of the excited wake is also close to *c*. The steepening of the wakefield due to the nonlinearity makes the electron density steepen as well, but does not necessarily easily break, due to the effect we term as relativistic coherence [18]. (b) The nonlinear ocean wave (right, by Hokusai) on the other hand also steepens for the same reason as the wakefield, but because of its nonrelativistic dynamics, the wave has the tendency to break at the highest point of the wave. (from ref. [18]).

wavefunction shift by an eV over an Angstrom, i.e. electric field of 10^8 eV/cm down to typically MeV/cm (or even less). In order to overcome this difficulty, Veksler suggested using the already broken down material of plasma to begin with. His second element is to resort to the collective field as opposed to collective force. As is known, the fields in plasma permeate in such a way that a charge feels nearly all other charges through the Coulombic interaction. If we further marshal the plasma to form a collection of charges made up with *Ne* (a collective collection of *N* charges), the interaction force is proportional to $(Ne)^2$, indicating that the collective force is proportional to N^2,

as opposed to the conventional linear force proportional to *N*. (If *N* is 10^6 , the collective force is 10^6 times greater than its linear counter part).

Lured by this concept, a large body of investigations ensued [21-24]. Norman Rostoker's program was one of them (some of these efforts are reviewed in this Proceedings of the Norman Rostoker Memorial Symposium [25]). For example, in one of these attempts [26] an electron beam is injected into a plasma to cause a large amplitude plasma wave by the beam-plasma interaction (a collective interaction);, it was suggested that such a large amplitude wave would trap ions and accelerate them to speeds near that of the electron beam. If ions were to be trapped by a speeding electron cloud or beam with energy ε_e , the ions would be accelerated to the energy of $\varepsilon_i = (M/m)\varepsilon_e$, where *M* and *m* are masses of ions and electrons, respectively, because they would speed with the same velocity. Since the mass ratio *M/m* of ions to electrons is nearly 2000 for protons and greater for other ions, the collective acceleration of ions would gain a large energy boost. None of the collective acceleration experiments in those days, however, found energy enhancement of the magnitude mentioned above. The primary reason for this was attributed to the sluggishness (inertia) of ions with electrons being pulled back to ions, instead of the other way around, or to too fast 'reflexing (return flow) of electrons' as described in [26]. The ion acceleration takes place only over the sheath of electrons (of the beam injected) that are ahead of ions, while the sheath is tied to the beam injection aperture (an immovable metallic boundary in this experiment). Mako and Tajima theoretically found that the ion energy may be enhanced only by a factor of 2α+1 (which is about 6 or 7 for typical experimental situations and α will be defined later) over the electron energy, instead of by a factor of nearly 2000, due to the electron reflexing and no co-propagation of the electron beam and the ions, while the formed sheath is stagnant where it was formed. (For example, Tajima and Mako [27] suggested reducing the culpable electron reflexing by providing a concave geometry. Similar geometrical attempt to facilitate the laser-driven ion acceleration would appear also later in 2000's-2010's.) In year 2000 the first experiments [28-30] to collectively accelerate ions by laser irradiation were reported. In these experiments a thin foil of metallic (or other solid materials) was irradiated by an intense laser pulse, which produced a hot stream of electrons from the front surface that faced the laser pulse, propagating through the thin foil emerging from the back surface of the foil. Now this physical situation of what is happening at the rear surface of the foil is nearly equivalent to what the group of Rostoker had done in 1970's and 80's in terms of the dynamics of electrons emanating from the metallic boundary and its associated ion response as a result of their injected electron beam. The superheated electrons by the laser caused the acceleration of ions in the sheath which was stuck stationary on the rear surface of the target, but not beyond. Such acceleration was then called the Target Normal Sheath Acceleration (TNSA) [28-31].

The experiments and simulations since then improved the understanding of the importance of increased adiabaticity in the ion acceleration. These studies showed that the proton energy increases as the target thickness decreases for a given laser intensity and that there is an optimal thickness of the target (at several nm) at which the maximum proton energy peaks and below which the proton energy now decreases [32-34]. Figure 3 shows the schematic changes in the original collective accelerator effort as well as the laser-driven acceleration in the TNSA regime in contrast with more adiabatic acceleration (with various improvements such as thinner target, circularly-polarized irradiation, or more intense laser regime of the Radiation Pressure Acceleration [35]). This optimal thickness for the peak proton energy is consistent with the thickness dictated by the relation $a_0 \sim \sigma = \frac{n_0}{n_c}\frac{d}{\lambda}$, where σ is the (dimensionless) normalized electron areal density, a_0, *d* are the (dimensionless) normalized amplitude of electric field of laser and target thickness [36-38]. We define here ξ as the ratio of the normalized areal density to the normalized laser amplitude $\xi = \sigma / a_0$. The optimal condition ξ ~ 1 is understood as arising from the condition that the radiation force pushes out electrons from the foil layer if $\sigma \le a_0$ or $\xi \le 1$, while with $\sigma \ge a_0$ or $\xi \ge 1$ the laser pulse does not have a sufficient power to cause maximal polarization to all electrons. Note that this optimal thickness for typically available laser intensity is much smaller than for cases with previously attempted target thicknesses (for ion acceleration). Thus we attribute the observed comparatively large value of the maximum proton energy in the experiment [32] to the ability to identify and provide prepared thin targets on the order of nm to reach this optimal condition.

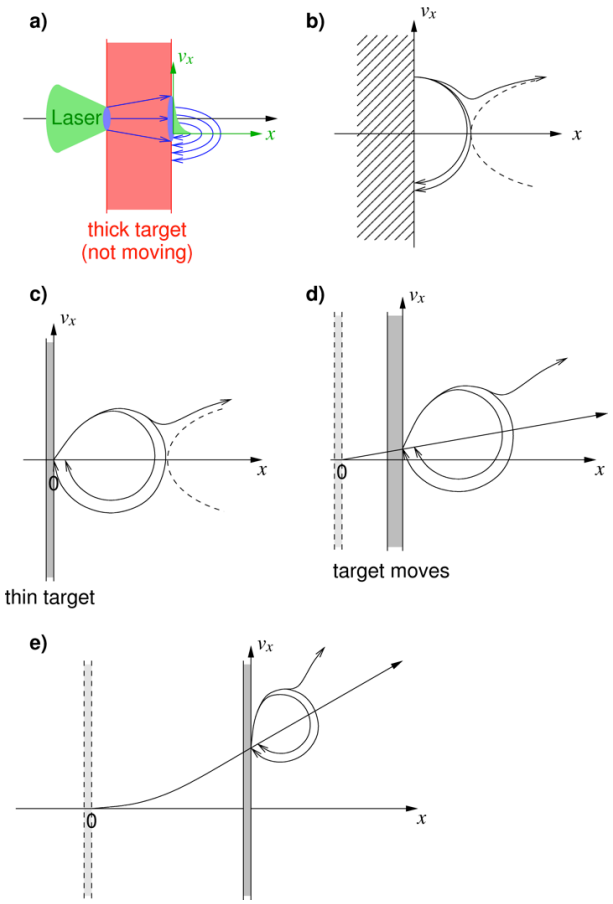

FIGURE 3. Non-moving to moderate commoving to commoving of target motions from the total detachment from the electron sheet (a) to totally commoving case (e). (a) TNSA. Laser generates energetic electrons on the front surface of the thick target. Electron travel through the target to emerge from the rear side with broad energy spread. These electrons exit into vacuum to pull ions. However, most electrons are pulled back to the immobile target before ions gain much energy. Electrons at the margin of the electron cloud are ejected out from the electron space charge. (b) The Mako-Tajima scenario. Electrons with a delta function energy spectrum enter from the metallic immobile (real) surface. Electrons rush out in vacuum to pull ions. However, most electrons are pulled back to the immobile boundary before ions gain large energy. Some electrons are ejected forward. The electron dynamics have much in common with case (a), although the electron spectrum is broad and has a tail in (a). (c) A case study with an ultra thin target that is immobile. One significant difference of (c) from (a) is that the electron energy directly determined by the laser and its ponderomotive potential beyond the rear surface of that target. Thus the energy of ions is expected to be narrow in its width and to have higher maximum than (a). (d) When the target is sufficiently thin, the rear surface of the target (and some times entire target) begins to move, while the laser interacts with the target. (e) When the target is pushed with the laser ponderomotive force (such as the circularly polarized laser pulse) without too much heating of electrons, ions in the target as a whole are trapped in an accelerating bucket with tight phase space circles. If and when the laser leaks through and electrons are ejected forward, the bucket may begin to collapse. Cases (c)–(e) belong to the regime of CAIL, while (e) is in particular in the RPA conditions. (from Ref. [33])

LASER WAKEFIELD ACCELERATORS AND ION ACCELERATION

The main lessons learned from the 1970's collective accelerator research effort (particularly those in which TT was involved in or observant of) are two fold. In order to scoop up ions at rest and bring them to higher energies, we first have to make the driver (the electron bunch in the case of Rostoker's lab) screech to stop at the entrance metal boundary and from there on, electrons start to pick up velocity. However, when this occurs, the driver strongly interacts and the plasma becomes unstable and generates unnecessary disturbances. This is similar to the tsunami

wave breaking onshore (see Fig. 1 (b)). On the surface of the electron entry point we form a sheath that cannot adiabatically pick up ions and is unable to gradually accelerate them. Only the sheath acceleration ensues and no acceleration beyond. Thus we learned that we have to make the driver gradually accelerates from the starting point of interaction. This is the need for adiabaticity for such application as ion acceleration, as we have already discussed in an introductory fashion in Secc.II. We show this transition from the sheath formation TNSA and the early experiment at Rostoker's lab to more adiabatic ion acceleration by a cartoon of Fig. 4.

The second lesson is to accelerate electrons instead of heavier ions. Because electrons are light, strong enough waves can immediately trap electrons (at least some of the injected electrons) and accelerate them. In so doing we wish to use a wave with a high phase velocity that can have large amplitude and still remain intact and robust without perturbing the plasma. Again this serenity of robust waves may be seen in Fig. 1(a) for the wake wave of the boat-driven lake surface wave and the offshore portion of the tsunami wave before it hits the shore (Fig.1 (b)).

In this section we focus on the topic of the second lesson: how to make more coherent and more adiabatic acceleration of ions. See Fig. 4. According to the analysis in [33,34] in 1D Particle-In-Cell (PIC) simulation it was observed that momenta of electrons show in fact coherent patterns directing either to the ponderomotive potential direction, the backward electrostatic pull direction, or the wave trapping motion direction, in a stark contrast to broad momenta of thermal electrons of TNSA. In another word, through a very thin target the partially penetrated laser fields enable the electrons to execute dynamic motions still directly tied with the laser rather than thermal motions. The ponderomotive force due to this trapped radiation contributes to the acceleration of electrons in this sheet and thus retards these electrons from being decelerated by the electrostatic force emanated from the diamond foil. This topic is a current research topic in the laser-driven ion acceleration (See example of [33]).

After Tajima witnessed the meager energy amplification as compared to the speculated large enhancement by an ion-to-electron mass ratio over the energy of the electron beam and exponentially decaying spectral shape in the laboratory of Professor Rostoker, as mentioned above, the lesson learned by him was to accelerate, instead of ions that need adiabatic acceleration, electrons which are light and can be trapped even with a sudden (or non-adiabatic) acceleration. As he went on to UCLA working with Dawson after graduation from UCI, he and Dawson employed a short laser pulse to cause a large ponderomotive force in plasma, whose collective accelerating field is the resonantly excited plasma wake. This wakefield traps electrons at rest from the bulk (They could be injected otherwise). In this scheme (now called Laser Wakefield Acceleration (LWFA)[10]) the wake propagates with the group velocity of the laser pulse, which is near the speed of light. Tajima and Dawson observed that because of the large phase velocity of the wake wave of $\sim c$, the wake wave grows robustly large without directly disturbing the plasma bulk particles that support the wake. This situation is similar to the serene surface water wake wave driven as a wake of the motorboat, as shown in Fig, 1(a). Because the wakefield propagates at $\sim c$, the wake does not trap (or otherwise disturb) the bulk electrons or ions, unlike the onshore tsunami wave whose phase velocity is near zero onshore and which delivers all the wave energy into the shore destruction. The laser wakefield can grow serenely till the trapping width of the wake becomes so large that the arms of the wakefield (e.g. in Fig. 2(a)) now reach from the thermal velocity of bulk cold plasma particles to the speed of the phase velocity which sits at (or near) the speed of light of the laser pulse. When this happens, the wake growth begins to stop and / or to trap a class of injected electrons. This is the first manifestation and example of the principle (or hypothesis) of robustness of waves with a high phase velocity in the example of LWFA. Such was experimentally demonstrated by many experiments including [13-15].

Thus employing this LWFA principle (or the robustness hypothesis), Esirkepov et al. [35] proposed a very intense laser pulse to excite so huge a ponderomotive force that even ions may be immediately trapped (i.e. non-adiabatically) in this ultrarelativistic laser intensity regime of the Radiation Pressure Acceleration scheme. In this scheme, not only are ions accelerated with a quasi-monoenergetic spectrum, but can also reach relativistic energies. The only inconvenience of [35] is the requirement of ultrarelativistic laser pulse amplitudes, where the normalized vector potential of the laser pulse $a_0 = eE_l / mc\omega_l$ is exceedingly greater than unity (such as $\sim 10^3$, where E_l and ω_l are the laser electric field and frequency.) Such laser requires an intensity on the order of 10^{23}W/cm^2, whose technology has yet to be realized. One more comment as to RPA in the ultrarelativistic regime is that in the when $a_0 >> 1$, the wakefield tends not to be resonantly excited any more (see [39]).

One way to improve this situation without the required laser intensity is to employ a circularly polarized laser on a thin target. For example, in [32] an experiment with a reduced target mass (by choosing nanometrically thin carbon (diamond)), even linearly polarized (LP) laser irradiation produced a much improved acceleration (higher energies and less spread energy spectrum) than that observed in the TNSA experiments in which the energy spectra is typically found to be exponentially decaying. With circularly polarized (CP) laser irradiation of the target, the experiment [32] found that in addition to the energy improvement, the energy spectrum had a quasi-monoenergetic

shape. A marked reduction of laser intensity that Esirkepov et al.[35] required may be accomplished if the ponderomotive acceleration of electrons by the laser pulse is smoother and more adiabatic when compared to linearly polarized laser irradiation with otherwise like parameters of laser and target even if the laser intensity is far less than that of Esirkepov [35]. This is because the ponderomotive acceleration of CP removes a component of electron acceleration at 2ω frequency, which is present in the LP pulse case. Recall that the longitudinal acceleration of electrons is exerted by the Lorentz term $\boldsymbol{v} \times \boldsymbol{B}$, in which $\boldsymbol{v}$ is proportional to $\boldsymbol{E}$, the laser field. In these experiments some evidence of semi-isolated or quasi-monoenergetic energy spectrum begins to manifest. However, their spectrum remains to be improved to become a beam of isolated single energy. There is some circumstantial evidence of ions trapped behind the electron charge sheet.

To increase the adiabaticity of ion acceleration, additional possibilities include making the group velocity of the laser to gradually increase from small (near zero) at the beginning of interaction to a high value at the end. This may be done by setting the plasma density at the entrance to the critical density and to reduce it gradually so that the group velocity of the laser tends to increase [40]. A possibly related method of controlling the accelerating velocity to be more adiabatic may be done by adopting nanoclusters distributed appropriately [41]. An enhanced energy production with nanoclusters in [42] may be attributable to such an effect.

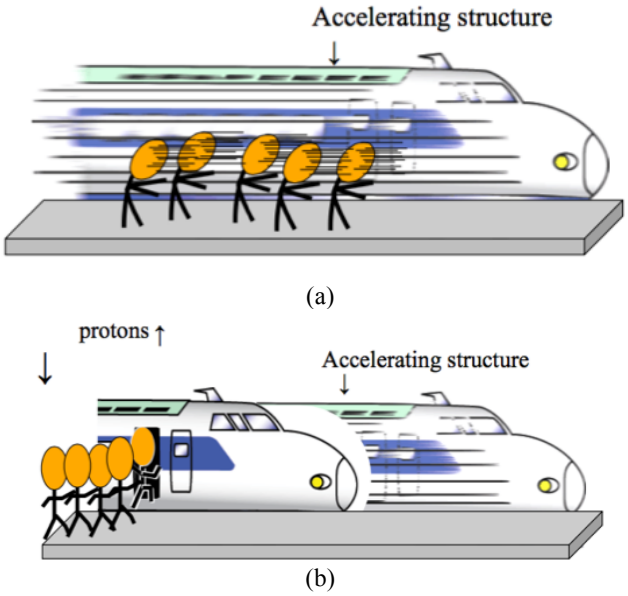

FIGURE 4. (a) Cartoon versions of non-adiabatic ion acceleration in which the accelerating structure does not stop and then accelerate. (b) That of the adiabatic smooth acceleration of ions in which the accelerating structure first stops and then adiabatically picks up the speed.

BEAM-DRIVEN PLASMA FUSION REACTORS

It is central to have an intense beam drive in an FRC plasma in the C-2U program at TAE [9], as discussed in Introduction, for the beam injection to stabilize macro-instabilities such as the tilt mode [7] and drift instabilities [46] as suggested by Norman's conjecture. In addition, we now observe in C-2U that (i) the beam drives robust kinetic bump-on-the-tail beam-plasma micro-instabilities; (ii) nonetheless, these instabilities incur no global plasma destruction; and (iii) even enhance the deuteron-deuteron (D-D) fusion reactivity. We are now led to a new hypothesis beyond Norman's Conjecture: waves with a high phase velocity can retain robustness and keep plasma from its total destruction over a substantial period of their evolution, i.e. the hypothesis of waves with a high phase velocity. Below we briefly review this phenomenon and we compare this with our own simulation that shows beam driven micro-instabilities that are non-destructive, but transfer energy from fast ions to the plasma, causing phase space bunching. This hypothesis shares the same philosophy with the wakefield excitation [10]. Such a mechanism may explain an experimentally observed anomalous neutron signal (10-100× the predicted thermonuclear fusion

yield), as other explanations have been eliminated (D in the beams, fast-thermal ion head-on collisions, and miscalculation of Ti). We propose that the hydrogen beam generates an energetic ion population that then drives collective modes in the plasma, giving rise to an instability and increased fusion rate. An electromagnetic (EM) particle-in-cell (PIC) code [44, 45] is used to simulate beam-plasma interaction and a two-body correlation function is employed to determine computational D-D reactivity enhancements. Modifying the experimentally injected beam's distribution function supports this theory. There are now two hypotheses which support the observed physical behaviors of the beam-driven FRC system: (i) Norman's Conjecture, (ii) the hypothesis of robustness of waves with a high phase velocity thus introduced.

The C-2U experiment, in the case of the deuteron plasma driven by the hydrogen beam, shows that the neutron (and proton) yield is enhanced over the value that may be attributed to the estimated thermonuclear value, so long as the beam is turned on and a short time has elapsed (some 0.1ms after the beam turn-on, we also observe enhanced magnetic fluctuations in the frequency region of 550 kHz that covers the typical ion cyclotron frequency in the core plasma (See Fig. 5.)

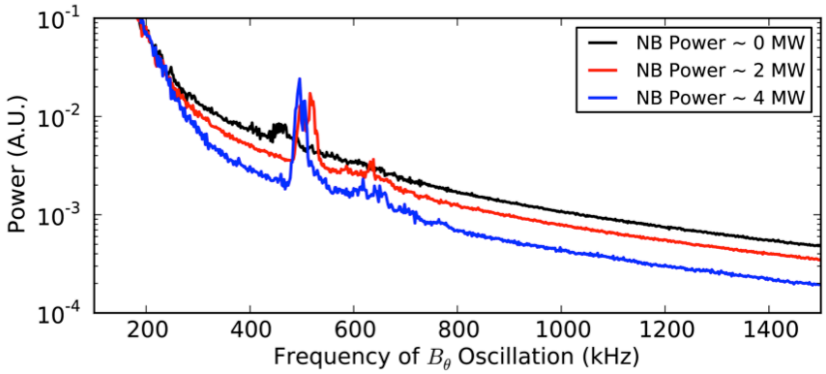

FIGURE 5. Magnetic fluctuation spectrum in the C-2U FRC plasma. In the absence of beams, the broadband magnetic fluctuation is high. Broadband magnetic fluctuations are suppressed for higher beam power. Resonant peak increases with beam power.

It is our working hypothesis that the observed enhancement of the fusion reactivity beyond the thermonuclear value and the increased magnetic fluctuations are incurred by a beam-driven kinetic instability whose frequency range is in the ion-cyclotron frequency domain. Nonlinear saturation of the exited waves reaches a large amplitude to drive the kinetic beam-plasma instability. Note that when the beam is composed of deuterons, the predominant fusion reaction occurs not between plasma deuteron particles, but rather between the beam deuterons and plasma deuterons, i.e. the beam-target fusion rate is larger than the target-target interaction.

We have constructed a theoretical analysis and computational simulation of the beam-plasma interaction process.

$$\frac{\omega_{pi}^2}{\lambda_i}\sum_{n=1}^{\infty}\exp[-\lambda_i]I_n(\lambda_i)\frac{2n^2}{\omega^2-n^2\Omega_i^2}+$$
$$\frac{\omega_{pi}^2}{kv_b}\sum_{n=1}^{\infty}\frac{2n^2\omega_{cb}}{\omega^2-n^2\Omega_b^2}J_n(\nu)[J_{n-1}(\nu)-J_{n+1}(\nu)]= \quad (1)$$
$$1+\left(\frac{\omega_{pe}}{\Omega_e}\right)^2\left(1+\frac{\omega_{pe}^2}{c^2k^2}\right)$$

where

$$\nu=\frac{kv_b}{\Omega_b},$$
$$\lambda_i=0.5\left(k\rho_i\right)^2.$$

Here ω_{pe}, ω_{pi} and ω_{pb} are the electron, thermal ion, and beam plasma frequency, respectively, and Ω_{ce}, Ω_{ci} and Ω_{cb} are the electron, thermal ion, and beam cyclotron frequency, ρ_i the thermal ion Larmor radius, v_b is the beam velocity, and J_n and I_n are the Bessel functions of the first kind of order n. The first term on the left is due to the plasma component, second is due to the beam, and the term on the right hand side is the vacuum and the electron terms. The electron term includes EM modification [46].

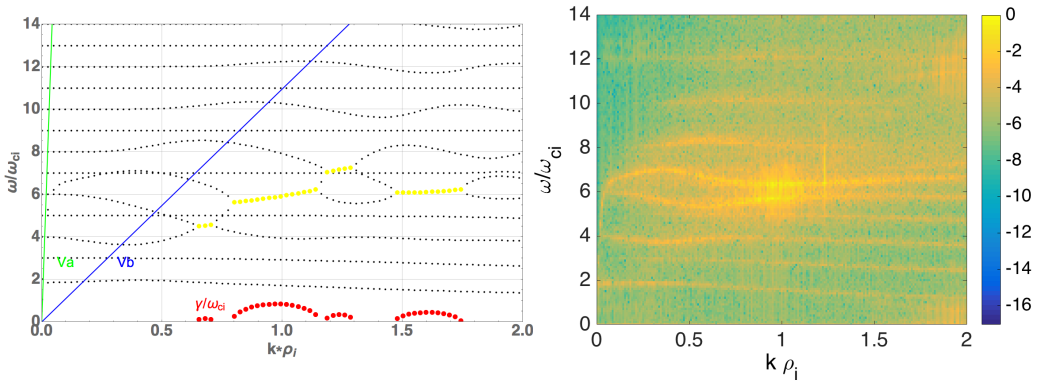

(a) (b)

FIGURE 6. The dispersion relation of the ion-beam driven plasma instabilities in the C-2U FRC plasma. (a) Weakly electromagnetic analytic dispersion relation solution to Eq. (1), (b) Fourier transform of the E_x field of the fully EM PIC code. (a) and (b) agree on the location of the dominant mode. The plasma parameters used: B=0.267 T, n_e=0.742x10^{16} m^{-3}, T_e-=T_i=500eV, beam is hydrogen and thermal plasma deuteron, and beam is 10% with energy 15 keV. The resonance at ω=6ω_{ci} is close to the lower hybrid frequency: $\omega_{LH} = \left(\frac{1}{\omega_{ci}^2+\omega_{pi}^2} + \frac{1}{\omega_{ci}\omega_{ce}}\right)^{-\frac{1}{2}}$.

Figure 6a shows the solution to the analytical weakly electromagnetic dispersion relation and Fig. 6b the 1D simulation with PIC code. We have found that as $\omega pb/\omega ci$ increases the modes shown in black eventually intersect giving rise to the absolute instability – the yellow dots, with associated growth rate represented by the red dots. The interaction is between the beam's ion Bernstein harmonic and plasma's lower hybrid wave discussed in [47] and can be seen in Fig. 7(a), n=6 Bernstein harmonic is observed. The phase velocity of the mode is 60% of the beam velocity and 5 times larger than the plasma thermal velocity, indicating the current beam-plasma system falls in the category of the regime that satisfy the high phase velocity hypothesis.

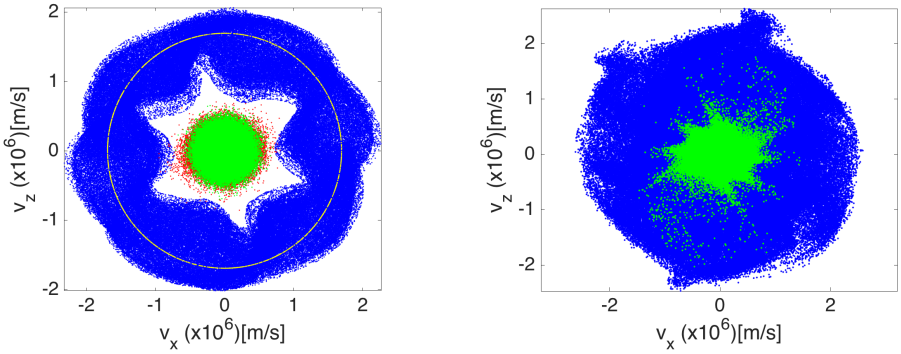

(a) (b)

FIGURE 7. Nonlinear evolution of the beam and plasma particles in the ion-beam driven instability. (a) Velocity space plot with the mode not yet fully saturated. Yellow ring – initial distribution of the beam, Green – initial velocity distribution of the thermal deuterons, red – thermal deuterons, blue – beam ring at t = 0.53 μs. n=3 Bernstein mode in the beam ring has grown substantially as also manifested in dispersion plots Figs. 6(a) and 6(b). Scattering of the beam particle to higher than initial velocity is observed. (b) Velocity space plot at saturation t=0.73 μs.

The incurred kinetic beam-plasma instability begins to draw a tail portion of the bulk plasma distribution [Figs. 7(a) and 7b]. On the other hand, at the time t=0.53 μs, a large portion of beam particles merge with the plasma bulk distribution, which shows a protruded structure Fig. 7(a) and is manifested in Fig. 7(b) as stretching the thermal distribution to higher velocities. Figure 6(b) shows the dispersion relation as obtained by 1D fully electromagnetic PIC simulation of the same physics as in Fig. 6(a). The two methods agree on the location of the mode in the ω-k plane as well as the growth rate of the most unstable mode to be 0.8 ω_{ci}. In Fig. 8 the computationally measured time history of the deuteron-deuteron reactivity normalized to the standard thermonuclear fusion reactivity at the given plasma parameters (the vertical number unity means that the observed reactivity is equal to that of thermonuclear reactivity) can only occur among the plasma particles in the simulated beam-plasma system, as the hydrogen beam and deuteron plasma do not react to yield fusion.

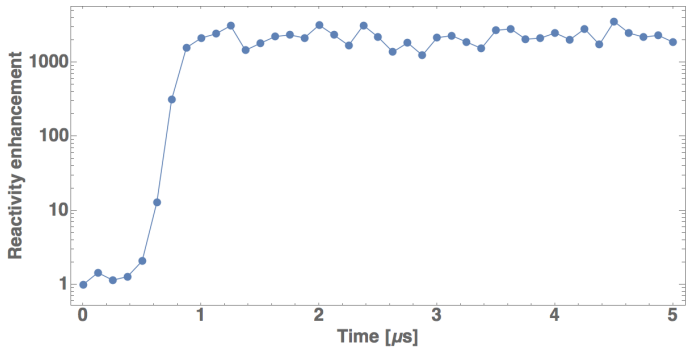

FIGURE 8. Enhancement of the D-D fusion reactivity over the thermonuclear value. Reactivity enhancement tracks the growth of the unstable mode as seen in Fig. 8. The normalization is to the thermonuclear value as unity.

In this example (which is not atypical of our simulations) the maximal enhancement factor is as large as 3000 over the well-known thermonuclear reactivity [48]. This enhancement arises in our simulation due to the creation of the energetic particles in the plasma bulk particles, as we see in Fig. 7(a,b). Shown also is a typical time history of the most unstable mode in Fig. 9.

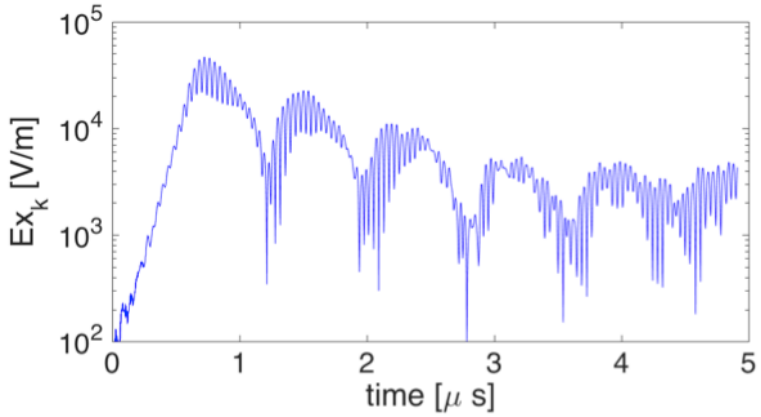

FIGURE 9: The fastest growing mode with location at $k\rho_i$=0.97. Plot of Fourier transform of E_x to k-space vs. time is shown. Linearly growing mode saturates at 0.7 μs, afterwards nonlinear phase commences and energy sloshing between particles and fields is observed.

Here the maximum amplitude of the most unstable mode occurs about the same time of the total wave energy saturation. (We note that the beam instability allows the wave amplitude to increase exponentially first (till t=0.75 μsec), followed by the saturation around t=1.0 μsec). The saturated amplitude of the electric field E=4.0 x 10^5 V/m. This value is high and robust, and the plasma shows relatively benign behavior overall, except that we observe some tongue-like structures of Fig. 7a. The amplitude of the mode is consistent with the estimated value by the hypothesis

of waves with a high phase velocity: $E=M\omega v_{phi}/q = n*2.4 \times 10^5$V/m = 7.2 x 10^5V/m, where M is the deuterium mass, $\omega \sim n*\omega_{ci}$ and ω_{ci} is the deuterium cyclotron frequency, v_{phi} is the phase velocity of this ion mode, and q is the deuteron charge. This theoretical value (E=7.2x10^5V/m) is on the same order of magnitude but is higher than the simulation value (E=4.0x10^5V/m). This may be due to the following reasons: (i) the simulation has several growing modes, whose phases tend to mix; (ii) the waves are not resonantly driven in the present case, a bit similar to the case of self-modulated (SM)LWFA [16; 49] in which the maximally available wave-breaking limit may not be reached; some partial particle-injection may have happened before the wave-breaking takes place. To delineate these further will take more future studies.

We may be able to interpret our simulation in light of our high phase velocity hypothesis, as follows. Robust ion-Bernstein cyclotron modes couple to the beam ring (sometimes the lower hybrid wave co-exists). These modes modulate and decelerate the beam, (Fig.7(a)). The wave phase velocity is less than the beam velocity but close to it and far above the plasma bulk thermal velocity. Thus this setup belongs to the category in which the hypothesis of robustness of waves with a high phase velocity. As the saturation of this kinetic instability of the beam-plasma interaction commences, the large body of the particles that belonged to the initial beam now plunges toward the bulk distribution, while the tails of the plasma distribution shows more prominent starfish-like arms (Fig. 7(b)). Because the phase velocity of the injected beam v_b is far greater than the ion thermal velocity v_{ti} ($<< v_b$), the instability grows the mode amplitude high enough and robustly enough to scatter the perpendicular (to field) energy from the beam velocity down to the bulk ion thermal range. Note that the bulk of the thermal plasma remains intact even when the robust kinetic instability has set in and grown to high amplitude that is characterized and limited by the phase velocity trapping reaching down the bulk. This is an extended version of a magnetized non-relativistic ion branch from the nonmagnetized relativistic "wave breaking" limit phenomenon [10]. This behavior is in fact observed in the wakefield physics, where the large amplitude wake is excited by the beam or laser pulse, supported by the plasma, and approaches the Tajima-Dawson wave limit [10] (and when the relativistic effects are included, it even exceeds this value because of the relativistic coherence [18]). In the resonantly excited wakefield in which the beam bunch or laser pulse is chosen in such a way to directly resonate with the plasma eigenmode wavelength, the saturation amplitude reaches typically E=4.0 x 10^5 V/m and usually causes the phenomenon called the self-injection [39-41]. The self-injection in the wakefield dynamics is similar to the present anomalous heating and its subsequent fusion enhancement in this D-D reactivity considered in this Section. While such intense acceleration and self-injection happens, the plasma and integrity of the wake waves are intact just as shown in Fig. 1 (a) or the offshore portion of the tsunami wave in Fig. 1 (b). The tsunami wave loses its integrity and transfer its total energy to the shore only when its phase velocity reached near zero at the onshore. In other words, the plasma does not lose its integrity nor is led to a total destruction, though the robust kinetic effects caused significant perturbation. In the present ion beam-driven phenomenology of the deuteron plasma, this anomalous heating gives rise to the anomalous fusion enhancement, as observed in C-2U beam-plasma interaction. This observation thus may again join as another example exhibiting the phenomenon of the hypothesis of robustness of waves with a high phase velocity. The robust effects we see in this interaction such as enhanced heating and fusion reactivity in the present example of the D-D bulk plasma is manifest, while the bulk plasma may be maintained under the circumstance.

CONCLUSIONS

Veksler's idea to avoid the metallic breakdown at higher accelerating fields was to adopt plasma as the medium and its collective field to increase the accelerating gradient inspired the research of Professor Norman Rostoker and others to investigate the processes involved. Since such strongly driven plasma exhibits highly nonlinear behaviors, the understanding of the phenomena involved took a long time and much effort. One such effort at the University of California at Irvine at the lab of Rostoker incubated many ideas and valuable lessons which his students learned. One of the experiments taught us the importance of accelerating ions in an adiabatic fashion, which led to the theory and understanding of how to ameliorate the sheath formation and its sudden cessation of the ion acceleration process. Such ideas led to revive research into more efficient acceleration in the new exploding efforts in laser driven ion acceleration that started in Year 2000 in the form of the Target Normal Sheath Acceleration. These efforts include Radiation Pressure Acceleration, Collective Acceleration of Ions by Laser (CAIL), and the more recent Single-Cycled Pulse Acceleration (SCPA) [50] methods. If any such methods produces the intended improvements over the abrupt acceleration characteristic of TNSA, the applications to various fields are immense, surpassing the conventional accelerators' reach with a huge impact.

Another impact that the Rostoker lab launched was for us to consider the electron acceleration with the collective method in order to avoid the difficulty of trapping and accelerating heavier particles to relativistic energies. This prepared the way to invent the idea of plasma acceleration by a relativistically fast wave to trap and accelerate electrons, as electrons are more tolerant of the nonadiabatic nature of acceleration due to their light mass. This endeavor led to the creation of the LWFA concept. In addition, it was realized that the fast phase velocity of the laser-driven plasma wave is capable of sustaining robust plasma waves without disrupting the plasma medium that supports the wave. Although this claim may have encountered suspicion that plasma may be too unstable and thus unable to keep its structure intact, the principle and the subsequent experiments proved instability to not be a concern, as the robustness of waves with a high phase velocity was instrumental in preserving the plasma integrity.

In more recent developments the beam-driven FRC plasma shows that in spite of strong kinetic beam-plasma instabilities the plasma remains intact. The excited plasma waves in this magnetized plasma exhibit a large enough amplitude that we observe wave-induced anomalous heating, leading to enhanced fusion reactivity in the deuteron FRC plasma . In this phenomenon, once again the hypothesis of robustness of waves with a high phase velocity helps us to understand why such beam-injection leads to a remarkable fusion reactivity enhancement. Here we have found that the beam-instability causes robust wave excitation in the range of ion Bernstein frequency. The wave amplitude is high, because the phase velocity of this ion-beam driven instability has a phase velocity much higher the thermal velocity of the bulk ions. Consistent with our hypothesis, such instability is capable of exciting robust ion waves that can draw sufficient amount of the tail plasma ion distribution toward the fusion enhancement. It is important to consider this phenomenon and mechanism in the proton-boron 11 fusion condition and to evaluate if and how this physics manifests in p-B^{11} fusion reactors.

In conclusion we have seen a broad applicability of the introduced hypothesis of the robustness of waves with a high phase velocity, including the improvement of the recent progress in laser-driven ion acceleration and the interpretation and possible extrapolation of the observed beam-driven fusion reactivity enhancement.

ACKNOWLEDGMENTS

We gratefully thank G. Mourou, M. L. Zhou, X. Q. Yan, F. Mako, J. A. Wheeler, K. Nakajima, M. Binderbauer, R. Magee, T. Roche, M. Thompson, S. Nicks, H. Gota, J. Douglas, H. Berk, T. O'Neil, B. Coppi, R. Davidson, R. Kulsrud, M. Yamada, and B. Richter for illuminating discussions and encouragements. We dedicate this paper to the memory of Professor Norman Rostoker, whose tutelage of us was so fundamental. The work was in part supported by the Norman Rostoker Fund at UCI.

REFERENCES

1. A. Mikhailovskii, "Theory of Plasma Instabilities" (Springer, NY, 1974).
2. W. Kohn, in this Proccedings (AIP, NY, 2016); W. Kohn and N. Rostoker, Phys.Rev. **94**, 1111 (1954).
3. K. Mackey, in this Proceedings (AIP, NY, 2016).
4. N. Rostoker, in "Physics of High Energy Particles in Toroidal Systems" Eds. T. Tajima and M. Okamoto (AIP, NY, 1994) p.323.
5. M. N. Rosenbluth, N. Krall, and N. Rostoker, Nucl. Fus. Suppl. **1**, 143 (1962).
6. H. Naitou, T. Kamimura, and J. M. Dawson, J. Phys. Soc. Jpn. **46**, 258 (1979).
7. H. Y. Guo, M. W. Binderbauer, T. Tajima, R. D. Milroy, L. C. Steinhauer, X. Yang, E. G. Garate, H. Gota, S. Korepanov, A. Necas, T. Roche, A. Smirnov, and E. Trask, Nature Comm. **6**, 6897 (2015).
8. M. Binderbauer et al., Phys. Plasmas **22**, 056110 (2015).
9. M. Binderbauer, in this Proceedings (AIP, NY, 2016).
10. T. Tajima and J.M. Dawson, Phys. Rev. Lett. **43**, 267 (1979).
11. P. S. Chen et al. , Phys. Rev. Lett. **54**, 693 (1985).
12. A. Caldwell, et. al., Nature Phys. **5,** 363 (2009).
13. Faure, J., Y. Glinec, A. Pukhov, S. Kiselev, S. Gordienko, E. Lefebvre, J.-P. Rousseau, F. Burgy, and V. Malka, Nature **431**, 541 (2004).
14. Geddes, C. G. R., C. Toth, J. van Tilborg, E. Esarey, C. B. Schroeder, D. Bruhwiler, C. Nieter, J. Cary, and W. P. Leemans, Nature **431**, 538 (2004).
15. Mangles, S. P. D., *et al.*, Nature **431**, 535 (2004).
16. K. Nakajima et al., PRL **74**, 4428 (1995).

17. Siders, C.W., LeBlanc, S.P., Fisher, D., Tajima, T., Downer, M.C., Babine, A., Stepanov, A., and Sergeev, A., Phys. Rev. Lett. **76**, 3570 (1996).
18. T. Tajima, Proc. Jpn. Acad. Ser. B **86**, 147(2010).
19. R. Davidson, "Methods in Nonlinear Plasma Theory" (Academic, NY, 1972).
20. V. I. Veksler, in "CERN Symposium on High Energy Accelerators and Pion Physics" (CERN, Geneva, 1956) p. 80.
21. S. E. Graybill and J. R. Uglum, J. Appl. Phys. **41**, 236 (1970).
22. J. W. Poukey and N. Rostoker, Plasma Physics, **13**, 897 (1971).
23. N. Rostoker and M. Reiser, "Collective Methods of Acceleration" (Harwood, London,1979).
24. D. D. Ryutov and G. V. Stupakov, Soviet J. Plasma Physics, **2**, 309 (1976).
25. F. Mako, in this Proc.(AIP, NY, 2016).
26. F. Mako, A. Fisher, N. Rostoker, D. Tzach, and C.W. Roberson, IEEE Trans. Nucl. Sci., **26**, 4199 (1979).
27. F. Mako and T. Tajima, Phys. Fluids **27**, 1815 (1984). See also T. Tajima and F. Mako, Phys. Fluids. **21**, 1459 (1978).
28. R.A. Snavely, M.H. Key, S.P. Hatchett, T.E. Cowan, M. Roth, T.W. Phillips, M.A. Stoyer, E.A. Henry, T.C. Sangster, M.S. Singh, S.C. Wilks, A. MacKinnon, A. Offenberger, D.M. Pennington, K. Ya- suike, A.B. Langdon, B.F. Lasinski, J. Johnson, M.D. Perry, E.M. Campbell, Phys. Rev. Lett. **85**, 2945 (2000).
29. E.L. Clark, K. Krushelnick, J.R. Davies, M. Zepf, M. Tatarakis, F.N. Beg, A. Machacek, P.A. Norreys, M.I.K. Santala, I. Watts, A.E. Dangor, Phys. Rev. Lett. **84**, 670 (2000).
30. A. Maksimchuk, S. Gu, K. Flippo, D. Umstadter, V. Yu. Bychenkov, Phys. Rev. Lett. **84**, 4108 (2000).
31. P. Mora, Phys. Rev. Lett. **90**, 185002 (2003).
32. A. Henig, S. Steinke, M. Schn¨urer, T. Sokollik, R. H¨orlein, D. Kiefer, D. Jung, J. Schreiber, B. M. Hegelich, X.Q.Yan, J. Meyer-ter-Vehn, T. Tajima, P.V. Nickles, W. Sandner, and D. Habs, Phys. Rev. Lett. **103**, 245003 (2009).
33. Tajima, T., Habs, D. and Yan, X. Q., Rev. Accel. Sci. Tech. **2**, 201 (2009).
34. Yan, X.Q., Tajima, T., Hegelich, B.M., Yin, L., and Habs, D., Applied Phys. B **98**, 711 (2009).
35. Esirkepov, T., Borghesi. M., Bulanov. S. V., Mourou, G., and Tajima, T, Phys. Rev. Lett.**92**, 175003 (2004).
36. T. Esirkepov, M. Yamagiwa, T. Tajima, Phys. Rev. Lett. **96**, 105001 (2006).
37. K. Matsukado, T. Esirkepov, K. Kinoshita, H. Daido, T. Utsumi, Z. Li, A. Fukumi, Y. Hayashi, S. Orimo, M. Nishiuchi, S.V. Bulanov, T. Tajima, A. Noda, Y. Iwashita, T. Shirai, T. Takeuchi, S. Nakamura, A. Yamazaki, M. Ikegami, T. Mihara, A. Morita, M. Uesaka, K. Yoshii, T. Watanabe, T. Hosokai, A. Zhidkov, A. Ogata, Y. Wada, T. Kubota, Phys. Rev. Lett. **91**, 215001 (2003).
38. X.Q. Yan, C. Lin, Z.M. Sheng, Z.Y. Guo, B.C. Liu, Y.R. Lu, J.X. Fang, J.E. Chen, Phys. Rev. Lett. **100**, 135003 (2008).
39. C. Lau, P. C. Yeh, O. Luk, J. McClenaghan, T. Ebisuzaki, and T. Tajima, Phys. Rev. STAB **18**, 024401 (2015).
40. X. Q. Yan, H. C. Wu, Z. M. Sheng, J. E. Chen and J. Meyer-ter-Vehn, Phys. Rev. Lett. **103,** 135001 (2009); Ronghao Hu, Bin Liu, Haiyang Lu, Meilin Zhou, Chen Lin, Zhengming Sheng, Chia-erh Chen, Xiantu He & Xueqing Yan, Sci. Rep**. 5,** 1549 (2015).
41. T. Tajima, *Laser Driven Compact Ion Accelerator*, US Patent 6,866,338B2 (filed: Jan. 8, 2001; date of patent: June 14, 2005).
42. Fukuda, Y., Faenov, A., Tampo, M., Pikuz., T., Nakamura, T., Kando, M., Hayashi, Y., Yogo, A., Sakaki, H., Kameshima, T., Pirozhkov, A., Ogura, K., Mori, M., Esirkepov, T., Koga., J., Boldarev, A., Gasilov, V., Magunov, A., Yamauchi, T., Kodama, R., Bolton, P., Kato, Y., Tajima, T., Daido, H., and Bulanov, S., Phys. Rev. Lett.**103**, 165002 (2009).
43. L. Schmitz, in this Proceedings (AIP, NY, 2016).
44. T.D. Arber et al., Plasma Phys. Control. Fusion **57**, 11(2015).
45. T. Tajima, "Computational Plasma Physics—with Applications to Fusion and Astrophysics" (Benjamin Frontier Series, Reading, MA, 1989).
46. J. K. Lee and C.K. Birdsall, Physics of Fluids,**22**, 1315, (1979)
47. J.D. Callen and G.E. Guest, Phys. Fluids, **14**, 1588 (1971)
48. J. Wesson, "Tokamaks" (Oxford.U. P., Oxford, 2011).
49. D. Fisher and T. Tajima, Phys. Rev. E **53**, 1844 (1996).
50. M. L. Zhou, X. Q. Yan, J. A. Wheeler**,** T. Tajima, and G. Mourou, submitted (2015).

Tribute to Norman Rostoker

W. Kohn

UCSB, Santa Barbara, CA 93106

Norman Rostoker was my first postdoc when I was a new assistant professor at Carnegie Tech. We had in common our Canadian backgrounds, his by birth and mine as my adopted country. He had a different undergraduate degree, an engineering degree, but then went into the field of plasma physics where he was hugely successful. We wrote some papers together, one became an acronym - KKR (Korringa Kohn Rostoker), but more importantly we became very good personal friends to the end of his life. He had a great sense of humor! And he once helped me buy a cheap reliable car so I could get to work. His scientific contributions will continue to be influential and my memory of him as a close friend will stay with me for the rest of my life.

Formation of Field-Reversed Configuration by Use of Two Merging Spheromaks with Opposing Toroidal Field

Yasushi Ono[1,a)]

[1]*Graduate School of Frontier Sciences, University of Tokyo, JAPAN*

[a)]Corresponding author: ono@k.u-tokyo.ac.jp

Abstract. In 1986, we, U. Tokyo group first reported the new formation of the field-reversed configuration (FRC) by two merging spheromaks with opposing toroidal field. This unique formation has been developed mainly in our TS-3 and TS-4 merging experiments, leading us to a new scenario of FRC slow-formation, heating and current-amplification. Its formation efficiency is much higher than the conventional field-reversed theta-pinch method. The relaxation from the force-free (β~0.05-0.1) spheromaks to the high-β (β~0.7-1) FRC is caused by conversion of the toroidal (partly poloidal) magnetic energy of the spheromaks to the ion thermal energy of the FRC through the reconnection outflow. The reconnection heating energy scales with square of the reconnecting magnetic field, suggesting direct access to the alpha heating without using any additional heating. A central solenoid (CS) coil was installed successfully to amplify the FRC plasma current by factor 2. Our toroidal mode observations suggest that the tilting stability of the oblate FRC is provided by ion kinetic effect. As another important extension, fast application of external toroidal magnetic field transformed this oblate FRC into an ultra-high-β spherical tokamak (ST) with diamagnetic toroidal magnetic field, suggesting close relationship between FRCs and high-β STs in the second stable region for ballooning mode.

INTRODUCTION

Field-reversed configuration (FRC) [1], spheromak [2] and spherical tokamak (STs) [3] are all compact and/or spherical torus plasmas (CT/STs) whose aspect ratio are close to 1. Their topologies allow their translation [4] and merging [5] in the axial direction. In this paper, we will review the FRC slow formation experiments by two merging spheromaks with opposing toroidal magnetic field, which have been developed in TS-3 [5] and TS-4 [6] devices. In this merging method, magnetic reconnection transforms toroidal and a part of poloidal magnetic energy of merging spheromaks into ion thermal energy of the produced FRC, as shown in Fig. 1 [7]. The spheromak with balanced amount of toroidal and poloidal magnetic fields B_t, B_p is based on the Taylor magnetic-energy-minimum state [8], which assures its global magnetohydrodynamic (MHD) stability. The Taylor state is widely known to be a stable force-free state with zero plasma thermal pressure. The FRC plasma solely with poloidal magnetic field B_p has the high-β (β: plasma thermal pressure / magnetic pressure) plasma equilibrium. Its stability is interpreted not by the MHD approximation but by some thermal and kinetic effects, whose *s*-parameter (*s*: average number of ion gyroradii between the magnetic field null and the separatrix). Conventional field-reversed theta-pinch (FRTP) method can produce high density (n_e~10^{21} m^{-3}) and high temperature (T_i+T_e~500 eV) plasma, but its low plasma formation efficiency and indispensability of fast capacitor banks make it difficult to produce FRCs with larger magnetic fluxes and to sustain them by central solenoid (CS) current drive/amplification and heating. The FRC plasma is predicted to be unstable against several MHD modes such as internal tilt mode, though many experimental results have shown that FRCs are reasonably stable against low-*n* modes. Substantial kinetic effects are expected to explain this discrepancy, leading many FRC researchers to a number of theoretical and numerical studies of the kinetic effects of FRCs [9-11]. On the other hand, MHD-like stable FRCs are required for future fusion core utilities. Therefore, an interest has grown in generating FRCs in MHD regime with large *s*-numbers for their confinement improvement, extending the FRC stability into non-kinetic MHD regime [12,13]. However, the conventional FRTP formation was found to have some difficulties to produce large-size FRCs stably and efficiently in the slow time

scale. Slow formation of FRC would be essential to the future large-scale confinement experiment, leading us to the plasma formation in the large-*s* MHD regime. Several slow formation techniques have been developed by use of double coaxial coils [14], rotating magnetic field [15,16] and by use of low-beta merging spheromaks [5,17-20]. The former two methods successfully inject the poloidal fluxes of FRCs in the slow time scale. However, their temperatures tend to be lower than 30 eV, probably due to lack of plasma heating source for high-β FRC formation. In contrast, we have successfully demonstrated the slow formation of FRC with ion temperature as high as 200 eV by use of reconnection heating [5,17-20].

This paper describes the novel merging formation and the developed scenario of FRC slow-formation, heating and flux (current)-amplification. As shown in Figs. 1(a) and 1(b), two force-free spheromaks with opposing toroidal magnetic fields B_t are axially collided. The magnetic reconnection annihilates their opposing B_t, forming an FRC with $B_t \sim 0$. The produced FRC is amplified / heated by use of a CS coil and is finally translated to a burning section, as illustrated in Figs. 1(c) and 1(d) [5]. Cause and mechanism for the equilibrium transition from the low-β spheromaks to the high-β FRC are made clear by means of selective ion heating properties of magnetic reconnection. The CS current amplification up to factor 2 and the large *s*-number properties of the produced FRC such as n=1 instability are studied experimentally. This merging formation has several advantages over the conventional FRTP formation of FRC: (1) slow formation (elimination of fast capacitor bank), (2) stable formation process with high energy-efficiency using a minimum energy state; spheromak, (3) usage of the merging process for high-power ion heating, (4) expected large *s*-number properties, and (5) usage of current transformer for the toroidal current amplification. We developed this FRC formation by two merging spheromaks in TS-3 experiment for the first time in 1986 [5], solved its conversion mechanism from toroidal magnetic energy to ion thermal energy [6] and finally demonstrated the scenario of the FRC merging formation and current simplification shown in Fig. 1 [5]. Since 1995, this merging formation of FRC has been widely used for new FRC experiments: MRX in Princeton University [20], SSX in Swarthmore University [23], Swift-FRC in NASA [26], FRC experiment in Colorado University [26]. After 1990, the reconnection/merging heating has been used not only in CTs but also in STs, because its heating power exceeds MW-class. Table 1 shows the merging/reconnection heating experiment under operations. The largest one is the MAST experiment in UK where the ST merging/reconnection heat plasma ions and electrons up to 1.2 keV and 0.8 keV, respectively [22]. Merging of two FRCs was used for its startup in C-2 in Tri-Alpha Energy [25]. Recently, we also applied this method to a new formation of ultra-high-β spherical tokamak plasma in the second-stable region for ballooning instabilities [28,29].

TABLE 1. Merging CT and ST Experiments.

Device	TS-3 [5]	START [3]	SSX [23]	TS-4 [18]	MAST [3,22]	UTST [24]	C-2 [25]	VEST [27]
Institute	U. Tokyo	CCFE	Swarthmore Co.	U. Tokyo	CCFE	U. Tokyo	Tri Alpha Energy	Soul N. U.
CT/ST Merging Initiation	1986	1990	1996	2000	2000	2005	2009	2011
Operation	Merging ST/Sph., RFP	Merging ST	Merging Sph.	Merging ST/Sph., RFP	Merging ST	Merging ST	Merging FRC	Merging ST
Major Radius	20 cm	35 cm	20cm	50 cm	90 cm	45 cm	35cm	45 cm
Aspect Ratio	1-1.6	1.6	1	1.4	1.3	1.3	1	1.5
I_p [kA]	70	200	1	150	1000	150		30
B_{t0} [T]	0-0.2	0.4	0	0.15	0.3	0.5	0	?
T_e [eV]	10-40	3-20	20	10-40	1400	20	100	?
T_i [eV]	10-200	3-20	20	150	1400	100	500	?

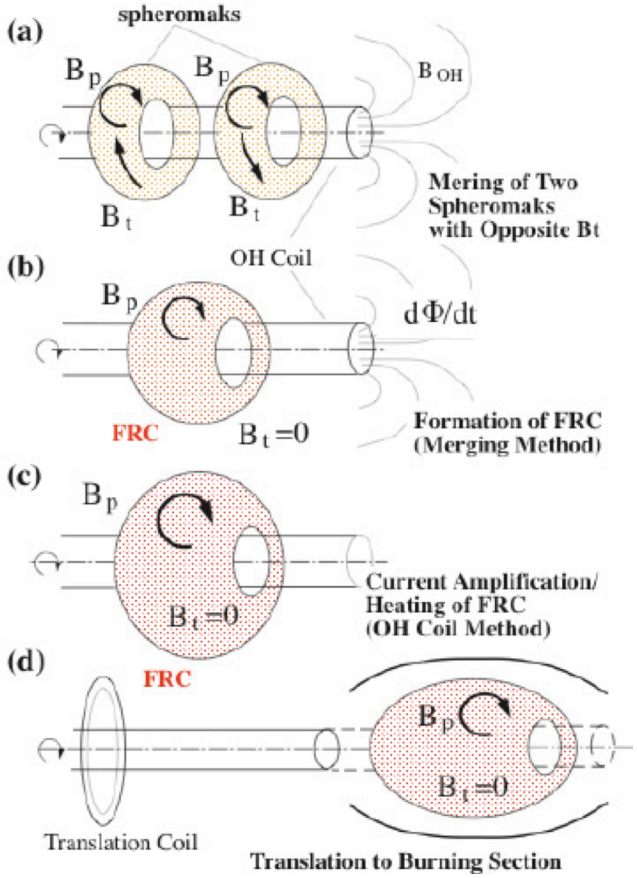

FIGURE 1. Merging formation of FRC by use of two spheromaks with opposing B_t (a)-(b), its flux (current) amplification / heating (c) and translation to a burning section (d) [5,36].

EXPERIMENTAL SETUP

The TS-3 merging device with eight pairs of electrodes and a poloidal field coil on both sides of the cylindrical vessel to produce two spheromaks with opposing B_t is shown in Fig. 2. Polarities of toroidal field B_t and magnetic helicity of the two spheromaks are determined independently by polarities of Z-discharge currents between the electrodes. A current transformer (CS coil) is located along the geometric axis to amplify the plasma current of the produced FRC. Its shell is also used to maintain the plasma stability against the n=1 (tilt and/or shift) modes.

A two-dimensional magnetic probe array composed of 144 pick-up coils is placed on the R-Z plane of the vessel to measure 2-D profiles of B_p and B_t on each single discharge. These data are used to calculate the evolutions of the poloidal flux Ψ, the toroidal current density j_t, and the magnetic energy W_m within the separatrix, using the following formulae:

$$\Psi = 2\pi \int_{r_c}^{r} r' B_z dr' \quad , \tag{1}$$

$$\mu_0 j_t = \frac{\partial B_r}{\partial z} - \frac{\partial B_z}{\partial r} \quad , \tag{2}$$

$$W_m = \int \frac{B^2}{2\mu_0} dv = \frac{\pi}{\mu_0} \iint \left(B_z^2 + B_r^2 + B_t^2 \right) r dr dz \tag{3}$$

Another replaceable 2-D array of magnetic probes is placed on the *R-q* plane to measure the toroidal mode amplitudes and phases from n=1 to n=4. An electrostatic probe is inserted to measure profiles of electron temperature T_e and electron density n_e. A CO_2 laser interferometer is used to calibrate the absolute value of n_e. Doppler shifts and widths of CII and H_β spectrum lines are measured by a polychromator with an optical multichannel analyzer (OMA) for the purpose of calculating radial profiles of ion temperature T_i and toroidal velocity V on the midplane.

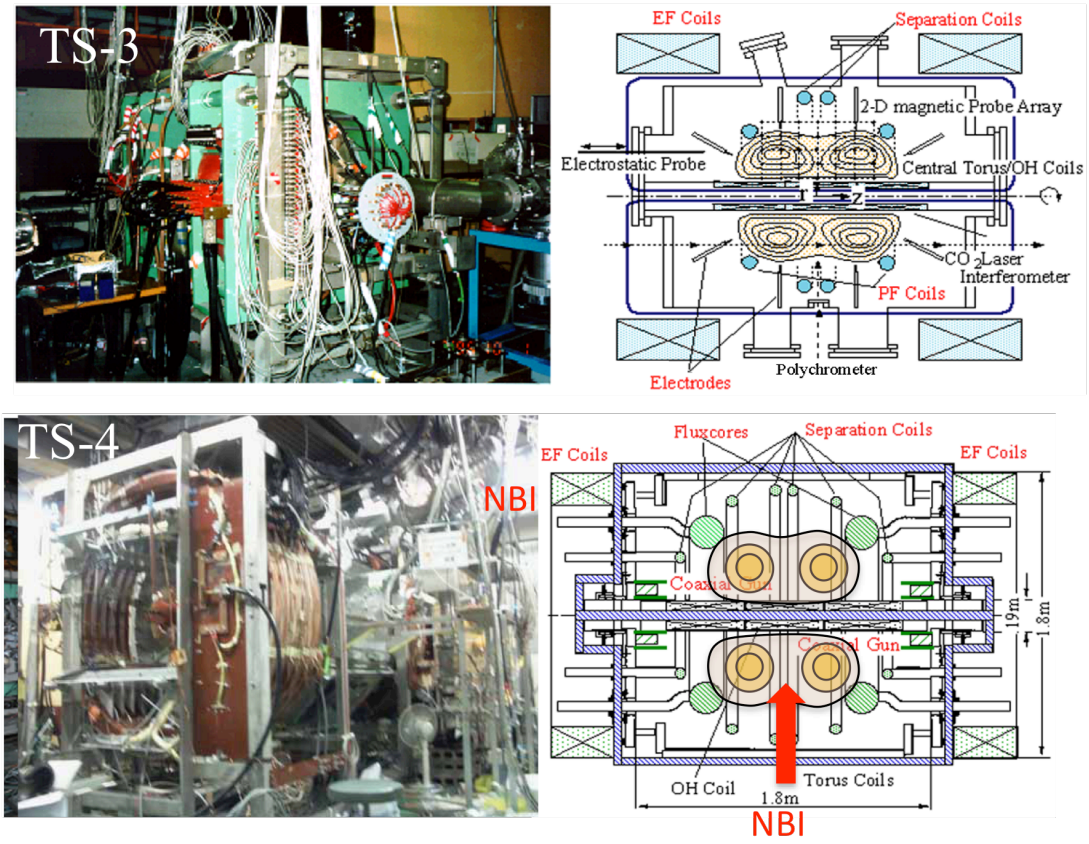

FIGURE 2. Experimental setup of the TS-3 (top) and TS-4 (bottom) merging devices at University of Tokyo.

EXPERIMENTAL RESULTS

Slow Formation of FRC by Two Merging Spheromaks with Counter-Helicity

Figures 3(a)-(c) show schematics of two merging spheromaks with opposing toroidal magnetic field and 2-D contours of toroidal magnetic field and poloidal flux, respectively. They are measured by the 2-D magnetic probe array on the *R-Z* plane. Two spheromaks with opposing B_t are produced in slow time scale (~40 μsec) and are merged together from t=40 μsec to 65 μsec. The opposing B_t fields are annihilated around the reconnection (*X*-) point and the field-null region gradually expands, as the counter-helicity reconnection proceeds. Note that the reconnected field lines offer an overshoot or an oscillation. As shown in Fig. 3(b), the polarity of B_t is positive on the left-hand side and negative on the right-hand side but it becomes negative and positive after t=60 μsec,

respectively. As shown in Fig. 3(a), the magnetic reconnection accelerates plasma in both edge regions during t=40 μsec - 60 μsec. Its polarity is positive on the outer-side and negative on the inner-side. As shown in Fig. 3(a), the inner-halves and the outer-halves of the reconnected field lines accelerate plasma ions oppositely in the toroidal direction [5,17-19]. The line-averaged velocity ~12 km/sec (at R=22 cm) is as large as 1/3 to 1 of the local Alfvén speed.

It is noted that ions are heated significantly and selectively from 20 eV to 250 eV from t=50 μsec to 65 μsec. This anomalous ion heating occurs when the large velocity shear is formed by the field line acceleration. During this period, the electron temperature T_e stays around 10-20 eV, indicating that the counter-helicity reconnection heats ions selectively. Since the increment in n_e is negligibly small, the large increase in T_i is the main cause for the large increase in β-value from 0.05-0.1 (spheromak) to 0.7-0.9 (FRC). The produced velocity shear and the B_t field with reversed polarity gradually vanish, relaxing the plasma to FRC state with uniform B_t~0 before t=65-75 μsec. As shown in Fig. 4, these B, T_i, T_e and n_e measurements indicate that the total increase in the ion thermal energy $W_{i,th}$~180 J is as large as 80% of the dissipated magnetic energy W_m~230 J (the whole toroidal magnetic energy and part of the poloidal energy) during the reconnection [18]. Dissipation of neutral current sheet $W_{sheet} \sim 2\pi R_X \delta L E_{t,X} j_{t,X}$ is estimated to be as small as 20 J, based on the measured electric field $E_{t,X}$, current density $j_{t,X}$, width δ, length L and radius R_X of the neutral current sheet. These facts indicate that W_m is converted directly to $W_{i,th}$ and that this merging formation is useful not only for the slow formation but also for the high-power ion heating of the produced FRC. Large ion viscosity probably plays an important role in thermalizing the accelerated ions in the bulk plasma. The viscosity force against the ion acceleration is significantly large because of wide field-null region around the reconnection (X-) point. This viscosity heating of plasma ions is considered to be much larger than that of electrons, because the reconnection outflow has the large kinetic-energy ratio of ions to electrons almost equal to their mass ratio. The ions with large gyroradii are unmagnetized much more widely around the X- and O-points with B_t~0 than the electrons with small gyroradii.

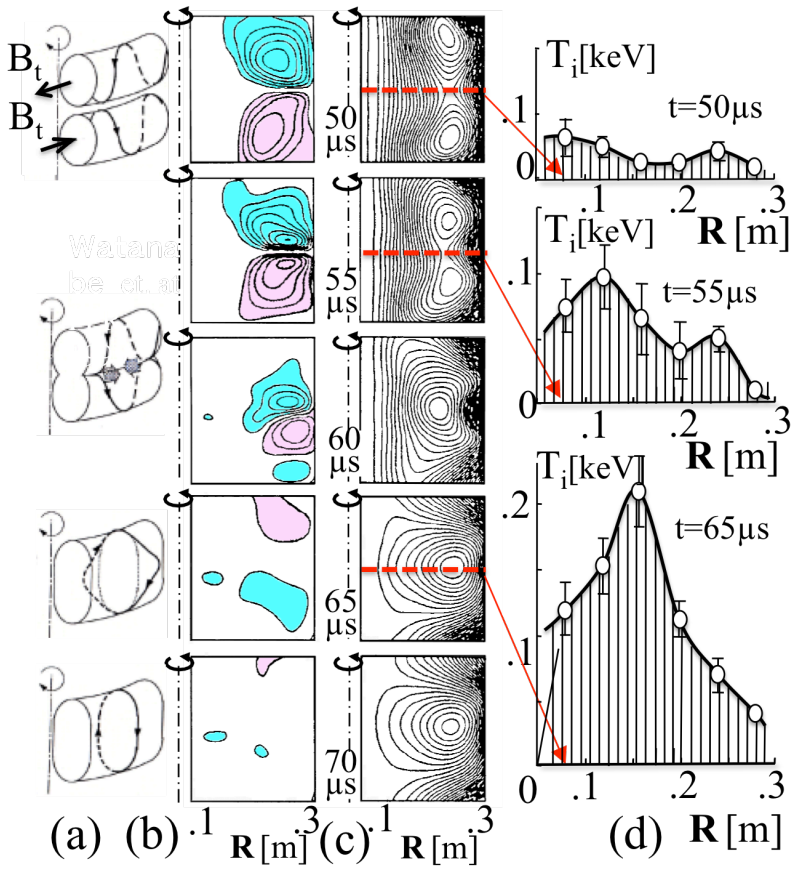

FIGURE 3. Time evolutions of 2-D contours of poloidal flux surface and toroidal magnetic field B_t on the R-Z plane (a)-(c), radial profiles of ion temperature T_i (d) on the midplane, during the merging of two spheromaks with equal but oppositely directed B_t. The red and blue colors are used to indicate the positive and negative amplitudes of B_t [22].

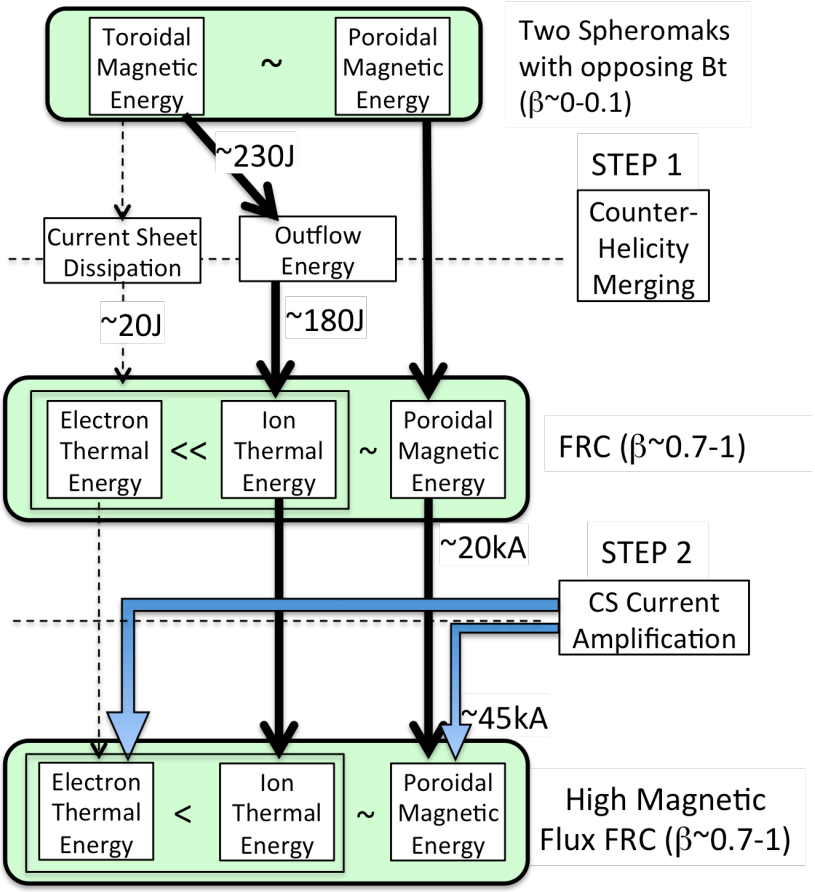

FIGURE 4. Energy flows during the merging formation and the OH current amplification of FRC.

Universal Scaring of Reconnection Heating

The reconnection heating was found to depend on the square of the reconnecting magnetic field and not on guide toroidal field [21,22]. Figure 5 shows dependence of ion temperature increment ΔT_i of magnetic reconnection on the reconnecting magnetic field B_{rec} during under constant electron density. The data include the two merging spheromaks with opposing toroidal field and two merging spheromaks/STs, whose B_{rec} are toroidal magnetic field and a part of poloidal field and just poloidal magnetic field, respectively. It is noted that the reconnection heating energy $\Delta W_{rec} \sim \Delta W_{rec,i}$ proportional to $\Delta n_i T_i$ and ΔT_i scales with B_{rec}^2 under constant n_i. The mechanism for this scaling is explained by the well-known Sweet-Parker model whose outflow speed is the Alfvén speed determined by the reconnection magnetic field B_{rec}. Since B_{rec} accelerates plasma, mainly ions to the Alfvén speed, the outflow speed scales with B_{rec}, indicating that ion heating energy scales with B_{rec}^2 after thermalization of the accelerated ions. The recent MAST and TS-3 ST merging experiments indicate weak or no dependence of bulk ion heating on the guide toroidal field B_t [24,22]. The reconnection speed is determined by the externally-driven inflow in the long time-scale. Under the constant external inflow, the reconnection speed transiently decreases with B_t but if the external inflow flux exceeds the inflow flux determined by the reconnection speed, the plasma and flux pileup inside the current sheet, finally ejecting them from the current sheet as a current sheet/plasmoid ejection. During the sheet ejection, the reconnection speed as well as the ion temperature increases significantly, indicating that the long-time averaged reconnection speed and ion heating do not or weakly depend on the guide field B_t.

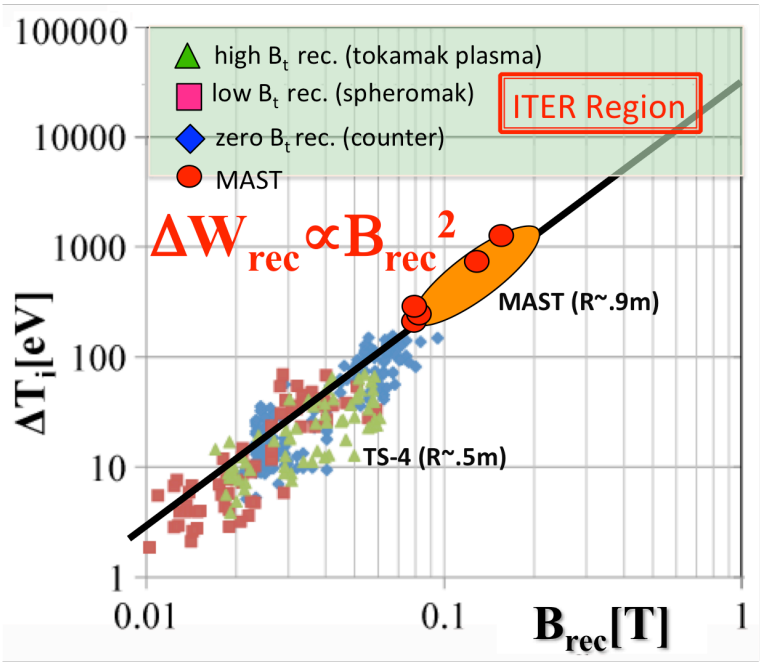

FIGURE 5. Ion temperature increments ΔT_i of the two merging spheromak and tokamak plasmas as a function of reconnecting (poloidal) magnetic field B_{rec}. The data points were obtained from TS-3 and MAST merging experiments with various guide (toroidal) fields [22].

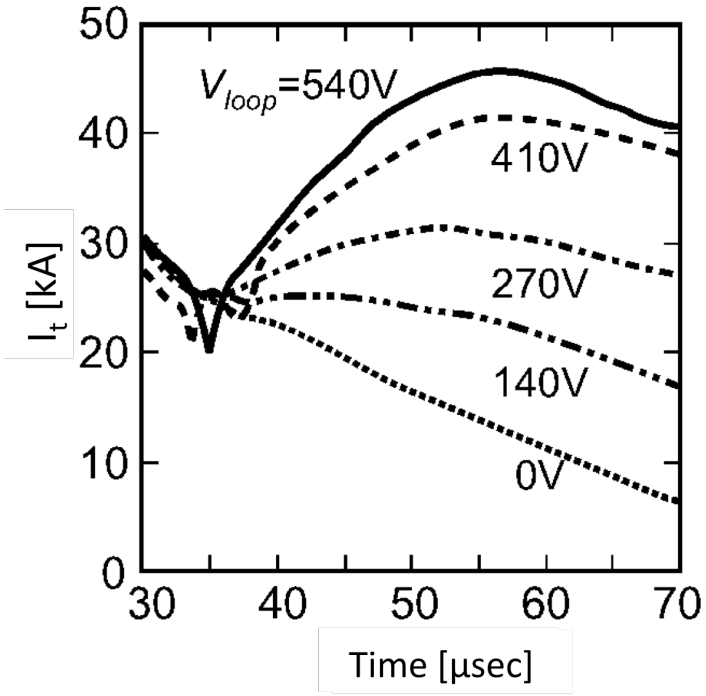

FIGURE 6. Time evolutions of toroidal plasma currents, when five different (vacuum) loop voltages V_{loop} from 0 to 540 V are applied to the produced FRCs [5].

FRC Current Amplification by Use of CS Coil

The merging formation of FRC also enables us to install a CS coil along the geometric axis [5,30]. After the merging formation is completed, the toroidal electric field is applied to the produced FRC for its current amplification, as illustrated in Fig. 1(c). Figure 6 shows the time evolutions of toroidal plasma currents of the FRCs for five different applied (vacuum) loop voltages V_{loop} varying from 0 to 540 V. The corresponding evolutions of poloidal flux contours (solid lines) and toroidal field amplitudes (red and blue colors) are also shown in Fig. 7 in the cases of V_{loop} =0 and 540 V. Since the total amount of capacitor bank energy is limited, the energy used for the FRC merging formation is about 50% as large as that in Fig. 4. When the applied V_{loop} is as large as 540 V, the toroidal current I_t of FRC is successfully amplified by factor 1.8 from 25 kA up to 45 kA within 20 μsec. The poloidal flux of FRC $\Psi=L_iI_t$ is also amplified by factor 2.5, because the CS current amplification expands the FRC, increasing its internal inductance L_i. In the case of V_{loop}=0, the FRC is observed to decay within 60 μsec, in sharp contrast with the cases of V_{loop}>0. It is noted that the current amplification does not cause the FRC to relax to a spheromak with B_f~B_p in the Taylor minimum magnetic-energy state but that B_t of the FRC is kept uniformly zero. It is suggested that the FRC equilibrium has some robust stability against the external flux injection. During the current amplification, T_i stays constant (around 100 eV for V_{loop}=540 V) for 10 μsec and starts decreasing and T_e increases slowly up to 30 eV. The plasma current increment is found to increase almost linearly with increasing V_{loop}. Based on these results, this CS coil method is attractive for the current-amplification and the possible electron heating of the produced FRC.

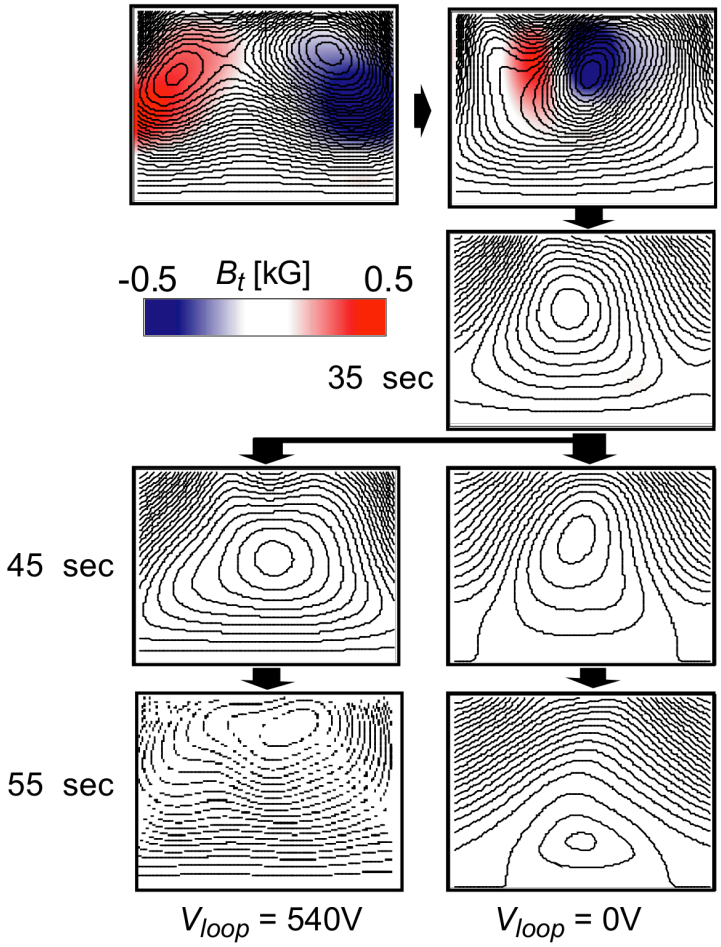

FIGURE 7. Time evolutions of poloidal flux contours and toroidal field amplitudes for the cases of V_{loop} =0 and 540 V. The red and blue colors are used to indicate the positive and negative amplitudes of B_t, respectively [5,36].

Suppression of FRC Tilt Instability by Kinetic Effects

Since the shell of the CS coil stabilizes the tilt mode, we carried out the FRC formation experiment without the CS coil to investigate the kinetic effect on tilt stability of the FRC. Figure 8 shows the time evolution of n=1 mode amplitude of produced FRCs with s-number of 6.4 and 2.9, together with the contours of axial magnetic field. In the large-s FRC (s=6.4), the n=1 mode amplitude keeps growing, causing collapse of the whole configuration at t=30 μsec. On the other hand, the n=1 mode in the small-s FRC (s=2.9) stays much longer than that in the large-s FRC. In both cases, the separatrix elongations are adjusted relatively large to stay in the tilt-unstable regime. These results indicate that ion kinetic effect plays important role on stabilization of n=1 mode. The decrease in s-number probably stabilizes the n=1 mode, probably because the number of ions meandering the separatrix repeatedly increases [31]. The toroidal rotation of the meandering ions is expected to suppress the n=1 mode through its gyro-stabilizing effect [31]. Recent experimental study also suggests another stabilizing mechanism of n=1 tilt mode by toroidal sheared flow [32]. In Fig. 8(b), large n=2 mode structure is identified at t=30 μsec after non-linear saturation of n=1 mode. This result qualitatively agrees with the hybrid simulation [10,11]. As the stabilizing process of n=1 mode, we observed the dynamic transformation of n=1 mode into n=2 mode together with the toroidal mode rotation.

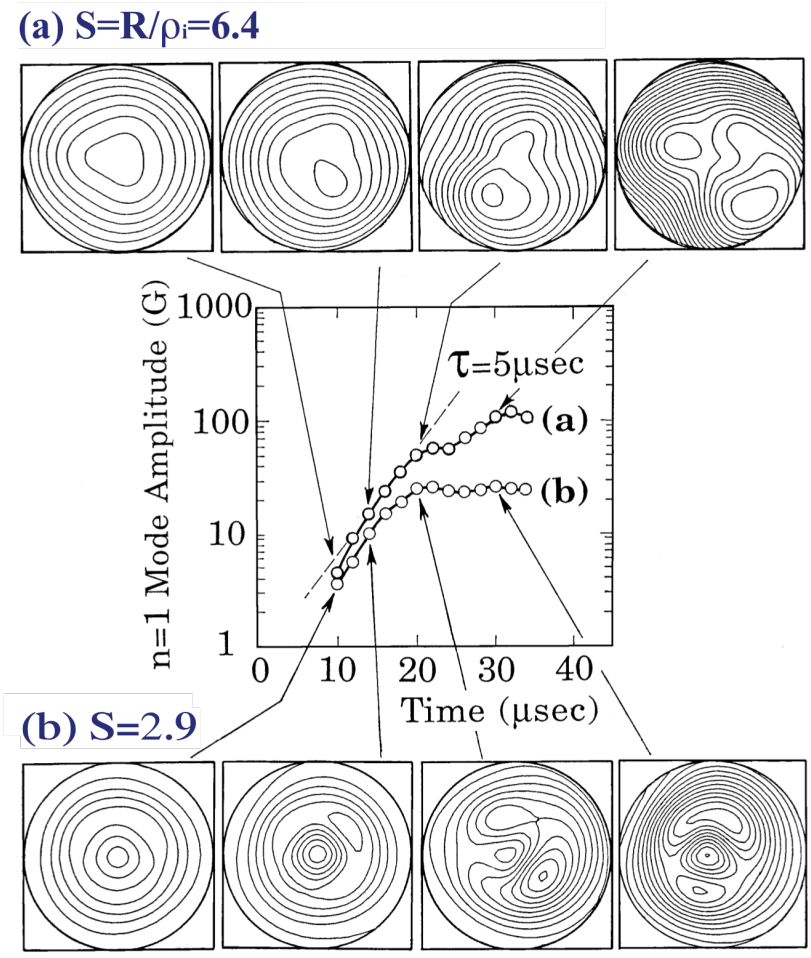

FIGURE 8. Axial magnetic field contours on the midplane (R-θ) for two produced FRCs with different s values: (a) 6.4 and (b) 2.9 (at t=18 μsec). Time evolutions of their n=1 toroidal mode amplitudes are also calculated at R=10 cm for these cases [5].

Transformation of FRCs to Ultra-High-Beta Spherical Tokamaks (STs)

One possible method to stabilize all MHD modes including n=1 of FRC in large s-number regime is to apply an external toroidal magnetic field to the produced FRCs. We produced an ultra-high-β ST in diamagnetic (high-β_p) regime, using close relationship between FRC and high-β ST equilibria. The high-β ST has received increased attention as a future economical reactor, partly because of their possible second stability (high-β_p) property. However, the formation of diamagnetic tokamaks requires the hollow current profile, limiting their start-up discharges. A question arises as to how we can suppress the paramagnetic component of toroidal field that tends to prevail in STs. The merging method, especially its direct ion heating effect, is useful for the current profile control of tokamaks, especially the start-up of the diamagnetic tokamak formation. We have demonstrated the ultra-high-β ST formation for the first time by application of external toroidal magnetic field right after the merging formation of FRC [33].

Figure 9 shows the evolutions of 2-D poloidal flux contour plots with toroidal field amplitude and radial profile

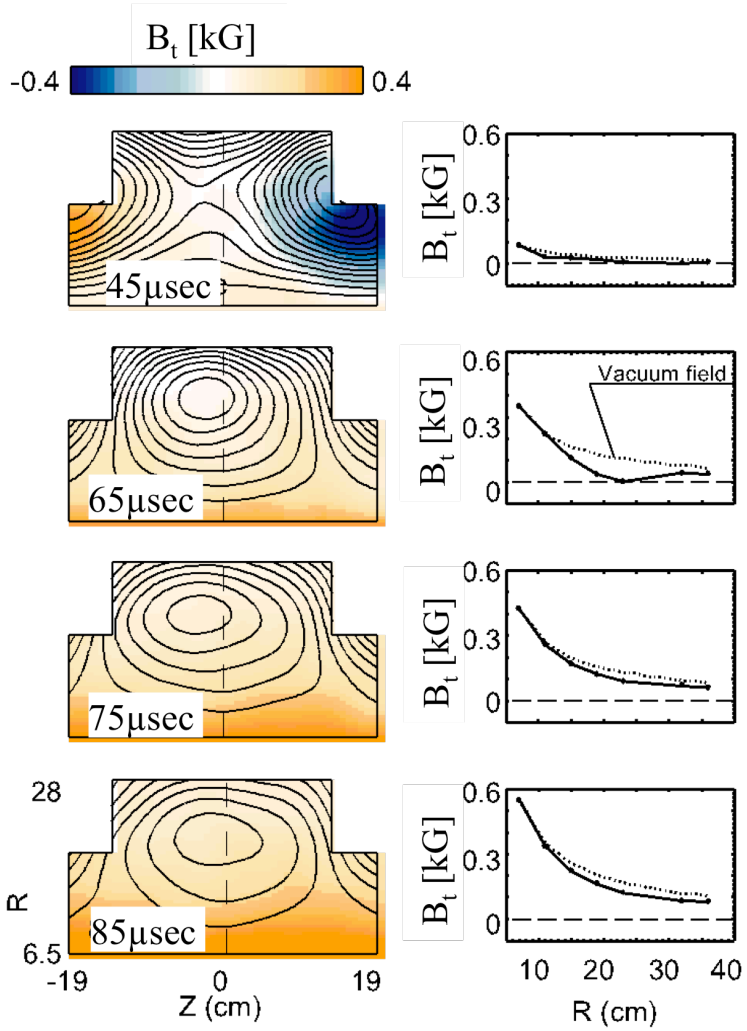

FIGURE 9. Time evolutions of 2-D poloidal flux contour plots and toroidal magnetic field amplitude (left column) and radial profile of toroidal magnetic field on the midplane (Z=0) (right column) of the high-β ST formation experiment [28].

of toroidal field B_t. At first, we merge two spheromaks with opposing B_t together, forming an FRC. In the last phase of the FRC merging formation, the toroidal field is applied with ramp-up time of 20 μsec and the FRC is stably transformed into a new ST equilibrium. The safety factor q_{95} of the final state is about 3. Note that the toroidal field inside the separatrix is smaller than the vacuum magnetic field, indicating formation of a diamagnetic ST with poloidal β_p larger than unity. This diamagnetic toroidal field is maintained about 30 μsec, which corresponds to 10 Alfvén transit time. In this experiment, the plasma is sustained by the CS coil for about 100 μsec.

Since the high-β ST in second-stable regime should have large pressure gradient, it is difficult to transform a low-β ST with large magnetic shear to a high-β ST without passing through unstable region of ballooning mode in *s*(magnetic shear)-alpha(pressure gradient) diagram. It probably requires detailed control of current and pressure profile using RF and NBI heating/current drive. In our proposed method, the initial FRC before the following transformation to ST is already equipped with the high-β properties including hollow current profile and large pressure gradient localized in the edge region. These properties are observed to be maintained after the application of external B_t, eliminating a need for the artificial current and/or pressure profile controls to produce the high-β ST from an FRC.

SUMMARY

A series of experiments has demonstrated the new scenario of the FRC merging formation, the flux-amplification by a CS coil and the sustainment of the produced FRCs in an external magnetic field. The merging formation process of FRC reveals the ion acceleration and direct ion heating effects of the counter-helicity magnetic reconnection with the wide area of field-null. The reconnected magnetic field-lines accelerate plasma ions toroidally up to order of the Alfvén velocity and heat them directly and selectively probably through the large ion viscosity around field-null (*X*-point) region. This efficient direct conversion of the toroidal magnetic energy to the ion thermal energy realizes the novel equilibrium-transition from the low-β merging spheromaks to the high-β FRC. The observed selective ion heating during the FRC formation is also consistent with particle and MHD simulations [34,35]. The ion heating energy scales with square of the reconnecting magnetic field, indicating the reconnection heating often observed in solar flare is useful for fusion plasma startup and heating. The CS current drive is observed to amplify the FRC current successfully by factor 2 within 20 μsec. The merging process is useful for the ion heating of the FRCs and the CS current drive for electron heating. The center conductor is found necessary to fully stabilize the n=1 tilt mode of the produced oblate FRC with large s-number up to 10. Without the center conductor, the produced oblate FRCs with s>4 suffer from large increase in the n=1 mode. However, the n=1 mode amplitude decreases with decreasing the s-number. The growth and suppression of the n=1 tilting instability observed in large-s and small-s regions agree qualitatively with the s-scan experiment in conventional FRTP FRC experiment [12]. Recently, we also applied 0.5 MW NBI to the produced FRC in TS-4 device (Fig. 2), improving its MHD stabilities possibly due to the finite Larmor radius effect. Finally, we demonstrated the transformation of FRCs into high-β STs with hollow current profile in high-β/diamagnetic regime by applying external toroidal magnetic field to the produced FRC. The high-β physics of FRCs are also useful to explore high-β ST equilibrium. The plasma merging technique extended various possibilities of FRC researches is now adopted by a number of experimental devices in Table 1.

REFERENCES

1. M. Tuszewski, Nucl. Fusion **28**, pp.2033-2092 (1988).
2. M. N. Rosenbruth and M.N. Bussac, Nucl. Fusion **19**, pp.489-498 (1979).
3. M. Gyaznevich, A. Bondeson, P. G. Carolan, G. Cunningham, R. Duck, T. Edlington, S. K. Erents, J. Ferreira, S. J. Fielding, K. Gibson et al., Proc. 14th Int. Conf. on Plasma Phys. Cont. Nuc. Fusion Res. (Wuerzburg, Germany) vol. **2**, (Vienna: IAEA), p. 575 (1992).
4. L.J. Perkins, S.K. Ho, J.H. Hammer, Nucl. Fusion **28**, 1365 (1988).
5. Y. Ono et al., in Proc. IEEE Int. Conf. Plas. Sci., (Saskatoon, 1988) p.77; Y. Ono et al. J. Plasma Fus. Res. **56**, 214 (1986); Y. Ono et al., Phys Fluids B **6**, 3691 (1993); Y. Ono, A. Morita, T. Itagaki, M. Katsurai, Plas. Phys. Cont. Nucl. Fus. Res. 1992 vol. **2**, p.619, IAEA, Vienna (1993).
6. Y. Ono, T. Matsuyama, K. Umeda, E. Kawamori, Nucl. Fusion **43**, 649 (2003).
7. Y. Ono et al., Phys. Rev. Lett. **76**, 3328 (1996).
8. J. B. Taylor, Phys. Rev. Lett. **33**, pp.1139-1141 (1974).

9. N. Iwasawa, A. Ishida, L.C. Steinhauer, Phys. Plasmas **8**, 1240 (2001).
10. E.V. Belova, S.C. Jardin, H. Ji, M. Yamada, R. Kulsrud, Phys. Plasmas **7**, 4996 (2000).
11. E.V. Belova, S.C. Jardin, H. Ji, M. Yamada, R. Kulsrud, Phys. Plasmas **8**, 1267 (2001).
12. M. Tuszewski, D.C. Barnes, R.E. Chrien, J.W. Cobb, D.J. Rej, R.E. Siemon, D.P. Taggart, B.L. Wright, Phys. Rev. Lett. **66**, 711 (1991).
13. J. Slough, A.L. Hoffman, Phys. Fluids B **5**, 4366 (1993).
14. W.F. Pieece, R.J. Maqueda, R.D. Brooks, R. Farengo, Nucl. Fusion **33**, 117 (1993).
15. I. R. Jones, Phys. Plasmas **6**, 1950 (1999).
16. A.L. Hoffman, Nucl. Fusion **40**, 1523 (2000).
17. Y. Ono, M. Inomoto, T. Okazaki, Y. Ueda, Phys. Plasmas **4**, 1953 (1997).
18. Y. Ono, M. Inomoto, Y. Ueda, T. Matsuyama, T. Okazaki, Nucl. Fusion **39**, 2001 (1999).
19. E. Kawamori and Y. Ono, Phys. Rev. Lett. **95**, 085003 (2005).
20. S. P. Gerhardt, E.V. Belova, M. Yamada, H. Ji, M. Inomoto, Y. Ren and B. McGeehan, Phys. Rev. Lett. **99**, 245003 (2007).
21. Y. Ono, H. Tanabe, Y. Hayashi, T. Ii, Y. Narushima, T. Yamada, M. Inomoto and C. Z. Cheng, Phys. Rev. Lett. **107**, 185001 (2011).
22. Y Ono, H Tanabe, T Yamada, M Inomoto, T Ii, S Inoue, K Gi, T Watanabe, M Gryaznevich, R Scannell, C Michael and C Z Cheng, Plasma Physics and Control. Fusion 54, 124039, (2012); Y. Ono, H. Tanabe, T. Yamada, K. Gi, T. Watanabe, T. Ii, M. Gryaznevich, R. Scannell, N. Conway, B. Crowley and C. Michael, Phys. Plasmas **22**, 055708 (2015).
23. M. Brown, Phys. Plasmas **6**, 1717 (1999).
24. Y. Ono, R. Imazawa, H. Imanaka, Y. Hayashi, S. Ito, M. Nakagawa, T. Yamada, M. Inomoto, A. Ejiri, Y. Takase, T. Asai, T. Takahashi, H. Sakakita, S. Kiyama, Y. Hirano, H. Koguchi, C. Z. Cheng, Fusion Energy 2008, EX/P9-4 (2008).
25. H. Y. Guo, M. W. Binderbauer, D. Barnes, S. Putvinski, N. Rostoker, L. Sevier, M. Tuszewski, M. G. Anderson, R. Andow, L. Bonelli, F. Brandi, R. Brown, D. Q. Bui, V. Bystritskii, F. Ceccherini, R. Clary, A. H. Cheung, K. D. Conroy, B. H. Deng, S. A. Dettrick, J. D. Douglass, P. Feng, L. Galeotti, E. Garate, F. Giammanco, F. J. Glass, O. Gornostaeva, H. Gota, D. Gupta, S. Gupta, J. S. Kinley, K. Knapp, S. Korepanov, M. Hollins, I. Isakov, V. A. Jose, X. L. Li, Y. Luo, P. Marsili, R. Mendoza, M. Meekins, Y. Mok, A. Necas, E. Paganini, F. Pegoraro, R. Pousa-Hijos, S. Primavera, E. Ruskov, A. Qerushi, L. Schmitz, J. H. Schroeder, A. Sibley, A. Smirnov, Y. Song, L. C. Steinhauer, X. Sun, M. C. Thompson, A. D. Van Drie, J. K. Walters, M. D. Wyman, and TAE Team, Phys. Plasmas **18**, 056110 (2011).
26. Private communication.
27. K. J. Chung, Y. H. An, B. K. Jung, H. Y. Lee, C. Sung, Y. S. Na, T. S. Hahm, and Y. S. Hwang, Plasma Sci. Technol. **15**, 244 (2013).
28. Y. Ono, M. Inomoto, Phys. Plasmas **7**, 1863 (2000).
29. Y. Ono, T. Kimura, E. Kawamori, Y. Murata, S. Miyazaki, Y. Ueda, M. Inomoto, A.L. Balandin, M. Katsurai, Nucl. Fusion **43**, 789 (2003).
30. E. Kawamori, T. Sumikawa, H. Imanaka, R. Imazawa, K. Yamashita, T. Hayamizu and Y. Ono, Nucl. Fusion **47**, 1232 (2007).
31. K. Nishimura, R. Horiuchi, T. Sato, Phys. Plasmas **4**, 4035 (1997).
32. Y. Ono, T. Matsuyama, K. Umeda, E. Kawamori, Nucl. Fusion **43**, 649 (2003).
33. Y. Ono, M. Inomoto, T. Matsuyama, T. Murakami and T. Tawara, Nuclear Fusion **41**, 971 (2001).
34. T. Tajima, J.I. Sakai, Sov. J. Plasma Phys. **15**, 519 (1989).
35. Horiuchi R and Sato T, Phys. Plasmas 4 27 (1997); C. Z. Cheng, S. Inoue, Y. Ono, and R. Horiuchi, Phys. Plasmas **22**, 101205 (2015).
36. M. Inomoto, Y. Ono, IEEJ Transactions on Electrical and Electronic Engineering 2, Issue **4**, 424 (2007).

Control of Ion Gyroscale Fluctuations via Electrostatic Biasing and Sheared $E \times B$ Flow in the C-2 Field Reversed Configuration

L. Schmitz[1,a)], E. Ruskov[2,b)], B.H. Deng[3,c)], M. Binderbauer[3,d)], T. Tajima[2,3,e)], H. Gota[3,f)], M. Tuszewski[3,g)], and the TAE Team

[1]*University of California Los Angeles, Los Angeles, CA 90095, USA*
[2]*University of California, Irvine, Irvine, CA 92697, USA*
[3]*Tri Alpha Energy, Inc., P.O. Box 7010, Rancho Santa Margarita, CA 92688, USA*

[a)]Corresponding author: lschmitz@trialphaenergy.com
[b)]eruskov@uci.edu
[c)]bdeng@trialphaenergy.com
[d)]michl@trialphaenergy.com
[e)]tajima@trialphaenergy.com
[f)]hgota@trialphaenergy.com
[g)]mgtu@trialphaenergy.com

Abstract. Control of radial particle and thermal transport is instrumental for achieving and sustaining well-confined high-β plasma in a Field-Reversed Configuration (FRC). Radial profiles of low frequency ion gyro-scale density fluctuations ($0.5 \leq k\rho_s \leq 40$), consistent with drift- or drift-interchange modes, have been measured in the scrape-off layer (SOL) and core of the C-2 Field-Reversed Configuration (FRC), together with the toroidal $\boldsymbol{E}\times\boldsymbol{B}$ velocity. It is shown here that axial electrostatic SOL biasing controls and reduces gyro-scale density fluctuations, resulting in very low FRC core fluctuation levels. When the radial $\boldsymbol{E}\times\boldsymbol{B}$ flow shearing rate decreases below the turbulence decorrelation rate, fluctuation levels increase substantially, concomitantly with onset of the n=2 instability and rapid loss of diamagnetism. Low turbulence levels, improved energy/particle confinement and substantially increased FRC life times are achieved when $\boldsymbol{E}\times\boldsymbol{B}$ shear near the separatrix is maintained via axial SOL biasing using an annular washer gun.

INTRODUCTION

Field-Reversed configurations (FRCs [1,2]), characterized by high normalized kinetic pressure β, are of interest as a fusion reactor concept due to their axisymmetric geometry and potential for aneutronic fusion based on advanced fuels, such as the proton-boron fusion reaction ($p\text{-}B^{11}$) [3]. FRCs also allow investigating the formation, stability, and kinetic properties of high β, high temperature, low collisionality plasmas in a laboratory environment. Compared to toroidal plama confinement concepts such as the tokamak [4] or stellarator [5], FRCs have intrinsically axisymmetric magnetic field configuration. Due to the larger ion Larmor orbits, FRCs are also expected to have favorable microstability properties, as recognized early by Rostoker and others [6,7,8]. However, similar to other plasma confinement concepts, anomalously large plasma resistivity, and radial particle and energy transport in excess of classical collisional transport have historically been observed in FRCs [9,10]. The increased radial losses have been attributed to microinstabilities, however the FRC life time in early experiments has often been too short to achieve transport-dominated states [1,2], and macroscopic MHD instabilities and micro-instabilities sometimes co-exist. Among the instabilities investigated in some detail are the lower hybrid drift instability (LHD), drift cyclotron instabilities, and density/temperature-gradient-driven drift waves [1,2]. So far, experimentally measured LHD fluctuation levels could not account for the observed radial transport level [11]. Unstable collisionless

electromagnetic drift waves have been predicted at finite $\beta_0 = \mu_0 n(T_e + T_i)/\, B_e^2$ (where μ_0 is the free space permeability and B_e is the external magnetic field) for a large toroidal wavenumber (k_θ) range ($1 \leq k_\theta \rho_s \leq 10$ or higher, where $\rho_s = c_s m_i/eB$ with $c_s = [(kT_e + kT_i)/m_i\,]^{1/2}$ is the ion sound gyroradius), with growth rates peaking for $0.2 \leq \beta_0 \leq 0.6$ [12]. The growth rate has been predicted to depend strongly on the ratio of density and temperature gradient scale lengths, L_n/L_{T_e} and L_n/L_{T_i}, where $L_n = n/(\partial n/\partial r)$ and $L_{T_{e,i}} = T_{e,i}/\left(\partial T_{e,i}/\partial r\right)$. According to analytical calculations presented in [11], ion mode instability is expected only for $L_n > L_{T_e}, L_{T_i}$, a criterion which is not satisfied in the C-2 plasma investigated here. Unstable electron mode may exist for $L_n/L_{T_i} < 1$ and $L_n/L_{T_e} \sim 1$, conditions which are satisfied in C-2. Experimentally, density fluctuations with toroidal wavelength in between the ion and electron gyroradius scale have indeed been observed in the C-2 FRC via Doppler Backscattering, as discussed in detail below. Extremely short wavelength electron temperature gradient (ETG) instabilities (linearly most unstable for $k_\theta \rho_e \geq 1$ and $L_n/L_{T_e} \geq 2$, where ρ_e is the electron gyroradius,[13]) are expected to be only weakly unstable for the experimentally relevant range of β_0 and $L_n/L_{T_e} \sim 1$ in C-2, and are not observable by present FRC diagnostics.

The (closed flux surface) FRC plasma in C-2 [14] is surrounded by an (open fieldline) mirror-confined scrape-off layer (SOL) plasma with mirror ratio R_M = 6-10. In addition to the instabilities discussed above, it is expected that the SOL plasma would be unstable to drift-interchange modes driven by density/temperature gradients and the (moderate) field line curvature, as observed experimentally in a tandem mirror experiment with very similar plasma parameters [15]. Also, at moderate/high β finite Larmor radius (FLR) effects do not always restrict interchange instability to $k_\theta \rho_s < 1$ as discussed in [16].

In this Letter we report the first systematic measurements of low frequency ($\omega < \omega_{ci}$) density turbulence and the turbulence decorrelation rate, the toroidal $\boldsymbol{E}\times\boldsymbol{B}$ flow velocity, and the radial $\boldsymbol{E}\times\boldsymbol{B}$ flow shear in the C-2 FRC plasma, both inside the FRC plasma and in the SOL. We present experimental evidence that (i) ion gyro-scale density fluctuations ($0.5 \leq k_\theta \rho_s \leq 40$) peak in the SOL, and decrease substantially in amplitude inside the FRC separatrix; (ii) fluctuation levels increase when the $\boldsymbol{E}\times\boldsymbol{B}$ shearing rate decreases below the turbulence decorrelation rate, with concomitant onset of the n=2 rotational mode, increased FRC radial losses, and radial contraction of the FRC separatrix; (iii) substantial $\boldsymbol{E}\mathrm{x}\boldsymbol{B}$ flow shear just outside the FRC separatrix, and low fluctuation levels are sustained when an annular plasma gun is activated, resulting in substantially increased FRC lifetime.

DESCRIPTION OF THE C-2 FIELD-REVERSED CONFIGURATION

The C-2 FRC plasma is created via injecting and merging of two preformed, compact high-β plasmoids into a central confinement chamber with radius R=0.7m and length L=4.5m, with an external solenoidal field of 0.05-0.14T, as described in detail elsewhere [14,17]. Typical line- averaged plasma densities in the experiments described here are 2.5-4 x 10^{19} m^{-3}, and the ion and electron temperatures in the FRC core are T_i~400-600 eV and T_e~80-130 eV. The FRC core plasma is surrounded by an open field line, mirror-confined scrape-off layer (SOL) plasma, terminating axially on metallic end plates located in divertor chambers at a distance of 8.8 m from the machine axial midplane. An annular washer plasma gun [18,19] (inner diameter 0.11 m, outer diameter 0.13 m, located in the south divertor chamber) injects plasma along open field lines outside the FRC separatrix, mapping to a 3 cm wide annular region at the machine midplane. The local magnetic field at the gun location is ~0.5T. The washer guns have anode-cathode voltages of ~0.5-1.0 kV, with typical discharge current ~10 kA. The plasma guns are electrically floating with respect to the vacuum chamber, producing a negative (inwards pointing) radial electric field transmitted to the SOL region just outside the FRC separatrix [20].

THE DOPPLER BACKSCATTERING DIAGNOSTIC

The rms density fluctuation level ($0.5 \leq k_\theta \rho_s \leq 4$), toroidal $\boldsymbol{E}\mathrm{x}\boldsymbol{B}$ velocity, and turbulence decorrelation rate near the FRC midplane are evaluated via multi-channel Doppler backscattering (DBS [21,22]), using five co-linear diagnostic microwave beams focused into the plasma at an oblique angle ζ in the toroidal plane, via an adjustable parabolic stainless steel mirror (Figure 1a). Beam spot sizes of $2W_0 \sim$ 3-4.5 cm are achieved depending on frequency (26 GHz $\leq f \leq$ 66 GHz; W_0 is the Gaussian $1/e^2$ power half width). Due to refraction in the plasma the microwave beams bend in the toroidal direction. Backscattering by plasma density fluctuations occurs preferentially near the cutoff layer [21], according to the selection rules $k_S = -k_I = k_\theta/2$ and $\omega_S = \omega_t + v_t k_\theta$, where the indices I and S denote the incident and backscattered wave, $v_t = v_{E\times B} + v_{ph}$ is the toroidal turbulence advection velocity (v_{ph} is

the turbulence phase velocity in the plasma frame), and k_θ is the resonant toroidal density fluctuation wavenumber. The backscattered signal, received via the same beam optics (monostatic detection), is proportional to the density fluctuation amplitude at the resonant wavenumber. The probed radial wavenumber is $k_r \sim 0$ as the beam propagates

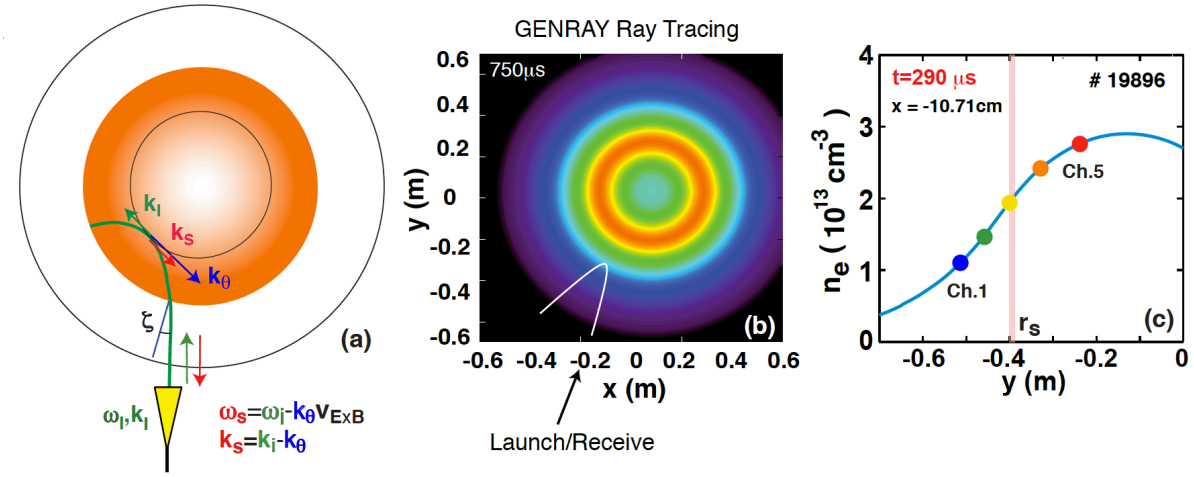

FIGURE 1. (a) FRC cross section illustrating DBS launched/ backscattered beam trajectory and relation between launched and backscattered frequency and wavenumber; (b) density contours in the FRC axial midplane, as measured by CO2 interferometry (red: ne=3x1013 cm-3, purple: ne=0.5x1013 cm -3), illustrating a typical microwave beam path calculated via GENRAY ray tracing; the turning point is located just outside the cut-off layer; (c) plasma density profile and typical DBS probing locations (x,y are laboratory frame coordinates).

toroidally near the cut-off layer. The toroidal wavenumber k_θ, and the probed radii r in the laboratory frame are calculated using GENRAY [23] ray tracing based on high time resolution (10 μs) radial electron density profiles reconstructed from a six channel CO_2 laser interferometer [24,25] located in the FRC axial midplane. A typical calculated microwave beam path is illustrated in Figure 2(b). Figure 2(c) shows the reconstructed density profile and typical DBS probing radii. All calculated DBS probing positions are mapped to the axial FRC midplane in laboratory (machine) coordinates and then mapped to plasma center coordinates.

A circular plasma cross section is assumed in the density profile reconstruction and validity of this approximation is checked via 2-D bolometry emission profile reconstruction at the FRC midplane, used also to determine the plasma center coordinates. The time-resolved $\boldsymbol{E}\times\boldsymbol{B}$ velocity is obtained from the instantaneous Doppler shift, $f_D = (\omega_R - \omega_I)/2\pi = v_t k_\theta/2\pi$. Neglecting the fluctuation phase velocity one obtains $v_{E\times B} \approx 2\pi f_D/k_\theta$. The DBS diagnostic is described in more detail in [26].

DENSITY FLUCTUATIONS AND EXB FLOW

Figure 2(a) shows an example of a DBS quadrature spectrum ñ(f) obtained in an FRC plasma without plasma gun activation. The contours represent the density fluctuation level ñ(f) in arbitrary units, on a logarithmic scale. The probed radius varies between r~0.38-0.43m in the SOL. The width of the observed DBS spectrum is mainly due to toroidal curvature [26,27], limiting the toroidal wavenumber resolution to $\Delta k_\theta/k_\theta \sim 1.5$, with a median probed wavenumber k_θ ~2-4 ($k_\theta \rho_s$~6-9). In Fig. 2(b) the integrated density fluctuation level is shown. The large modulation in fluctuation envelope (and in the spectrum-averaged Doppler shift) is primarily due to strong n=1 MHD activity and the resulting elliptical plasma deformation. The time history of the excluded flux radius [Fig. 2(c)] indicates rapid FRC contraction. In contrast, Figs. 2(d-e) show the corresponding quantities for an FRC actively maintained via SOL biasing (plasma gun activated).

The quadrature spectrum (Fig. 2(d) shows predominant negative frequencies, in particular after t=0.8 ms. The toroidal $\boldsymbol{E}\times\boldsymbol{B}$ velocity can be extracted from the power-averaged Doppler-shifted spectrum, which here indicates flow in the ion diamagnetic direction (or positive E_r) in the SOL. The contribution of the turbulence phase velocities to the measured Doppler shift/ is estimated to be less than 10%. Fig. 2(e) shows substantially lower integrated fluctuation levels. Most importantly, the integrated fluctuation level is substantially lower with plasma gun active,

concomitantly with a very pronounced increase in FRC lifetime and more gradual radial separatrix contraction [Fig. 2(f)].

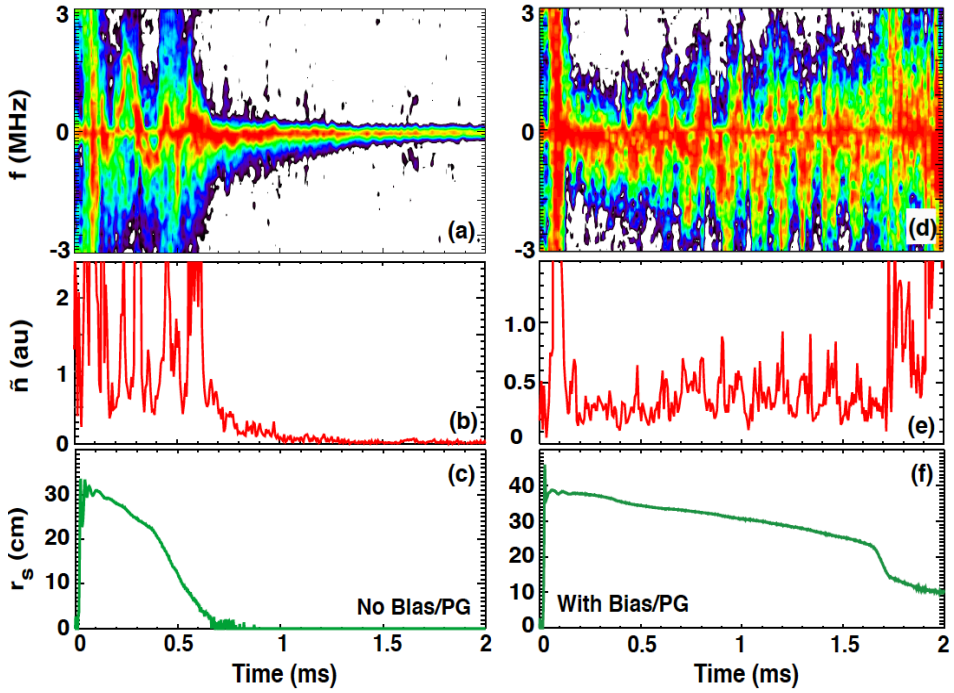

FIGURE 2. a) Time evolution of quadrature DBS spectrum in the SOL; plasma gun not active (contours are density fluctuation level ñ in a.u.; logarithmic scale); (b) Frequency-integrated density fluctuation level $\tilde{n}$; (c) excluded flux radius; (d) quadrature spectrum in discharge sustained via electrostatic biasing (plasma gun active); negative average frequency indicates $\boldsymbol{E}\times\boldsymbol{B}$ flow in the ion diamagnetic direction; (e) reduced density fluctuation level with biasing (note the difference in vertical scale); (f) time history of excluded flux radius with plasma gun active, indicating substantially increased FRC lifetime.

Figure 3 shows a comparison of rms density fluctuation levels in the near SOL (about 5 cm outside the excluded flux radius r_s), and several cm inside the FRC separatrix, for two plasma shots, without and with plasma gun activated. The time evolution of the FRC excluded flux radius, r_s (in practice very close to, but outside the FRC separatrix) is indicated by grey lines.

The toroidal wavenumber range, determined by the beam launch angle ξ and the plasma geometry, is centered around k_θ ~ 2-3 cm^{-1} ($k_\theta\rho_s \sim 2$), with $\Delta k_\theta/k_\theta$ ~1.8–2.3 due to plasma curvature [27] for the data in Fig. 3; hence a relatively broad wavenumber range is included in the measurement.

In both shots $\tilde{n}/n$ is relatively low for 150 μs < t < 250 μs after an initial high turbulence period likely related to FRC translation and merging. However, without plasma gun (# 19986), the fluctuation level increases substantially between 250 μs and 450 μs both outside and inside the separatrix [Fig.3(a,b)], typically concomitantly with the appearance of an n=2 rotational mode, producing a fast oscillation in the detected density fluctuation level due to the elliptical deformation of the FRC, and leading to radial FRC contraction (indicated by rapid reduction of r_s). In contrast, with the plasma gun active [shot #20957, Fig.3(d,e)] the fluctuation level increases only slightly outside and inside the separatrix, the n=2 rotational mode is absent, and the separatrix radius contracts much less rapidly. There is a "benign" n=1 wobble of the FRC present that does not appear to cause FRC radial contraction (loss of diamagnetism), or substantial radial losses [17,20,28]. In later shots, where a second plasma gun has been employed in the north divertor, the n=1 and n=2 modes have been stabilized [17,29].

Fig. 3(c) shows the time evolution of the measured $\boldsymbol{E}\times\boldsymbol{B}$ velocity for shot #19896 (0.15 ms < t < 0.38 ms), at four density levels spanning the separatrix. The turbulence phase velocity has been neglected as the real frequency in the (generic) drift/interchange dispersion is expected to scale as $\omega_r \sim v_{D_e} k_\theta/(1+k_\theta^2\rho_s^2)$ due to finite Larmor radius (FLR) effects (v_{D_e} is the electron diamagnetic drift velocity), hence substantially reducing ω_r for $k_\theta\rho_s > 1$. The radial $\boldsymbol{E}\times\boldsymbol{B}$ velocity shear is largest between 0.17-0.28 ms; this is the time interval where a relatively low fluctuation level is observed [Fig. 2(a,b)]. The $\boldsymbol{E}\times\boldsymbol{B}$ shear decreases substantially later during this shot. In contrast, with the plasma gun active (shot #20957), the shear between channels 2 and 3 [as indicated in Fig.1(b)] is maintained for at

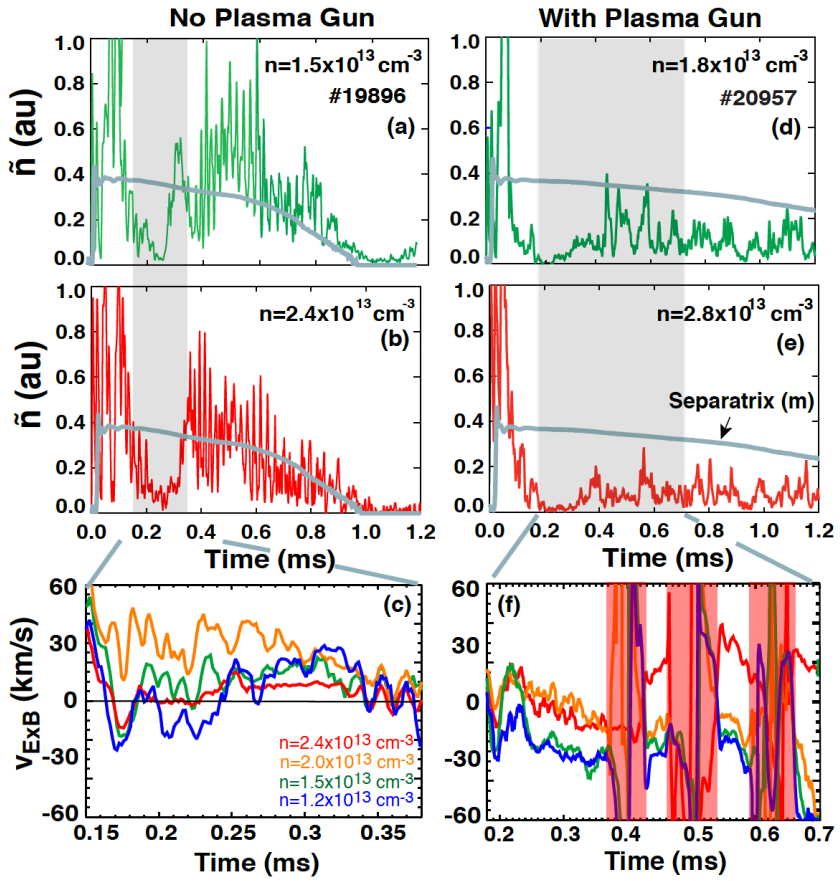

FIGURE 3. Normalized density fluctuation level $\tilde{n}/n$ without plasma gun; (a) in the SOL; (b) inside the FRC separatrix; (c) toroidal $\boldsymbol{E}\times\boldsymbol{B}$ velocity for four probed densities, without plasma gun; (d) density fluctuation level $\tilde{n}$ in the SOL; (e) $\tilde{n}$ inside the separatrix; (f) $\boldsymbol{E}\times\boldsymbol{B}$ velocity, with plasma gun active.

least for $t \leq 0.7$ ms [Fig.3(f)], and fluctuation levels remain low [Fig.3(d,e)]. During the shaded time periods, the n=1 wobble causes the beam incidence angle ζ to switch sign, preventing proper interpretation of the DBS data.

Figure 4 shows the normalized rms density fluctuation level vs plasma radius, at different times throughout the discharge. Fluctuation levels are clearly always highest in the SOL, but increase in amplitude substantially between 280 μs and 340 μs, both in the SOL and in the FRC core without plasma gun [Fig. 4(a)]. In contrast, it is remarkable that core fluctuations remain low throughout the discharge when the plasma gun is active [Fig. 4(b)]. SOL fluctuations increase after 300 μs but always remain lower by a factor of 2-3 compared to the case without plasma gun (note the reduced ordinate scale).

The toroidal turbulence wavenumber spectrum has been measured just inside and outside the FRC separatrix in the gun-assisted plasma ($r \sim r_s$+5cm). Initial results have been reported [17] and a more detailed description will be provided in a separate publication [30]. In the SOL, the dependence on normalized toroidal wavenumber is best described by an exponential spectrum with a decay constant of $\alpha_k \sim 0.16$ (the corresponding exponent for the decay of the fluctuation energy density $[\sim(\tilde{n}/n)^2]$ is ~0.33]). Exponential spectra have also been observed in the core of tokamak low confinement mode (L-mode) plasmas for lower normalized (poloidal) wavenumber, $k_\theta \rho_s \leq 3$ [31,32]. In both the FRC and the tokamak plasmas referenced here, $(\tilde{n}/n)^2$ decays by roughly 3 orders of magnitude as $k_\theta \rho_s$ increases by a factor of 5. This may indicate that the fluctuation energy cascades towards high wavenumbers, and that the viscous damping at small scales may be the dominant energy sink.

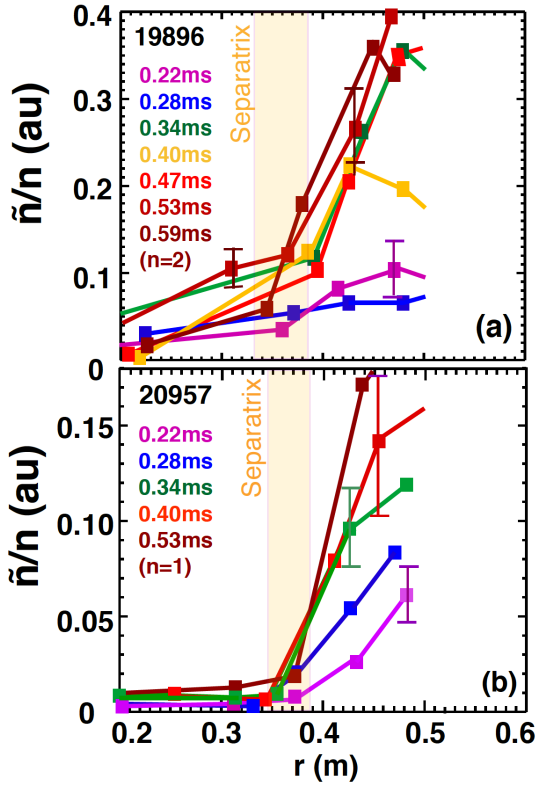

FIGURE 4 Time evolution of relative density fluctuation level vs. radius (plasma frame); (a) plasma gun not activated; (b) plasma gun active.

E×B SHEAR AND TURBULENCE DECORRELATION

We now examine the spatial structure of the ***E×B*** shear and its influence on the turbulence level. Figure 5(a,d) show radial profiles of the radial electric field, evaluated from the measured ***E×B*** velocity. The radial profile of the axial magnetic field has been estimated from the FRC rigid rotor model [31], approximating the measured density profile by a rigid rotor profile. The electric field is positive outside the FRC separatrix and reverses in the FRC core. It has been predicted that turbulent eddies are elongated and eventually sheared apart if the flow shearing rate $\omega_{\mathbf{E\times B}}$ exceeds the turbulence decorrelation rate $\Delta\omega_D, \omega_{\mathbf{E\times B}} > \Delta\omega_D$, [33], a process shown to suppress edge turbulence in the low-to high confinement-mode transition (L- to H-mode transition), and in internal barriers in tokamaks [34,35]. The shearing rate ω_{ExB} is determined from the differential flow between two neighboring DBS probing locations r_1, r_2 : $\omega_{\mathbf{E\times B}} = [v_{\mathbf{E\times B}}(r_1) - v_{\mathbf{E\times B}}(r_2)]/(r_1 - r_2)$. The turbulence decorrelation rate is estimated from the width of the auto-correlation coefficient of the backscattered signal.

Fig. 5(b,c) shows a comparison of the ***E×B*** shearing rate with the turbulence decorrelation rate $\Delta\omega_D$. With ***E×B*** turbulence advection present, the decorrelation rate in the laboratory frame is given by $\Delta\omega_D{}^{\mathrm{lab}} = \Delta\omega_D(v_{\mathbf{E\times B}}/\lambda_\theta)[\Delta\omega_D{}^{-2} + \lambda_\theta{}^2/v_{\mathbf{E\times B}}{}^2]^{1/2}$. The radial turbulence correlation length λ_r is measured by DBS (λ_r~2-6 cm here, which is on the order of the ion gyroradius). Estimating the poloidal correlation length $\lambda_\theta \geq \lambda_r$, we obtain $\Delta\omega_D{}^2 > v_{\mathbf{E\times B}}{}^2/\lambda_\theta{}^2$ and to good approximation $\Delta\omega_D \sim \Delta\omega_D{}^{\mathrm{lab}}$. Importantly, when the plasma gun is not active, $\omega_{\mathbf{E\times B}}$ is observed to exceed the decorrelation rate early in the shot (220 μs) over a ~0.1m wide radial range, but $\omega_{E\times B} < \Delta\omega_D$at a later time (340 μs). At that time, fluctuation levels and radial transport increase and FRC radius/flux confinement begin to decline rapidly [Fig. 2(a,b)].

The toroidal wavenumber range, determined by the beam launch angle ζ and the plasma geometry, is centered around k_θ ~ 2-3 cm^{-1} ($k_\theta\rho_s \sim 2$), with $\Delta k_\theta/k_\theta$ ~1.8–2.3 due to plasma curvature [25] for the data in Fig. 3; hence a relatively broad wavenumber range is included in the measurement.

In contrast, in shot #20957 (plasma gun active), the shearing rate exceeds the turbulence decorrelation rate early (280 μs) as well as later (450 μs) in the discharge [Fig.5(e,f)]. Correspondingly, magnetic flux confinement is improved (the FRC separatrix does not contract rapidly as in shot #19896 without plasma gun [Fig.3 (a,b)]), and radial particle and thermal transport is reduced. The n=2 mode is absent, possibly due a combination of axial line-tying due to the gun-injected SOL plasma, and/or modification of the ***E×B*** and toroidal ion rotation velocity.

CONCLUSIONS

In conclusion, we have characterized density fluctuations with toroidal scale lengths on the order of and smaller than the ion gyroradius in a large FRC plasma. Fluctuation levels peak in amplitude in the region of strong radial density/temperature gradients just outside the FRC separatrix. Density fluctuation levels *ñ/n* near the separatrix and in the SOL increase beyond a critical density gradient. The observed strong SOL turbulence is ascribed to drift- or drift-interchange modes driven unstable by the radial density and/or temperature gradients, possibly in combination with unfavorable curvature in the open field line, mirror-confined SOL plasma region. Further experimental and modeling/simulation work is under way to identify unambiguously the underlying instability drive [36].

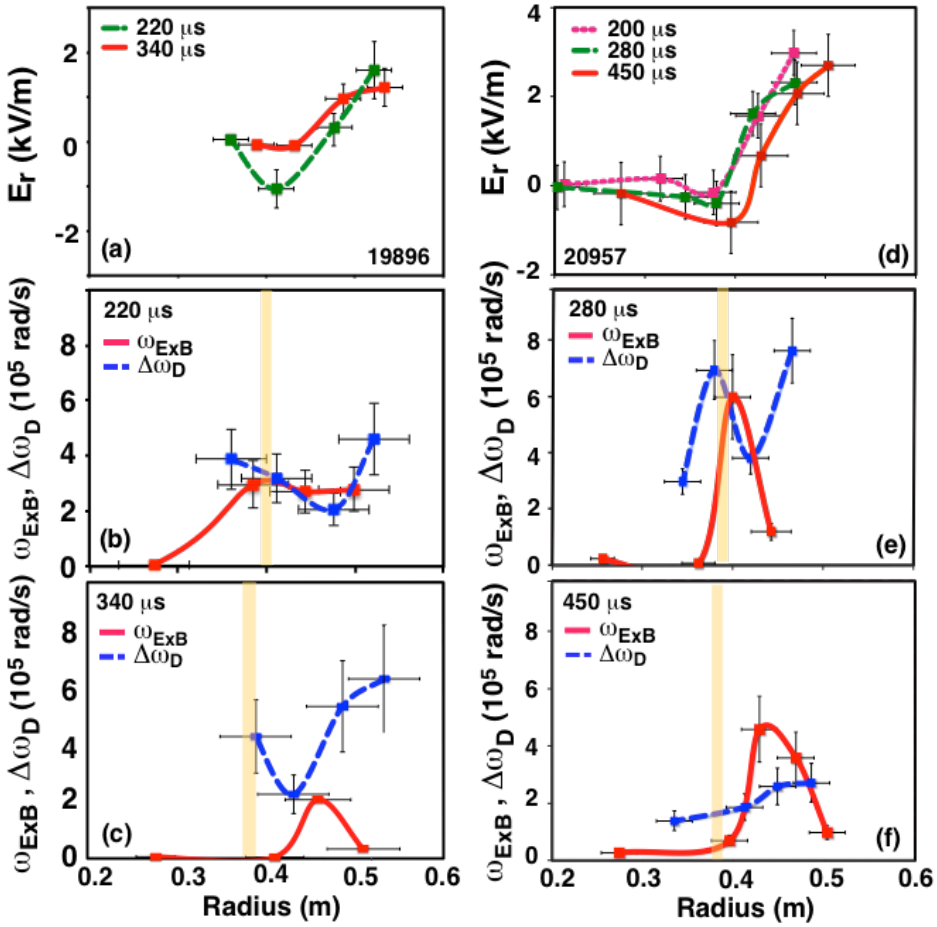

FIGURE 5: (a) Radial electric field (plasma gun not active); ***E*× *B*** shearing rate and decorrelation rate at (b) 220 μs, and (c) 340 μs; d) radial electric field (plasma gun active; shear maintained at 450 μs); ***E*× *B*** shearing rate and decorrelation rate at (e) 280 μs, and (f) 450 μs.

Density fluctuation levels, in particular in the FRC core, are substantially reduced via electrostatic biasing of the peripheral diverted (SOL) plasma, and the C-2 FRC lifetime is substantially extended. Core turbulence observations are qualitatively consistent with quenching of long wavelength ion modes via finite Larmor radius effects, For the first time, direct evidence for sustained turbulence reduction via ***E*× *B*** flow shear has been observed in FRC geometry. Similar to the well-documented observations in tokamak edge and core transport barriers [33,34], turbulence reduction requires that the radial shearing rate must exceed the ambient turbulence decorrelation rate. The observed radial transport barrier spans the transition region between closed and open flux surfaces, with the peak ExB shearing rate in the open fieldline region (SOL). The prospect of turbulence control across the FRC separatrix via ***E*× *B*** shear opens up the possibility of reducing radial thermal and particle loss from the confined FRC region, and hence advancing towards long-pulse FRC operation with reduced fueling and auxiliary heating requirements.

ACKNOWLEDGEMENTS

We gratefully acknowledge contributions, valuable discussions, and support of the experiments by T. Akhmetov of Budker Institute, D. Barnes, R. R. Clary, S.A. Dettrick, J. Douglass, E. Garate H.Y. Guo, D. Gupta,, S. Gupta, A. Ivanov, S. Korepanov, Y. Mok, S. Primavera, A. Necas, A. Smirnov, A. Sibley, M. C. Thompson, E. Trask, A. D. Van Drie, and the entire TAE team.

REFERENCES

1. Tuszewski, M., "Field-reversed configurations," *Nucl. Fusion* **28**, 2033-3093 (1988).
2. Steinhauer, L.C., "Review of field-reversed configurations," *Phys. Plasmas* **18**, 070501 (2011).
3. Rostoker, N. et al., "Colliding beam fusion reactor. *Science* 278 1419-1423 (1997).
4. Wesson, I., *Tokamaks* 4th edn. (Oxford University Press, 2011).
5. Spitzer, L. , "The Stellarator concept," *Phys. Fluids* **1**, 253 (1958).
6. Rosenbluth, M.N., Krall, N. and Rostoker, N., "Finite Larmor radius stabilization of "weakly" unstable confined plasmas," *Nucl. Fusion* Supplement Pt. 1 143-150 (1962).
7. Rostoker, N. in "Physics of High Energy Particles in Toroidal Systems" Editors T. Tajima and M. Okamoto (American Institute of Physics, New York, 1994), pp.323.
8. Naitou, H., Kamimura, T., and Dawson, "J.M. Kinetic effects on the convective plasma diffusion and the heat transport," *JPSJ* **46**, 258-265 (1979).
9. Hoffman A.L. and Slough, J.T., "Field reversed configuration lifetime scaling based on measurements from the large s experiment," *Nucl. Fusion* **33**, 27-38 (1993).
10. McKenna, K.F., Armstrong, W.T., Bartsch, R.R., Chrien, R.R., Cochrane, J.C. et al., "Particle confinement scaling in field-reversed configurations," *Phys. Rev. Lett.* **50**, 1787-1790 (1983).
11. Carlson, A.W. "A search for lower-hybrid-drift fluctuations in a field-reverse configuration using CO_2 heterodyne scattering," *Phys. Fluids* **30**, 1497-1509 (1987).
12. Chirkov A. Yu, and Khvesyuk, V.I., "Electromagnetic drift instabilities in high-β plasma under conditions of a field-reversed configuration," *Phys. Plasmas* **17**, 012105 (2010).
13. Farengo, R., Guzdar, P.N., and Lee, Y.C., "Collisionless electron temperature gradient-diven instability in field-reversed configurations," *Phys. Fluids* B **1**, 2181 (1989).
14. Binderbauer, M. et al., "Dynamic formation of a hot field reversed configuration with improved confinement by supersonic merging of two colliding high-β compact toroids," *Phys. Rev. Lett.* **105**, 045003 (2010).
15. Mase, A. et al., "Ambipolar potential effect on drift-wave mode in a tandem-mirror plasma," *Phys. Rev. Lett* **64**, 2281-2284 (1990).
16. Zhu, P. et al., "Absence of Complete Finite-Larmor-Radius Stabilization in Extended MHD," *Phys. Rev. Lett*. **101**, 085005 (2008).
17. Binderbauer, M.W., T. Tajima, T., Steinhauer, L., et al., "A high performance field-reversed configuration," *Phys. Plasmas* **22**, 056110 (2015).
18. G. I. Dimov, A.A. Ivanov, and G.V. Roslyakov, Sov. J. Plasma Phys. 8, 546 (1982).
19. Akhmetov, T.D. et al. "Experiments with dense plasma in the central solenoid of AMBAL-M," *Trans. Fusion Sci. Technology* **43**, 58-62 (2003).
20. Tuszewski, M. et al., "Field reversed configuration confinement enhancement through edge biasing and neutral beam injection," *Phys. Rev. Lett.* **108**, 255008 (2012).
21. Peebles, W.A., Rhodes, T.L., et al., "A novel, multichannel, comb-frequency Doppler backscatter system," *Rev. Sci. Instrum*. **81**, 10D902 (2010).
22. Hillesheim, J., Peebles, W.A., Rhodes, T.L., Schmitz, L. White, A.E., and Carter, T.A., "New plasma measurements with a multichannel millimeter-wave fluctuation diagnostic system in the DIII-D tokamak," *Rev. Sci. Instrum.* **81**, 10D907 (2010).
23. Smirvov, A.P. and Harvey, R.W. (2001), "The GENRAY ray tracing code," *Comp-X Report COMPX-2000-01*
24. Gornostaeva, O., Deng, B.H., et al., "Two-color CO2/HeNe laser interferometer for C-2 field reversed configuration," *Rev. Sci. Instr.* **81**, 10D516 (2010).
25. Deng, B.H., Kinley, J.S., and Schroeder, J. "Electron density and temperature profile diagnostics for C-2 field reversed configuration plasmas," *Rev. Sci. Instr.* **83**, 10E339 (2012).
26. Schmitz, L. et al., "Multi-channel Doppler backscattering measurements in the C-2 field reversed configuration," *Rev. Sci. Instrum*. **85** 11D840 (2014).
27. Blanco, E., Estrada, T., et al., "Doppler Reflectometry studies using a two-dimensional full-wave code," *Plasma Phys. Control. Fusion* **48**, 699-714 (2006).
28. Guo, H.Y., Binderbauer, M.W., D. Barnes, D., et al., "Formation of a long-lived hot field reversed configuration by dynamically merging two colliding high-beta compact toroids," Phys. Plasmas **18**, 056110 (2011).
29. Guo, H.Y., Binderbauer, M.W., Tajima, T., et al., "Achieving a long-lived-high-beta plasma state by energetic beam injection," *Nature Communications* **6**, 6897 (2015).

30. Schmitz, L., Fulton, D., Ruskov, E., et al., "First evidence of suppressed ion-scale turbulence in a hot high-β plasma," submitted to *Nature Communications*.
31. Hennequin, P., et al., "Fluctuation spectra and velocity profile from Doppler backscattering on Tore Supra," *Plasma Phys. Controlled Fusion* **46**, S771-S779 (2006).
32. Schmitz, L., Holland C., Rhodes, T.L. et al., "Reduced electron thermal transport in low collisionality H-mode plasmas and the importance of TEM/ETG-scale turbulence," *Nuclear Fusion* **52**, 023003 (2012).
33. Biglari, H., Terry, P., and Diamond, P.H., "Influence of sheared poloidal rotation on edge turbulence," *Phys. Fluids* B **2**, 1-4 (1990).
34. Burrell, K.H. et al., "Role of the radial electric field in the transition from L (low) mode to H (high) mode to VH (very high) mode in the DIII-D tokamak," *Phys. Plasmas* **1**, 1536-1544 (1994).
35. Greenfield, C.M., Burrell, K.H., DeBoo, J.C., et al., "Quiescent double barrier regime in the DIII-D tokamak," *Phys. Rev. Lett*. **86**, 4544 (2001).
36. Fulton, D.P., Lau C.K., Holod I., Lin Z., Dettrick, S. "Gyrokinetic Particle Simulation of a Field Reversed Configuration," *Phys. Plasmas* **23**, 012509 (2016).

Recent Breakthroughs on C-2U: Norman's Legacy

M.W. Binderbauer,[1] T. Tajima,[1] M. Tuszewski,[1] L. Schmitz,[1,2] A. Smirnov,[1] H. Gota,[1] E. Garate,[1] D. Barnes,[1] B.H. Deng,[1] E. Trask,[1] X. Yang,[1] S. Putvinski,[1] R. Andow,[1] N. Bolte,[1] D.Q. Bui,[1] F. Ceccherini,[1] R. Clary,[1] A.H. Cheung,[1] K.D. Conroy,[1] S.A. Dettrick,[1] J.D. Douglass,[1] P. Feng,[1] L. Galeotti,[1] F. Giammanco,[3] E. Granstedt,[1] D. Gupta,[1] S. Gupta,[1] A.A. Ivanov,[4] J.S. Kinley,[1] K. Knapp,[1] S. Korepanov,[1] M. Hollins,[1] R. Magee,[1] R. Mendoza,[1] Y. Mok,[1] A. Necas,[1] S. Primavera,[1] M. Onofri,[1] D. Osin,[1] N. Rath,[1] T. Roche,[1] J. Romero,[1] J.H. Schroeder,[1] L. Sevier,[1] A. Sibley,[1] Y. Song,[1] L.C. Steinhauer,[1] M.C. Thompson,[1] A.D. Van Drie,[1] J.K. Walters,[1] W. Waggoner,[1] P. Yushmanov,[1] K. Zhai,[1] and the TAE Team

[1] *Tri Alpha Energy, Inc., P.O. Box 7010, Rancho Santa Margarita, CA 92688, USA*
[2] *Department of Physics and Astronomy, UCLA, Los Angeles, CA 90095-1547, USA*
[3] *Department of Physics, University of Pisa, Largo B. Pontecorvo 3, 56127 Pisa, Italy*
[4] *Budker Institute of Nuclear Physics, 11 Lavrentyev Avenue, 630090 Novosibirsk, Russia*

Abstract. Conventional field-reversed configurations (FRC) face notable stability and confinement concerns, which can be ameliorated by introducing and maintaining a significant fast ion population in the system. This is the conjecture first introduced by Norman Rostoker multiple decades ago and adopted as the central design tenet in Tri Alpha Energy's advanced beam driven FRC concept. In fact, studying the physics of such neutral beam (NB) driven FRCs over the past decade, considerable improvements were made in confinement and stability. Next to NB injection, the addition of axially streaming plasma guns, magnetic end plugs, as well as advanced surface conditioning lead to dramatic reductions in turbulence driven losses and greatly improved stability. In turn, fast ion confinement improved significantly and allowed for the build-up of a dominant fast particle population. This recently led to the breakthrough of sustaining an advanced beam driven FRC, thereby demonstrating successful maintenance of trapped magnetic flux, plasma dimensions and total pressure inventory for times much longer than all characteristic system time scales and only limited by hardware and electric supply constraints.

INTRODUCTION

The field-reversed configuration (FRC) is a prolate compact toroid with poloidal magnetic fields [1,2]. FRCs hold great promise because of their very high-beta, simple geometry, natural divertor, and ease of translation. As such they could lead to economic fusion reactors with high fusion power density, and capable of burning aneutronic fuels. However, as in other high-beta plasmas, there have been serious stability and confinement concerns. It may be possible to address most of these issues by introducing and maintaining a significant large orbit ion population in the system. This is the conjecture first introduced by Norman Rostoker multiple decades ago and adopted as the central design tenet in Tri Alpha Energy's (TAE) first of a kind C-2 and C-2U devices.

The idea can roughly be viewed as combining elements of accelerator and high-beta plasma topology to create highly kinetic large orbit particle plasmas. Throughout the past 50 years this theme has guided much of Norman Rostoker's work, but was also studied by a wide spectrum of other researchers. Early elements of the idea were first introduced by Rosenbluth, Krall and Rostoker in their famous 1962 paper on finite Larmor radius corrections [3]. This was followed in the late seventies and eightoies by sets of simulations showing that particles are predominantly affected by fluctuations of wavelengths that are greater than a particle's orbital radius [4,5]. Ultimately, multiple studies on various tokamaks,

such as JET and TFTR, demonstrated that large orbit ions slow down and diffuse with near classical rates as long as $E/T > \sim 10$, where E is the large orbit particle energy and T the temperature of the background plasma [6].

The main goal of the C-2 experiments was to elucidate the physics of advanced FRCs driven by Neutral Beam (NB) injection. In pursuit of this goal, significant improvements were made in FRC confinement and stability. Early C-2 discharges [7] had relatively good confinement, but global power losses considerably exceeded the available NB input power. The addition of axially streaming plasma guns, together with magnetic end plugs as well as advanced surface conditioning, such as Ti and Li gettering, have led to dramatic reductions in turbulence driven losses and greatly improved stability [8]. As a result, fast ion confinement significantly improved and allowed for build-up of a dominant fast particle population yielding highly reproducible, long-lived, macroscopically stable FRCs with lifetimes far beyond conventional theta-pinch formed FRCs [5,6]. These achievements clearly demonstrated the many beneficial effects of Norman's large orbit conjecture and its performance impact on FRCs.

Based on these groundbreaking successes, neutral beam power was boosted from around 4 to 10+ MW during a comprehensive upgrade between September 2014 to March 2015. The resulting C-2U device then achieved in only 3 months of operations the breakthrough of sustainment of an advanced beam driven FRC, thereby demonstrating successful maintenance of trapped magnetic flux, plasma dimensions and total pressure inventory for times much longer than all characteristic system time scales and only limited by hardware and electric supply constraints.

Together these achievements provide a solid foundation on the ascent toward aneutronic fusion reactors. This paper will review and expand on these recent breakthroughs, present context for their interpretation and thereby celebrate the genius and legacy of Norman Rostoker. The paper is organized in a short section describing the C-2U hardware, followed by a discussion of fast particle effects on equilibrium profiles and plasma shape. Sections summarizing stability and confinement aspects follow and precede a discussion of the C-2U plasma sustainment milestone. Finally a summary is presented and findings are discussed in view of Norman Rostoker's vision.

C-2U HARDWARE

The C-2U research facility is a substantial upgrade of the C-2 machine described in detail elsewhere [6,10]. The most important upgrade in C-2U occurred with respect to the neutral beam injection system, which is illustrated in Fig. 1, with critical performance characteristics delineated in Table 1. The C-2U beams are characterized by a downgrade in energy from 20 to 15 keV, but with a simultaneous factor of close to 3x upgrade in neutral current. The resultant total beam power for all 6 injectors is well over 10 MW, over 2.5 times the power available in C-2. The reduced beam energy and higher currents also guarantee tighter radial fast ion orbits together with higher instantaneous fast ion deposition rates due to the higher beam currents. As depicted in Fig. 1, the beams are also aimed at a 20° angle relative to the machine midplane. This provides for better beam plasma coupling, even under pronounced axial FRC shrinkage. The combined purpose of all these changes was to substantially increase the fast ion population in C-2U and so provide a foundation to study fast ion pressure dominated FRC states.

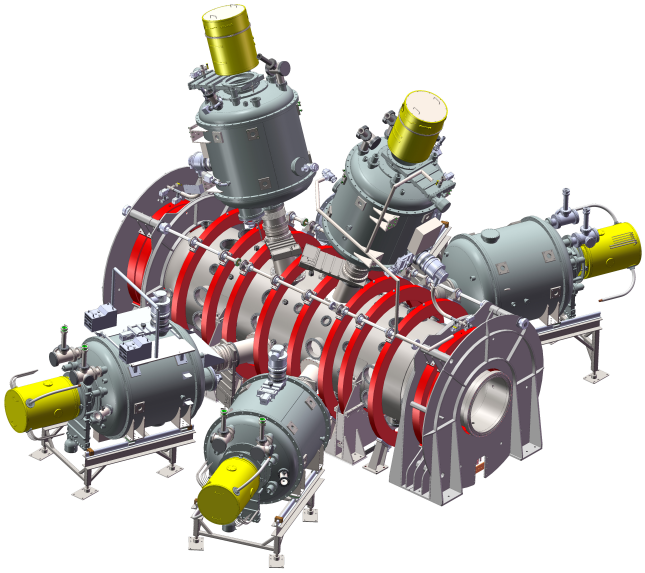

Figure 1. Layout of the central section of the C-2U device, including neutral beam orientation and central magnetic field coils.

Table 1. Key performance metrics of the C-2U neutral beam system.

Parameter	Value
Beam energy	15 keV
Total power in neutrals	10+ MW
# of injectors	6
Pulse duration	8 ms flat top
Beam radial e-fold. size	< 10 cm
Beam divergence	< 28 mrad
Ion current per source	145 A

Other system upgrades focused on the magnetic coil arrangements and associated power supplies, more optionality and voltage capability for the plasma guns and biasing electrodes, and lastly significant upgrades to the diagnostic systems. The goal of the magnet upgrades was to accommodate the angled beam injectors and also to allow for some compensation of the diffused (lost through the vessel wall) magnetic flux, which can be appreciable on timescales of 5+ ms. The upgrades to the end biasing and gun systems were motivated by studies in C-2 that showed that higher bias potentials and more flexible placement of guns can be very advantageous with respect to stability control and conducive to longer plasma life together with reduced energy, flux and particle losses.

The most significant advances in diagnostics occurred around a new 4 chord far infrared reflectometry system that was deployed in the upper radial half of the midplane and complements the prior existing two color 6-chord CO_2/HeNe system. This new system and the resultant advantages are detailed in [11].

The rest of the machine operates as in C-2, meaning that target FRCs are created by merging compact tori that are simultaneously formed at both ends and injected at supersonic

speeds into the central confinement chamber. The compound FRCs so form are then sustained by the new neutral beam system and supported by the upgraded edge/end biasing means and new magnetic correction coils. Overall, the total C-2U hardware proved remarkably reliable and produced record FRC performance with good reproducibility within weeks of the start of physics operations.

FAST PARTICLE EFFECTS ON EQUILIBRIUM FEATURES

Comparing equilibrium profiles in C-2U with typical C-2 measurements immediately demonstrates the significant difference produced by the fast ion pressure. Typical radial electron density is illustrated in Fig. 2(a). While the overall plasma radius is not very different from C-2, with separatrix radii around 32-35 cm, the most striking feature is the existence of a "double-humped" structure on top of the typical hollow center and steep separatrix gradients. The two density peaks are located on either side of the null field radius. This feature is indicative of the substantial fast ion pressure presence in C-2U. The radial betatron oscillations of the fast ions lead to a broad fast ion distribution that modifies the electron profiles accordingly, producing the characteristic features found in the C-2U measurements. Similar features are also found in 2-D simulations as reported in [12]. As can be seen from the Thomson scattering derived electron temperature profiles depicted in Fig. 2(b), a similar structure is visible in the radial temperature profile and should be expected based on profile consistency and the FRC topology.

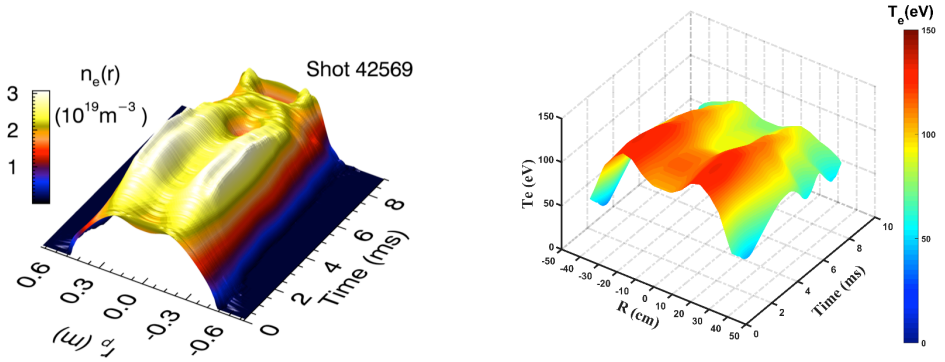

(a) (b)

Figure 2. Typical C-2U radial electron equilibrium profiles. (a) Density vs time, (b) Temperature vs time.

Moving on to the evolution of the axial plasma shape, the pronounced effect of the fast ion pressure is present here as well. In fact, in C-2 and most prior FRC experiments, the axial size of the plasma was monotonically shrinking throughout the discharge and typically at a faster rate than the contraction of the radius. This is a direct result of the loss of plasma energy. While axial length contraction is visible early on in C-2U discharges as well, it is evident from the temporal evolution depicted in Fig. 3 that the rate of shrinkage decreases over the first few micro-seconds and that the FRC ultimately ceases to shrink around 3 ms. This is a direct consequence of the build-up of fast ion pressure. Given the finite fast ion source of the neutral beams, it takes a few milli-seconds to develop significant fast ion pressure. In fact, Fig. 4, illustrates that fast ion pressure is about comparable to the thermal plasma pressure at around 2+ ms under full beam power, i.e. all 6 neutral beam systems operating at maximum settings. Once the fast particle pressure becomes dominant, it is the

footprint of the fast particles (as determined by injection angle and externally applied magnet field) that determines the axial extend of the FRC. As can be seen in Fig. 3, C-2U has sufficient fast ion injection and retention to allow for maintenance of the axial extend of the plasma for as long as feed energy is supplied to the machine.

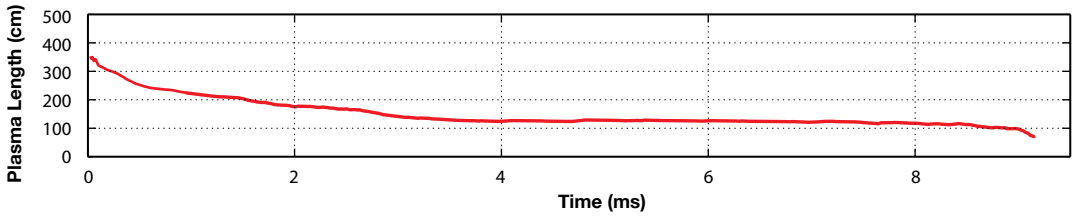

Figure 3. Temporal evolution of axial FRC length.

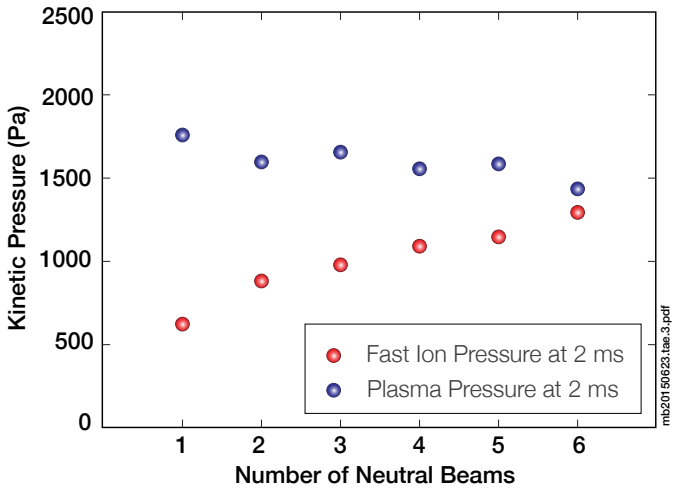

Figure 4. Dependence of fast ion pressure on neutral beam power at 2 ms.

These new findings are in addition to other fast particle induced effects reported in [10] with regards to reductions in energy decay time and enhanced macro-stability as functions of injected beam power.

PLASMA STABILITY

FRC stability has always been regarded as difficult to achieve. In fact, FRCs have been widely assumed to be fairly unstable and difficult to control. Early theoretical work by Rosenbluth and Bussac [13] almost put a premature stop to the concept's exploration due to the theoretically perceived fundamental problem of tilt instability. While experimental findings throughout the years did not produce evidence of strong tilting, the majority of theoretical work was focused on explaining this apparent discrepancy. It was broadly believed that the kinetic nature of the FRC is responsible for the better than predicted tilt stability. Indeed, a large empirical database was assembled that strongly supports this fact and established that tilting is suppressed as long as S^*/E < 3-3.5, with S^* being the ratio of the separatrix radius, r_s, to the ion collisional skin depth, c/ω_{pi}, and E the FRC elongation, the

ratio of axial half length, $l_s/2$, to separatrix radius. C-2U data is certainly not in disagreement with these prior experimental findings of robust FRC tilt stability. In fact, we have found that in C-2U the additional strong angular momentum produced by the dominant fast particle population provides additional tilt stability, which is also corroborated by theory and simulations. Further discussion can be found in [9].

In contrast to tilting, the most dangerous experimental instability for FRCs is the rotational n=2 mode. It is driven by centrifugal forces developing from the free energy in the FRC rotation and causes plasma to redistribute into an elliptical cross section. In past experiments its stabilization was achieved by application of modest external multipole fields [14]. As discussed in [10], this suppression technique causes azimuthal asymmetries and is, therefore, prohibitive with regards to maintaining a robust fast ion population. During the course of C-2 research, TAE developed an active means of n=2 stability compatible with fast ions by biasing the boundary-plasma with plasma guns and/or electrodes at the end divertors [8]. This produces a radially inward electric field E_r in the edge layer of the FRC, which causes an $E_r \times B_z$ drift with opposite polarity to the indigenous FRC ion diamagnetic drift, causing shear and thus reduced bulk plasma rotation. This technique proved critical in building up the dominant fast ion population in C-2U. Such fast ion pressure then provides a stiffening of the FRC and further stability against the growth of n=2 and higher order such modes.

Good centering of the plasma is equally important to assure fast ion pressure buildup. This requires suppression of plasma wobble around the central machine axis. Wobble modes are driven by plasma rotation and end mirror effects. In C-2/C-2U these modes are suppressed via line-tying between the plasma and conductive end surfaces, such as plasma gun electrodes. Field line tension then provides an effective restoring force. Stability requires edge/end plasma densities of about 10^{12} cm^{-3} to guarantee sufficiently low sheath resistance. As practiced in C-2U, active plasma guns and up to 1 kV of biasing potential on the central field lines reduces wobble to negligible levels, especially during the early phase of the discharge, which is critical to rapid fast ion pressure built-up. The reader is referred to reference [10] for further details of this mechanism.

Outside of the stabilizing influence discussed so far, it is well known that substantial fast ion pressure can cause considerable effects on the bulk plasma and lead to macroscopic instabilities. While C-2 experiments noted the existence of fast-ion-related magnetic fluctuations, which is also supported by theory, there was no evidence of any destructive modes induced by the fast ion population. This finding is still true even in the C-2U environment, where ultimately over 60% of the thermal pressure is replaced by fast particle pressure. However, there are clearly observable beam based effects in C-2U. For example, macro-fluctuations of the magnetic field tend to decrease overall, except in the neighborhood of the ion-cyclotron frequency. Another effect that is found is the occurrence of kinetic beam plasma micro-instabilities. These are again not macroscopically destructive, but do, for instance, enhance the neutron production rate resultant from D-D reactions in C-2U. The current interpretation of these findings is centered around the conjecture that the beam induced modes exhibit high phase velocity, retain robustness and keep the plasma from total destruction, essentially sharing the same philosophy as the wake-field excitations described by Tajima and Dawson [15]. Further experimental details and simulation efforts are discussed by Tajima and Necas in this set of proceedings [16].

TRANSPORT RELATED OBSERVATIONS

Robust confinement has been reported throughout the C-2 experiments [7,8,10,17]. The

most significant hallmark has been the relative absence of density fluctuations in the FRC core next to edge turbulence localized outbound of the separatrix. This has been widely credited to the large orbit particle conjecture of Norman Rostoker. As conjectured in the 1990s by Rostoker and Binderbauer [17] a dominant population of large-orbit ions in beam driven FRCs, such as in C-2U, can average out short-wavelength fluctuations and as such substantially stabilize both macroscopic and microscopic modes. The latter effect also suppresses transport driven by microscale modes. On the other hand, modes on the pronounced sub-ion gyroradius scale are not strongly influenced by large-orbit ions as evidenced by the presence of anomalous electron losses in C-2U. Nonetheless, the observed core plasma quiescence and small-scale structure of the observed micro-turbulence, together with the reported shear based fluctuation suppression, leads to dramatically reduced transport losses and the favorable strong positive correlation between T_e and the electron energy confinement time, τ_{Ee}, as $\tau_{Ee} \propto T_e^{1.6}$ and reported in [10]. Further details on the measurements and characteristics of the turbulence can be found in the paper by Schmitz et al., also included in this set of proceedings [18].

From previously reported results, there is a rich interdependence between the FRC core and the edge plasma or so-called scrape off layer (SOL). In fact, particle and energy transport times across these regions are sequential, meaning that particles and energy experience sequential core and SOL transport processes on their migration to the outside. At the same time, the processes and underlying time scales are also coupled.

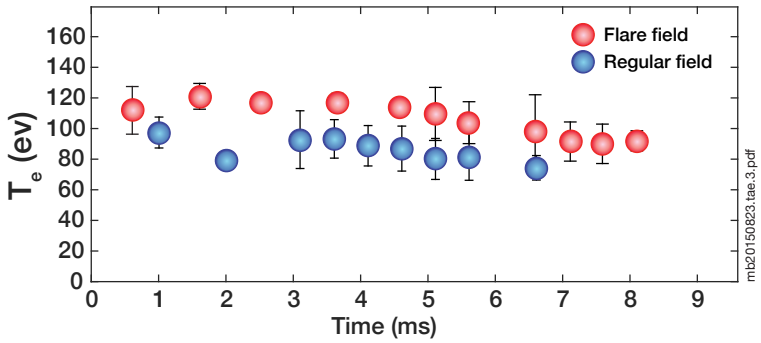

Figure 5. Temporal evolution of core electron temperature under flared and regular magnetic fields in the end divertors.

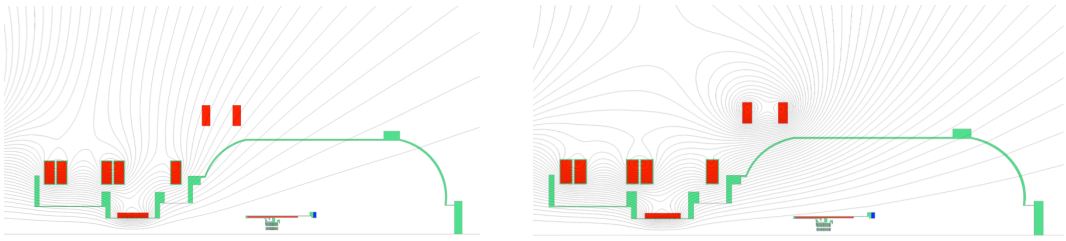

(a) (b)

Figure 6. Magnetic topology of (a) flared and (b) regular magnetic fields in C-2U end divertors.

A new example that emerged out of the C-2U data, is the fact that topological changes in the magnetic field in the far downstream divertors can have a profound impact on the core

electron temperature. As shown in Fig. 5, 20-30% higher electron temperatures can be achieved by changing the flaring of the magnetic field in the divertors. Turning the set of external divertor magnetic coils on and off produces either strongly bundled or widely flaring magnetic flux lines as illustrated in the top and bottom panels of Fig. 6. These topological changes affect the contact points of different flux surfaces with respective divertor surfaces and, in particular, which flux bundles are coupled to the divertor mounted plasma guns. More importantly, the flared field structure provides effective inverse mirrors from the perspective of particles streaming from the divertor towards the core FRC. For example, stronger flux expansion reduced the number of secondary cold electrons produced by plasma wall interactions on the inner divertor surfaces from crossing these pinch points towards the core, thereby providing some thermal insulation for the inner electron population. Techniques such as these hold great promise for achieving even higher energy confinement times in future devices. Given the importance of these issues, TAE is putting a heavy emphasis on such edge related improvements for its next machine, C-2W.

PLASMA SUSTAINMENT MILESTONE

The main goal of C-2U was to demonstrate current drive and plasma sustainment by neutral beam injection in excess of all characteristic system timescales. The broader meaning of this milestone was (1) achievement of record stability for a high beta topology; (2) demonstration of the strength of the large orbit/fast ion physics paradigm (combination of elements of accelerator and high-beta plasma topology to create highly kinetic large orbit particle plasmas); and (3) the mastery of beam-driven advanced FRCs as a foundation for ascend toward a future aneutronic reactor.

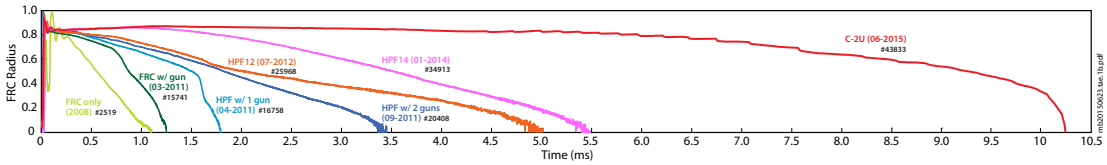

Figure 7. Comparison of FRC radius evolution during various C-2 and C-2U operating regimes.

C-2U delivered these capabilities after only 3 months of operations in June of 2015. As illustrated in Fig. 7, there is a dramatic improvement in diagmagnetic lifetime of the plasma between C-2 and C-2U operation, as evidenced by the temporal evolution of the excluded flux radius. The plasma radius in C-2U is essentially being kept constant for about 5+ ms, while there is instantaneous decay associated with all traces from C-2. In fact, the performance in C-2U is only limited by pulse length constraints arising from finite on-site stored energy in the power supplies of many critical systems, such as beams and biasing equipment. This was a conscientious choice made at the onset of the upgrade process. However, it does not diminish the strength of the scientific validation arising out of this achievement. The 5 ms sustainment capability is sufficient as all other intrinsic system time scales are considerably shorter, such as (a) beam circulation time (on order 1 μs), (b) typical MHD like instabilities such as tilt (on order of 10s to 100 μs), (c) fast particle instabilities (on order <10 μs), (d) various confinement times (on order of 1 ms or less), (e) charge exchange times (on order 1 ms), and (f) fast particle slowing down times (from 1 up to below 3 ms). Figure 8 depicts a shot with 4 ms beam drive to illustrate the sustainment of some of the critical plasma quantities such as FRC radius, plasma density and total plasma temperature. During the 4 ms duration all C-2U systems are operating at optimum power levels and with full supply energy.

Alternatively, the stored energy can also be delivered over a longer period, but at reduced power. This gives rise to the additional ability to also study pulses and system behavior for even longer timescales and to provide additional demonstration of the robust physics that underlies the system's performance. In fact, in this mode it is possible to achieve discharges in excess of 10 ms, as illustrated in Fig. 7. Here the biasing power supply limitation are most constraining and result in the application of < 850 V to the plasma gun electrodes, compared to optimal settings at 1+ kV for the shorter duration pulses. It is also important to realize that there is no active feedback control on any equipment, a very strong indication of the robustness of the large orbit physics principles at work.

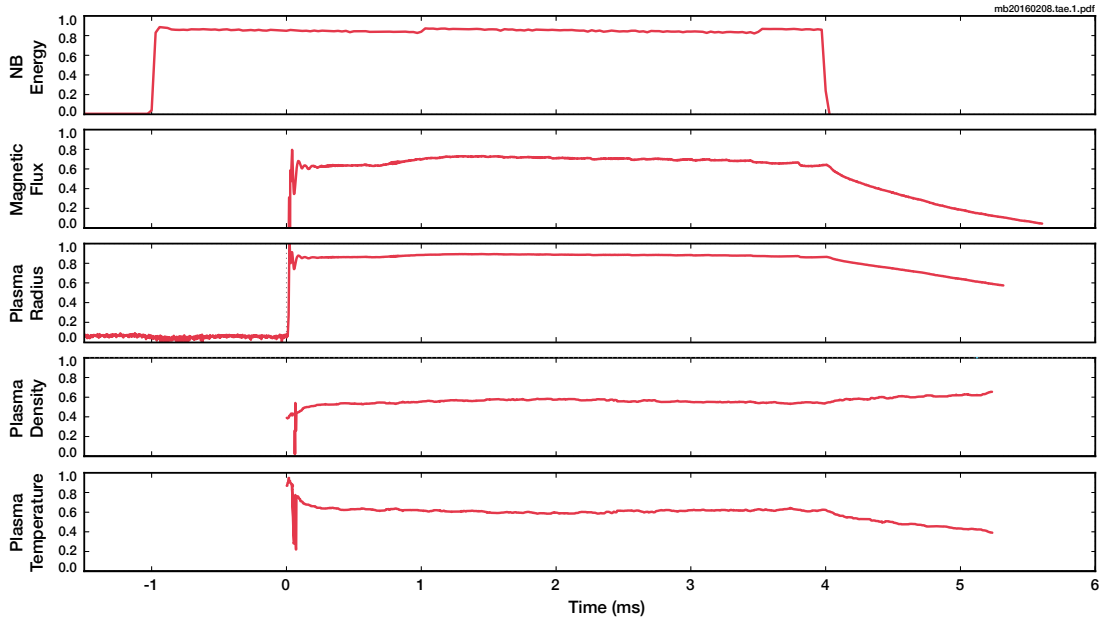

Figure 8. Evolution of magnetic flux as well as plasma radius, density and temperature vs neutral beam drive.

Finally, it should be noted that the *L/R* time scale of the C-2U vacuum vessel is on order 5-6 ms with a skin time of ~100 μs. Therefore, the wall no longer acts as an ideal flux conserver during the long C-2U discharges and there is measurable flux leakage of >10% through the wall for a good fraction of the shot, with commensurately higher losses later in the pulse. The data presented here are not corrected for this effect and so provide a conservative lower bound relative to the true machine performance.

A GLIMPSE AHEAD

Motivated by these breakthrough achievements, the displayed strong scientific foundation for the large orbit conjecture and associated robust beneficial physics, TAE has begun the design and construction of a successor machine, C-2W. The goal of this device will be to test the emerging energy confinement at higher temperatures and elevated system energies. The aim is for total plasma temperatures of 3 keV, with 1 keV electrons. Plasma densities will be similar to C-2U, i.e. around mid 10^{13} cm^{-3} and with applied magnetic fields around 3 kG. These parameters assure that all plasmas in C-2W will be fully collisionless and that the system will operate at about an order of magnitude higher stored energy than C-2U. Beams in C-2W will be angled as in C-2U, but there will be a total of 8 injectors for a total of >13 MW

of beam power and with an upgraded pulse length of 30 ms. Perhaps the most critical improvement will be with regards to edge control and insulation of the SOL plasma from the walls and ends of the machine. Driven by the findings in C-2U, the divertor capabilities will be dramatically upgraded and a new set of inner divertors will be deployed. This will improve the connection between the edge plasma in the central part of the machine and the divertors. The overall layout and key system elements are depicted in Fig. 9. First scientific operation of this new facility is slated for the summer of 2017.

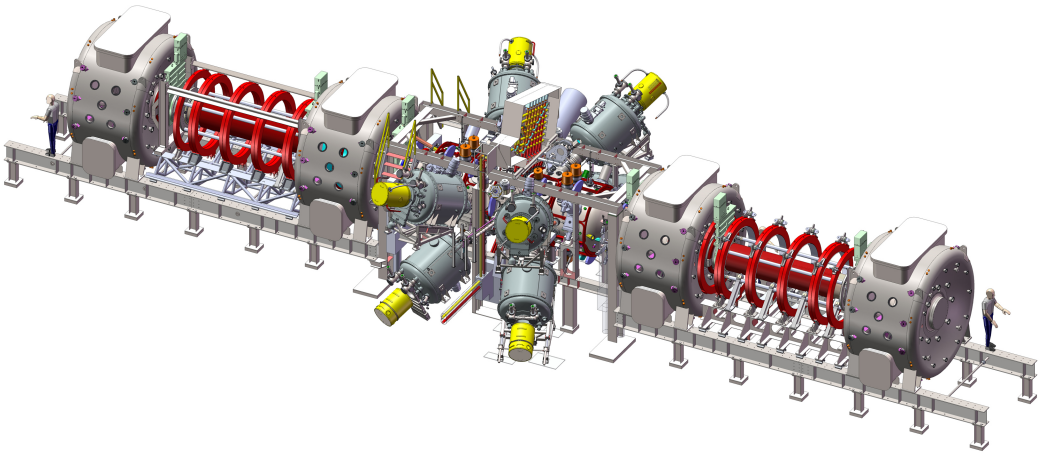

Figure 9. Schematic and component layout of the C-2W machine.

SUMMARY

Over the past year C-2U has substantially added to the capabilities inherited from C-2. As such, the combined C-2/C-2U program has demonstrated an impressive list of breakthrough achievements: (1) successful operation and study of advanced beam driven FRCs characterized by (a) dynamic formation, (b) fast ion pressure dominated equilibria, and (c) successful engineering integration of major system components; (2) discovery of the high performance FRC regime identified by (a) synergetic combination of neutral beam injection with edge biasing and gettering to feature excellent shot-to-shot reproducibility, (b) FRC macro stability and improved confinement, (c) record >11 ms FRC lifetimes limited only by transport, and (d) emerging beneficial confinement scaling and coupled core-SOL transport barriers; and (3) advanced beam driven FRC sustainment with (a) current drive and plasma sustainment in excess of characteristic system and plasma time scales for ~ 5+ ms, and (b) such performance limited only by hardware and stored energy constraints.

These successes provide a strong validation of Norman Rostoker's conjecture that large orbit energetic particles are relatively immune to perturbations of wavelength smaller than the orbit size due to phase averaging. Emerging throughout his career, his vision was to design a reactor based on this paradigm. Specifically, he proposed that a reactor plasma composed predominantly of a large orbit energetic particle population will bring about improved stability and also a reduction in observable transport [17]. In this sense, the C-2/C-2U advances are directly derivative of Norman's guiding philosophy and form a compelling foundation for the ascent towards aneutronic fusion reactors.

ACKNOWLEDGEMENTS

First the authors want to express their deepest appreciation to Norman Rostoker. He was a singular visionary and his exceptional intuition and scientific genius have been of great inspiration to all. Besides giving all of us a guiding principle (his large orbit conjecture), boundless creativity and much invaluable advice over the years, we mostly appreciate his humanity, hospitality and unwavering friendship and loyalty. Norman was as much a pioneer and member of the founding class of plasma physicists as he was a maverick and out of the box thinker. He taught many of us to follow our instincts, question the orthodox, have courage and "never surrender". The company he helped to cofound and the research reported here are direct testament to these indelible character traits. and all of us are grateful for having crossed paths with him and will cherish our memories of interacting with him for the rest of our lives.

We also want to thank our shareholders for their support and trust, and all fellow TAE staff for their dedication, excellent work and extra efforts. Finally, we are indebted to the many members of the Budker Institute for their excellent technical contributions and superb assistance during all of this research.

REFERENCES

1. M. Tuszewski, Nucl. Fusion **28**, 2033 (1988).
2. L.C. Steinhauer, Phys. Plasmas **18**, 070501 (2011).
3. M.N. Rosenbluth, N.Krall, and N.Rostoker, Nucl. Fus. Suppl. **1**, 143 (1962).
4. H. Naitou, T. Kamimura and J. Dawson, J. Phys. Soc. Jpn. **46**, 258 (1979).
5. R. Horiuchi, T. Sato, Phys. Fluids B **1**, 581 (1989).
6. W.W. Heidbrink and G.J. Sadler, Nucl. Fusion **34**, 535 (1994).
7. M.W. Binderbauer, *et al.*, Phys. Rev. Lett. **105**, 045003 (2010).
8. M. Tuszewski *et al*., Phys. Rev. Lett. **108**, 255008 (2012).
9. H.Y. Guo, *et al.*, Nature Communications **6**, 6897 (2015).
10. M.W. Binderbauer, *et al.*, Phys. Plasmas **22**, 056110 (2015).
11. B. H. Deng, *et al.*, Rev. Sci. Instrum. **85**, 11D401 (2014).
12. M. Onofri, *et al*., to be submitted to Phys. Plasmas (2016).
13. M.N. Rosenbluth and M.N. Bussac, Nucl. Fusion **19**, 489 (1979).
14. S. Ohi, *et al*., Phys. Rev. Lett. **51**, 1042 (1983).
15. T. Tajima and J.M. Dawson, Phys. Rev. Lett. **43**, 267 (1979).
16. T. Tajima and A. Necas, in this Proceedings (AIP, NY, 2016).
17. M. Binderbauer and N. Rostoker, J. Plasma Phys. **56**, 451 (1996).
18. L. Schmitz, in this Proceedings (AIP , NY, 2016).

Norman's Vision

Arno Penzias

New Enterprise Associates,
2855 Sand Hill Road
Menlo Park, CA 94025
United States

Norman approached fusion with the end in mind. This meant developing a reactor concept that was balanced between scientific feasibility, engineering/technological viability and commercial competitiveness. This central consideration led readily to (a) requiring reactor compactness and (b) considering the much harder to use advanced or aneutronic fuels, with p-B11 being free of primary neutrons and hence least radioactive but requiring 30× higher reaction temperatures and only producing half the energy yield of the conventional D-T fuel. Together these secondary choices demand a fusion concept with considerably better confinement than what is found in tokamaks and other fusion ideas. The paradigm that then emerges is one of wrestling with much harder science up front for the benefit of technological readiness, compactness and economic competitiveness.

Therefore, the natural thing for Norman was to search for a superior confinement solution, a process that spanned most of his scientific career and involved close to all of his more than 40 students as well as many of his collaborators. This systematic approach of assessing, dismissing after careful consideration and brick-by-brick concept assembly, together with development of critical technology and infrastructure, culminated in the mid nineties in what we now call the Plasma Electric Generator or PEG.

Plasma Electric Generators, Large Orbit Particles and the FRC Architecture

A critical phenomenon lies at the center of the Plasma Electric Generator concept: Unlike the remarkably fast losses encountered by common small-orbit particles in fusion, *energetic large orbit charged particles* are well confined in accelerators and storage rings. Furthermore, while this confinement phenomenon (and supporting data) was available to many, Norman Rostoker was unique in realizing its potential for fusion, together with his formulation of a conjecture that plasmas made up predominantly of such large orbit particles would exhibit superior confinement and stability. The physics behind this theoretical model lies in a key fact: over the course of their large orbits, these energetic particles should average out the effects of the typical small-wavelength electro-magnetic fluctuations they encounter. Owing to averaging, then, should make large-orbit particles largely immune to deflection and turbulence-induced transport.

With these key insights in mind, Norman and his team set out to assemble a complete reactor concept around it. He focused upon a plasma-dominated by such large orbit particles. Large orbits are aided by high particle energy and low magnetic field. To achieve this Norman needed accelerators to inject beams of high-energy particles and a magnetic confinement topology with low interior field. Finally, to allow for fuel particles of considerably different charge-to-mass-ratios (B has about half the charge-to-mass-ratio of protons) to stay in close proximity/overlap, and thereby provide enough propensity for fusion, a steep radial magnetic field gradient would be necessary as well. All this led Norman and his team to ultimately consider an FRC (or Field Reversed Configuration), a magnetic topology he co-developed in the late fifties wherein the plasma creates its own magnetic bottle.

Combining the desired large orbit particles, produced by energetic beam injectors, with the field reversed topology and the neutron-free p-B11 fuel mix gave rise to the basic elements of the PEG concept (which he first proposed in totality with his collaborators in 1997 in SCIENCE magazine). Since then TAE, which was co-founded by Norman in 1998, has successfully evolved the concept in a series of groundbreaking experiments, culminating with the sustainment breakthrough achieved this summer on the latest C-2U machine and announced at today's symposium. This recent data validates Norman's large orbit conjecture and dramatically advances the PEG concept towards fusion based energy generation.

Glimpse from the Past: Norman's Visits to Budker Institute in Novosibirsk

A.A. Prokopenko[1, a)]

[1]*Budker Institute of Nuclear Physics, 11 Acad. Lavrentyev Ave, Novosibirsk, 630090, Russia*

[a)] Corresponding author: a.a.prokopenko@inp.nsk.su

I am honored and pleased to join you all who have gathered here to commemorate and pay respects to the memory of our friend Norman Rostoker, an outstanding physicist and a unique personality.

It is hard (if ever possible) to find appropriate words adequate to the situation, especially concerning infinity, and when we are talking in terms of eternity (and this is just the case) all the appropriate words seem to immediately loose their intrinsic meaning and become too dull, too flat, inexpressive and insignificant.

Norman is an extraordinary man. Even in his absence he has managed to put together here so many people from various parts of the world with a great diversity of interests, social positions, and personal preferences.

I am talking about Norman in the present tense since I am not yet accustomed to the fact that he is not with us and that all he represents has left a continuing imprint on our lives, long-formed relationships, and scientific traditions.

We met for the first time in 1979 at the Conference on high-power electron and ion beams held at the Novosibirsk Institute of Nuclear Physics (INP) in Akademgorodok. I was responsible for hosting our foreign guests, because at that time our country was not always agreeable and comfortable with foreign visitors.

He asked, "Andrey, can you explain to me why in Moscow we could not talk about the things of interest but here we somehow can?"

And I replied, "That is very easy: It's because we are already in Siberia!"

To some extent that was true. We were too far from Moscow where all the essence of the political, scientific, and cultural life was concentrated. And the founder of the INP, Professor Budker, complained, "I can convince the researchers to leave Moscow for Siberia by the opportunities opened up at this new place, but how could I convince their wives?"

The success of Akademgorodok was tremendous and inevitable because of the lucky concurrence of three fundamental and mandatory prerequisites of success, namely: The right time, right place and right company.

The right time: It was 1958, the so-called Khrushchev thaw, when the soviet people could feel the fresh air of great changes;

The right place: The unknown, cold Siberia, remote, and too far from the total control of Moscow officials; and finally: The right company. Despite the lack of available information, the scientific center in Akademgorodok with its university, physico-mathematical school for gifted youngsters and 29 research institutes attracted many intelligent, romantic, and enthusiastic young people from various parts of our huge country. All of them were young, romantic, full of enthusiasm, and could afford the risk – which produced an unbelievable and fantastic atmosphere for the intense creative work.

The intellectual concentration in Akademgorodok was much higher than any-where else in the USSR, and using the analog of Silicon Valley, people called Akademgorodok "Silicon Taiga" (the wild forest in Siberia, "bear jungle"). For our generation, it was a rare chance to live, study, and work in such a place, and this chance was used to its fullest. Akademgorodok became the intellectual and cultural island in the ocean of Soviet life. That is why so many famous people sat at the famous Round Table at INP over the past several decades: Charles de Gaulle, George Pompidou, Rajiv Gandhi, Jiang Zemin, Kim Jong-il, Nikita Khrushchev, Alexei Kosygin, Boris Yeltsyn, Vladimir

Putin, Aleksandr Solzhenitsyn, Lev Gumilev, Georges Charpak, Carlo Rubbia, Herwig Schopper,,Masatoshi Koshiba, Hiroshi Amano, Pief Panofsky, Burton Richter, Viki Weisskopf, Jim Cronin, Edward Ginzton, Neil Armstrong, and, of course, Norman Rostoker, who were all the kind of people who had an influence on the intellectual climate of the epoch.

We can talk a lot about Norman and only in the superlative degree:

He was an excellent father, grandfather and great-grandfather - that alone is a great achievement.

He was a remarkable teacher whose lectures and speeches were rather parables with a worldly wisdom and profound penetration into the essence of the subject with philosophic conclusions and bright examples.

His whole-heartedness and good will, the magnetic attractiveness of his personality, and his sense of humor created a special emotional bond and evoked admiration and love from his relatives, colleagues and friends.

His curiosity as a scholar extended the boundaries of reality and imagination. Even in his early studies, he felt the enormous hidden complexities and altogether the enchanting beauty and inexhaustible opportunities of the complex systems that he later so skillfully explored in his works on the reversed field reactor.

In his studies on the beam-plasma interactions, he could combine the fields and phenomena that seemed quite remote from each other and had a unique ability to get valuable information even from fragmentary comments of his colleagues. Afterwards he would construct a complete picture in his mind and, as a rule, this picture was not only correct but enhanced by addition of his own ideas.

Norman was a comet that made a flamboyant trace on the sky of physics of the last century.

I would like to complete my short speech with the worlds of Saint Sebastian: "My God, I do not know why you took him from us, but Almighty, I will always be thankful to you that you gave him to us."

Traveling with Norman From 1973

C. W. Roberson

Office of Naval Research 875 N Randolph St, Arlington, VA 22217

I came to UC Irvine from Yale in 1973, Amnon Fisher came from Cornell the year before. Toshiki Tajima and Kim Molvig had signed on as Norman's first UCI students. Norman's proposals to the National Science Foundation (NSF) and the Department of Energy (DoE) were soon funded. DoE provided funding for a 1MeV, 100kA, 100nsec Mark Pulse - Accelerator to carry out Rotating Beam Plasma experiments. The lab was operational in a couple of years.

The first experiment was a Collective Ion experiment with the rotating beam in a plasma. The results were published in Physical Review Letters. The second was an experiment on upper hybrid radiation from the rotating beam plasma interaction. The results were used to support a proposal for high power microwave experiments.

Our paper on the rotating beam plasma interaction was chosen by DoE to be presented at the 1978 International Atomic Energy Agency Fusion meeting in Innsbruck, Austria. It was the first time I traveled abroad with Norman. Afterwards we visited the Max Planck lab nea Munich, Germany. Their Stellerator was the largest fusion experiment we had ever seen. This year they have announced results with an even larger Stellerator.

In 1978 I accepted a position at the Naval Research Laboratory were the focus of my research shifted to advanced accelerator concepts and Free Electron Lasers. In addition to my NRL work I started the Plasma Physics program at the Office of Naval Research. From my ONR position I was able to provide modest support to the Irvine group.

I continued my research at NRL on a part time basis until I retired. Our paper on the concept of a High Current Betatron with Stellerator Fields(1) was first confirmed experimentally by the Irvine group. My Review of Free Electron Lasers became a citation classic (2) and my paper on the Effects of Longitudinal Beam Compression in a Free Electron Laser was key to understanding the effects of beam quality in an X-Ray FEL(3)

The American Physical Society acknowledged my contributions to plasma physics in my 1995 Fellowship Citation. "In recognition of his seminal contributions to free electron laser beam quality, Stellarator focusing of intense beams and outstanding beam plasma experiments."

The thing I enjoyed most about traveling with Norman was his humor. It was a running commentary on the human condition from some one who knew the view from the mountain top. The second thing I enjoyed most about traveling with Norman was Tennis. He always traveled with his Tennis Racquet. I was at Irvine for Norman's 80th Birthday Celebration. He ask me if I wanted to get back in Fusion Research. When I declined, he immediately challenged me to a tennis match. I was sorry I had to pass on my last chance to get one up on him.

1. C. W. Roberson, A. Mondelli, and D. Chernin, Phy. Rev. Lett. 50, 507, (1983)
2. C. W. Roberson and P. Strangle, Phys. Fluids B. 1, 3, (1989)
3. C. W. Roberson and B. Hafizi, Phys. Rev. Lett. 72, 1654, (1994)

Novel Particle and Radiation Sources and Advanced Materials

Frederick Mako

FM Technologies, Inc. and Electron Technologies, Inc.

Abstract. The influence Norman Rostoker had on the lives of those who had the pleasure of knowing him is profound. The skills and knowledge I gained as a graduate student researching collective ion acceleration has fueled a career that has evolved from particle beam physics to include particle and radiation source development and advanced materials research, among many other exciting projects. The graduate research performed on collective ion acceleration was extended by others to form the backbone for laser driven plasma ion acceleration. Several years after graduate school I formed FM Technologies, Inc., (FMT), and later Electron Technologies, Inc. (ETI). Currently, as the founder and president of both FMT and ETI, the Rostoker influence can still be felt. One technology that we developed is a self-bunching RF fed electron gun, called the Micro-Pulse Gun (MPG). The MPG has important applications for RF accelerators and microwave tube technology, specifically clinically improved medical linacs and "green" klystrons. In addition to electron beam and RF source research, knowledge of materials and material interactions gained indirectly in graduate school has blossomed into breakthroughs in materials joining technologies. Most recently, silicon carbide joining technology has been developed that gives robust helium leak tight, high temperature and high strength joints between ceramic-to-ceramic and ceramic-to-metal. This joining technology has the potential to revolutionize the ethylene production, nuclear fuel and solar receiver industries by finally allowing for the practical use of silicon carbide as furnace coils, fuel rods and solar receptors, respectively, which are applications that have been needed for decades.

INTRODUCTION

This paper is not intended to be a typical technical document. It is instead a combination of honoring Norman Rostoker, illuminating his effect on my life, and talking about my work.

Norman Rostoker was a world renowned plasma physicist, visionary, mentor, and good friend. He is known for being a nuclear fusion pioneer, but in the early days at UC Irvine he was working on collective ion acceleration. Norman Rostoker was my thesis advisor during 1974-1979 at UC Irvine, where I completed an experimental, and theoretical thesis on Collective Ion Acceleration using an Intense Electron Beam. However, as my thesis was largely experimental I must give credit to Amnon Fisher, who was the main driving force behind the laboratory, and Chuck Roberson, who along with Amnon provided invaluable expertise in the laboratory.

Norman was also my professor for several graduate level courses covering plasma physics, math-physics, and pulsed power. I learned a tremendous amount directly from Norman both in classes and in discussions with him, namely, pulsed power and electron/ion beam formation and transport. Also, indirectly or serendipitously, I gained experience and knowledge of pulsed power and particle/radiation beam interaction with materials. For example, the Titanium anode foil used in my thesis experiment (see Fig. 1) would partially vaporize and the Ti vapors would bond to the graphite cathode forming TiC. As a result of the TiC formation I learned that TiC has many uses, including applications I have personally utilized like TiC electrical contacts with diamond for detectors and TiC with WC as cutting tools for enhanced performance. The lessons in physics and life Norman gave me have been invaluable. In the years following my doctoral thesis, Norman and I maintained a close relationship.

In this article a collection of topics that are related to the global subject of novel particle and radiations sources and advanced materials are discussed. First, a model for understanding collective ion acceleration, a brief history of collective ion acceleration and the authors' experimental and theoretical results are covered. Second, the fundamentals of the Micro-Pulse

Electron Gun (MPG), experimental verification of the technology, and applications of the MPG are examined. The two discussed applications of the MPG are accelerators, specifically a medical accelerator called 3DRad™, and microwave tubes, specifically a klystron called the Micro-Pulse Klystron (MPK). 3DRad™ is a proprietary MPG driven medical linac that has clinical advantages over current medical accelerators. The MPK is a MPG based klystron amplifier with substantially improved efficiency, thus making the MPK a green technology. Third, advanced material usage and joining are reviewed, in particular the applications of SiC joining to ethylene production and the applications of SiC joining to nuclear fuel rods and solar receivers.

COLLECTIVE ION ACCELERATION VIA REFLEXING ELECTRON BEAM

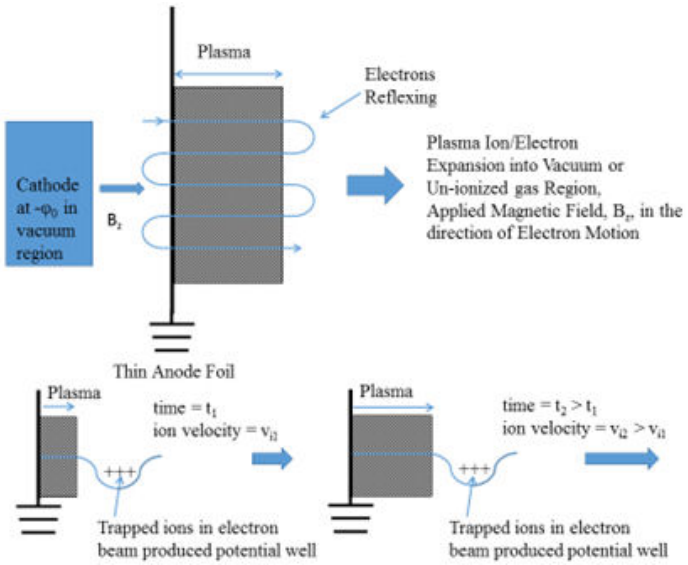

FIGURE 1. Ions are trapped in a potential well formed by the reflexing electron beam and ideally reach the same speed as the electrons. Note a strong magnetic field, B_z, is assumed that is parallel to the electron motion.

Figure 1 illustrates a pre-formed plasma on the right side of a thin anode foil that is opposite the cathode, the anode is at ground potential to the cathode. An electron beam is produced at the cathode surface, then accelerated to the anode foil. Electrons have sufficient kinetic energy to easily pass through the thin anode foil with minimal inelastic energy loss, and with a modest elastic energy change. For example, electrons with a kinetic energy of 1MeV can easily penetrate an anode foil made of titanium or aluminum alloy that is 12.5 microns thick, the single pass energy loss is approximately 1% with a full angular spread of less than 1^o for 99% of the electrons. Many passes through the anode foil will of course cause substantial modification to the originally delta function like electron energy distribution. Furthermore, the electron beam can easily pass through the pre-formed plasma, where it is assumed that the plasma density is greater than the electron beam density to maintain at least charge neutrality in the plasma. Low energy plasma electrons will be expelled out of the plasma and be absorbed in the anode foil. With an intense electron beam, where the field energy is comparable to the particle kinetic energy, the beam forms a virtual cathode potential well with a magnitude about equal to the cathode potential. This virtual cathode is responsible for the majority of the energetic beam electrons stopping and turning around in their own formed potential well. These “turned around” electrons travel towards the cathode through the plasma, pass again through the anode foil if they have sufficient parallel energy and if the potential is still applied at the cathode will turn around again. This process continues until the cathode potential is turned off or the electrons lose enough parallel energy to be absorbed in the plasma or anode foil. This recycling of electrons is called reflexing. Note, there is an assumed parallel or axial magnetic field of sufficient strength to prevent radial electron escape.

Ions located near the plasma and vacuum/un-ionized gas boundary will be accelerated to the right, as indicated in the lower half of Fig. 1, by the electron beam formed virtual cathode. In order for ion acceleration to continue the virtual cathode or potential well formed at a time t_1 must be at least charge neutralized so as to allow the potential well with trapped ions to move to a new position at a time t_2 and in such a way as to not lose the originally trapped ions. Furthermore, the potential well must accelerate to allow trapped ions to gain increasing energy. The ultimate acceleration limit is that the ions reach the incoming electron velocity thus achieving the ion to electron mass ratio times the electron energy. For protons this is 1836 times the electron energy! To date, only modest energy multipliers of roughly 5-10 have been achieved for a single charge state ion (higher atomic number ions give higher absolute energies proportional to their charge state). Factors which limit reaching high ion energies are: (1) cathode turn off which stops the supply of energy, (2) multiple electron beam passes through the anode foil which causes a loss of electron energy, but more importantly the electron beam conversion of parallel electron energy to perpendicular energy from elastic scattering, again limiting the available energy, and (3) a synchronized charge neutralization and ion acceleration process.

A BRIEF HISTORY OF COLLECTIVE ION ACCELERATION

The history of collective ion acceleration is quite extensive so I will mainly focus on the background as it pertains to my affiliation with Rostoker. Graybill and Uglum [1] in 1970 appear to be the first to have experimentally studied collective field acceleration of positive ions driven by a relativistic electron beam. The beam was injected into a metallic cylindrical chamber which was uniformly filled with a neutral gas. One of the first theoretical developments demonstrating the formation of a potential well comparable to the electron kinetic energy for an intense electron beam was established in 1971 by Poukey and Rostoker [2]. Poukey provided the expertise in relativistic PIC (Particle-In-Cell) code simulations and Rostoker formed the analytical foundation for the potential well. Further, Rostoker showed that gas ionization could be exploited to provide subsequent charge neutralization and acceleration of the potential well with trapped ions. What was missing at this time was a simulation or theory demonstrating that the ion velocity could reach the electron velocity. This result partially came in 1975 by Crow, Auer and Allen [3], where non-relativistic finite difference equations were solved with a constant electron temperature, which is unrealistic as it provides a source of infinite electron energy, although they did utilize a Boltzmann distribution. A year later Ryutov and Stupakov [4] provided a more realistic form for the electron density as a function of electron potential energy by including the cathode turn-off time and energy spread due to anode foil scattering. This was quite exciting at the time as this was an excellent model which partially treated the situation in many experiments.

Mako established in his thesis work the theoretical and experimental basis for the reflexing description given above. A summary of Mako's thesis work was presented in a 1979 paper, and in a book chapter by Mako, Fisher, Rostoker, Tzach and Roberson [5,6]. A brief description follows with a more extensive presentation in the next section. By experimentally measuring the electron beam current density dependence on energy, the electron density distribution as a function of the electron potential energy can be derived. This experimentally constrained electron density distribution is used to predict (through the ion equations of motion) the ion energy distribution, which is then compared to the experimental ion energy distribution. This

work represents the first validation of the theory by experiment. Furthermore, it established that for non-relativistic electrons the maximum ion energy is given by $E_{imax} = q\ \phi_o\ (2\alpha)$, where q is the ion charge, ϕ_o is the cathode potential and α is an experimentally determined parameter that determines how rapidly electron current density as a function of energy is modified during the acceleration process. In 1984 Mako and Tajima [7] added PIC code simulation to the above results and further clarified phase unstable characteristics of the reflexing acceleration mechanism. Later in 2008, Tajima, Habs and Yan [8] used an ultra-relativistic treatment for the electrons to show that the maximum ion energy is given by $E_{imax} = q\ \phi_o\ (2\alpha+1)$, thus confirming the maximum ion energy limit but in a laser driven ion accelerator. This high field gradient laser driven scheme may well be the future for high energy ion acceleration since much higher electron energies can be attained in a short distance, hence the ion accelerator is also very short.

THEORETICAL REFLEXING MODEL AND EXPERIMENTAL COMPARISON

Electron motion will be considered in a steady state with respect to the ions. Electron and ion motion will be considered one-dimensional, in the axial z-direction, since the electrons are tied to a strong axial magnetic field, B_z, and the ions are constrained to the electron beam. Equations (1) and (2) are used to describe the ion motion as a fluid [5-7].

The ion continuity equation is given by

$$\frac{\partial n_i}{\partial t} + \frac{\partial (v_i n_i)}{\partial z} = 0 \tag{1}$$

The ion equation of motion is as follows,

$$\frac{\partial v_i}{\partial t} + v_i \frac{\partial v_i}{\partial z} = -\frac{q}{M}\frac{\partial \phi}{\partial z} \tag{2}$$

Where v_i, n_i, M and q are the ion velocity, density, mass and charge, respectively. ϕ is the electrostatic potential, z is the axial coordinate for the ion with it origin at the plasma/vacuum front and t is the time where t=0 corresponds to the beginning of the plasma expansion and acceleration. Closing of equations (1) and (2) will be accomplished by determining the electron density dependence on potential and using quasi-neutrality. An analytic solution is arrived at with the assumption of a self-similar state. A reflexing electron beam will have a symmetric distribution function. Also, with elastic scattering and inelastic losses in the anode foil and energy given to the ions, the forward electron current density will be energy dependent. Thus the electron density may be expressed as follows [5-7],

$$n_e(\phi) = \frac{\sqrt{2m}}{e}\int_{-e\phi}^{E_{\max}} \frac{1}{v_e}\frac{dJ_e}{dE_e}dE_e \tag{3}$$

Where, m, e, E_{max} and v_e are the electron mass, charge, maximum energy and velocity. From measurements of the electron current density as a function of energy the result can be formalized as

$$J_e(E_e) = -J_{e_0}\left(1 - E_e/E_{\max}\right)^{\alpha} \tag{4}$$

J_{e_0}, is the injected electron current density. Note that equation (4) is the measured current density from the beginning to the end of the ion acceleration process, thus this equation contains information about what transpired during the beam reflexing through the anode foil, plasma and what energy was transferred to the ions. It is a radical modification to the initial mono-energetic delta function electron distribution that was injected through the anode foil into the plasma. Ryutov and Stupakov [4] found the exponent in equation (4) to be α=1/2 by including anode foil elastic scattering, energy loss and diode shut-off. From Mako's [5-7] experiment, the exponent in equation (4) is found to be, α=3.42. The reason the Mako exponent value is much higher than what was predicted by Ryutov and Stupakov is not completely understood. However, Mako's result includes real materials and the actual physics of the interaction. Furthermore, when Mako's exponent is used to compute the ion energy distribution (shown later) the theory has very good agreement with the experiment ion distribution. When equation (4) is combined with equation (3) the integration must be performed by including an expression for the electron velocity. In the most general case, the result involves hyper-geometric functions [9]. Only two special cases, namely, non-relativistic [5-7] and ultra-relativistic [8] electrons are considered. For non-relativistic [5-7] equation (5) is the result,

$$n_e(\phi) = \sqrt{\frac{2m}{E_{\max}}}\frac{J_{e_0}\alpha}{e}\frac{\Gamma(1/2)\Gamma(\alpha)}{\Gamma(1/2+\alpha)}\left(1+\frac{e\phi}{E_{\max}}\right)^{\alpha-1/2} \tag{5}$$

Where Γ is the Gamma function. The rationale for the non-relativistic treatment of the electrons is that in the experiment [5-7] the initial electrons started off as mildly relativistic but ended up mostly non-relativistic. In the ultra-relativistic[8] (setting v_e = c = speed of light) electron case,

$$n_e(\phi) = \frac{2J_{e_0}}{e\,c}\left(1+\frac{e\phi}{E_{\max}}\right)^{\alpha} \tag{6}$$

By allowing a self-similar state to form, thus setting $\zeta = z/(v_o\, t)$, where $v_o=(q\phi_o/M)^{1/2}$ and $e\phi_o=E_{max}$. Defining the normalized variables, $U=v_i/v_o$, $N=n_i/n_o$, $\Psi=\phi/\phi_o$ then equations (1), (2) and (5) or (6) become,

$$N'(U-\zeta) + N\,U' = 0 \tag{7}$$

$$U'(U-\zeta) + N'\,d\Psi/dN = 0 \tag{8}$$

$$N = (1+\Psi)^{\chi} \tag{9}$$

Where, $N' = dN/d\zeta$ and $U' = dU/d\zeta$ and $\chi=\alpha-1/2$ for non-relativistic electrons and $\chi=\alpha$ for ultra-relativistic electrons. Note, also n_o takes a slightly different form for different electron energies. Equations (7)-(9) may easily be solved with energy conservation as a boundary condition [5,7] at the plasma/vacuum front (ζ =0). The resulting maximum ion energy is then,

$$E_{imax} = q\,\phi_o\,(2\alpha) \text{ non-relativistic} \tag{10}$$

$E_{imax} = q\ \phi_o\ (2\alpha+1)$ ultra-relativistic (11)

With the measured value of α, there is not a substantial difference in the two results. Figure 2 is a comparison of the ion distribution versus ion energy for the experiment and the theory. Non-relativistic treatment gives better agreement to data than ultra-relativistic because the largest proportion of electrons are well below the relativistic injection energy. For the experiment it was found that $\alpha = 3.42$, for $e\phi_0 = 0.8$ MeV, and $J_{e_0} = 3.06$ kA/cm^2. Observe that the alpha particle density is on a log scale. The ion density drops off rapidly at higher energy, which makes practical applications unlikely. Low maximum ion energy and low number of high energy ions resulted in funding termination for collective ion acceleration in the USA during the early 80's.

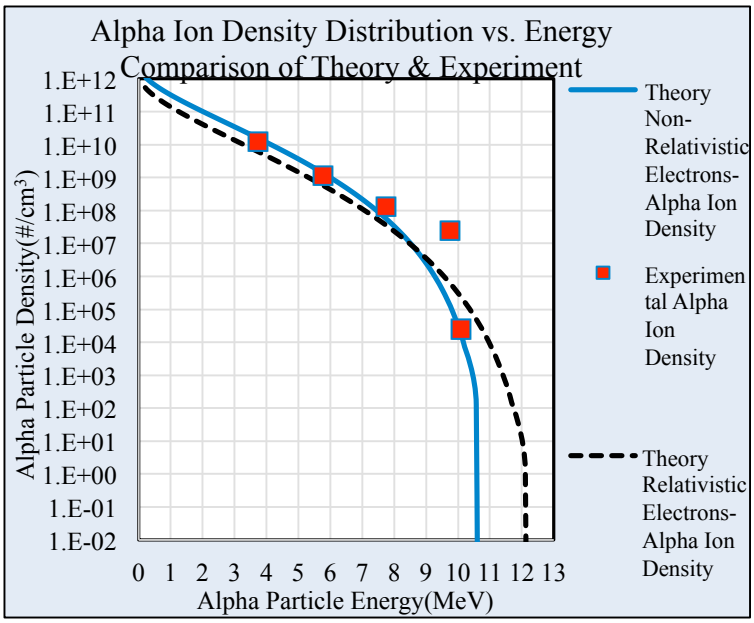

FIGURE 2. – Alpha ions distribution versus alpha ion energy comparison of theory and experiment. Reds dots are experimental data, black curve is for the ultra-relativistic electrons and the blue curve is for the non-relativistic electrons.

THE MICRO-PULSE ELECTRON GUN

Multipacting is an almost universally unwanted feature in accelerator and microwave tube designs. However, FMT has found a unique device for the utilization of multipacting that improves accelerator and microwave tube designs. The Micro-Pulse Gun (MPG) [10-15] exploits secondary electron emission and more specifically multipacting to form a narrow self-bunching RF fed electron gun. Figure 3 is a schematic of an RF cavity operating in, for example, a TM_{010} mode. Now assume at the anode wall (the grid), there is a single electron at rest near the axis. This electron is then accelerated across the cavity gap d, then strikes the cathode surface. A number δ_1 of secondary electrons are emitted off the cathode electrode. Provided the average transit time of an electron in the cavity is one-half the RF period, and that secondary electrons are in the proper phase with the RF field, these electrons will be accelerated towards the anode or grid electrode. Upon reaching the anode grid, $\delta_1 T$ electrons will transmitted through the grid, where T is the fractional transmission. The number of electrons which are not transmitted is then δ_1 (l-T). This is the number of electrons which are stopped or absorbed by the grid. If δ_2 is the

secondary electron yield per primary electron of the anode grid, then the grid can produce $\delta_1 \delta_2$ (1-T) secondary electrons. In order to have a gain of electrons, the number of secondaries produced must be greater than the beginning number of electrons (during this RF period), namely one, that is $\delta_1 \delta_2$ (1-T) > 1. The current density will grow exponentially until space charge limits the maximum current. Furthermore, this is a resonant phenomenon which only allows a narrow phase angle of electron charge or current.

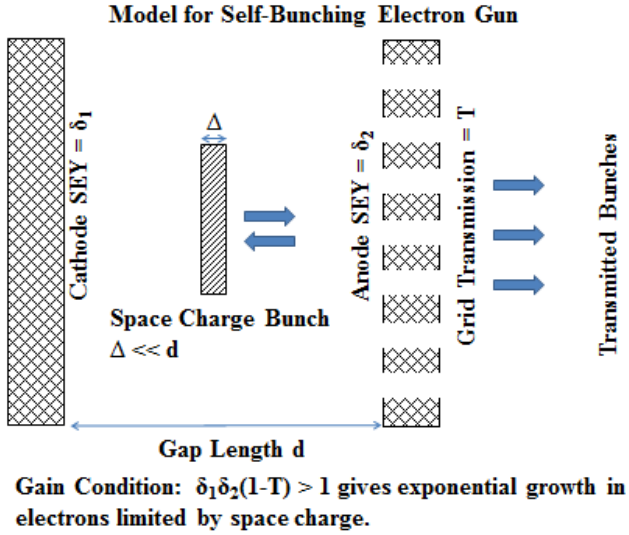

FIGURE 3. – Schematic illustration of the Micro-Pulse Gun (MPG) concept.

Figure 4 is obtained from our PIC code, FMTSEC, and shows a series of snapshots in configuration space of the rapid bunching of electrons by phase selection or natural bunching process in the cavity. The frequency is 1.497 GHz, the gap spacing is d=1.35 mm. There is no grid in this demonstration. At t = 0 electrons are emitted off the cathode electrode at z = 0; they then form a continuous spatial distribution of electrons inside the gap. At a time $t \approx$ 0.35 ns (0.52 RF period), the cavity is filled with a large number of electrons and no bunching is observed. A short time later, at a time t = 1.7 ns (2.5 RF periods) the broad spatial distribution of electrons has substantially diminished, and the formation of a narrow bunch of electrons can be seen within the cavity. Only those electrons which strike the opposite electrode at the right phase and velocity can provide additional electrons (which in turn make their way to the original electrode and continue amplification in the number of electrons). At a time of t = 193.5 ns (289 RF periods), electrons with the *"wrong"* phase have been filtered out of the simulation, and only particles with the *"right"* phase are present. The broad distribution of electrons has vanished and a narrow bunch of electrons remains and continues to amplify in density. Figure 5 top, shows a plot of the PIC bunch current as a function of time for an FMTSEC simulation with an RF frequency of 1.497 GHz and a cavity gap of 1.35 mm. The current is measured near the grid or anode electrode in Fig. 3. Hence, this is the current pulse which will exit the MPG. This figure illustrates the long pulse stability of the resonant bunching phenomenon. However, one cannot identify the single bunch shape. In Fig. 5 bottom, three current bunches are shown which clearly show the very narrow current bunches (~3% of the RF period) that are separated by the RF period.

The Micro-Pulse Gun (MPG) is an experimentally proven technology that has been developed over a period of two decades. Figure 6 left, shows the measurement of the bunched current in an L-band MPG. A 50 GHz sampling oscilloscope is used to directly measure the micro-bunch current. A 5 ns slice of the macro-pulse as indicated in Fig. 6 right is examined, thus micro-pulses can be observed. Figure 6 left, shows a measurement of the current bunches on a 500 ps/div. time scale. The current bunches appear with the periodicity of the RF field (~792 ps), in excellent agreement with simulation[10-14]. The pulse amplitude appears to decrease slightly

in time because of the location of the 5 ns slice in the macro-pulse. More detailed measurements show that the actual bunch length is about 39.6 ps (FWHM), which is about 5% of the RF period for this parameter set. In Figure 6 left, the micro-pulse current density is about 40 A/cm^2 and is in good agreement with simulation. For this result there is about 1.6 nC or ~9.9 x 10^9 electrons per RF period.

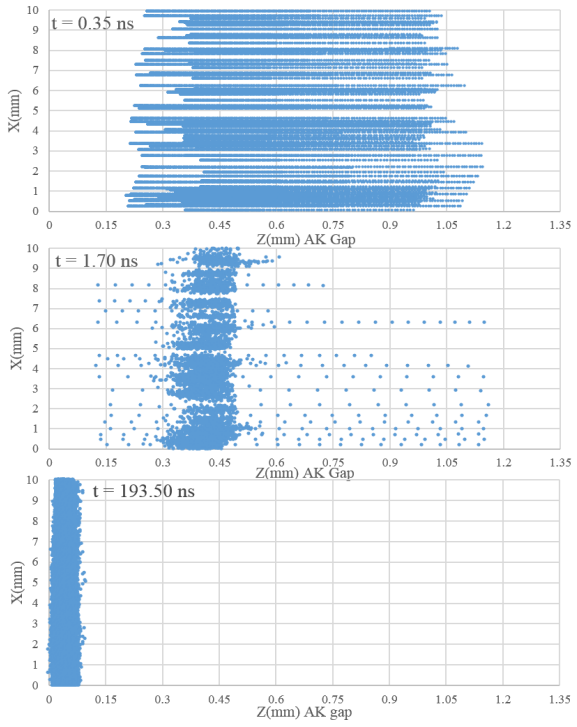

FIGURE 4. – Illustration of bunch formation.

Lifetime testing has been carried out for about 18 months at almost 24 hours per day with a repetition rate of 300 Hz and 5 μs macro-pulses. During that time, approximately 8.96 × 10^{13} micro-bunches or 143,000 coulombs (189,600 C/cm^2) have passed through this gun and it is still working flawlessly. Figure 6 center, is a picture of the L-band MPG that was used in these experiments. Figure 6 right, shows the macro-pulse operation of an L-band MPG experiment. The L-band MPG cavity is designed for a TE$_{101}$ mode and is powered by an L-band (1.2-1.3 GHz) tunable magnetron. The magnetron is operated at 300 Hz repetition rate. Each microwave pulse lasts for 5 μs (at the base) and contains about 6,313 electron bunches (1 for each RF period). The top trace is the RF power in the cavity and the bottom trace is the transmitted macro-pulse beam current from the MPG on a 1 μs/div. time scale.

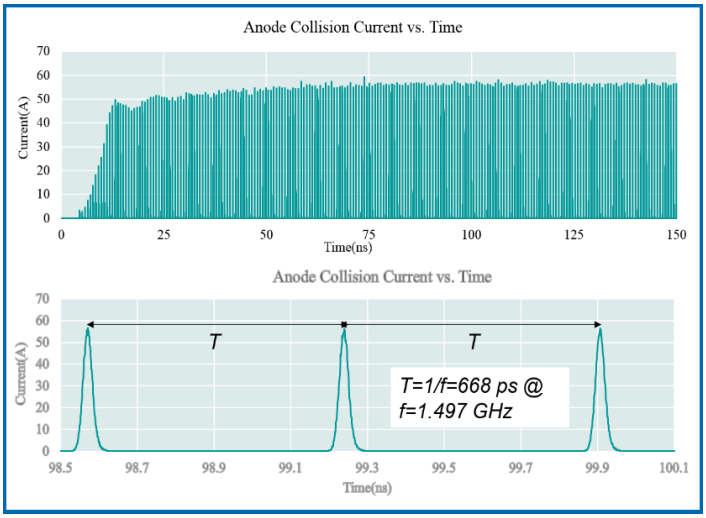

FIGURE 5. – PIC simulation of bunch current after 225 RF periods and magnification of individual bunch current traces.

The pulsed RF power delivered to the beam is about 50 kW and the beam current density is about 2 A/cm^2 in the macro-pulse. The current and current density above are not a hard limit, but were the design values for this particular experiment. Note the clean current trace over the full RF pulse length. The MPG is a resonantly-driven short-pulsed electron gun with pulses generally between 3-5 % of the RF period. The MPG has a resonance window in the input RF power. Driving the gun with either too little or too much power results in average electron

energies too small or too large, respectively, to stay in resonance. Outside of the resonance window results in no bunch current. Inside the resonance window the MPG is a current source, where an increase in input power yields higher average emission currents and minimal change in the average electron energy (less than 3% over the entire resonance window). The constancy of the electron energy occurs because as the RF input power is increased the RF electric field grows thus allowing higher electron current but at the same time the space charge electric field grows proportionally thus fixing the electron energy.

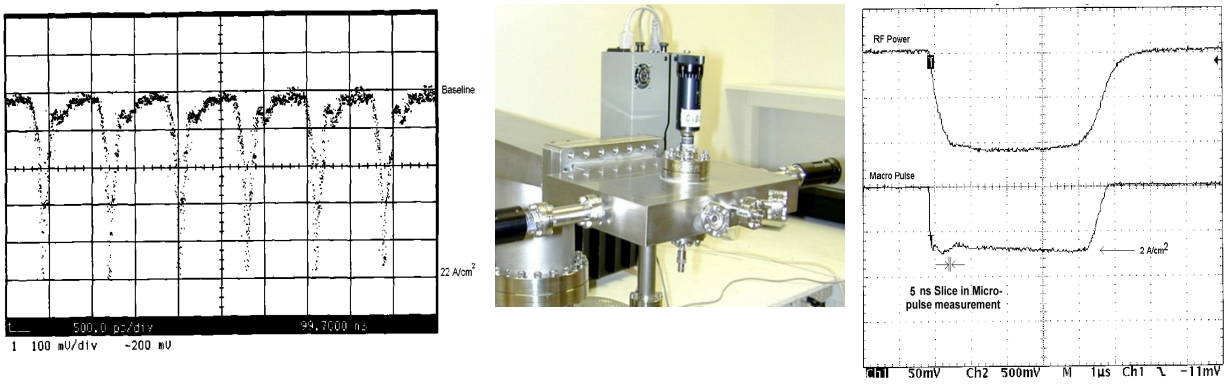

FIGURE 6. Left- shows the measured bunch current, Center- shows the experimental configuration and Right- shows the RF power and macro-pulse current.

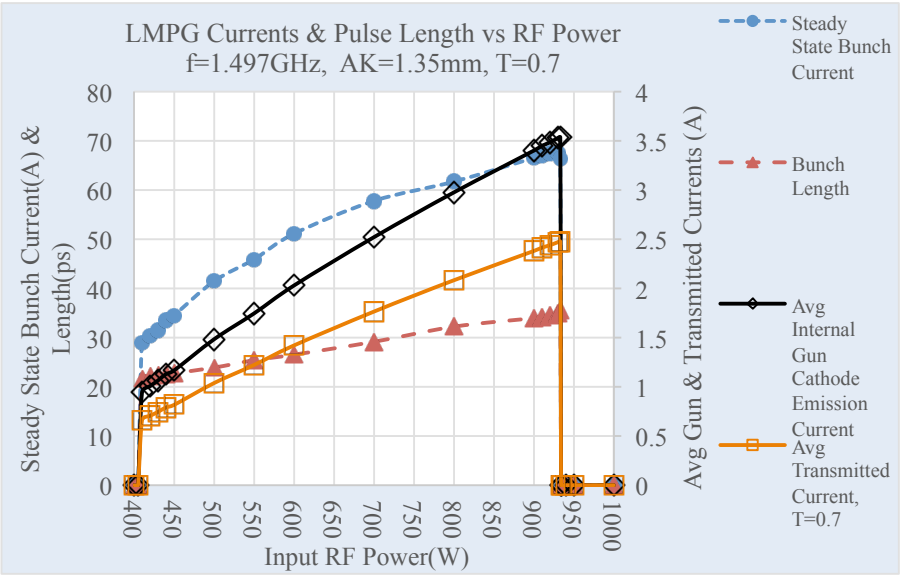

FIGURE 7. Bunch Length varies between 3 and 5% of the RF period. The average transmitted current varies between 0.7 and 2.5 A over an input RF power range of 400 to 930 W.

Figure 5 shows the time evolved bunch current, but after a few hundred RF periods the bunch current reaches a steady state, this steady state current is shown in Fig. 7 under varying RF input power. Furthermore, Fig. 7 shows average currents along with the bunch duration within the resonance window. In this case an anode grid has been added with a transmission factor T of 0.7. The RF period averaged beam currents, both internal to the MPG and transmitted, are shown.

In Fig. 8, starting from the bottom left to bottom right are single bunch per RF period MPGs that are L-band, S-band, and X-band. These are just a few MPG examples that are described in the Mako and Peter patent [16]. Top right is a multi-bunch per RF period MPG. This special case

MPG is called a “Gatling MPG”, which was invented by Mako [17] since this gun delivers four bunches per RF period and is used for frequency multiplying. For the Gatling MPG, there are two RF input ports, where the cavity is designed to set-up the TM_{110} rotating mode. RF power is fed 90^{o} out of phase, thus causing the peak electric field positioned at about half the cavity radius to rotate azimuthally at the input RF period. With N multipacting emission sites, in this example N=4, located at the electric field peak, N bunches will be produced separated in time by one-quarter of the RF period. If this multi-bunch Gatling MPG current is post-accelerated and sent into a cavity tuned to four times the input MPG frequency then a frequency multiplying klystron is formed. For any of the Figure 8 MPG’s the transmitted current may be amplified by passing the electron bunches through an appropriate negative electron affinity amplifier stage (such as diamond) as is done in the Mako and Fisher patent [18].

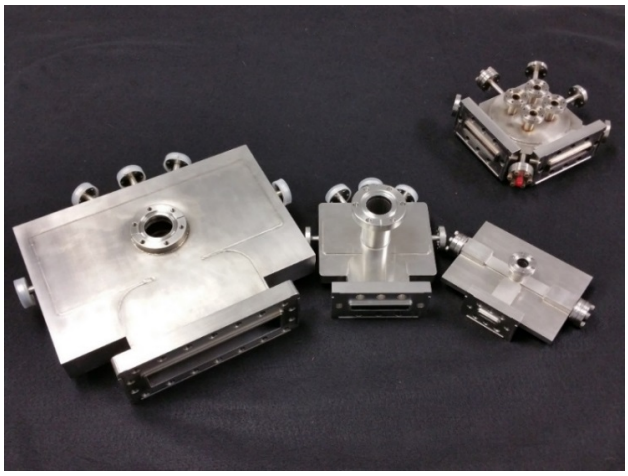

FIGURE 8. A few examples of MPG’s for different frequencies.

THE MICRO-PULSE ELECTRON GUN-KLYSTRON APPLICATION

The MPG has applications to both microwave tubes and accelerators. Of particular interest is CW klystrons, as depicted in Figure 9, which are used for television transmitters and in large accelerator facilities. Generally, CW klystrons are not very energy efficient. Given they are CW, if used continuously, will waste a lot of energy and operating budget. With the MPG’s compact size and short bunch length, CW klystrons can be made much more efficient. For example VKL-7811 klystrons (versions E and W) are barely 35% efficient at L-band. Using the LMPG for a klystron yields greater than 81% efficiency. Table 1 shows a comparison of an MPG driven klystron versus two commercial klystrons. The MPG driven klystron saves a factor of about eight in electrical operating cost and a similar savings in wasted energy, therefore the MPG is a green technology.

Parameter	MPG Klystron	VKL-7811E	VKL-7811W
Output Power (kW)	11.26	11	5.5 need 2 tubes
Beam Voltage (kV)	15	15	11.6
Beam Current (A)	0.816	1.95	1.3 need 2x current

Drive Power(W)	450	3.5	1.5 need 2x power
Frequency(GHz)	1.497	1.3	1.497
Wall Plug Efficiency (%)	81.11	~35.7	~34.6
Annual Energy Wasted (kW-hr) per 1000 Tubes Operating 24/7	2. 3 x 10^7	1.73 x 10^8	1.82 x 10^8
Annual Cost for Wasted ($MM) per 1000 Tubes Operating 24/7 @ $0.1/kW-hr	2.3	17.34	18.18

TABLE 1. Benefits of a high efficiency klystron, reduced CO_2 emissions and substantial annual operating costs.

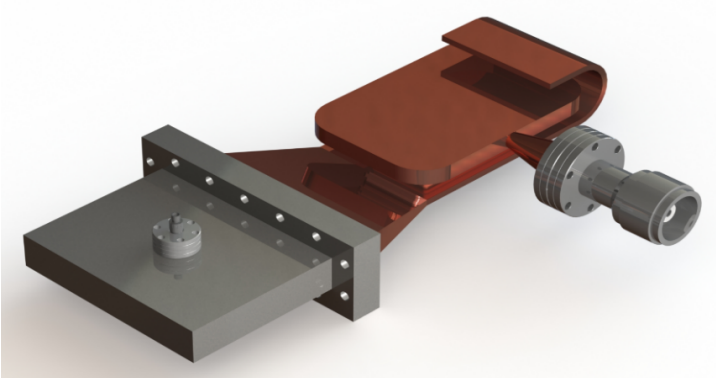

FIGURE 9. A conceptual image of a CW L-band klystron. The input power is fed into the MPG from a waveguide launcher as shown on the left side and the output power is taken out on the right through a 1-5/8 coaxial cable.

THE MICRO-PULSE ELECTRON GUN-RF ACCELERATOR APPLICATION

Figure 10 shows the application of an S-band MPG brazed to an RF accelerator (left) and installed in a magneton driven RF system (right). The beam reached a final energy of 1.25 MeV at 160 mA average over the macro-pulse with a normalized emittance of 3.8 mm-mrad. This was a successful proof of principle demonstration. Furthermore, an X-band MPG (XMPG) has recently been tested for delivering over 1.5A macro-pulse current or greater than 30A in the micro-pulse for installation into an X-band RF linear accelerator (linac). There are enormous economic and patient benefits to an XMPG medical linac than is presently available by current medical devices.

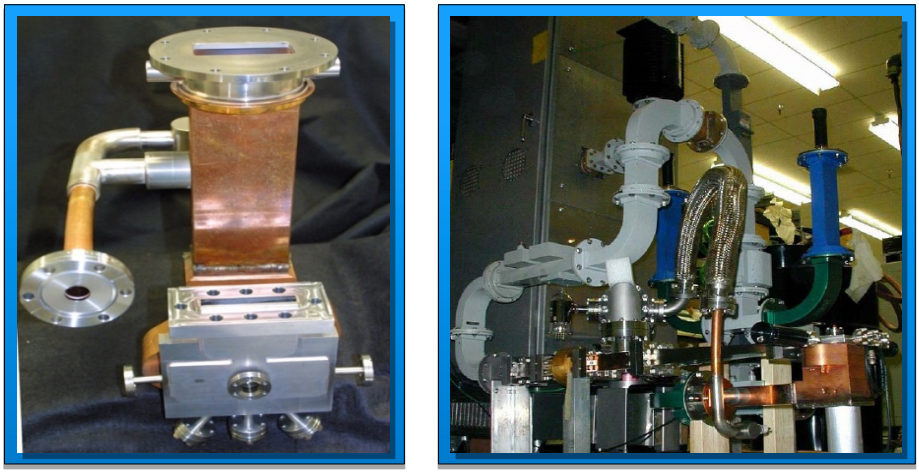

FIGURE 10. Left - S-band MPG brazed to a short 1.5 cell RF accelerator. Right- S-MPG RF accelerator installed with appropriate RF waveguide components.

The new XMPG medical linac, see Fig. 11, is called

3DRad™. Its patient benefits are:
(1) Radiation oncologists can select tighter margins of treatment, i.e., minimal unnecessary irradiation damage to healthy tissue and decreased patient treatment morbidity and collateral damage.
(2) Rapid or "instant" energy selection during exposure provides true 3D conformal doses in a single treatment.
(3) Rapid energy selection and high dose rate give more efficient treatment or "dose painting" of the tumor target and results in minimal impact from patient motion during treatment.
(4) 3DRad™ would be the most efficient adaptive radiation therapy treatment system.

Economic benefits of 3DRad™ are:
(1) Cost of ownership is much lower than existing technologies.
(2) Revenues are higher from more patient treatments and with less interrupted treatments due to system failure, because of decreased need of system repair with longer and more assured system lifetime.
(3) Capital costs are reduced by $4-5 million every seven years (present lifetime limited by antiquated DC electron gun driven linacs).
(4) The floor space savings are $1 million due to reduced footprint.
(5) It is readily installable in existing radiation oncology vaults because of small size, relatively low maximum energy requirement, and flexibility of location.
(6) The operator training is simplified because only one accelerator is needed to perform treatment as well as existing technology.

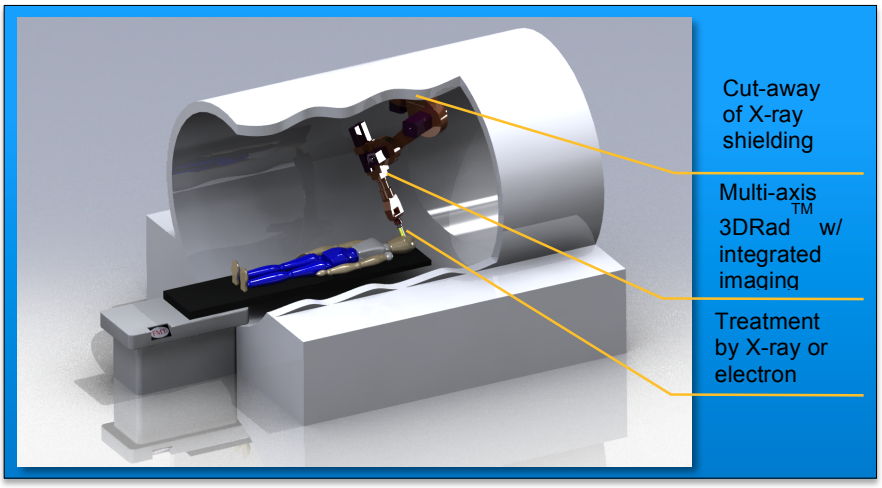

FIGURE 11. 3DRad™ shows shielding cut-away and patient exposure to high energy and high current, energy tunable source on a robotic arm with integrated imaging allowing for dynamic treatment of tumors.

CERAMIC JOINING FOR ETHYLENE PRODUCTION

Ethylene is generally produced by hydrocarbon feedstock that is cracked in a pyrolysis furnace. The superalloy pipes in every pyrolysis furnace are limited to ~1150°C before drooping under their own weight. Ethylene producers are interested in increased production for greater revenues. For a given pyrolysis furnace, the production capacity can be increased by cracking at a higher

operating temperature, which is limited by the high temperature strength of the current furnace coil material, namely superalloys.

Furnace coils are traditionally superalloy because coils experience extreme thermal cycling, coking, carburization, oxidation, and creep during service. The superalloys in the Fe-Ni-Cr family are used at their operation limits. Silicon Carbide (SiC) furnace coils are better in almost every way and allow the furnace coil operating temperature to move up to as high as 1400°C. By just moving operating temperatures from 1150°C to 1250°C results in 10% more product throughput, which given the current market is a $10B increase in revenue.

Ceramics may be an unconventional choice for furnace coils, but with appropriate design there are tremendous upsides. Ceramics are chemically and atmospherically inert, have high mechanical strength at high temperature, and have high creep resistance, where creep is the slow permanent deformation of a material due to stress. Chemical and atmospheric inertness is important when the furnace coils have high temperature reactions occurring on the inside of the pipe and the outside is exposed to atmosphere. High mechanical strength at high temperature and high creep resistance are both necessary when running the furnace coils at high temperature 24/7 annually for the coils to not droop or deform. Ceramics that could be reasonable candidates for ethylene production include Silicon Nitride (Si_3N_4), Fused quartz (SiO_2), Alumina (Al_2O_3), and Silicon Carbide (SiC). It will be shown that SiC has superior properties compared to other ceramics and other metals that are candidates for furnace coils for ethylene production.

The thermal conductivity of SiC is more than three times greater than Al_2O_3. The thermal shock resistance of SiC is twice that of Si_3N_4. The mechanical strength as a function of temperature of SiC does not decrease for increasing temperature up to 1900°C. The hardness of SiC is 65% greater than the hardness of Si_3N_4 or Al_2O_3. The tensile strength of SiC is more than 5 times the tensile strength of superalloys for temperatures greater than 1150°C. The thermal conductivity of SiC is equal to the thermal conductivity of superalloys for temperatures greater than 1150°C. Also SiC has reduced coking (carbon deposition on inner wall of pipe), is oxidation resistance, and has almost no creep rate.

SiC has to be shaped into U-bend pipes to be used in a furnace coil and SiC is made only in pipe form when sintered. FMT has more than 20 years of research and development in ceramic joining. Early work showed that SiC to metal joining was possible via pulsed electron beam technology [19-21] and SiC to SiC joining was possible via polymer and microwave joining technologies [22-26]. The joints were oxidation resistant and strong. Since then, the joining technology has improved to be helium leak tight, oxidation and coke resistant, very strong (equal to SiC received material), and has a service temperature range of 1150-1400°C for SiC to SiC and 700-900°C for SiC to metal [27-30]. SiC and the use of SiC joining technology can be applied to nuclear fuel rods and solar receivers in addition to petrochemical furnace coils. Nuclear fuel rods require a high temperature material that is strong, helium leak tight, has high thermal conductivity and has a low neutron cross-section. SiC fits these requirements. Furthermore, solar receivers require an optically dark sunlight absorber that is strong, helium gas tight and has high thermal conductivity. Again, SiC has these characteristics.

FMT has SiC joining technology that works on numerous types of SiC to SiC tube joints including cap, collar, and plug joints. All joints are helium leak tight and have a service temperature range of 1150-1400°C. Figure 12 is a 400x photomicrograph showing the joining material, Makotite™ (portmanteau of Mako and tight because the joints are helium gas tight) between two SiC edges in a plug joint. Notice that Makotite™ can fill joint line features on the scale of 0.25 micron. FMT also has SiC joining technology that works on numerous SiC to metal tube joints, including cap, inside plug, and outside plug joints. All joints are helium leak tight and have a service temperature range of 700-900°C.

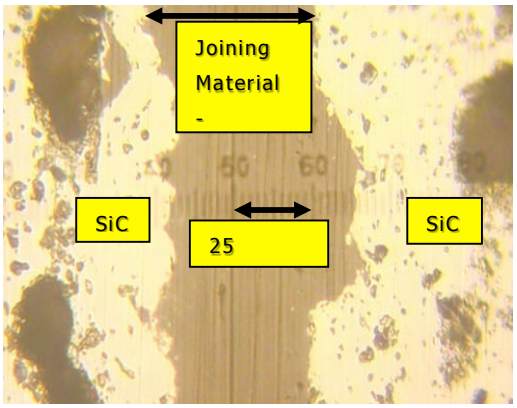

FIGURE 12. 400x photomicrograph of SiC to SiC helium leak tight plug joint with Makotite™ joining and flowing into below 0.25µm features of SiC surfaces.

SiC to metal joints are necessary because retrofitting an entire petrochemical plant with all SiC is much more expensive than only the SiC coils inside the firebox. If a petrochemical company desired to upgrade their plant, then the SiC coils in the firebox would transition to superalloy outside the firebox, where the pipe temperature would be below 900°C. Using all of the joining techniques together a miniature SiC coil was assembled (see Fig.13 left) to simulate the U-turn in an ethylene production plant. The entire structure is helium gas tight, structurally strong, oxidation resistant, and coke resistant. The service temperature range is 1150-1400°C for the SiC portion and 700-900°C for the metal portion. The metal can then be welded to superalloy pipe. Furthermore, due to thermal expansion of the pipes, bellows are present to reduce stress. Also included below is a model of SiC coils installed in an ethylene production facility.

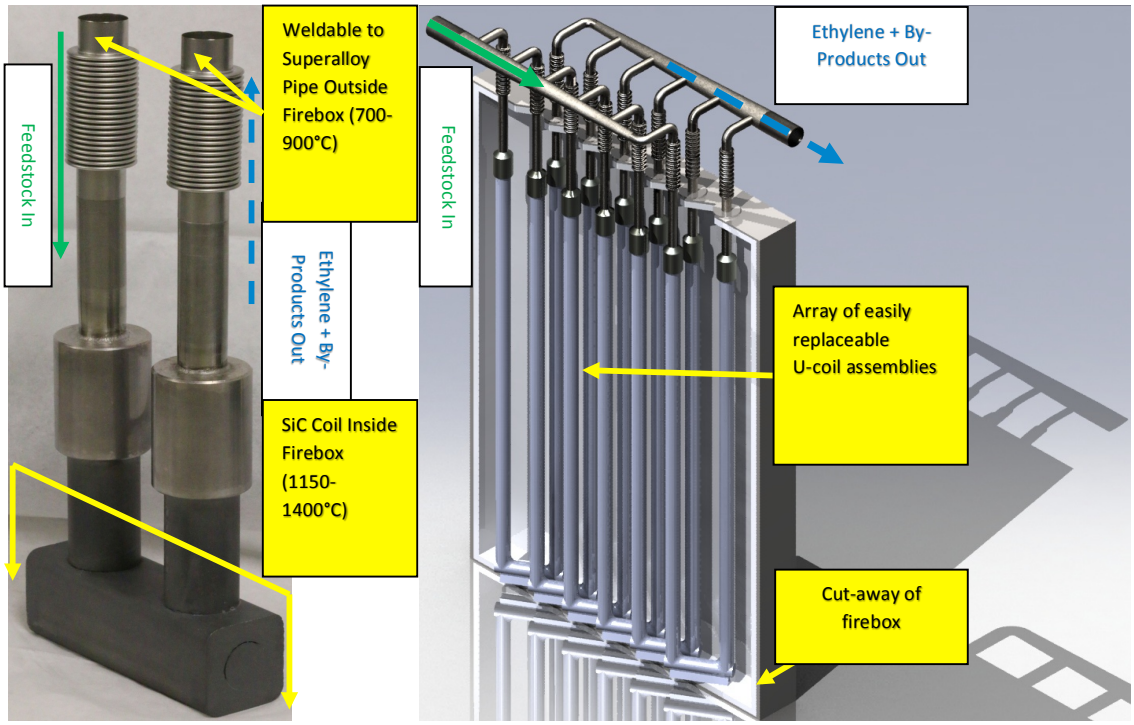

FIGURE 13. Left – Miniature SiC coil assembly that is helium leak tight and structurally strong that has bellows for stress relief to weldable superalloy pipe. Right – Model of installation of SiC coils that allows U-coil assemblies to be easily replaced.

REFERENCES

1. S. E. Graybill and J. R. Uglum, “Observation of Energetic Ions from a Beam-Generated Plasma," J. Appl. Phys. 41(1), 236, (1970).
2. J. W. Poukey and N. Rostoker, "One-Dimensional Model of Relativistic Electron Beam Propagation," *Plasma Physics,* v13, 897, (1971).
3. J. E. Crow, P. L. Auer and J. E. Allen, "The Expansion of a Plasma into a Vacuum," *Journal of Plasma Physics,* vol. 14, P1, p. 65, (1975).
4. D. D. Ryutov and G. V. Stupakov, "Formation of Fast-Electron Cloud during Injection of Intense Relativistic Electron Beam into Vacuum," *Soviet J. Plasma Physics,* vol. 2, N4, p. p309, (1976).
5. F. Mako, A. Fisher, N. Rostoker, D. Tzach, and C.W. Roberson, “Collective Ion Acceleration Controlled by a Gas Gradient”, IEEE Trans. Nucl. Sci., **26**, 4199 (1979).
6. F.Mako, A. Fisher, C.W. Roberson, N. Rostoker and D. Tzach, Collective Ion Acceleration Controlled by a Gas Gradient, "Collective Methods of Accelerations", edited by N. Rostoker and M. Reiser, Harwood Academic, New York, 317 (1979).
7. F. Mako and T. Tajima, “Collective Ion Acceleration by a Reflexing Electron Beam: Model Scaling”, Phys. Fluids, **27**(7), 1815 (1984).

8. T. Tajima, D. Habs and X. Yan., "Laser Acceleration of Ions for Radiation Therapy," *Reviews of Accelerator Science & Technology,* v1, 1, (2008).
9. F. M. Mako III, private communication.
10. F. Mako and W. Peter, "High-Current Micro-Pulse Electron Gun", Proc. Particle Accelerator Conf., IEEE Cat. 93CH3279-1, 2702, (1993).
11. F. Mako and L. K. Len, "Self-Bunching Electron Guns", Proc. Particle Accelerator Conf., IEEE Cat. 99CH36366-1 70 (1999).
12. F. Mako, L. K. Len and W. Peter, "Self-Bunching Electron Guns", Advanced Accelerator Conf., CP472, 875, AIP Press, NY (1999).
13. J. A. Nation, L. Schachter, F. Mako, L. K. Len, W. Peter, C. M. Tang and T. Srinivasan-Rao, "Advances in Cold-Cathode Physics and Technology", Proc. IEEE, **87**(5), 865 (1999).
14. F. Mako and L. K. Len, "Self-Bunching Electron Guns", in High Energy Density Microwaves, ed. R. M. Phillips, AIP, CP474, 41 (1999).
15. S. K. Guharay, L.K. Len and F. Mako, "High-Current Micro-Pulse Electron Guns and Accelerator Applications", Proceedings of the Particle Accelerator Conference, 2084 (2001).
16. F. Mako and W. Peter, Electron Gun for Producing Incident and Secondary Electrons, Pat. No. 7,285,915 B2 10/23/ (2007).
17. F. Mako, Electron Gun Having Multiple Transmitting and Emitting Sections, Pat. No. 6,633,129 B2 10/14/ (2003).
18. F. Mako and A. Fisher, Robust Pierce Gun Having Multiple Transmitting and Emitting Section, Pat. No. 6,642,657 B2 11/04/ (2003).
19. F. Mako, Pulsed Electron Beam Joining, "Proceedings of a Workshop on Applications of Accelerators", edited by W.B. Herrmannsfeldt, A.M. Sessler and J.R. Alonso, (SLAC-430, LBL-35023, CONF-931248, UC-400, 49, (1993).
20. F. Mako, R. Silberglitt and L. K. Len, Pulsed Electron Beam Joining of Materials, (Israel) Pat. No. 118126/2 10/03/ (1994).
21. F. Mako, R. Silberglitt and L. K. Len, Pulsed Electron Beam Joining of Materials, Pat. No. 5,599,468 02/04/ (1997).
22. R. L. Bruce, S. K. Guharay, F. Mako, W. Sherwood, E. Lara-Curzio, "Polymer-Derived SiC/SiC Composite Fabrication and Microwave Joining for Fusion Energy Applications", Proc. 19th IEEE/NPSS Symp.on Fusion Engr., Atlantic City, NJ, Jan. 22-25, 426, (2002).
23. F. Mako and R. L. Bruce, Ceramic Joining, US Pat. No. 6,692,597 B2 02/17/ (2004).
24. S. K. Guharay, F. Mako, Y. Tian, "Joining of SiC components and evaluation of joint characteristics", Plasma Facing Components 2004 Workshop at Univ. Illinois at Urbana-Champaign, IL., "http://fusion.anl.gov/ALPS_Info_Center/2004-05-04/agenda.html" May 3-5 (2004).
25. F. Mako and R. L. Bruce, Ceramic Joining, PRC (China) Pat. No. ZL02824111.8 06/11/ (2008).
26. F. Mako and R. L. Bruce, Ceramic Joining, US Pat. No. 8,337,648 B2 12/25/ (2012).
27. F. Mako, E. Cruz, Y.Tian, J. Schilling, "New Silicon-Carbide Joining Technology", AIChE, #352574, Ethylene Producers Conf., 2014 Spring National Meeting, New Orleans, LA, March 30 – April 3 (2014).
28. F. Mako, E. Cruz and F. M. Mako III, "System and Method for Producing Chemicals at High Temperature", filed 12 March (2015).
29. F. Mako, E. Cruz and F. M. Mako III, "Mixed Oxide Materials for Helium Leak Tight, Oxidation Resistant and High Strength Joints Between High Temperature Engineering Materials", filed 27 March (2015).
30. F. Mako, E. Cruz and F. M. Mako III, "Method for Joining Ceramics to Ceramics or Ceramics to Metals, and Apparatus", filed 27 March (2015).

Studies of High-Current Relativistic Electron Beam Interaction with Gas and Plasma in Novosibirsk

S.L. Sinitsky,[1, 2 a)] A.V. Arzhannikov,[1, 2] and A.V. Burdakov[1, 3]

[1]*Budker Institute of Nuclear Physics, 11 Acad. Lavrentyev Ave, Novosibirsk, 630090, Russia*
[2]*Novosibirsk State University, 2 Pirogova St., Novosibirsk, 630090, Russia*
[3]*Novosibirsk State Technical University, 20 Prospekt K. Marksa, Novosibirsk, 630073, Russia*

[a)]Corresponding author: s.l.sinitsky@inp.nsk.su

Abstract. This paper presents an overview of the studies on the interaction of a high-power relativistic electron beam (REB) with dense plasma confined in a long open magnetic trap. The main goal of this research is to achieve plasma parameters close to those required for thermonuclear fusion burning. The experimental studies were carried over the course of four decades on various devices: INAR, GOL, INAR-2, GOL-M, and GOL-3 (Budker Institute of Nuclear Physics) for a wide range of beam and plasma parameters.

INTRODUCTION

The 1970's were marked by intensive studies on generation and applications of high-power relativistic electron beams (REBs). The interest in such beams is explained by enormous power that they can readily have. This property of REBs revolutionized studies in various fields including nuclear fusion, generation of high-power X-rays, development of high-power microwave oscillators and amplifiers. In those years Norman Rostoker became one of the lead researchers in the field of the high-power beams. As a founder of the Laboratory for Plasma Studies at Cornell University, Professor N. Rostoker applied a lot of effort to stimulate the studies on intense electron beam transport under various experimental conditions. In a series of papers published during 1970-1975, he described the results of theoretical and experimental investigations of physical processes that determine the efficiency of the beam transport in plasma and gas media for two fundamentally different cases: With and without the guiding magnetic field.[1-4] This basic knowledge is widely used in the modern experimental physics.

Approximately at the same time, the studies on generation and propagation of high current (10 - 100 kA) REBs with duration ~ 100 ns was started in the Budker Institute of Nuclear Physics (Novosibirsk).[5,6] During the next fifteen years the beam duration was extended to 10 μs while keeping the beam power at a practically constant level (~10 - 30 GW). This development of the beam generation technology was motivated by the application of REBs for fast plasma heating in open magnetic traps. Experimental studies on such application of the electron beams were carried out at the INAR device (1971 - 1985),[7,8] REBEX machine (1978 - 1990),[9] GOL-1M facility (1971 -2005),[10] and GOL-3 facility (1987 - 2014).[11] As a result of these experiments, it was established that the plasma temperature dramatically increased during the microsecond beam injection and achieved several keV for the plasma density about 10^{15} cm^{-3}. Conditions for microscopically stable transport of intense electron beam in these experiments were chosen based on the results obtained by Professor N. Rostoker. The REB community greatly appreciates Prof. Rostoker's scientific discoveries and technological achievements.

In this paper we present an overview of experimental and theoretical studies on the intense electron beam transport and beam-plasma interaction in Budker Institute.

EXPERIMENTS ON PLASMA HEATING WITH 100-NANOSECOND RELATIVISTIC ELECTRON BEAMS

The first phase of experimental studies on the interaction of high-current, 100-ns relativistic electron beam with dense plasma was carried out at several devices in Budker Institute: INAR, GOL, INAR-2, GOL-M, and REBEX machine at the Institute of Plasma Physics in Prague. The first experiments were carried out by two groups headed by Dr. R.Kh. Kurtmulaev[5] in 1970 and Dr. V.S. Koidan[6] in 1971. The main goal of this research was to investigate the physics of beam-plasma interaction and based on this knowledge to achieve the highest possible plasma parameters. It should be mentioned beforehand that in these investigations the typical energy loss of the electron beam in a plasma column with a few meter length was about one half of its initial energy. This level of energy loss is determined entirely by collective phenomena of the beam relaxation in plasma, and not by the beam electron collisions with plasma particles. For reference, the classical mean free path of a relativistic electron in a 10^{14}-10^{15} cm^{-3} plasma is much greater than a thousand kilometers.

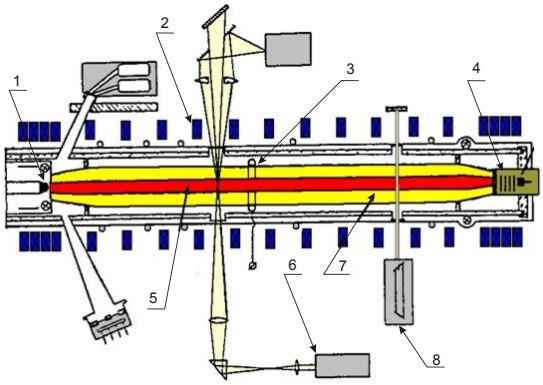

FIGURE 1. Schematic of the INAR experiment. 1- planar diode, 2 - magnetic trap, 3 - Penning discharge electrode, 4 - multifoil analyzer, 5 - electron beam, 6 - Thomson scattering system, 7 - plasma column, 8 - interferometer

All mentioned devices were conceptually similar. The layout of the INAR device[12] is presented in Fig. 1. In this device, the electron beam was generated by a quasi-planar axially symmetric diode and injected through a thin metal anode foil into a plasma column. The target plasma was produced by a Penning discharge in the gas contained in a quartz chamber. The diode and the quartz chamber were mounted inside a magnetic trap. The typical parameters of the beam were as follows: The electron energy of ~1 MeV, the current of up to 25 kA, the pulse duration of 70 ns, and the beam diameter in the plasma about 2 - 4 cm. The plasma column had the length of 230 cm at the diameter of 8 cm. The plasma density was varied from 10^{12} cm^{-3} up to 10^{16} cm^{-3}. The plasma was confined in a mirror magnetic field of up to 2.5 T in the central section and up to 4.2 T in the mirrors.

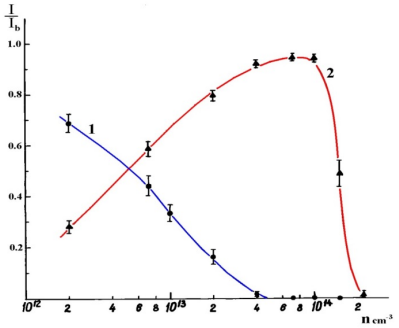

FIGURE 2. Beam current neutralization in the INAR device versus the plasma density for t = 7 ns after the beam start. 1 - return current in the chamber wall, 2 - return current in the plasma outside the beam cross section

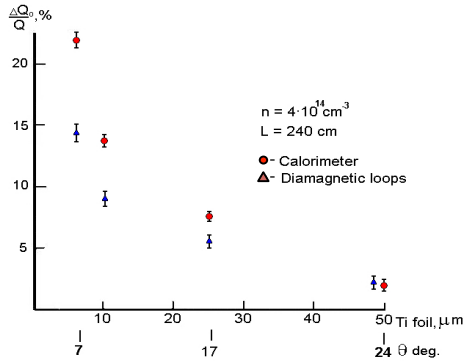

FIGURE 3. Efficiency of the beam energy transfer to the plasma as a function of electron angular spread for $N_b = 2\times10^{11}$cm^3, $N_p = 4\times10^{14}$cm^{-3}

At first one had to find the conditions for stable beam transport through the plasma column, because any kind of macroscopic instabilities could deflect the beam to the chamber wall and thereby damage the chamber. As shown in the experiments,[13] the key driver for beam stability is the radial distribution of the return current in the chamber. If the distribution of the return plasma current is asymmetric or the current is disrupted, the beam is deflected to the wall. Figure 2 demonstrates two parts of the return current. One part is flowing in the conducting wall outside the quartz chamber (1) and the other one − in the plasma outside the beam (2). The third, remaining part is the return current that goes through the plasma column inside the beam (this part is equal, in normalized units, to one minus the sum of the two parts plotted in Fig. 2). As seen in Fig. 2, with increasing plasma density the return current initially transitions from the metal wall to the plasma annulus outside the beam, and then (at plasma density > 2×10^{14} cm^{-3}) gets concentrated within the beam cross section. This last regime, in which the return current propagates inside the beam, is most favorable for stable beam transport. Theoretical analysis proved that only when the ratio of the beam density, N_b, to plasma density, N_p, is less than 10^{-3}, the effects of anomalous plasma conductivity and excitation of Buneman and ion-sound instabilities do not preclude stable transport of the beam in the plasma column.[14]

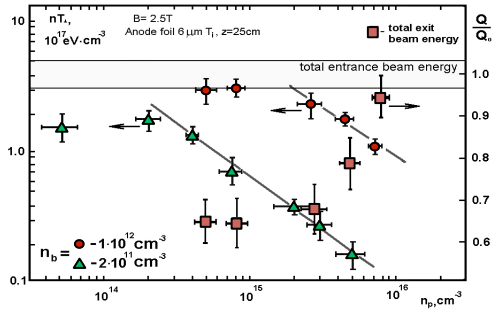

FIGURE 4. Transverse plasma pressure (triangles for $N_b = 2\times10^{11}$ cm^{-3}, circles for $N_b = 10^{12}$ cm^{-3}) and the beam energy transported through the plasma column Q/Q_0 (squares for $N_b = 10^{12}$ cm^{-3}) for various plasma densities (INAR).

It is well known from non-relativistic electron beam studies that the two-stream instability plays a key role in the deceleration of the beam electrons. The kinetic theory of this instability[15] produces the increment proportional to the beam density and inversely proportional to the square of the mean angular spread of the beam electrons. Important evidence of the role of this instability in the beam-plasma interaction comes from the measurements of the energy deposition in the plasma as a function of the angular spread of the beam electrons.[7] Figure 3 demonstrates that the energy transfer from the beam to the plasma is roughly inversely proportional to the square of the angular spread of the beam electrons. Moreover, a strong non-uniformity of the energy transfer along the beam path is observed experimentally: The efficiency of interaction is maximal near the entrance of the beam to the plasma (where the angular spread of the beam is the smallest) and reduces along the beam path. This behavior is explained by the

growth of the energy and angular spread in the electron distribution function due to the intense beam-plasma interaction.[16]

The suppression of the two-stream instability due to a high rate of electron-ion collisions in a cold, dense plasma is demonstrated experimentally in Fig. 4. Both the beam energy loss and transverse plasma pressure decrease with increasing plasma density, as a result of the suppression of the two-stream instability due to collisions with the cold plasma electrons in a sufficiently dense plasma. In order to drive strong Langmuir oscillations at higher plasma density, one has to increase the increment of the two-stream instability. As shown in Fig. 4, this was accomplished by increasing the beam density from 2×10^{11} to 10^{12} cm^{-3}.

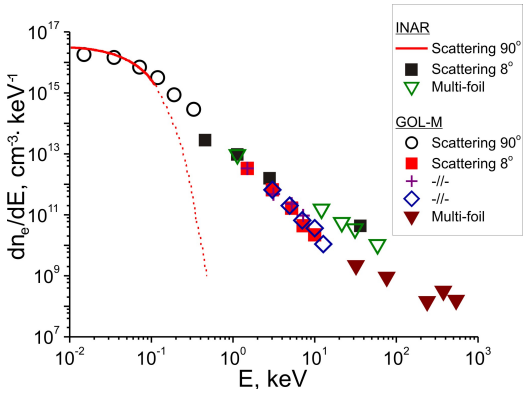

FIGURE 5. Energy distribution function of the plasma electrons (INAR, GOL-M).

Another characteristic feature of the plasma heated by an REB is a non-Maxwell energy distribution of plasma electrons, as measured in INAR and GOL-M experiments. To measure the energy spectrum of the plasma electrons, the 90° and 8° Thomson scattering systems and a multi-foil analyzer were used.[8,17] As can be seen in Fig. 5, the electron energy distribution function obtained in these measurement[8] has a high-energy tail that decreases inversely proportional to the electron energy to the power of ~ 2.5 - 2.7.

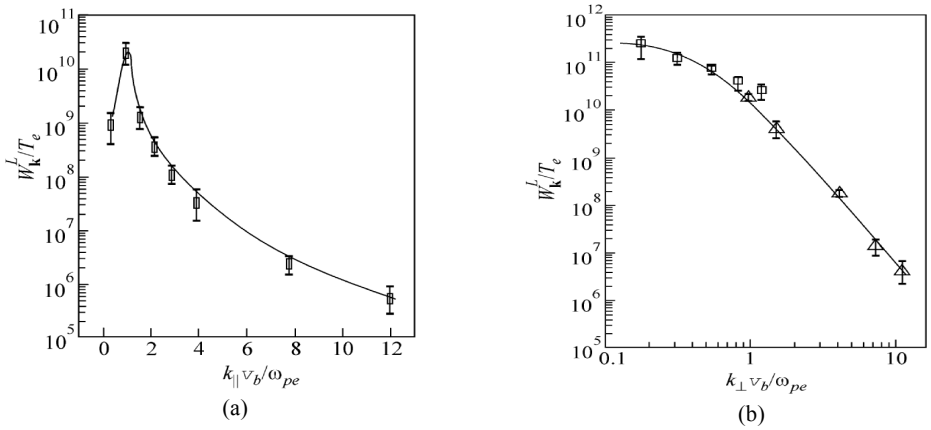

FIGURE 6. Spectra of Langmuir oscillations measured along the line $k_\perp = \omega_{pe}/V_b$ (a) and along the $k_{||} = \omega_{pe}/V_b$ (b)

According to the theory of two-stream instability in a magnetized plasma (see, for example, Ref. 18) the relativistic electron beam excites long wavelength Langmuir oscillations that meet the resonance condition: $\omega - k_{||}V_{||} = n\omega_{Be}$, where k is the wave vector, V is the beam electron velocity, ω_{Be} is the cyclotron frequency of the plasma electrons, and n is an integer. The maxima of magnetic resonance at visible angular spread of electrons overlap and form a disk-shaped region in k-space. At typical parameters of beam-plasma experiments, the energy density of Langmuir oscillations exceeds by far the thermal energy of plasma, and the modulation instability of Langmuir oscillations occurs, which gives rise to Langmuir turbulence. The Langmuir turbulence leads to low frequency

modulation of plasma density and plasma wave transfer from the resonant to non-resonant region of *k*-space. In the short wavelength part of this region, where the wave phase velocity is close to the thermal velocity of plasma electrons, there occurs an effective energy transfer from waves to plasma electrons. The direct measurements of the Langmuir oscillation spectra were performed on GOL-M[19] for the beam and plasma parameters similar to those in the INAR experiment. The measured energy density spectra of the waves with the wave vector satisfying $k_\perp = \omega_{pe}/V_b$ and $k_\| = \omega_{pe}/V_b$ confirmed the existence of a broad spectrum in the region of *k*-space non-resonant with the beam (see Fig. 6). Moreover, the level of Langmuir oscillations exceeded the threshold of the modulation instability by more than one order of magnitude.

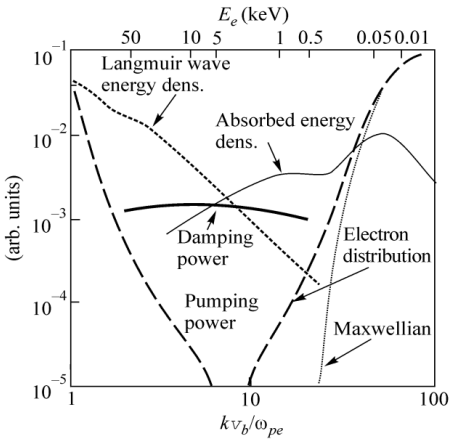

FIGURE 7. Structure of pumping and absorption of Langmuir oscillations in the GOL-M device.

The integrated diagram of pumping of the non-resonant waves and their absorption by the plasma electrons is shown in Fig. 7. The bottom horizontal axis shows the normalized wavenumber, kV_b/ω_{pe}, while the top axis provides the energy of electrons that efficiently interact with the waves of a given wave number. The damping power and absorbed energy density allow to explain the existence of a non-thermal tail in the distribution function of the plasma electrons. To summarize, the main findings of the beam-plasma interaction studies at 100-ns beam duration are as follows:

- For stable transport of a high-current REB in plasma, the plasma return current has to be concentrated inside the beam cross-section and, for the beam with $N_b \sim 2\times10^{11}$ cm^{-3} this condition is reached only at plasma densities higher than 2×10^{14} cm^{-3}.
- It is established that the two-stream instability plays the key role in the process of energy transfer from the beam to the plasma.
- The experimental conditions were found for which the high-current REB with $N_b \sim 10^{11}$-10^{12} cm^{-3} can lose a substantial part (~ 40%) of its energy in the plasma with density $N_p \sim 10^{15}$-10^{16} cm^{-3}.
- The measured distribution function of the plasma electrons heated due to the development of the two-stream instability is fundamentally non-equilibrium. The average energy of the plasma electrons is about 1 - 2 keV, while the Maxwellian part of the distribution function is characterized by the temperature of about a few tens of electron-Volts.
- The energy density of the heated plasma is proportional to the magnetic field in the trap (results of INAR-2 experiments).[20]
- The Langmuir turbulence driven by the high-current REB in a magnetized plasma has a broad spectrum with spectral density exceeding the thermal level by 5 - 11 orders of magnitude. Through several nonlinear effects, the wave energy is pumped from resonant to non-resonant regions, where it is absorbed by plasma electrons.

BEAM-PLASMA INTERACTION FOR 10-MICROSECOND RELATIVISTIC ELECTRON BEAMS

A new era in the investigations of the beam-plasma interaction was started when a new acceleration technique was developed in the early 1980's. This technique made it possible to generate electron beams with 5 - 10 μs pulse duration and the same electron energy and current density as was previously available for 100 ns beams. The first accelerator of this kind at BINP was U-1, which was built in 1982.[21] This accelerator could produce e-beam with the energy content about 100 kJ instead of ~1 kJ that was achieved in accelerators with 100 ns beam duration. In order to generate the beam with such a long pulse, the current density of the beam electrons directly in the diode was decreased from ~1 kA/cm^2 to ~100 A/cm^2. To reach the required beam current density in the plasma, 1 - 4 kA/cm^2, the magnetic compression of the beam cross section was applied. However, magnetic compression led to undesirable growth of the beam angular spread.

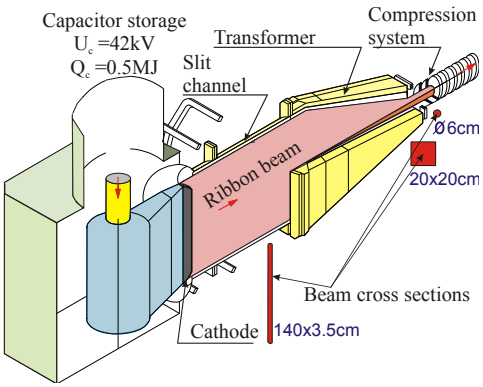

FIGURE 8. Schematic of the U-2 accelerator.

To overcome this challenge, we proposed to use a magnetically insulated diode of ribbon geometry. Based on this proposal, the U-2 accelerator was built.[22] The angular spread of the compressed beam in U-2 was reduced to ~10 - 15° by 1) removing the anode foil in the accelerator and 2) fine-tuning the magnetic field profile in the cathode-anode gap.[23] Moreover, due to the application of a carbon fiber material to cover the cathode surface, the beam energy was doubled for a 10 μs pulse. It is important to note one more advantage of such ribbon beams. They can be easily transported through slit vacuum channels with guiding magnetic field about a few kG and switched from one channel to another by pulsed magnetic field. Thus, ribbon beams from multiple diodes[24] can be injected in series into the plasma column by fast reconnection of magnetic field lines.

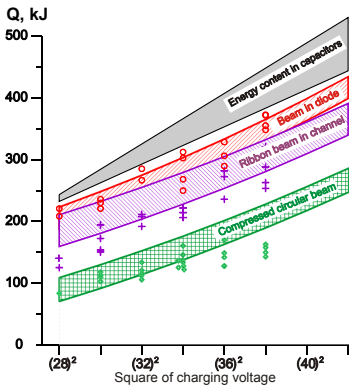

FIGURE 9. Energy flow through different parts of the U-2 accelerator. Shaded areas correspond to the experiments with the 140 cm cathode, markers to the 70 cm cathode.

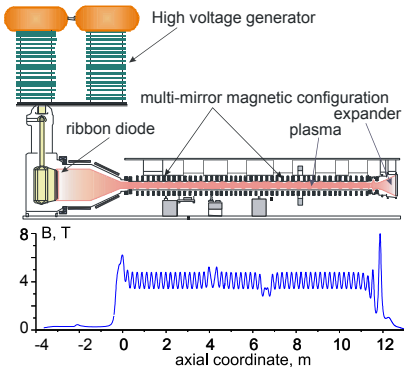

FIGURE 10. Schematic of the GOL-3 facility and the magnetic field configuration.

The schematic of the U-2 accelerator producing the ribbon beam is shown in Fig. 8. This accelerator was operated in two modes. In the first mode, the initial beam produced in the diode had the current of up to 50 kA and the cross section of 3.5×140 cm. This rectangular cross section was compressed to a circular one by varying the cross section of the guiding magnetic flux tube along the beam path. The final circular beam had the diameter of 6 cm, the energy of ~ 250 kJ, and the current density in the plasma of ~ 1 kA/cm^2.[25] In the second mode, the ribbon beam had the initial cross section of 4×70 cm at the same current. The final circular beam had the diameter of 4 cm, the energy of ~ 150 kJ, and the current density in the plasma of ~ 2 kA/cm^2. The diagram of the energy flow through different parts of the U-2 accelerator is shown in Fig. 9. At the charging voltage of 42 kV, the efficiency of energy transfer from the capacitor bank to the compressed beam is about 40%. The energy of the compressed beam is about 150 - 200 kJ, which is suitable for plasma heating experiments.

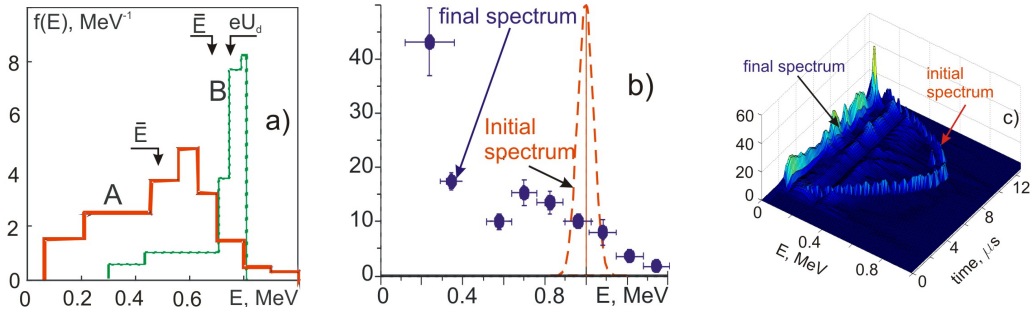

FIGURE 11. Energy spectra of the beam electrons after crossing the GOL-3 plasma: a) Spectrum measured with the multifoil analyzer in the case of beam injection in 7 m plasma column through the 5 μm anode foil (A) and residual gas (B) for the homogeneous magnetic field, t = 1.8 μs after the beam start; b) Spectrum measured by magnetic spectrometer for the case of the beam injection without the anode foil into 12 m plasma column in uniform magnetic field, t = 4 μs; c) Spectrum measured by multifoil analyzer in the case of beam injection without the anode foil into 12 m plasma column in the corrugated magnetic field

The plasma heating experiments were performed at the GOL-3 facility, whose diagram is shown in Fig. 10. The facility consists of the U-2 accelerator and a multi-mirror magnetic trap. The magnetic trap can be operated in several different modes. In the first mode, the uniform, axially symmetric mirror trap with the magnetic field of up to 4.5 T in the central section and up to 9 T in the end mirrors can be produced. In the second mode, in a part of the trap, up to its total length of ~12 meters, the magnetic field of can be corrugated with the period of 22 cm. The number of cells in a fully corrugated configuration is 55; the maximal and minimal magnetic fields in each cell are 4.8/3.3 T.

The first experiment on beam-plasma interaction at the beam duration of 5 - 10 μs was started for the uniform magnetic configuration with two end mirrors. The first task in these experiments was to prepare a 12 m plasma column with the density in the range of 10^{14}-10^{16} cm^{-3} in a vacuum chamber with a metallic wall. This task was solved by the application of a direct discharge in gas. This discharge was produced by a set of special electrodes at the end of the trap.[26] The next problem was to find the conditions for stable beam transport in the plasma column. A

few basic requirements must be satisfied for the stable transport of the 30 kA beam in the 12-m-long plasma in the magnetic field of 4 - 5 T. First, the plasma density has to exceed 10^{14} cm-3; second, the discharge current in the target plasma has to be greater than 7 kA and be axially symmetric and directed oppositely to the electron beam motion.[27]

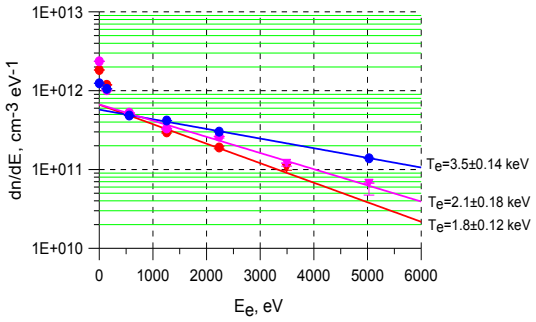

FIGURE 12. Thomson scattering spectra for three shots at t = 6 μs after the beam start, $N_p = 4\times10^{14}$cm^{-3}.

The first experiments showed that the main features of beam-plasma interaction for 5 - 10 μs beams are similar to those for 100 ns beams. For example, the energy loss of the beam after passing the plasma column with the length of 12 m was in the range of 50 - 60%, as compared with ~ 40% for the 100 ns REB that passed through the 2.4 m plasma column. The energy spectrum of the beam electrons exiting from the plasma was strongly dependent on the angular spread of the injected beam. The beam injection through the anode foil (5 μm Mylar film covered by 0.3 μm aluminum) and subsequent magnetic compression gave the electron angular spread of about 25° in the point of the beam entrance into the plasma. In this case, the measured difference between the maximum of the electron energy spectrum after passing the plasma and the initial electron energy was not much and the widening of the spectrum was substantial (see Fig.11a).[28] In contrast to this case, the beam injection into the plasma without the anode foil and the same magnetic compression gave the initial angular spread of the electrons about 10-15°. Under these conditions we observed strong relaxation of the beam with a much larger loss for both uniform[29] (Fig.11b) and corrugated[30] (Fig.11c) magnetic fields. One can see that the electron spectral density decreases monotonously with the energy growing from one hundred keV up to the initial beam energy. It is worth noting that in the case of the beam injection into a residual gas (practically, vacuum) the energy spectrum of the beam at the exit from the vacuum chamber was very narrow, except the low level tail.

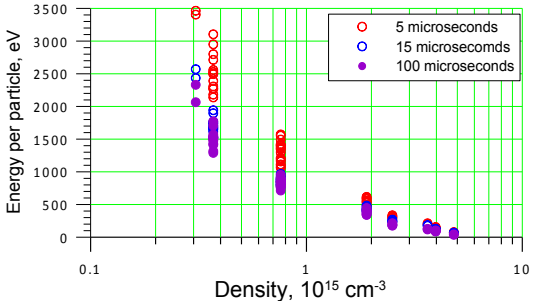

FIGURE 13. Average energy of plasma particles for various initial plasma densities at the beam current density ~2 kA/cm^2 at 5, 15, and 100 μs after the beam start.

The energy spectrum of the plasma electrons in the range of 0 - 5 keV was measured with the Thomson scattering system[29,31]. Figure 12 shows that the electron energy spectrum between 0 - 5 keV is close to the Maxwellian distribution function with the average temperature varying (in different shots) from 2 - 4 keV. These values exceed by factor of ~100 the electron temperatures measured for 100 ns beams. This dramatic increase in temperature is due to the increase in the beam energy content.

The performed experiments showed the decrease of the energy per particle in the heated plasma with increasing plasma density (see Fig. 13). This dependence of the energy per particle is similar to that for 100 ns beams. We

explain this dependence by the suppression of the two-stream instability by electron-ion collisions in the initial cold plasma.

SIGNIFICANT PHYSICAL EFFECTS IN PLASMA HEATING AND CONFINEMENT PRODUCED BY TURBULENCE

Suppression of the Electron Heat Conductivity

Since the first experiments on the microsecond REB injection into the plasma confined in the homogeneous magnetic field it was observed that the transverse pressure of heated plasma measured by diamagnetic loops and Thomson scattering is very non-uniform along the axis of the plasma column.[29] This result was similar to the case of 100 ns beam injection. The example of data obtained in one series of typical shots is shown in Fig. 14.

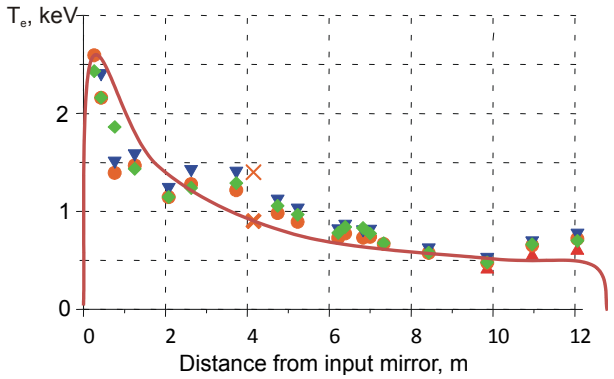

FIGURE 14. Axial profile of the electron temperature: Calculated from diamagnetic signals (various markers for several shots) with predicted by the model based on the suppression of the plasma electron thermal conductivity (solid line). Plasma density was held constant at ~ 0.8 - 1×10^{15} cm^{-3}. Thomson scattering data points are shown by crosses (×).

The existence of such strong non-uniformity in the plasma energy distribution contradicts with the estimates of classical plasma cooling time at keV-level of the electron temperature. Heat conductivity along the axis in case of the classical scattering of the electrons should be so high that the cooling time has to be much less than 1 μs. The estimations showed that in the case of the classical cooling rate the energy lost along the magnetic field should preclude reaching the electron temperatures observed in the experiments. One can explain experimental results by invoking the assumption of strong anomalous scattering of plasma electrons on small-scale fluctuations of the electric field in the plasma. The best candidate for this process is the fluctuations of the electric field in the plasma produced by the developed Langmuir turbulence. In accordance with observed temperature gradients, the classical collisional frequency should be multiplied by the factor of ~1000. This non-classical collisional frequency is close to the increment of two-stream instability for the experimental conditions. The model based on the anomalous collision frequency close to the increment well describes the temporal and spatial behavior of the electron temperature in the trap.[32]

The existence of strong Langmuir turbulence in the plasma at the beam-plasma interaction is additionally confirmed by the observation of high-power sub-mm emission near the double plasma frequency registered at the 10 μs duration experiments.[33]

Fast Ion Heating

One could assume that after the beam termination the axial heat conductivity should return to its classical value and the plasma pressure should quickly disappear. Actually it was observed for the case of homogeneous magnetic field in the trap: In time of the beam injection (a few microseconds) the heated plasma electrons cannot transfer noticeable part of their energy to the ions through collisions and the ion temperature does not exceed one hundred electron-Volts. But in the case of fully or partially corrugated magnetic field in the trap we have observed the ion

heating during the beam injection to the temperatures 1 - 2 keV that are comparable with the electron one. The existence of fast ion heating was confirmed by direct measurements of the ion temperature with Doppler broadening of Da spectral line (see Fig. 15) and by registration of a neutron flux from the plasma heated by the beam.[34] The time behavior of the neutron flux was shown in two scales in Fig. 16.

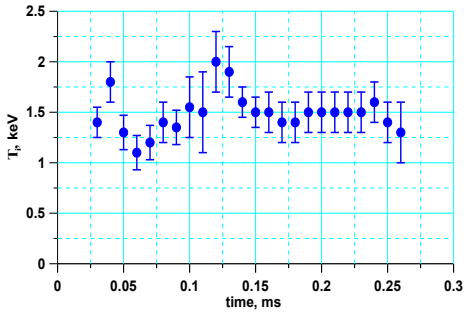

FIGURE 15. Temporal variation of ion temperature measured by Doppler broadening of D_a spectral line. Initial plasma density is equal to 3×10^{14} cm^{-3}.

This new phenomenon was studied in the special experiment with magnetic well.[35] To do that in some part of the homogeneous magnetic configuration we decreased the magnetic field and as a result the current density of the electron beam was also decreased here. The electron beam effectively heated plasma everywhere except the region of the magnetic well because of the beam current density was too low. Due to suppression of the axial thermal conductivity mentioned before, the plasma pressure had a dip in this region. The axial non-uniformity of the electron pressure produced a longitudinal ambipolar electric field that accelerated the plasma ions on both sides of the magnetic well toward its central plane where the counter-propagating plasma flows collided. As a result the kinetic energy of the directed ion motion was transformed into their thermal energy. Efficiency of this heating mechanism is much higher than that determined by binary electron-ion collisions.

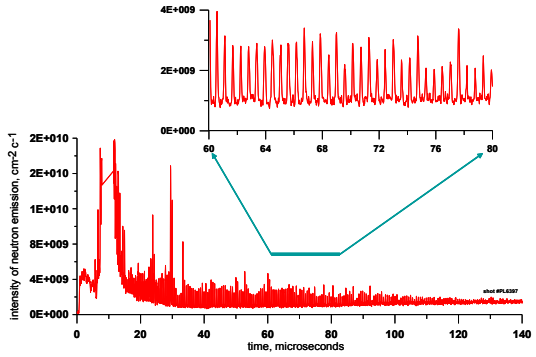

FIGURE 16. Fine structure of DD neutron emission intensity that corresponds to the bounce oscillations of fast ions in the multi-mirror trap cells.

In the case of heating plasma in the multi-mirror trap the beam energy deposition is not uniform along the axis of the trap. It results in high pressure gradients inside mirror cells along the magnetic field and macroscopic motion of the plasma. These pressure gradients determine two kinds of plasma motion: local - inside each cell and global one - along the entire magnetic trap. Both of these types of motion lead to fast energy transfer from electrons to ions. This process is much faster than the energy transfer due to binary collisions of the particles. As a result, we achieved the ion plasma temperatures up to 2 keV at the plasma density ~0.3×10^{15} cm^{-3}.

Increase in the Ion Lifetime

In addition to the fast ion heating, we experimentally observed a substantial increase in the ion lifetime in the multi-mirror magnetic trap, which was predicted by theoretical models.[36,37] Following these models we assume that there are two types of ions in the multi-mirror trap: Trapped and transiting. Due to collisions, transiting ions get trapped in magnetic cells and, after a few axial bounces in the cell, become de-trapped and transiting again. The direction of the ion motion upon leaving the cell changes randomly with respect to the initial direction. Such diffusive character of ion motion leads to the increase in the plasma lifetime proportional to the number of cells in the trap (the lifetime amplification is about factor of 100 for our experimental conditions). According to the theory, the amplification factor is maximal only when the ion mean free path is about the cell length (the solid curve for the classical theory in Fig. 17). The comparison of theoretical and experimental data in Fig. 17 indicates that the absolute value of the energy confinement amplification factor agrees well with the theoretical value, but the plasma density at which the best confinement is achieved is lower than theory predicts.

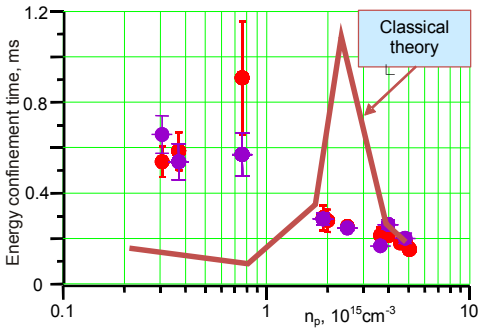

FIGURE 17. The dependence of the energy confinement time on plasma density.

Good agreement between theory and experiments would ensue if one assumed anomalous ion collisions with frequency exceeding the classical value by the factor of a few tens. In fact, the improvement of the longitudinal plasma confinement at the densities much lower than the classical prediction is due to the excitation of bounce oscillations in magnetic cells by the axial flow of the plasma.[38,39] These oscillations were directly observed in the measurements of the neutron emission from the cells, which is proportional to the square of the ion density.[34] Periodic oscillations can be easily identified in the neutron emission signals shown in Fig. 16. The theoretical model explains the improved plasma confinement in the multi-mirror trap in the range of plasma densities 2×10^{14}-10^{15}cm^{-3}, in which the effective ion mean free path is about the cell length. The experimental frequency of bounce oscillations agrees well with the theoretical one with good accuracy. To eliminate any doubt about the origin of such additional scattering of ions in the trap, the measurements of the effective ion charge were performed. The measured Z_{eff} = 1.2 - 1.6 could not explain the substantial increase in the ion scattering.[40]

PROGRESS IN PLASMA PARAMETERS OVER THE LAST 30 YEARS

The progress with the electron and ion temperatures achieved at the GOL-3 facility over the last 30 years is summarized in Fig. 18. These achievements in the sub-fusion plasma parameter range were enabled by several factors: 1) the decrease in the beam electrons angular spread, 2) the increase in the current density and the e-beam energy content, 3) the suppression of the electron heat conductivity in plasma, 4) the fast ion heating and the increase in the plasma lifetime due to the full length corrugation of the magnetic field in the trap. The main experimental results on beam-plasma interaction for 10 μs beams can be summarized as follows:

- Conditions for stable beam transport in the multi-mirror trap with the target plasma have been found.
- The characteristic features of the beam-plasma interaction observed fro 100 ns REBs have been studied in the experiments with 10 μs beams.

- New collective effects were discovered in the multi-mirror trap heated by REBs: The suppression of the electron conductivity, the fast ion heating, MHD stabilization and self-organized confinement due to the bounce instability.
- As a result of these collective effects, the sub-fusion plasma parameters have been achieved in the GOL-3 facility: The electron temperature of ~2 - 4 keV, the ion temperature of up to ~2 keV for the plasma density of ~10^{15} cm^{-3}, and energy confinement time ~1 ms.

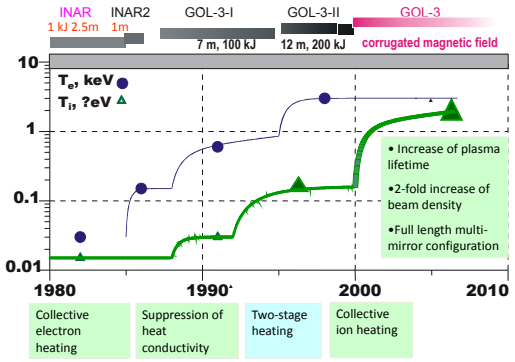

FIGURE 18. Historical trends of electron and ion temperatures in the GOL-3 facility.

ACKNOWLEDGMENTS

The work was supported in part by the Ministry of Education and Science of Russian Federation (project No. RFMEFI61914X0003). The study of the sub-mm emission from plasma was supported by RSCF under Project #14-12-00610.

REFERENCES

1. M. L. Andrews, H. Davitian, D.A. Hammer, H.H. Fleischmann, J.A. Nation, and N. Rostoker, Appl. Phys. Lett. **16**, 98-106 (1970).
2. M. Andrews, J. Bzura, H. H. Fleischmann, and N. Rostoker, Phys. Fluids **13**, 1322-1327 (1970).
3. D.A. Hammer and N. Rostoker, Phys. Fluids **13**, 1831-1850 (1970).
4. K.R. Chu and N. Rostoker, Phys. Fluids **16**, 1472-1479 (1973).
5. A.T. Altyntsev B.N. Breizman, A.G. Es'kov et al., "Collisionless relaxation of an ultrarelativistic electron beam in a plasma," in *Plasma Physics and Controlled Nuclear Fusion Research, Vol. 2* (IAEA, Vienna, 1971), pp. 309-316.
6. Yu.I. Abrashitov, V.S. Koidan, V.V. Konukhov et al., JETP **66**, 1324-1337 (1974).
7. A.V. Arzhannikov, A.V. Burdakov, V.S. Koidan et al., JETP Lett. **27**, 173-177 (1978).
8. A.V. Arzhannikov, A.V. Burdakov, V.S. Koidan et al., Phisica Scripta **T2/2**, 303-309 (1982).
9. V. Babicky, V. Bonachek, M. Clupek et al., "New results on REB-plasma heating in the REBEX machine," in Proceedings of the 8th International Conference on High-Power Particle Beams, edited by B.N. Breizman and B.N. Knyazev, (World Scientific Publishing, NY, 1991), V. 1, pp. 225-232.
10. I.V. Kandaurov, Eh.P. Krugluakov, M.V. Losev,"Study of HF plasma turbulence excited by REB," in Proceedings of the 8th International Conference on High-Power Particle Beams, edited by B.N. Breizman and B.N. Knyazev, (World Scientific Publishing, NY, 1991), V. 1, pp. 233-240.
11. R.Yu. Akentjev, A.V. Arzhannikov, V.T. Astrelin et al., Trans. Fusion Technol. **43**, 30-36 (2003).
12. Yu.I. Abrashitov, V.S. Koidan, V.V. Konukhov et al., JETP **39**, 647-651 (1974).
13. A.V. Arzhannikov and V.S. Koidan, "Dynamics of return current excited by relativistic electron beam in plasma," in Proceedings of the XII International Conference on Phenomena in Ionized Gases, (Eindhoven, 1975), p. 278-284.

14. A.V.Arzhannikov. “Macroscopic characteristics of the interaction of relativistic electron beam with plasma in magnetic field” (in Russian), Candidate thesis, Novosibirsk, USSR, 1980.
15. B.N. Breizman and D.D. Ryutov, JETP **33**, 220-225 (1971).
16. A.V. Arzhannikov, V.S. Koidan, and S.L. Sinitsky, “Deceleration and scattering of relativistic electrons at collective interaction of REB with plasma”, in Proceedings of the XVI International Conference on Phenomena in Ionized Gases, (Duesseldorf, 1983), p. 348-354.
17. A.V. Arzhannikov, A.V.Burdakov, V.S.Burmasov et al., “Heating of dense plasma by relativistic electron beam,” in Proceedings of the International Conference on Plasma Physics, (Nagoya, Japan, 1980), pp. 74-82.
18. B.N. Breizman,”Collective interaction of relativistic electron beams with plasmas,” in *Reviews of Plasma Physics*, edited by B.B. Kadomtsev (Consultants Bureau, New York, 1978), V. 15 (1978).
19. L.N. Vyacheslavov, V S. Burmasov, I.V. Kandaurov et al., Phys. Plasmas 2, 2224-2229 (1995).
20. A.V. Arzhannikov, A.V. Burdakov, V.A. Kapitonov et al., Plasma Phys. Contr. Fusion **30**, 1571-1583 (1988).
21. S.V. Lebedev, V.V. Chikunov and M.A. Shcheglov, Pis’ma v ZhTF **8**, p. 693-696 (1982) (in Russian).
22. A.V. Arzhannikov, V.S. Nikolaev, A.V. Smirnov et al., J. App. Phys. **72**, 1657-1659 (1992).
23. A.V. Arzhannikov, V.B. Bobylev, V.S. Nikolaev et al., “New results of the full scale ribbon beam experiments on U-2 device,“ in Proceedings of the 10th International Conference on High-Power Particle Beams, edited by R. White, (NTIS, Springfield, VA, 1994), pp. 136-140.
24. A.V. Arzhannikov, S.L. Sinitsky, and A.V. Tarasov, “First experimental observation of switching the microsecond electron beam by reconnection of the magnetic field lines,“ in Proceedings of the 10th International Conference on High-Power Particle Beams, edited R. White, (NTIS, Springfield, VA, 1994), pp. 315-316.
25. A.V. Arzhannikov, V.B. Bobylev, V.S. Nikolaev et al., "Ribbon REB research on 0.7MJ generator U-2, " in Proceedings of the 9th International Conference on High-Power Particle Beams, edited by D. Mosher and G. Cooperstein, (NTIS, Springfield, VA, 1992), Vol. II, pp. 1117-1124.
26. A.V. Burdakov, V.S. Koidan, K.I. Mekler et al., Plasma Phys. Reports **40**, 161-177 (2014).
27. V.T. Astrelin, A.V. Burdakov, V.S. Koidan et al., Trans. Fusion Technol. **35**, 223-227 (1999).
28. A.V. Arzhannikov, A.V. Burdakov, V.V. Chikunov et al., “GOL-3 programme,” in Proceedings of the 8th International Conference on High-Power Particle Beams, edited by B.N. Breizman and B.N. Knyazev, (World Scientific Publishing, NY, 1991), pp. 14-25.
29. A.V. Arzhannikov, V.T. Astrelin, A.V. Burdakov et al., Trans. Fusion Technol. **35**, 112-118 (1999).
30. A.V. Arzhannikov, M.A. Makarov, S.L. Sinitsky et al., Fusion Sci. and Technology **59**, 304-306 (2011).
31. S.S. Popov, L.N. Vyacheslavov, M.V. Ivantsivskiy et al., Fusion Sci. and Technology **59**, 292-294 (2011).
32. A.V. Burdakov, I.A. Kotelnikov, and V.I. Erofeev, Fusion Sci. and Technology **47**, 74-77 (2005).
33. A.V. Arzhannikov, A.V. Burdakov, S.A. Kuznetsov et al. Fusion Sci. and Technology **59**, 74-77 (2011).
34. V.S. Koidan, A.V. Arzhannikov, V.T. Astrelin et al., Fusion Sci. and Technology **47**, 35-42 (2005).
35. A.V. Arzhannikov, V.T. Astrelin, A.V. Burdakov et al., Plasma Phys. Reports **31**, 462-475 (2005).
36. G.I. Budker, V.V. Mirnov, and D.D. Ryutov. JETP Lett. **14**, 320-324 (1971).
37. B.G. Logan, A.G. Lichtenberg, M.A. Lieberman. Phys. Rev. Lett. **28**, 144-147, (1972).
38. A.D. Beklemishev, Fusion Sci. and Technology 51, 180-183 (2007).
39. A.V. Burdakov, A.V. Arzhannikov, V.T. Astrelin et al., Fusion Sci. and Technology 59, 9-16 (2011).
40. N.V. Sorokina, A.V. Burdakov, I.A. Ivanov et al., Plasma Phys. Reports **41**, 529-534 (2015).

Laser Wakefield Accelerated Electron Beam Monitoring and Control

J. K. Koga[1], M. Mori[1], H. Kotaki[1], S. V. Bulanov[1,2], T. Zh. Esirkepov[1], H. Kiriyama[1] and M. Kando[1]

[1]*Japan Atomic Energy Agency, Kizugawa, Kyoto 619-0215 Japan*
[2]*Prokhorov Institute of General Physics, Russian Academy of Sciences, ul. Vavilova 38, Moscow, 119991 Russia*

Abstract. We will discuss our participation in the ImPACT project, which has as one of its goals the development of an ultra-compact electron accelerator using lasers (< 1 GeV, < 10 m) and the generation of an x-ray beam from the accelerated electrons. Within this context we will discuss our investigation into electron beam monitoring and control. Since laser accelerated electrons will be used for x-ray beam generation combined with an undulator, we will present investigation into the possibilities of the improvement of electron beam emittance through cooling.

INTRODUCTION

Recent years have seen a large amount of activity in the applications of electron laser wakefield acceleration (LWFA) [1]. This is due to the extremely large electric fields available in plasmas and the resulting drastic reduction of acceleration distance. There has been a lot of interest in using LWFA electron beams for free-electron lasers (FELs) (for example see [2, 3, 4, 5]). Laser acceleration and x-ray FEL (XFEL) demonstration is one of the goals of the Ubiquitous Power Laser for Achieving a Safe, Secure and Longevity Society project within the larger Impulsive Paradigm Change through Disruptive Technologies (ImPACT) program [6]. The required parameters for the LWFA electrons is that they have energies above 1 GeV, a charge of over 10 pC, be stable, have relative energy spreads between 10^{-4} to 10^{-3}, and have a transverse emittance of less than 0.1 mm mrad. Electron beam energies of above 4 GeV [7] and total charge above 10 pC (see [8] and references cited therein) have already been achieved. The stability of the electron bunches in terms of energy has been steadily improving (see for example [9, 10]). However, the necessary small energy spread for conventional undulators has yet to be obtained. To overcome this difficulty transverse-gradient undulators (TGU) have been investigated as a possibility to achieve a compact XFEL with currently available energy spreads of LWFA electron beams [11, 3, 12, 13, 14]. In addition, using conventional accelerator technology phase space rotation of the bunch resulting in decompressed bunches with reduced energy spread [4] and chromatic focusing [5] have also been investigated. In this paper we present our considerations for reducing the energy spread of LWFA electron beams for injection into conventional undulators and electron bunch monitoring.

STAGED ACCELERATION

One method we are considering to achieve the necessary energy spread and transverse emittance is staged acceleration of LWFA electrons. In this scheme the electron beam is accelerated in three stages: (1) beam injector, (2) phase rotator, and (3) booster. The beam injector involves LWFA of electrons with a moderate power laser pulse to generate electron beams of the order of 30 to 40 MeV. These electron beams are then phase space rotated via conventional accelerator components or a wakefield so that their energy

spread is reduced. The phase space rotated electron beams are then further accelerated in a booster using LWFA with a high power laser to 1 GeV. The final electron beam is expected to have sufficiently low energy spread and transverse emittance to be injected into an undulator for lasing. Here we concentrate on the beam injector stage.

In order to control the beam energy we are considering injection due to a sharp density gradient [15, 16, 17]. Experimentally, this has been shown to obtain consistent beam energies [9, 10]. In order to investigate this injection mechanism we have performed 2D particle-in-cell (PIC) simulations using the REMP code [18]. The simulation box is $300\lambda_0$ and $240\lambda_0$ in the x (laser propagation direction) and y direction, respectively, where the grid size is $\Delta x = \lambda_0/16$ and $\Delta y = \lambda_0/8$. The simulation box moves at the speed of light c. Fig. 1 shows the density profile we have chosen for the simulation along the laser propagation direction where the laser pulse enters from the left. The density is normalized by the peak electron density n_e which is chosen to correspond to $\omega_{pe}/\omega_0 = 0.05$ where $\omega_{pe} = \sqrt{4\pi e^2 n_e / m_e}$ with e being the electron charge and m_e being the electron mass and ω_0 is the laser frequency. The density is uniform in the direction perpendicular to the laser propagation direction (y). In the propagation direction (x) there is an initial vacuum region up to $x_1 = 50\lambda_0$ at which the density starts from $n_1 = 0.1n_e$ and then increases to a peak of $n_2 = n_e$ at $x_2 = 175\lambda_0$ as $n(x) = n_1 + (n_2 - n_1)[3 - 2(x - x_1)/(x_2 - x_1)][(x - x_1)/(x_2 - x_1)]^2$. After the peak the density drops off linearly to $n_3 = 0.6n_e$ at $x_3 = 180\lambda_0$ over $\Delta x = 5\lambda_0$. Such a sharp density drop off has been shown to be possible due to the generation of a shock from the insertion of a razor blade into the supersonic gas jet emerging from a de Laval nozzle [9]. Finally, the density drops off to $n_4 = 0$ at $x_4 = 1780\lambda_0$ as $n(x) = n_3 + (n_4 - n_3)[3 - 2(x - x_3)/(x_4 - x_3)][(x - x_3)/(x_4 - x_3)]^2$. A maximum of 6 macro-particles per cell are loaded at the peak density.

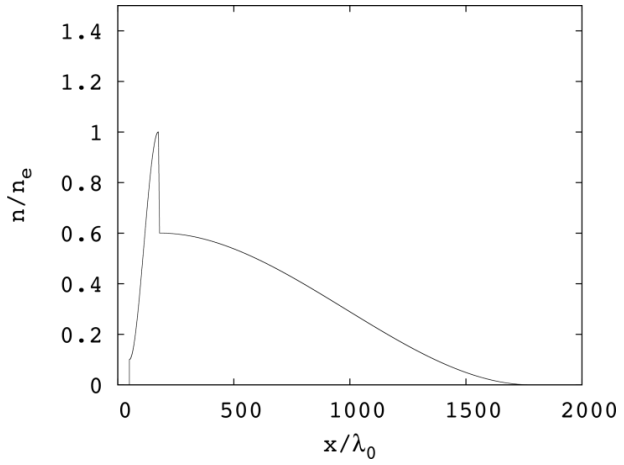

FIGURE 1. Density profile of the plasma which a sharp density gradient of thickness $5\lambda_0$ at $x = 175\lambda_0$ along the laser propagation direction with the laser entering from the left where the density is normalized by the peak plasma density n_e and the propagation distance is normalized by the laser wavelength λ_0.

The laser is injected initially from the left boundary of the simulation box. The pulse length is $12.5\lambda_0$ (FWHM) and has a spot size of $12.5\lambda_0$ (FWHM) at the focus point, which occurs at the beginning of the sharp density drop off at $175\lambda_0$, assuming Gaussian focusing. The normalized amplitude, $a_0 \equiv eE_0/m_e\omega_0 c$, where E_0 is the peak field amplitude, is taken to be 1.5. Fig. 2 shows the density of the plasma just after the laser pulse has passed the sharp density gradient at $x = 175\lambda_0$ where the laser is propagating from the left to the right. The density is normalized by n_e where darker colors are assigned to higher densities on a logarithmic scale as indicated by the color bar on the top right. In Fig. 3 we show the density profile of the electron bunch which is on the right side of the simulation box enclosed in the oval after it has exited the plasma. It can be seen that the electron bunch has a spatial duration of $\Delta x < 10\lambda_0$ and width of $\Delta y < 30\lambda_0$.

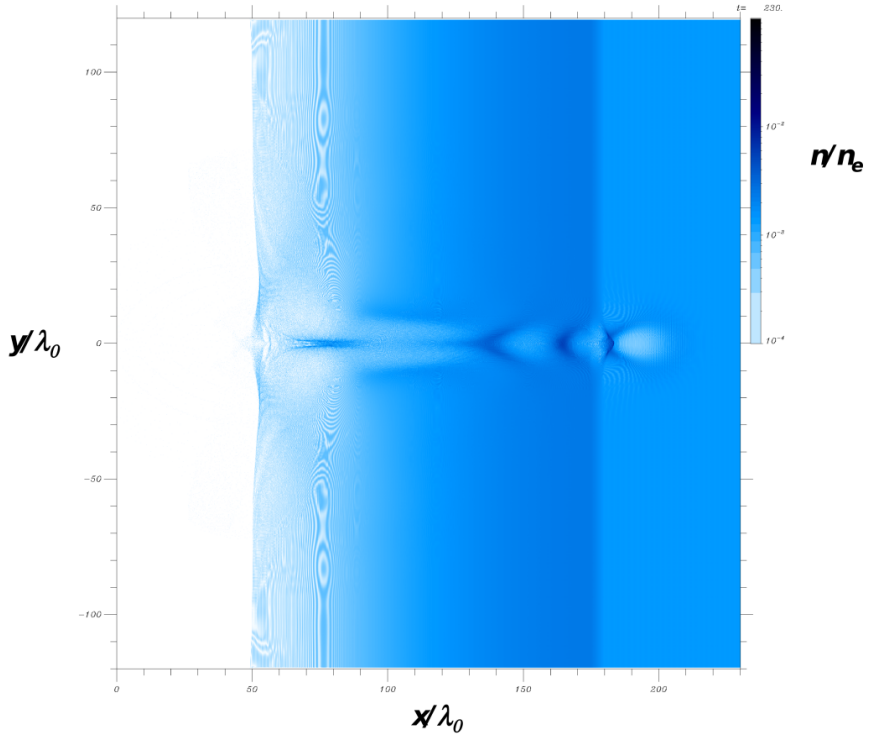

FIGURE 2. Density of the plasma just after the laser has passed the sharp density gradient at $x = 175\lambda_0$ along the laser propagation direction with the laser entering from the left where the density is normalized by the peak plasma density n_e and the x and y axes are normalized by the laser wavelength λ_0.

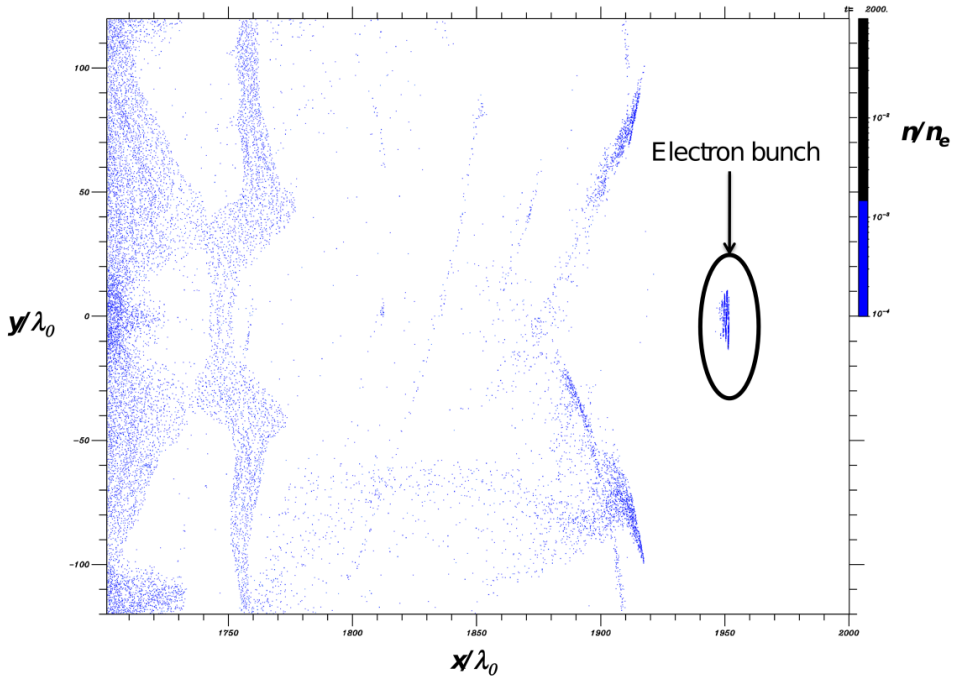

FIGURE 3. Density of the plasma after the laser has exited the plasma. On the right side of the simulation box enclosed in the oval the electron bunch can be seen where the density is normalized by the peak plasma density n_e and the x and y axes are normalized by the laser wavelength λ_0.

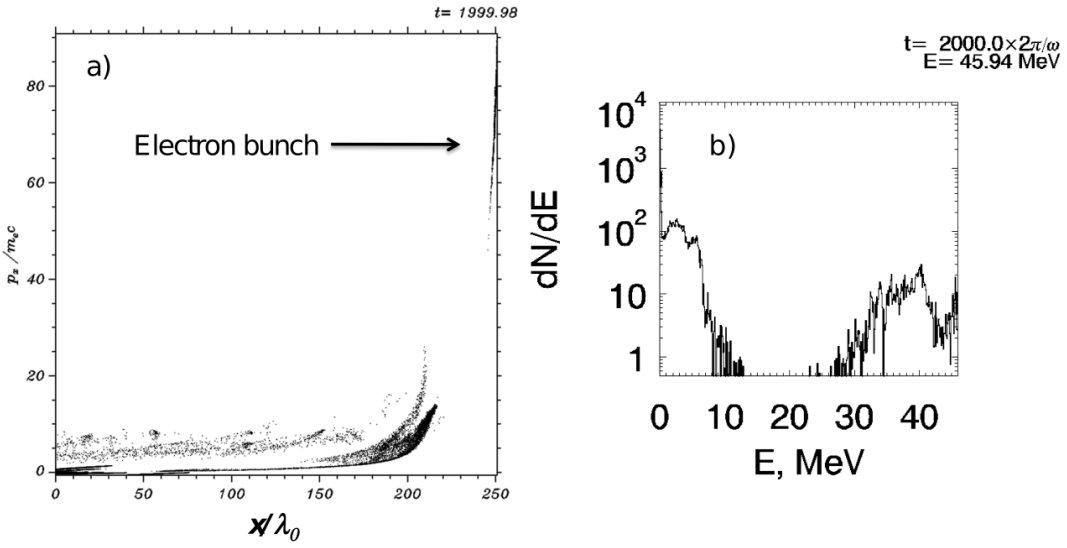

FIGURE 4. Electron phase space x-p_x a) and energy distribution b) after the laser has exited the plasma. On the right side of a) the electron bunch is indicated by the arrow where the x axis is normalized by the laser wavelength λ_0 and the momentum p_x is normalized by $m_e c$.

Figures 4 a) and b) show the electron phase space x-p_x and energy distribution, respectively. It can be seen from the phase space plot that the electron bunch has a spread in longitudinal momentum $\Delta p_x \sim 30 m_e c$.

From the energy distribution it can be seen that the bunch is quasi-monoenergetic with a peak at around 40 MeV. The peak energy is 45.94 MeV as indicated in the figure. Although the current energy distribution is quite broad, through further parameter surveys we expect to find electron bunches with smaller energy spread.

RADIATIVE BEAM COOLING

One way to achieve low emittance and small energy spread electron bunches is via radiative cooling where a strong laser pulse counter-propagates with the bunches [19, 20, 21, 22]. Since the total emitted energy of the electron scales as $(\gamma m_e c^2)^2$, higher energy electrons lose more energy than lower energy electrons [21]. However, because the electrons lose their energy by radiating discrete photons, this process affects the final energy spread of electrons [19, 20, 21, 22].

The minimum energy spread σ_γ and normalized emittance ε_n of the electron bunch are with certain assumptions given by [21]:

$$\left(\frac{\sigma_\gamma}{\lambda}\right)_{\min} \cong \sqrt{\frac{\alpha_{cr}\lambda_C\gamma}{\lambda_0}}, \tag{1}$$

$$\varepsilon_{n,\min} \cong \frac{\alpha_{cr}\gamma_\perp^2\beta^*\lambda_C}{2\lambda_0}, \tag{2}$$

where $\alpha_{cr} \simeq 1$ for $a_0^2 << 1$ and $\alpha_{cr} \simeq 3a_0/2$ for $a_0^2 >> 1$, $\lambda_C = h/mc$, $\gamma_\perp = \sqrt{1+a_0^2}$, and β^* is the beta-function of the beam. In [21] it was shown that for fast cooling times of L_R/c = 1ps where radiation damping length is $L_R \simeq 337\lambda_0^2(\mu m)/\, a_0^2\gamma_\perp$ with $\gamma_\perp = 400$, $\lambda_0 = 1$ μm, and $a_0 = 5.3$ that $(\sigma_\gamma/\gamma)_{\min} \simeq 0.09$ and $\varepsilon_{n,\min} \simeq 3$ mm mrad taking $\beta^* = 1$cm. These values are too large for a conventional XFEL. So it appears that fast radiative beam cooling is difficult without the suppression of the quantum fluctuations. The suppression of quantum fluctuations was shown to be possible by using a continuous focusing channel [23] or in an electron storage ring when the radiation formation length is comparable to the transverse oscillation wavelength [24]. One suggested medium for such a continuous focusing channel for channeling, acceleration and cooling is carbon nanotubes [25].

BEAM MONITORING

An important aspect of progress towards a compact XFEL is the monitoring of the electron beam which emerges from the LWFA. One such monitor is the betatron radiation emitted by the beam as it oscillates in the wakefield [26, 27].

In the case of the wiggler regime of electron motion, $K >> 1$ (see Eq. 5), the spectrum of the betatron radiation is expected to be that of synchrotron radiation from a relativistic charged particle in instantaneous circular motion [27]. The synchrotron spectrum is calculated from [28]:

$$\frac{1}{I}\frac{dI}{y} = \frac{9\sqrt{3}}{8\pi} y \int_0^\infty K_{5/3}(x)dx \tag{3}$$

where $y \equiv \omega/\omega_c$ with $\omega_c = (3/2)\,\gamma^3(c/\rho)$ being the critical frequency and $I \equiv 4\pi e^2\,\gamma^4/3\,\rho$.

The critical frequency can be expressed for $K >> 1$ as [27]:

$$\hbar\omega_c = \frac{3}{2}K\gamma^2\frac{hc}{\lambda_u}, \tag{4}$$

where the K-parameter and the transverse sinusoidal oscillation wavelength of an electron orbit in an ion cavity without acceleration are given by [27]:

$$K = 1.33\times10^{-10}\sqrt{\gamma n_e\left[cm^{-3}\right]}\, r_\beta\left[\mu m\right], \tag{5}$$

$$\lambda_u\left[\mu m\right] = 4.72\times10^{10}\sqrt{\gamma / n_e\left[cm^{-3}\right]}, \tag{6}$$

in which γ is the relativistic gamma of the electron, n_e is the electron plasma density, and r_β is the betatron oscillation amplitude.

Using γ = 2000 (1 GeV), electron plasma density of $n_e = 10^{17}\text{cm}^{-3}$, and r_β = 15 μm we get K = 28.2 >> 1, $\lambda_u \sim$ 0.7mm, and $\hbar\omega_c = 31.45$ keV. For these parameters it can be seen that the quantum corrections to the emissions are small around the critical frequency, $\hbar\omega_c / m_e c^2 << 1$ [29].

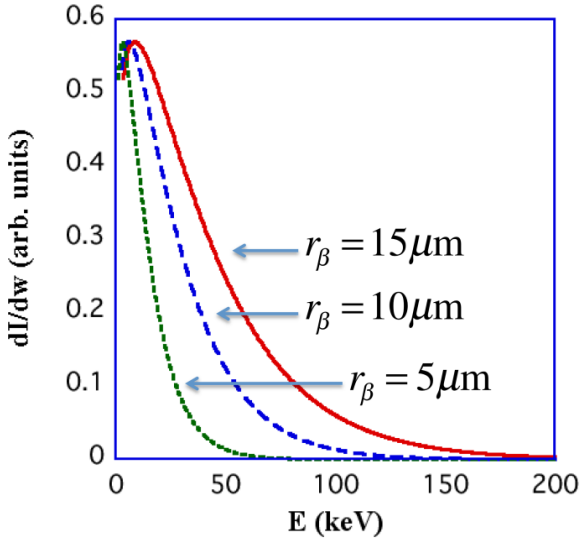

FIGURE 5. Photon spectra for different betatron oscillation amplitudes r_β.

In Fig. 5 we plot the spectra using these same parameters with the exception that r_β is varied between 5 μm to 15 μm using Eq. 3. We have integrated Eq. 3 using the Quadpack routine dqagi [30]. The modified Bessel function $K_{5/3}(x)$ was calculated using the Netlib routine rkbesl [31]. The spectrum is seen to range between 0 and 200 keV. As expected from Eq. 5 K and, as a result, $\hbar\omega_c$ linearly depend on r_β.

Due the dependence of the spectra on electron plasma density, electron energy, and betatron oscillation amplitude this measurement needs to be coupled with other measurements of the laser-plasma interaction such as an electron energy spectrograph, frequency domain interferometry [32, 33, 34, 35], and frequency domain holography[36]. Such simultaneous measurements have been previously used to measure the normalized transverse electron beam emittance from a LWFA where the x-ray emission was used to measure the electron transverse bunch size [37].

CONCLUSIONS

In this paper we have presented our considerations on achieving a compact XFEL from LWFA electrons. Specifically, we have considered how to reduce the energy spread of LWFA electrons via staging and radiative cooling. In regards to the staging we have concentrated on the first stage involving injection of electrons into the wakefield behind the laser pulse via a sharp density gradient. Via 2D PIC simulations we have obtained a quasi-monoenergetic electron bunch with a peak of around 40 MeV. This energy is sufficient for our current considerations for the injection stage, although further parameter survey will be necessary to reduce the quite broad energy distribution. We have examined the possibility of fast radiative cooling of the electron bunch, however, rapid cooling appears to be difficult due to quantum fluctuations. Suppression of the quantum fluctuations could be possible using special materials such as carbon nanotubes

[25]. Finally, we investigated the possibility of monitoring the accelerated beams through measurement of the betatron radiation. We have found that simultaneous measurements of the beam energy and electron plasma density will be necessary in order to get the beam properties. Achieving a compact XFEL from LWFA electrons is challenging, however, its achievement would allow investigation at small facilities in a wide range of fields.

ACKNOWLEDGMENTS

J. K. K. dedicates this paper to Norman Rostoker and wishes to thank Y. Hayashi, T. Tajima, X. Zhang, and C. Lau for fruitful discussions. This research was funded by ImPACT Program of Council for Science, Technology and Innovation (Cabinet Office, Government of Japan)

REFERENCES

1. T. Tajima and J. M. Dawson, Phys. Rev. Lett. **43**, 267 (1979).
2. K. Nakajima, Nat. Phys. **4**, 92 (2008).
3. Z. Huang, Y. Ding, and C. B. Schroeder, Phys. Rev. Lett. **109**, 204801 (2012).
4. A. R. Maier, A. Meseck, S. Reiche, C. B. Schroeder, T. Seggebrock, and F. Grüner, Phys. Rev. X **2**, 031019 (2012).
5. A. Loulergue, M. Labat, C. Evain, C. Benabderrahmane, V. Malka, and M. E. Couprie, New Journal of Physics **17**, 023028 (2015).
6. http://www.jst.go.jp/impact/en/program03.html.
7. W. P. Leemans, A. J. Gonsalves, H.-S. Mao, K. Nakamura, C. Benedetti, C. B. Schroeder, C. Tóth, J. Daniels, D. E. Mittelberger, S. S. Bulanov, J.-L. Vay, C. G. R. Geddes, and E. Esarey, Phys. Rev. Lett. **113**, 245002 (2014).
8. E. Esarey, C. B. Schroeder, and W. P. Leemans, Rev. Mod. Phys. **81**, 1229 (2009).
9. K. Schmid, A. Buck, C. M. S. Sears, J. M. Mikhailova, R. Tautz, D. Herrmann, M. Geissler, F. Krausz, and L. Veisz, Phys. Rev. ST Accel. Beams **13**, 091301 (2010).
10. A. Buck, J. Wenz, J. Xu, K. Khrennikov, K. Schmid, M. Heigoldt, J. M. Mikhailova, M. Geissler, B. Shen, F. Krausz, S. Karsch, and L. Veisz, Phys. Rev. Lett. **110**, 185006 (2013).
11. T. I. Smith, J. M. J. Madey, L. R. Elias, and D. A. G. Deacon, Journal of Applied Physics 50, 4580 (1979).
12. T. Zhang, C. Feng, H. Deng, D. Wang, Z. Dai, and Z. Zhao, Opt. Express **22**, 13880 (2014).
13. H. Deng and C. Feng, Phys. Rev. Lett. **111**, 084801 (2013).
14. P. Baxevanis, Z. Huang, R. Ruth, and C. B. Schroeder, Phys. Rev. ST Accel. Beams **18**, 010701 (2015).
15. S. Bulanov, N. Naumova, F. Pegoraro, and J. Sakai, Phys. Rev. E **58**, R5257 (1998).
16. P. Tomassini, M. Galimberti, A. Giulietti, D. Giulietti, L. A. Gizzi, L. Labate, and F. Pegoraro, Phys. Rev. ST Accel. Beams **6**, 121301 (2003).
17. A. V. Brantov, T. Z. Esirkepov, M. Kando, H. Kotaki, V. Y. Bychenkov, and S. V. Bulanov, Physics of Plasmas **15**, 073111 (2008).
18. T. Esirkepov, Computer Physics Communications **135**, 144 (2001).
19. V. Telnov, Phys. Rev. Lett. **78**, 4757 (1997).
20. V. Telnov, Phys. Rev. Lett. **80**, 2747 (1998).
21. E. Esarey, Nuclear Instruments and Methods in Physics Research Section A: Accelerators, Spectrometers, Detectors and Associated Equipment **455**, 7 (2000).
22. K. Yokoya, Nuclear Instruments and Methods in Physics Research Section A: Accelerators, Spectrometers, Detectors and Associated Equipment **455**, 25 (2000).
23. Z. Huang, P. Chen, and R. D. Ruth, Phys. Rev. Lett. **74**, 1759 (1995).
24. Z. Huang and R. D. Ruth, Phys. Rev. Lett. **80**, 2318 (1998).
25. Y. M. Shin, A. H. Lumpkin, and R. M. Thurman-Keup, Nuclear Instruments and Methods in Physics Research Section B: Beam Interactions with Materials and Atoms **355**, 94 (2015).
26. E. Esarey, B. A. Shadwick, P. Catravas, and W. P. Leemans, Phys. Rev. E **65**, 056505 (2002).

27. S. Corde, K. Ta Phuoc, G. Lambert, R. Fitour, V. Malka, A. Rousse, A. Beck, and E. Lefebvre, Rev. Mod. Phys. **85**, 1 (2013).
28. J. D. Jackson, Classical electrodynamics, 3rd ed. (Wiley, New York, 1999).
29. J. Schwinger, Proceedings of the National Academy of Sciences of the United States of America **40**, 132 (1954).
30. http://www.netlib.org/quadpack/.
31. http://www.netlib.org/specfun/rkbesl.
32. E. Tokunaga, T. Kobayashi, and A. Terasaki, Opt. Lett. **17**, 1131 (1992).
33. C. W. Siders, S. P. Le Blanc, D. Fisher, T. Tajima, M. C. Downer, A. Babine, A. Stepanov, and A. Sergeev, Phys. Rev. Lett. **76**, 3570 (1996).
34. J. R. Marquès, F. Dorchies, P. Audebert, J. P. Geindre, F. Amiranoff, J. C. Gauthier, G. Hammoniaux, A. Antonetti, P. Chessa, P. Mora, and T. M. Antonsen, Jr., Phys. Rev. Lett. **78**, 3463 (1997).
35. H. Kotaki, M. Kando, T. Oketa, S. Masuda, J. K. Koga, S. Kondo, S. Kanazawa, T. Yokoyama, T. Matoba, and K. Nakajima, Physics of Plasmas **9**, 1392 (2002).
36. N. H. Matlis, S. Reed, S. S. Bulanov, V. Chvykov, G. Kalintchenko, T. Matsuoka, P. Rousseau, V. Yanovsky, A. Maksimchuk, S. Kalmykov, G. Shvets, and M. C. Downer, Nat. Phys. **2**, 749 (2006).
37. S. Kneip, C. McGuffey, J. L. Martins, M. S. Bloom, V. Chvykov, F. Dollar, R. Fonseca, S. Jolly, G. Kalintchenko, K. Krushelnick, A. Maksimchuk, S. P. D. Mangles, Z. Najmudin, C. A. J. Palmer, K. T. Phuoc, W. Schumaker, L. O. Silva, J. Vieira, V. Yanovsky, and A. G. R. Thomas, Phys. Rev. ST Accel. Beams **15**, 021302 (2012).

Particle Rings and Astrophysical Accretion Discs

R. V. E. Lovelace[1,a)] and M. M. Romanova[1]

[1]*Department of Astronomy, Cornell University, Ithaca, NY 14850.*

[a)]Corresponding author: RVL1@cornell.edu
[b)]romanova@astro.cornell.edu

Abstract. Norman Rostoker had a wide range of interests and significant impact on the plasma physics research at Cornell during the time he was a Cornell professor. His interests ranged from the theory of energetic electron and ion beams and strong particle rings to the related topics of astrophysical accretion discs. We outline some of the topics related to rings and discs including the Rossby wave instability which leads to formation of anticyclonic vortices in astrophysical discs. These vorticies are regions of high pressure and act to trap dust particles which in turn may facilitate planetesimals growth in proto-planetary disks and could be important for planet formation. Analytical methods and global 3D magneto-hydrodynamic simulations have led to rapid advances in our understanding of discs in recent years.

INTRODUCTION

Norman Rostoker was the IBM Professor of Engineering at Cornell University from 1967 to 1972. During this time he energized the Cornell plasma physics research which was distributed amongst several departments. Also during this time one of the authors (RL) was a post-doc working in the Laboratory of Plasma Physics at Cornell. Rostoker was highly interactive and influential during weekly meetings with all of the plasma people at Cornell. At that time there was active theoretical and experimental work on particle beams, relativistic electron beams, ion beams, and field-reversing electron rings [1]. Rostoker was knowledgeable and interested in everything going on at Cornell. He was also well-known for his generosity in suggesting interesting ideas for research. An example of this was his suggestion to RL to work on "magnetic insulations". The simplest example of magnetic insulation is the case of a high voltage planar diode with the cathode/anode gap is initially filled with a transverse magnetic field B_y^0. An exact relativistic, self-consistent equilibrium was found in [2] for the electron sheath which is predicted to form under the condition where the applied magnetic field is sufficiently strong to prevent electrons from flowing between the electrodes [2]. The condition for magnetic insulation was found to be $(eB_y^0 d/mc^2)^2 > 2|eV_0/mc^2| + (eV_0/mc^2)^2$. where V_0 is the voltage across the diode, d is the cathode/anode separation in the $x-$direction, and $-e$ and m are the electron charge and mass. Magnetically insulated transmission lines have proven useful for transporting energy stored in capacitor banks to a central Z-pinch chamber [e.g., 3].

Important questions discussed with Rostoker at Cornell included the stability of electron and ion beams as well as the stability of field-reversing electron and ion rings. Stability of the rings is important for their stability as magnetic traps for holding high temperature plasmas [4]. The rings have the characteristic that the azimuthal velocity of the particles is larger than the thermal velocities. A similar inequality holds for astrophysical discs where the centrifugal force approximately balances the gravitational attraction of a central star or black hole. The stability issues for the laboratory rings are similar to those for astrophysical discs. The next section of this paper discusses some aspects of the ring and disc stability. This is followed by a review of some phenomena exhibited by magnetized astrophysical discs.

STABILITY OF RINGS AND DISCS

The stability of field-reversing rings of energetic particles is important for the use of the rings for plasma confinement [4]. Of particular importance is the stability of the rings to macro or low mode number perturbations such as the tilt

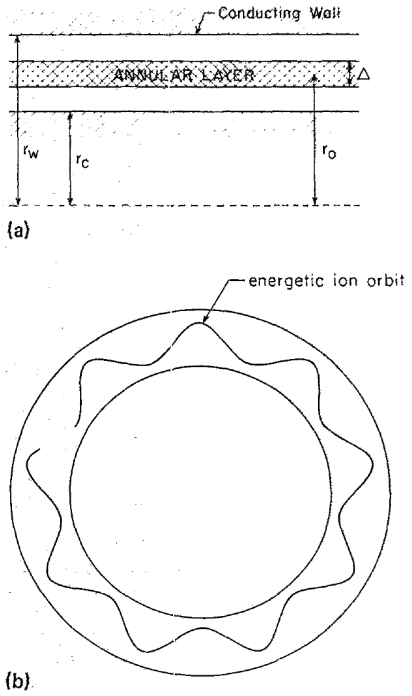

FIGURE 1. (a) Annular equilibrium of energetic ions of mean radius r_0 and thickness Δ bounded by conducting walls at radii r_c and r_w. (b) Cross-section of annulus with a sample orbit of an ion. Figure adapted from [5].

of the ring or the radial shift of the ring's center (the precession mode) and the kink mode. One of the authors (RL) had the good fortune of having a sabbatical at the University of Texas at Austin where he worked with Profs. Rostoker and Berk and with Dr. Wong on the kink stability of long ion layers [5] as sketched in Figure 1. This work generalized some of the earlier work on ring stability [6].

A variety of instabilities are known to occur in astrophysical discs with or without the presence of a magnetic field. An important instability is the Magneto-Rotational-Instability (MRI) which occurs in the presence of a weak magnetic field [7]. The differential rotation of the disc acts to amplify the magnetic field. This growth leads to small-scale turbulence in the disc which gives a turbulent viscosity and magnetic diffusivity [7]. The viscosity is important for the outward transport of angular momentum in the disc. There are other instabilities which can be important under different conditions. Here, we discuss the recently discovered Rossby wave instability (RWI) in astrophysical discs. In non-self-gravitating discs, around for example a newly forming stars, the instability can be triggered by an axisymmetric bump at some radius r_0 in the disc surface mass-density. It gives rise to exponentially growing non-axisymmetric perturbation [$\propto \exp(im\phi)$, $m = 1, 2..$] in the vicinity of r_0 consisting of *anticyclonic* vortices. These vortices are regions of high pressure and consequently act to trap dust particles which in turn can facilitate planetesimal growth in proto-planetary discs. The Rossby vortices in the discs around stars and black holes may cause the observed quasi-periodic modulations of the disc's thermal emission.

The theory of the Rossby wave instability (RWI) in accretion discs was developed by [8] and [9] for thin Keplerian discs with negligible self-gravity and earlier by [10] for thin disc galaxies where the self-gravity may or may not be important and where the rotation is in general non-Keplerian. In the first case the instability can occur if there is an axisymmetric bump (as a function of radius) in the inverse potential vorticity

$$\mathcal{L}(r) = \frac{\Sigma\, S^{2/\gamma}}{2(\nabla \times \mathbf{u}) \cdot \hat{\mathbf{z}}}\,, \tag{1}$$

at some radius r_0, where Σ is the surface mass density of the disc, $\mathbf{u} \approx r\Omega(r)\hat{\phi}$ is the flow velocity of the disc, $\Omega(r) \approx (GM_*/r^3)^{1/2}$ is the angular velocity of the flow (with M_* the mass of the central star), S is the specific entropy

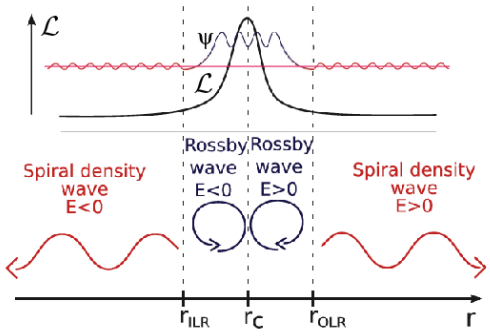

FIGURE 2. Schematic view of the Rossby wave instability with the two propagating regions for the Rossby waves, and in between the evanescent regions close to the inner and outer Lindblad resonant radii, ($r_{\rm ILR}$ and $r_{\rm OLR}$), respectively, adapted from [10]. The radii of these Lindblad resonances are given by the equations $\omega = m\Omega(r_{\rm LR}) \pm \kappa(r_{\rm LR})$, where $\kappa(r)$ is the radial epicyclic frequency which approximately equal to $\Omega(r)$ for a Keplerian disc. The corotation radius $r_{\rm C}$ is the radius where $\omega = m\Omega(r_{\rm C})$.

of the gas, and γ is the specific heat ratio. The approximations involve the neglect of the relatively small radial pressure force. Note that $\mathcal{L}$ is related to the inverse of the *vortensity* which is defined as $(\nabla \times \mathbf{u})_z/\Sigma$. A sketch of a bump in $\mathcal{L}(r)$ is shown in Figure 2.

Rossby waves are important in planetary atmospheres and oceans and are also known as *planetary waves* (see [11] - [13]). These waves have a significant role in the transport of heat from equatorial to polar regions of the Earth. They may have a role in the formation of the long-lived (> 300 yr) Great Red Spot on Jupiter which is an anticyclonic vortex (e.g., [14]). The Rossby waves have the notable property of having the phase velocity opposite to the direction of motion of the atmosphere or disc in the comoving frame of the fluid ([11], [12]).

Linearization of the Euler and continuity equations for a thin fluid disc with perturbations proportional to $f(r)\exp(im\phi - i\omega t)$ (with azimuthal mode number $m = 1, 2, ..$ and angular frequency ω) leads to a Schrödinger-like equation for the enthalpy perturbation $\psi = \delta p/\rho$,

$$\frac{d^2\psi}{dr^2} = V_{\rm eff}(r)\,\psi\ . \tag{2}$$

The effective potential well $V_{\rm eff}(r)$ is closely related to $\mathcal{L}(r)$: If the height of the bump in $\mathcal{L}(r)$ is too small, the potential well is shallow and there are no 'bound Rossby wave states' in the well. On the other hand for a sufficiently large bump in $\mathcal{L}(r)$ the potential $V_{\rm eff}$ is sufficiently deep to have a bound state. The condition for there to be just one bound state allows one to solve for the imaginary part of the wave frequency, $\omega_i = \Im(\omega)$ which is the growth rate of the instability [8]. For moderate strength bumps (with fractional amplitudes $\Delta\Sigma/\Sigma \lesssim 0.2$), the growth rates are of the order of $\omega_i = (0.1 - 0.2)\Omega(r_0)$. The real part of the wave frequency, $\omega_r = \Re(\omega)$, is approxiamtely $m\Omega(r_0)$.

A more complete analysis ([16] - [18]) reveals that the Rossby wave is not completely trapped in the potential well $V_{\rm eff}$, but leaks outward across a forbidden region at an outer Lindblad resonance (at $r_{\rm OLR}$ indicated in Figure 3) and inward across another forbidden region at an inner Lindblad resonance (at $r_{\rm ILR}$). Once the waves cross the forbidden regions they propagate as spiral density waves. The full expression for the effective potential for a thin *homentropic* (S = const) disc is

$$V_{\rm eff} = \frac{2m\Omega}{r(\Delta\omega)}\frac{d}{dr}\left[\ln\left(\frac{\Omega\Sigma}{\kappa^2 - (\Delta\omega)^2}\right)\right] + \frac{m^2}{r^2} + \frac{\kappa^2 - (\Delta\omega)^2}{c_s^2}\ , \tag{3}$$

where $\Delta\omega \equiv \omega - m\Omega$ is the Doppler shifted wave frequency in the reference frame moving with the disc matter, c_s is the sound speed in the disc, and κ is the radial epicyclic angular frequency, with $\kappa^2 = r^{-3}d\ell^2/dr$ and $\ell = ru_\phi$ the specific angular momentum. Figure 3 shows the effective potential for sample cases. Note that the inward propagating waves with $\omega_r < m\Omega(r)$ have negative energy ($E < 0$) whereas the outward propagating waves with $\omega_r > m\Omega(r)$ have positive energy ($E > 0$) [10].

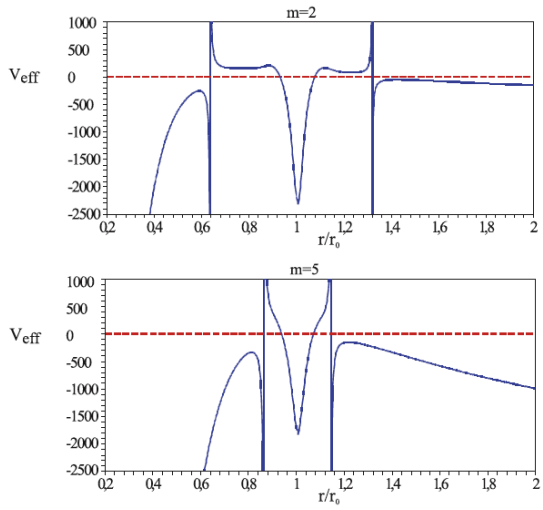

FIGURE 3. Effective potential for a Gaussian surface density bump of peak amplitude $\Delta\Sigma/\Sigma = 0.2$ and width $\Delta r/r = 0.05$ for $m = 2$ (upper panel) and $m = 5$ (lower panel) adapted from [18]. Waves can propagate only in the regions where $V_{\rm eff}(r) < 0$. The large positive values of $V_{\rm eff}$ occur at the inner and outer Lindblad resonance radii.

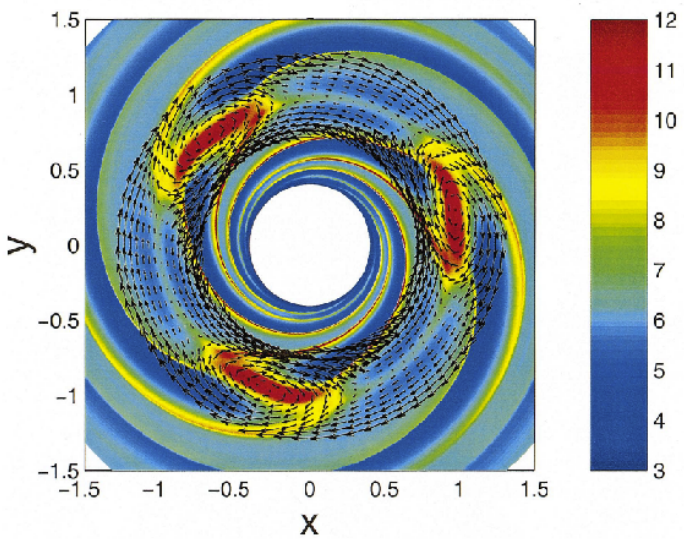

FIGURE 4. Hydrodynamic simulations of Rossby vortices in a disk adapted from [22] for an $m = 3$ initial perturbation. Pressure is color-coded (in units of $10^{-3}\,p_0$). Arrows indicate the flow pattern near r_0 in a comoving frame moving with velocity $u_\phi(r_0)$. The vortices are *anticyclonic*, enclosing high-pressure regions. Large-scale spiral waves are produced at large and small radii.

The Rossby wave instability occurs because of the local wave trapping in a disc. It is related to the Papaloizou and Pringle ([20], [21]) instability where the wave is trapped between the inner and outer radii of a disc or torus.

More information on the Rossby wave instability in astrophysical discs can be found in [22]. Figure 4 shows the surface density of a disc resulting from the growth and saturation of the $m = 3$ Rossby wave instability [22].

JETS FROM ACCRETION DISCS

A surprising aspect of observed astrophysical accretion discs is that they often show the presence of collimated jets of high velocity matter moving perpendicular to the disc's surfaces. Most of the matter of the discs is slowly spiraling into the central star or black hole. The power of the disc emission and the power driving the jet is from the gravitational infall of matter in the disc. Professor Rostoker was intrigued by this problem. It is now accepted that the jets from accretion discs arise from the presence of an ordered magnetic field ([23], [24]). Outflows in the form of jets and winds are observed from many disc accreting objects ranging from young stars to systems with white dwarfs, neutron stars, and black holes. A large body of observations exists for outflows from young stars at different stages of their evolution, ranging from protostars, where powerful collimated outflows - jets - are observed, to classical T Tauri stars (CTTSs) where the outflows are weaker and often less collimated (see review by Ray [25]). Correlation between the disc's radiated power and the jet power has been found in many CTTSs ([26], [27]). A significant number of CTTSs show signs of outflows in spectral lines, in particular in He I where two distinct components of outflows had been found ([28], [29], & [30]). Outflows are also observed from accreting compact stars such as accreting white dwarfs in symbiotic binaries [31], or from the vicinity of neutron stars, such as from Circinus X-1 ([32]).

Different theoretical models have been proposed to explain the outflows from protostars and CTTSs (see review by [33]). The commonly favored model for the origin of protostellar jets and outflows are the radially distributed *magneto-centrifugal disc winds* which originate from discs threaded by a poloidal magnetic field ([34], [35]). MHD simulations disc winds were pioneered by ([36], [37]) who used a Lax-Wendroff method to solve the axisymmetric MHD equations for a sub-Keplerian disc initially threaded by a vertical magnetic field. Subsequently, a large number of MHD simulation studies of the disc winds have been carried out with different codes and different assumptions (e.g., [38], [39] - [43], [33], [44]-[46]).

A less favored model for the origin of protostellar jets discussed in this review is one where the jets originate from the innermost region of the accretion disc [24] or the disc/magnetosphere boundary. This model is related to the *X-wind model* ([47] - [50]) where the outflow originates from the vicinity of the disc-magnetosphere boundary. Progress in understanding the theoretical models has come from MHD simulations of accretion discs around rotating magnetized stars as discussed below. Laboratory experiments are also providing insights into jet formation processes ([51]; [52]) but these are not discussed here.

Outflows or jets from the disc-magnetosphere boundary were found in early axisymmetric MHD simulations by [53] and [54]. A one-time episode of outflows from the inner disc and inflation of the innermost field lines connecting the star and the disc were observed for a few dynamical time-scales. Somewhat longer simulation runs were performed by [55] - [59], where several episodes of field inflation and outflows were observed. These simulations hinted at a possible long-term nature for the outflows. However, the simulations were not sufficiently long to establish the behavior of the outflows. MHD simulations showing long-lasting (thousand of orbits of the inner disc) outflows from the disc-magnetosphere boundary have been obtained by our group ([60], [61]) and independently by [62].. We obtained these outflows/jets in two main cases: (1) where the star rotates slowly but the field lines are bunched up into an X-type configuration, and (2) where the star rotates rapidly, in the "propeller regime" ([63], [64], & [65]). Field bunching occurs for conditions where the viscosity is larger than the magnetic diffusivity. Figure 5 shows sketches of the equatorial angular rotation rate $\Omega(r, z = 0)$ of the plasma in the two cases. Here, r_* is the radius of the star; $r_{\rm m}$ is the magnetospheric radius where the kinetic energy density of the disc matter is about equal to the energy density of the magnetic field; and $r_{\rm cr} = (GM/\Omega_*^2)^{1/3}$ is the co-rotation radius where the angular rotation rate of the star Ω_* equals that of the Keplerian disc $\Omega_K = (GM/r^3)^{1/2}$. For a slowly rotating star $r_{\rm m} < r_{\rm cr}$ whereas for a rapidly rotating star in the propeller regime $r_{\rm m} > r_{\rm cr}$.

Figure 6 shows examples of the outflows in the two cases. In both cases, two-component outflows are observed: One component originates at the inner edge of the disc near $r_{\rm m}$ and has a narrow-shell conical shape close to the disc and therefore is termed a "conical wind". It is matter dominated but can become collimated at large distances due to its toroidal magnetic field. The other component is a magnetically dominated high-velocity "axial jet" which flows along the open stellar magnetic field lines. The axial jet may be very strong in the propeller regime. A full discussion of the simulations and analysis can be found in [60] and [61].

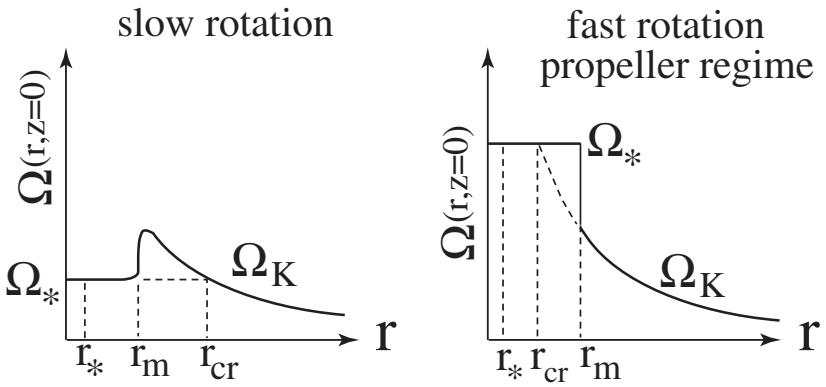

FIGURE 5. Slowly/rapidly rotating stars. Schematic profiles of the midplane angular velocity of the plasma for the case of a slowly rotating star (left-hand panel) and a rapidly rotating star (right-hand panel) which is in the propeller regime. Here, Ω_* is the angular rotation rate of the star, Ω_K is the Keplerian rotation rate of the disc, r_* is the star's radius, $r_{\rm m}$ is the radius of the magnetosphere, and $r_{\rm cr}$ is the corotation radius.

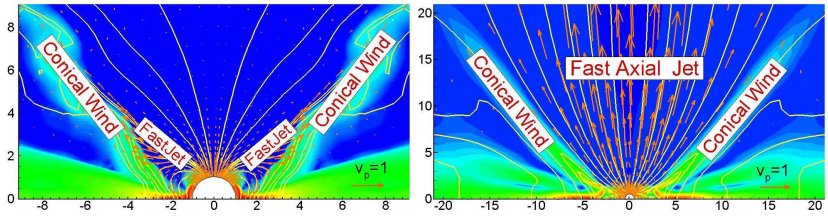

FIGURE 6. Two-component outflows observed in slowly (left) and rapidly (right) rotating magnetized stars. The background shows the poloidal matter flux $\mathbf{F}_m = \rho \mathbf{v}_p$, the arrows are the poloidal velocity vectors, and the lines are sample magnetic field lines. The labels point to the main outflow components. In the left-hand panel $\alpha_\nu = 0.3$ and $\alpha_\eta = 0.1$ while in the right-hand panel $\alpha_\nu = 0.1 = \alpha_\eta$.

The simulation codes used by our US/Russia group have been extensively tested and refined in many respects over the past fifteen years. The tests include the different well-known shock problems described for example by Mignone et al. [66] in regard to the testing of the PLUTO code as well as the magnetic rotor tests described by Romanova et al. [60]. More importantly, our group has pioneered the detailed comparison of MHD simulation results of Ustyugova et al. [41] with the analytic theory of stationary axisymmetric MHD flows [67]. Furthermore, detailed analysis of the simulations have been made to evaluate the different forces acting to drive outflows and jets [61]. A major effort by our group has been to implement physically consistent boundary conditions at the outer boundaries of the simulation regions. We were the first to point out the necessity of having the fast-magnetosonic Mach cone of an outflow pointing outwards from the simulation region [41]. A number of published MHD simulations of jets in long axial cylindrical regions violate this requirement and are therefore unphysical.

The next subsection describes the simulations. This is followed by a discussion of the conical winds and axial jets, the driving and collimation forces, and the variability of the winds and jets. The final subsection discusses lopsided jets.

MHD Simulations

We simulate the outflows resulting from disc-magnetosphere interaction by solving the equations of axisymmetric MHD on grids using a Godunov type method. Outside of the disc the flow is described by the equations of ideal MHD. Inside the disc the flow is described by the equations of viscous, resistive MHD. In an inertial reference frame

the equations are:

$$\frac{\partial \rho}{\partial t} + \nabla \cdot (\rho \mathbf{v}) = 0 \,, \tag{4}$$

$$\frac{\partial (\rho \mathbf{v})}{\partial t} + \nabla \cdot \mathcal{T} = \rho \, \mathbf{g} \,, \tag{5}$$

$$\frac{\partial \mathbf{B}}{\partial t} - \nabla \times (\mathbf{v} \times \mathbf{B}) + \nabla \times (\eta_t \nabla \times \mathbf{B}) = 0 \,, \tag{6}$$

$$\frac{\partial (\rho S)}{\partial t} + \nabla \cdot (\rho S \, \mathbf{v}) = Q \,. \tag{7}$$

Here, ρ is the density, S is the specific entropy, $\mathbf{v}$ is the flow velocity, $\mathbf{B}$ is the magnetic field, η_t is the magnetic diffusivity, $\mathcal{T}$ is the momentum flux-density tensor, Q is the rate of change of entropy per unit volume, and $\mathbf{g} = -(GM/r^2)\hat{\mathbf{r}}$ is the gravitational acceleration due to the star which has mass M. In the simulations reviewed here it is assumed that the viscous plus Ohmic heating is balanced by radiative cooling so that $Q = 0$. Most of the volume of the simulated flows does not have shocks and there is no shock heating; however, at the surface of the star where the funnel flows impact the star's surface there are strong shocks and the shock heating is included [68]. The total mass of the disc is assumed to be negligible compared to M. Here, $\mathcal{T}$ is the sum of the ideal plasma terms *and* the $\alpha-$viscosity terms discussed in the next paragraph. The plasma is considered to be an ideal gas with adiabatic index $\gamma = 5/3$, and $S = \ln(p/\rho^\gamma)$. We use spherical coordinates (r, θ, ϕ) with θ measured from the symmetry axis. The equations in spherical coordinates are given in [69].

Both the viscosity and the magnetic diffusivity of the disc plasma are considered to be due to turbulent fluctuations of the velocity and the magnetic field. Both effects are non-zero only inside the disc as determined by a density threshold. The microscopic transport coefficients are replaced by turbulent coefficients. The values of these coefficients are assumed to be given by the α-model of Shakura and Sunyaev [70], where the coefficient of the turbulent kinematic viscosity is $\nu_t = \alpha_\nu c_s^2/\Omega_K$, where c_s is the isothermal sound speed and $\Omega_K(r)$ is the Keplerian angular velocity. We take into account the viscous stress terms $\mathcal{T}_{r\phi}^{\rm vis}$ and $\mathcal{T}_{\theta\phi}^{\rm vis}$ (Lii et al. [61]). Similarly, the coefficient of the turbulent magnetic diffusivity $\eta_t = \alpha_\eta c_s^2/\Omega_K$. Here, α_ν and α_η are dimensionless coefficients which are treated as parameters of the model. The inward advection of matter and large-scale magnetic field in accretion discs with different $(\alpha_\nu,\ \alpha_\eta)$ values has been studied by Dyda et al. [71]. Note that shearing box simulations by Guan and Gammie [72] suggest that $\alpha_\nu \sim \alpha_\eta$. In the simulation studies of our group we have studied cases with $(\alpha_\nu,\ \alpha_\eta)$ in the ranges $0.03 - 0.3$. For these values the viscosity and diffusivity are much larger than the numerical values due to the finite grids.

The MHD equations are solved in dimensionless form so that the results can be readily applied to different accreting stars. Table 1 gives typical parameters for some of the different types of stars.. Equations (4-7) have been integrated numerically in spherical (r, θ, ϕ) coordinates using a Godunov-type numerical scheme. The flux densities of the different quantities are calculated using an eight-wave Roe-type approximate Riemann solver analogous to one described by Powell et al. [73]. The calculations were done in the region $R_{\rm in} \le r \le R_{\rm out}$, $0 \le \theta \le \pi/2$. Matter flowing into the star is absorbed. The grid is uniform in the θ-direction with N_θ cells. The N_r cells in the radial direction have $dr_{j+1} = (1 + 0.0523) dr_j$ $(j = 1..N_r)$ so that the poloidal-plane cells are curvilinear rectangles with approximately equal sides. This choice results in high spatial resolution near the star where the disc-magnetosphere interaction takes place while also permitting a large simulation region. We have used a range of resolutions going from $N_r \times N_\theta = 51 \times 31$ to 121×51 in order to establish the numerical convergence of our results.

Conical Winds and Axial Jets

A large number of simulations were done in order to understand the origin and nature of conical winds. All of the key parameters were varied in order to ensure that there is no special dependence on any parameter. We observed that the formation of conical winds is a common phenomenon for a wide range of parameters. They are most persistent and strong in cases where the viscosity and diffusivity coefficients are not very small, $\alpha_\nu \gtrsim 0.03$, $\alpha_\eta \gtrsim 0.03$. Another important condition is that $\alpha_\nu \gtrsim \alpha_\eta$; that is, the magnetic Prandtl number of the turbulence, $\mathcal{P}_m = \alpha_\nu/\alpha_\eta \gtrsim 1$. This condition favors the bunching of the stellar magnetic field by the accretion flow.

The velocities in the conical wind component in the propeller regime are similar to those in conical winds around slowly rotating stars. Matter launched from the disc-magnetosphere region initially has an approximately Keplerian azimuthal velocity, $v_K = \sqrt{GM_*/r}$. It is gradually accelerated to poloidal velocities $v_p \sim (0.3 - 0.5) v_K$ and the azimuthal velocity decreases. The flow has a high density and carries most of the disc mass into the outflows. The

TABLE 1. Reference values for different types of stars. We choose the mass M, radius R_*, equatorial magnetic field B_* and the period P_* of the star and derive the other reference values. The reference mass M_0 is taken to be the mass M of the star. The reference radius is taken to be twice the radius of the star, $R_0 = 2R_*$. The surface magnetic field B_* is different for different types of stars. The reference velocity is $v_0 = (GM/R_0)^{1/2}$. The reference time-scale $t_0 = R_0/v_0$, and the reference angular velocity $\Omega_0 = 1/t_0$. We measure time in units of $P_0 = 2\pi t_0$ (which is the Keplerian rotation period at $r = R_0$). In the plots we use the dimensionless time $T = t/P_0$. The reference magnetic field is $B_0 = B_*(R_*/R_0)^3/\tilde{\mu}$, where $\tilde{\mu}$ is the dimensionless magnetic moment which has a numerical value of 10 in the simulations discussed here. The reference density is taken to be $\rho_0 = B_0^2/v_0^2$. The reference pressure is $p_0 = B_0^2$. The reference temperature is $T_0 = p_0/\mathcal{R}\rho_0 = v_0^2/\mathcal{R}$, where $\mathcal{R}$ is the gas constant. The reference accretion rate is $\dot{M}_0 = \rho_0 v_0 R_0^2$. The reference energy flux is $\dot{E}_0 = \dot{M}_0 v_0^2$. The reference angular momentum flux is $\dot{L}_0 = \dot{M}_0 v_0 R_0$. The poloidal magnetic field of the star (in the absence of external plasma) is an aligned dipole field.

	Protostar	CTTS	Brown dwarf	White dwarf	Neutron star
$M(M_\odot)$	0.8	0.8	0.056	1	1.4
R_*	$2R_\odot$	$2R_\odot$	$0.1R_\odot$	5000 km	10 km
R_0 (cm)	$2.8 \cdot 10^{11}$	$2.8 \cdot 10^{11}$	$1.4 \cdot 10^{10}$	10^9	$2 \cdot 10^6$
v_0 (cm s^{-1})	$1.95 \cdot 10^7$	$1.95 \cdot 10^7$	$1.6 \cdot 10^7$	$3.6 \cdot 10^8$	$9.7 \cdot 10^9$
P_*	1.04 days	5.6 days	0.13 days	89 s	6.7 ms
P_0	1.04 days	1.04 days	0.05 days	17.2 s	1.3 ms
B_* (G)	$3.0 \cdot 10^3$	10^3	$2 \cdot 10^3$	10^6	10^9
B_0 (G)	37.5	12.5	25.0	$1.2 \cdot 10^4$	$1.2 \cdot 10^7$
ρ_0 (g cm^{-3})	$3.7 \cdot 10^{-12}$	$4.1 \cdot 10^{-13}$	$1.4 \cdot 10^{-12}$	$1.2 \cdot 10^{-9}$	$1.7 \cdot 10^{-6}$
n_0 (cm^{-3})	$2.2 \cdot 10^{12}$	$2.4 \cdot 10^{11}$	$8.5 \cdot 10^{11}$	$7 \cdot 10^{14}$	10^{18}
$\dot{M}_0(M_\odot \mathrm{yr}^{-1})$	$1.8 \cdot 10^{-7}$	$2 \cdot 10^{-8}$	$1.8 \cdot 10^{-10}$	$1.3 \cdot 10^{-8}$	$2 \cdot 10^{-9}$
$\dot{E}_0$ (erg s^{-1})	$2.1 \cdot 10^{33}$	$2.4 \cdot 10^{32}$	$2.5 \cdot 10^{30}$	$5.7 \cdot 10^{34}$	$6 \cdot 10^{36}$
$\dot{L}_0$ (erg s^{-1})	$3.1 \cdot 10^{37}$	$3.4 \cdot 10^{36}$	$1.7 \cdot 10^{33}$	$1.6 \cdot 10^{35}$	$1.2 \cdot 10^{33}$
T_d (K)	2290	4590	5270	$1.6 \cdot 10^6$	$1.1 \cdot 10^9$
T_c (K)	$2.3 \cdot 10^6$	$4.6 \cdot 10^6$	$5.3 \cdot 10^6$	$8 \cdot 10^8$	$5.6 \cdot 10^{11}$

situation is the opposite in the axial jet component where the density is $10^2 - 10^3$ times lower, while the poloidal and total velocities are significantly higher. Thus, in the propeller regime we find a *two-component outflow*: a matter dominated conical wind and a magnetically dominated axial jet.

We observe conical winds in both slowly and rapidly rotating stars. In both cases, matter in the conical winds passes through the Alfvén surface (and shortly thereafter through the fast magnetosonic point), beyond which the flow is matter-dominated in the sense that the energy flow is carried mainly by the matter. The situation is different for the axial jet component where the flow is sub-Alfvénic within the simulation region. For this component the energy flow is carried by the Poynting flux and the angular moment flow is carried by the magnetic field. X-ray observations of the jet from the protostellar object L1551 IRS 5 suggest a high-velocity, highly collimated inner jet and a lower-velocity, less-collimated outflow component [75].

Collimation and Driving of the Outflows

Figure 7 shows the long-distance development of a conical wind from a slowly rotating star. At large distances the conical wind becomes collimated. To understand the collimation we analyzed total force (per unit mass) perpendicular to a poloidal magnetic field line (Lii et al. [61]). For distances beyond the Alfvén surface of the flow this force is approxiamtely

$$f_{\mathrm{tot},\perp} = -v_{\mathrm{p}}^2 \frac{\partial \Theta}{\partial s} - \frac{1}{8\pi\rho} \frac{\partial \mathbf{B}_p^2}{\partial n} - \frac{1}{8\pi\rho(r\sin\theta)^2} \frac{\partial (r\sin\theta B_\phi)^2}{\partial n} + \frac{v_\phi^2}{r} \frac{\cos\Theta}{\sin\theta}. \tag{8}$$

([41]). Here, Θ is the angle between the poloidal magnetic field and the symmetry axis, s is the arc length along the poloidal field line, n is a coordinate normal to the poloidal field, and the $p-$subscripts indicate the poloidal component of a vector. Once the jet begins to collimate, the curvature term $-v_{\mathrm{p}}^2 \partial\Theta/\partial s$ also becomes negligible. The magnetic force may act to either collimate or decollimate the jet, depending on the relative magnitudes of the gradient of

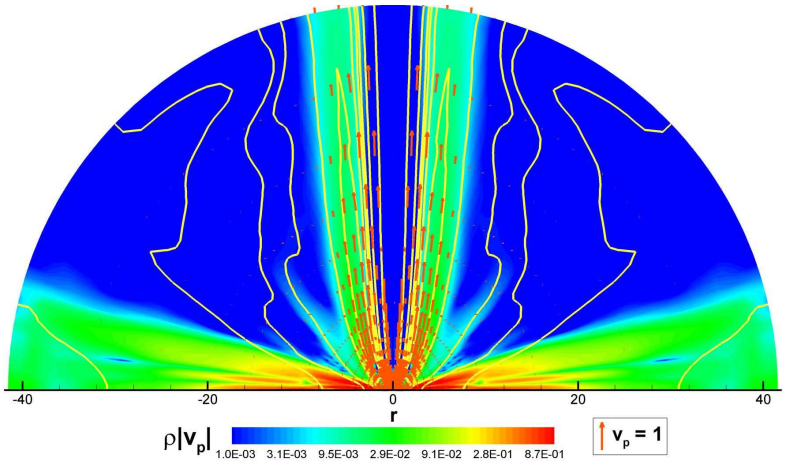

FIGURE 7. The conical wind/jet from a slowly rotating star at time $t = 860$. The background shows the poloidal matter flux density $\rho \mathbf{v}_p$ and the lines show the poloidal projections of the magnetic magnetic field. The red vectors show the poloidal matter velocity $\mathbf{v}_p$. Dimensional values can be obtained from Table 1. For example for a CTTS, $t_0 = 0.366$ days, $R_0 = 2$, $t = 860$ corresponds to 315 days, and the simulation region is 0.39 AU in radius. The horizontal axis shows the distance from the star in units of the reference radius R_0. For this case $\alpha_\nu = 0.3$ and $\alpha_\eta = 0.1$.

$(r \sin\theta B_\phi)^2$ (which collimates the outflow) and the gradient of $\mathbf{B}_p^2$ (which "decollimates". In our simulations, the collimation of the matter implies that the magnetic hoop stress is larger than the poloidal field gradient. Thus the main perpendicular forces acting in the jet are the collimating effect of the toroidal magnetic field and the decollimating effect of the centrifugal force and the gradient of $\mathbf{B}_p^2$. The collimated effect of B_ϕ dominates. Note that in MKS units $2\pi r \sin\theta B_\phi/\mu_0$ is the poloidal current flowing through a surface of radius r from colatitude zero to θ. For the jets from young stars this current is of the order of 2×10^{13} A.

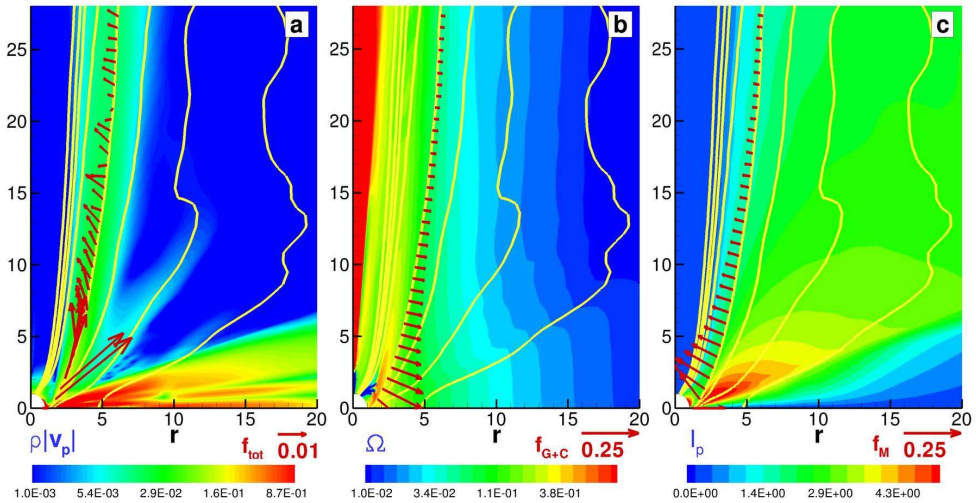

FIGURE 8. Forces along a field line in the jet. **Panel (a)** shows the poloidal matter flux density as a background overplotted with poloidal magnetic field lines. The vectors show the *total* force $\mathbf{f}_{\rm tot}$ along a representative field line originating from the disk at $r = 1.24$. **Panel (b)** plots the angular velocity Ω as the background. The vectors show the sum of the *gravitational* + *centrifugal* forces $\mathbf{f}_{\rm G+C}$ along the representative field line. **Panel (c)** shows the poloidal current I_p as the background. The vectors show the total *magnetic* force $\mathbf{f}_{\rm M}$ along the representative field line.

The driving force for the outflow is simply the force parallel to the poloidal magnetic field of the flow $f_{\rm tot,\|}$. This

is obtained by taking the dot product of the Euler equation with the $\hat{\mathbf{b}}$ unit vector which is parallel to the poloidal magnetic field line $\mathbf{B}_p$. The derivation by Ustyugova et al. [41] gives

$$f_{\rm tot,\|} = -\frac{1}{\rho}\frac{\partial P}{\partial s} - \frac{\partial \Phi}{\partial s} + \frac{v_\phi^2}{r\sin\theta}\sin\Theta + \frac{1}{4\pi\rho}\hat{\mathbf{b}}\cdot[(\nabla\times\mathbf{B})\times\mathbf{B}]\,. \tag{9}$$

Here, the terms on the right-hand side correspond to the pressure, gravitational, centrifugal and magnetic forces, respectively denoted $\mathbf{f}_{\rm P,G,C,M}$. The pressure gradient force, $\mathbf{f}_{\rm P}$, dominates within the disk. The matter in the disk is approximately in Keplerian rotation such that the sum of the gravitational and centrifugal forces roughly cancel ($\mathbf{f}_{\rm G+C} \approx 0$). Near the slowly rotating star, however, the matter is strongly coupled to the stellar magnetic field and the disk orbits at sub-Keplerian speeds, giving $\mathbf{f}_{\rm G+C} \lesssim 0$. The magnetic driving force (the last term of Eq. 9) can be expanded as

$$f_{\rm M,\|} = -\frac{1}{8\pi\rho(r\sin\theta)^2}\frac{\partial}{\partial s}(r\sin\theta B_\phi)^2\,, \tag{10}$$

(Lovelace et al. [24]). Figure 8 shows the variation of the total force $\mathbf{f}_{\rm tot}$, the gravitational plus centrifugal force, and the magnetic force along a representative field line. This analysis establishes that the predominant driving force for the outflow is the magnetic force (Eq. 10) and not the centrifugal force. This in agreement with the analysis of Lovelace et al. [24].

Variability

For both rapidly and slowly rotating stars the magnetic field lines connecting the disc and the star have the tendency to inflate and open ([76]). Quasi-periodic reconstruction of the magnetosphere due to inflation and reconnection has been discussed theoretically ([77]) and has been observed in a number of axisymmetrtic simulations ([55],-[57]). Goodson et al. [78] discuss the physics of inflation cycles. They have shown that each cycle of inflation consists of a period of matter accumulation near the magnetosphere, diffusion of this matter through the magnetospheric field, inflation of the corresponding field lines, accretion of some matter onto the star, and outflow of some matter as winds, with subsequent expansion of the magnetosphere. There simulations show $5-6$ cycles of inflation and reconnection. Our simulations are much longer and often show $30-50$ cycles of inflation and reconnection.

Kurosawa and Romanova [79, 80] have calculated spectra from modeled conical winds and accretion funnels combining 3D MHD simulations with 3D radiative transfer code TORUS. They have shown that conical winds may explain different features in the hydrogen spectral lines, in the He I line and also a relatively narrow, low-velocity blue-shifted absorption components in the He I λ10830 which is often seen in observations [79]. Further, the 3D MHD+3D radiative transfer codes have been used to model the young star V2129 Oph, where the parameters of the star including the surface magnetic field distribution are known [81]. The spectrum in several Hydrogen lines was calculated and compared with observed spectra. A good match was obtained between the modeled and observed spectra [81].

Lopsided Jets and Outflows from Discs

There is clear evidence, mainly from Hubble Space Telescope (HST) observations, of the asymmetry between the approaching and receding jets from a number of young stars. The objects include the jets in HH 30 (Bacciotti et al. [82]), RW Aur (Woitas et al. [83]), TH 28 (Coffey et al. [84]), and LkHα 233 (Perrin & Graham [85]). Specifically, the radial speed of the approaching jet may differ by a factor of two from that of the receding jet. For example, for RW Aur the radial redshifted speed is $\sim$ 100 km/s whereas the blueshifted radial speed is $\sim$ 175 km/s. The mass and momentum fluxes are also significantly different for the approaching and receding jets in a number of cases. It is possible that the observed asymmetry of the jets could be due to differences in the gas densities on the two sides of the source. However, it is more likely that the asymmetry of the outflows arises from the asymmetry of the star's magnetic field. Substantial observational evidence points to the fact that young stars often have *complex* magnetic fields consisting of dipole, quadrupole, and higher order poles misaligned with respect to each other and the rotation axis (Jardine et al. [86]; Donati et al. [87]). Analysis of the plasma flow around stars with realistic fields have shown that a significant fraction of the star's magnetic field lines are open and may carry outflows (Gregory et al. [88]).

The complex magnetic field of a star will destroy the commonly assumed symmetry of the magnetic field and the plasma about the equatorial plane. MHD simulations by Lovelace et al. [89] fully support the qualitative picture suggested in the sketch in Fig. 1 of [89]. The idea of mixing of even and odd symmetry magnetic fields about $z = 0$

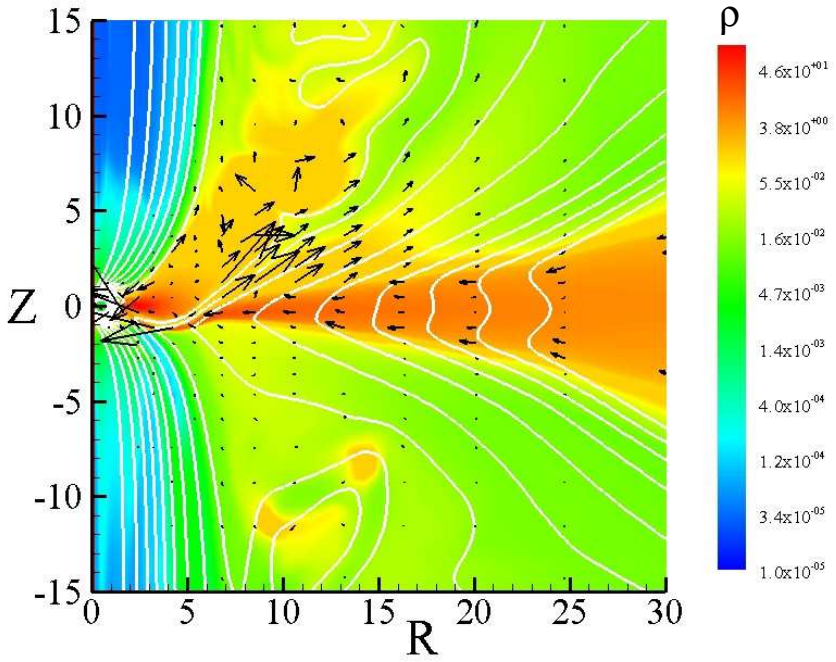

FIGURE 9. Lop-sided outflow from the disc-magnetosphere boundary at a time corresponding to 203 rotation periods of the disc at the corotation radius $r_{\rm cr}$, which is twice the star's radius R_*. The initial magnetic field, which is symmetric about $z = 0$, is the sum of the stellar dipole (equation 8) and the disc field (equation 9), where the dipole and disc fields are parallel and equal in magnitude at $r = 4.4R_*$ and $z = 0$. The color background shows the density and the white lines the poloidal projection of the magnetic field lines. The arrows inside the disc (the orange region) are the poloidal velocity vectors, while the arrows external to the disc show the momentum density $\rho\mathbf{v}$.

to get lopsided outflows was proposed earlier by Wang et al. [90]. The time-scale during which the jet comes from the upper hemisphere is set by the evolution time-scale for the stellar magnetic field. This is determined by the dynamo processes responsible for the generation of the field. Remarkably, once the assumption of symmetry about the equatorial plane is dropped, the conical winds alternately come from one hemisphere and then the other *even* when the stellar magnetic field is a centered axisymmetric dipole [89]. This symmetry breaking has also been found by Fendt & Sheikhnezami [91]. The time-scale for the 'flipping' is the accretion time-scale of the inner part of the disc which is expected to be much less than the evolution time of the star's magnetic field.

We have revisited the problem of the asymmetry of the jets and outflows using a new axisymmetric code with a high-resolution stretched-grid [92]. The star has a radius of 1 in our simulation units, and the first 30 grid cells have lengths $\delta R = 0.1$. At larger R, the cell lengths are given recursively by $\delta R_{i+1} = 1.025\delta R_i$. Similarly, in the $Z-$direction, the first 30 grid cells above and below the equatorial plane have lengths $\delta Z = 0.1$. At larger $|Z|$, the cell lengths are given recursively by $\delta Z_{j+1} = 1.025\delta Z_j$. This grid gives high resolution in the region occupied by the disc and by the jet. Here, we present sample results with as simulation region of 135×216 ($R \times Z$) cells.

The initial magnetic field is taken to be a superposition of a dipole field centered in the star described by the flux function

$$\Psi_D = \frac{\mu R^2}{(R^2 + Z^2)^{3/2}} \,, \tag{11}$$

and a Zanni-type distributed field in the disc,

$$\Psi_Z = \frac{4}{3} B_0 r_0^2 \left(\frac{r}{r_0}\right)^{3/4} \frac{m^{5/4}}{(m^2 + Z^2/R^2)^{5/8}} , \tag{12}$$

(Zanni et al. [93]), where μ is the magnetic moment of the star, B_0 is a reference value for the disc field, and m is a dimensionless parameter which controls the initial disc field geometry.

Figure 9 shows a zoomed-in view of results from the new stretched-grid code for an episode of lopsided jet formation for a case where the dipole field of the rotating star is parallel to the disc field in the disc midplane. The outflow from the top side of the disc is at super escape speed velocities with the result that the mass outflow is predominantly from the top side of the disc. During the duration of the run (203 rotation periods of the disc at the corotation radius), the poloidal flux of the disc field advects inward and accumulates in the low-density axial blue region in the figure. In this region there are magnetically collimated Poynting flux outflows of energy and angular momentum in the $\pm z$ directions.

CONCLUSIONS

Professor Rostoker was an inspiring leader and mentor of many students in a broad array of fields of physics, plasma physics, and astrophysics.

REFERENCES

[1] J.J. Bzura, T.J. Fessenden, H.H. Fleischmann, D. A. Phelps, A. C. Smith, Jr., and D. M. Woodall, 1972, "Trapping of High-Current Relativistic Electron Beams in a Magnetic Mirror Trap," Phys. Rev. Let., 29. 256-259.

[2] R.V.E. Lovelace, and E. Ott, 1974, "Theory of Magnetic Insulation," Physics of Fluids, 17, 1263-1268;E. Ott, and R.V.E. Lovelace 1975, "Magnetic Insulation and Microwave Generation," Applied Physics Letters, 27, 378-380;A. Ron, A. Mondelli, and N. Rostoker, 1973,"Equilibria for Magnetic Insulation," IEEE Transactions on Plasma Science, V. I, 85-93

[3] R.J. Leepera, T.E. Albertsa, J.R. Asaya, P.M. Bacaa, K.L. Bakera, S.P. Breezea, G.A. Chandlera, D.L. Cooka, G.W. Coopera, C. Deeneya, M.S. Derzona, M.R. Douglasa, D.L. Fehla, T. Gillilanda, D.E. Hebrona, M.J. Hursta, D.O. Jobea, J.W. Kellogga, J.S. Lasha, S.E. Laziera, M.K. Matzena, D.H. McDaniela, J.S. McGurna, T.A. Mehlhorna, A.R. Moatsa, R.C. Mocka, D.J. Murona, T.J. Nasha, R.E. Olsona, J.L. Portera, J.P. Quintenza, P.V. Reyesa, L.E. Rugglesa, C.L. Ruiza, T.W.L. Sanforda, F.A. Schmidlappa, J.F. Seamena, R.B. Spielmana, M.A. Starka, K.W. Struvea, W.A. Stygara, D.R. Tibbetts-Russella, J.A. Torresa, M. Vargasa, T.C. Wagonera, C. Wakefielda, J.H. Hammerb, D.D. Ryutovb, M. Tabakb, S.C. Wilksb, R.L. Bowersc, K.D. McLenithanc and D.L. Petersonc, 1999, "Z pinch driven inertial confinementfusion target physics research at Sandia National Laboratories," NuclearFusion, **39**, 1283-1294

[4] M.W. Binderbauer, T. Tajima, L.C. Steinhauer, E. Garate, M. Tuszewski, L. Schmitz, H.Y. Guo, A. Smirnov, H. Gota, D. Barnes, B.H. Deng, M.C. Thompson, E. Trask, X. Yang, S. Putvinski, N. Rostoker, R. Andow, S. Aefsky, N. Bolte, D.Q. Bui, F. Ceccherini, R. Clary, A.H. Cheung, K.D. Conroy, S.A. Dettrick, J.D. Douglass, P. Feng, L. Galeotti, F. Giammanco, E. Granstedt, D. Gupta, S. Gupta, A.A. Ivanov, J.S. Kinley, K. Knapp, S. Korepanov, M. Hollins, R. Magee,R. Mendoza, Y. Mok, A. Necas, S. Primavera, M. Onofri, D. Osin, N. Rath, T. Roche, J. Romero, J.H. Schroeder, L. Sevier, A. Sibley, Y. Song, A.D. Van Drie, J.K. Walters, W. Waggoner, P. Yushmanov, K. Zhai, and TAE Team, 2015,"A high performance field-reversed configuration," Physics of Plasmas, **22**, 056110-1 to 056110-16

[5] H.V. Wong, H.L., Berk, R.V.E. Lovelace, and N. Rostoker, 1991, "Stability of annular equilibrium of energetic large orbit ion beam", Physics of Plasmas, V. 3, 2973-2986

[6] R.V.E. Lovelace, 1975, "Low-Frequency Stability of Astron Configurations," Phys. Rev. Lett., 35, 162-164; R.V.E. Lovelace,1975, "Low-frequency stability of high-current particle rings," Physics of Fluids, 19, 723-737; R.V.E. Lovelace 1979, "Precession and kink motion of ion astron layers," Physics of Fluids, 22, 708-717; R.V.E. Lovelace, 1978, "Astron Kink Stability with a Toroidal Magnetic Field," Phys. Rev. Lett., 26, 1801-1804

[7] S.A. Balbus, and J.F. Hawley, 1998, "Instability, turbulence, and enhanced transport in accretion disks, " Rev. Mod. Phys., 70, 1-53
[8] R.V.E. Lovelace, H. Li, S.A. Colgate, and A.F. Nelson. 1999, "Rossby Wave Instability of Keplerian Accretion Disks", ApJ, 513, 805-810
[9] H. Li, J.M. Finn, R.V.E. Lovelace, and S.A. Colgate, 2000, "Rossby Wave Instability of Thin Accretion Disks. II. Detailed Linear Theory", ApJ, 533, 1023-1034
[10] R.V.E. Lovelace and R.G. Hohlfeld 1978, "Negative mass instability of flat galaxies", ApJ, 221, 51-61
[11] H. Meheut, R.V.E. Lovelace, and D. Lai 2013, "How Strong are Rossby Vortices", MNRAS, 430, 1988-1993
[12] C. G. Rossby and Collaborators 1939,"Relation between variations in the intensity of the zonal circulation of the atmosphere and the displacements of the semi-permanent centers of action", Journal of Marine Research, 2, 38-55
[13] L. M. Brekhovskikh, and V. Goncharov 1993, *Mechanics of Continua and Wave Dynamics* (Berlin : Springer), pp 246-252
[14] D. B. Chelton, and M.G. Schlax, 1996, "Global Observations of Oceanic Rossby Waves", Science, 272, 234-238
[15] R. S. Lindzen, 1988, "Instability of plane parallel shear flow (toward a mechanistic picture of how it works", Pure Appl. Geophys., 126, 103-121
[16] P.S. Marcus, 1993, "Jupiter's Great Red Spot and other Vortices", Ann. Rev. Astron. and Astrophys., 31, 523-573
[17] M. Tagger, 2001, "On Rossby waves and vortices with differential rotation", A&A, 380, 750-757
[18] D. Tsang, and D. Lai, 2008,"Super-reflection in fluid discs: corotation amplifier, corotation resonance, Rossby waves and overstable modes", MNRAS, 387, 446-462
[19] D. Lai, and D. Tsang, 2009, "Corotational instability of inertial-acoustic modes in black hole accretion discs and quasi-periodic oscillations", MNRAS, 393, 979-991
[20] J. C.B. Papaloizou and J.E. Pringle, 1984, "The dynamical stability of differentially rotating discs with constant specific angular momentum", MNRAS, 208, 721-750
[21] J. C.B. Papaloizou and J.E. Pringle, J. E. 1985,"The dynamical stability of differentially rotating discs. II", MNRAS, 213, 799-820
[22] R.V.E. Lovelace and M.M. Romanova 2014,"Rossby Wave Instability in Astrophysical Discs", Fluid Dynamics Research, 46, 041401-041412
[23] R.V.E. Lovelace 1976, "Dynamo Model of Double Radio Sources," Nature, 262, 649-652
[24] R.V.E. Lovelace, H.L. Berk, and J. Contopoulos 1991, "Magnetically Driven Jets and Winds," ApJ, 379, 696-705
[25] T.P. Ray, 2007, "Thee generation of jets from young stars: an observational perspective," Proc. of IAU Symposium, V. 243, 183-194
[26] S. Cabrit, S. Edwards, S.E. Strom, and K.M. Strom, 1990,"Forbidden-line emission and infrared excesses in T Tauri stars - Evidence for accretion-driven mass loss?," ApJ, 354, 687-700
[27] P. Hartigan, S. Edwards, and L. Gandhour, 1995"Disk Accretion and Mass Loss from Young Stars,"ApJ, 452, 736-768
[28] S. Edwards, W. Fischer, J. Kwan, L. Hillenbrandt, and A.K. Durpee, 2003, "He I λ10830 as a Probe of Winds in Accreting Young Stars," ApJ, 599, L41-L44
[29] S. Edwards, W. Fischer, L. Hillenbrand, and J. Kwan, 2006,"Probing T Tauri Accretion and Outflow with 1 Micron Spectroscopy,"ApJ, 646, 319-341
[30] J. Kwan, S. Edwards, and W. Fischer, 2007,"Modeling T Tauri Winds from He Iλ10830 Profiles,"ApJ, 657, 897-915
[31] J.L. Sokoloski, and S.J. Kenyon, 2003,"CH Cygni. I. Observational Evidence for a Disk-Jet Connection,"ApJ, 584, 1021-1026
[32] S. Heinz, N.S. Schulz, W.N. Brandt, and D. K. Galloway, 2007,"Evidence of a Parsec-Scale X-Ray Jet from the Accreting Neutron Star Circinus X-1,"ApJ, 663, L93-L96
[33] J. Ferreira, C. Dougados, and S. Cabrit, 2006, "Which jet launching mechanism(s) in T Tauri stars?" A&A, 453,785-796
[34] R.D. Blandford and D.G. Payne, 1982, "Hydromagnetic flows from accretion discs and the production of radio jets," MNRAS, 199, 883-903

[35] A. Königl and R.E. Pudritz, 2000,"Disk Winds and the Accretion-Outflow Connection," in *Protostars and PlanetsIV*, Mannings, V., Boss, A.P., Russell, S. S. (eds.), University of Arizona Press, Tucson, p. 759-791
[36] K. Shibata and Y. Uchida, 1985, "A magnetodynamic mechanism for the formation of astrophysical jets. I - Dynamical effects of the relaxation of nonlinear magnetic twists," Publ. Astron. Soc. Japan, 37, 31-46
[37] Y. Uchida and K. Shibata, 1985, "Magnetodynamical acceleration of CO and optical bipolar flows from the region of star formation," Publ. Astron.Soc. Japan, 37, 515-535
[38] G.V. Ustyugova, A.V. Koldoba, M.M. Romanova, V.M. Chechetkin and R.V.E. Lovelace, 1995, "Magneto-hydrodynamic simulations of outflows from accretion disks," ApJ, 439, L39-L42
[39] R. Ouyed and R.E. Pudritz, 1997,"Numerical Simulations of Astrophysical Jets from Keplerian Disks. I. Stationary Models," ApJ, 482, 712-732
[40] M.M. Romanova, G.V. Ustyugova, A.V. Koldoba, V.M. Chechetkin and R.V.E. Lovelace, 1997, "Formation of Stationary Magnetohydrodynamic Outflows from a Disk by Time-dependent Simulations," ApJ, 482, 708-711
[41] G.V. Ustyugova, A.V. Koldoba, M.M. Romanova, V.M. Chechetkin, and R.V.E. Lovelace, 1999,"Magneto-centrifugally Driven Winds: Comparison of MHD Simulations with Theory," ApJ, 516, 221-235
[42] R. Krasnopolsky, Z.Y. Li and R. Blandford, 1999,"Magnetocentrifugal Launchinng of Jets from Accretion Disks:I. Cold Axisymmetric Flows," ApJ, 526, 631-641
[43] F. Casse and R. Keppens, 2004, "Radiatively Inefficient Magnetohydrodynamic Accretion-Ejection Structures," ApJ, 601, 90-103
[44] S. Matt, and R.E. Pudritz, 2008, "Accretion-powered Stellar Winds. II. Numerical Solutions for Stellar Wind Torques," ApJ, 678, 1109-1118
[45] S. Matt, and R.E. Pudritz, 2008, "Accretion-powered Stellar Winds. III. Spin-Equilibrium Solutions,"ApJ, 681, 391-399
[46] P. Tzeferacos, A. Ferrari, A. Mignone, C. Zanni, G. Bodo and S. Massaglia, 2009,"On the magnetization of jet-launching discs,"MNRAS, 400, 820-834
[47] F. Shu, J. Najita, E. Ostriker, F. Wilkin, S. Ruden, S. Lizano, 1994,"Magnetocentrifugally driven flows from young stars and disks 1: A generalized model,"ApJ, 429, 781-796
[48] F.H Shu, D. Galli, S. Lizano, A.E Glassgold and P.H. Diamond, 2007,"Mean Field Magnetohydrodynamics of Accretion Disks,"ApJ, 665, 535-553
[49] J.R. Najita and F.H Shu, 1994,"Magnetocentrifugally driven flows from young stars and disks. 3: Numerical solution of the sub-Alfvenic region," ApJ, 429, 808-825
[50] M.J. Cai, H. Shang, H.-H. Lin, and F.H Shu:, 2008,"X-Winds in Action," ApJ,672, 489-503
[51] S.C. Hsu and P.M. Bellan, 2002,"A laboratory plasma experiment for studying magnetic dynamics of accretion discs and jets," MNRAS, 334, 257-261
[52] S. V. Lebedev, A. Ciardi, D. J. Ampleford, S.N. Bland, S. C. Bott, J. P. Chittenden, G. N. Hall, J. Rapley, C. A. Jennings, A. Frank, E. G. Blackman, T. Lery, 2005,"Magnetic tower outflows from a radial wire array Z-pinch,"MNRAS, 361, 97-108
[53] M. R. Hayashi, K. Shibata, and R. Matsumoto, 1996,"X-Ray Flares and Mass Outflows Driven by Magnetic Interaction between a Protostar and Its Surrounding Disk," ApJ, 468, L37-L40
[54] K.A. Miller and J.M. Stone, 1997,"Magnetohydrodynamic Simulations of Stellar Magnetosphere–Accretion Disk Interaction,"ApJ, 489, 890-902
[55] A.P. Goodson, R.M. Winglee, and K.-H. Bohm, 1997,"Time-dependent Accretion by Magnetic Young Stellar Objects as a Launching Mechanism for Stellar Jets," ApJ,489, 199-209
[56] A.P. Goodson, and R.M. Winglee, 1999, "Jets from Accreting Magnetic Young Stellar Objects. II. Mechanism Physics," ApJ, 524, 159-168
[57] S. Hirose, Y. Uchida, K. Shibata and R. Matsumoto, 1997,"Disk Accretion onto a Magnetized Young Star and Associated Jet Formation," PASJ, 49, 193-205
[58] S. Matt, A.P. Goodson, R.M. Winglee and K.-H. Bohm,2002, "Simulation-based Investigation of a Model for the Interaction between Stellar Magnetospheres and Circumstellar Accretion Disks,"ApJ, 574, 232-245
[59] M. Küker, T. Henning and G. Rüdiger, 2003,"Magnetic Star-Disk Coupling in Classical T Tauri Systems," ApJ, 589, 397-409
[60] M.M. Romanova, G.V. Ustyugova, A.V. Koldoba, and R.V.E. Lovelace, 2009,"Launching of conical winds and axial jets from the disc-magnetosphere boundary: axisymmetric and 3D simulations," MNRAS, 399, 1802-1828

[61] P.S. Lii, M.M. Romanova and R. Lovelace, 2012,"Magnetic launching and collimation of jets from the disc-magnetosphere boundary: 2.5D MHD simulations,"MNRAS, 420, 2020-2033
[62] C. Fendt, 2009, "Formation of Protostellar Jets as Two-Component Outflows from Star-Disk Magnetospheres," ApJ, 692, 346-363
[63] A.F. Illarionov and R.A. Sunyaev, 1975"Why the Number of Galactic X-ray Stars Is so Small?" A&A, 39, 185-195
[64] M.A. Alpar and J. Shaham, 1985, "Is GX5-1 a millisecond pulsar?"' Nature, 316, 239-241
[65] R.V.E. Lovelace, M.M. Romanova, and G.S. Bisnovatyi-Kogan, 1999,"Magnetic Propeller Outflows,"ApJ, 514, 368-372
[66] A. Mignone, G. Bodo, S. Massaglia, T. Matsakos, Tesileanu, O. C. Zanni, and A. Ferrari, 2007, "PLUTO: A Numerical Code for Computational Astrophysics," ApJS, 170, 228-242
[67] R.V.E. Lovelace, C. Mehanian, C.M. Mobarry and M.E. Sulkanen, 1986,"Theory of axisymmetric magnetohydrodynamic flows - Disks,"ApJS, 62, 1-37
[68] A.V. Koldoba, G.V. Ustyugova, M.M. Romanova and R.V.E. Lovelace, 2008,"Oscillations of Magnetohydrodynamic Shock Waves on the Surfaces of T Tauri Stars," MNRAS, 388, 357-366
[69] G.V. Ustyugova, A.V. Koldoba, M.M. Romanova and R.V.E. Lovelace, 2006, "Propeller Regime of Disc Accretion to Rapidly Rotating Stars,"ApJ, 646, 304-318
[70] N.I . Shakura and R.A. Sunyaev, 1973, "Black holes in binary systems: Observational appearance," A&A, 24, 337-355
[71] S. Dyda, R.V.E. Lovelace, G.V. Ustyugova, P.S. Lii, M.M. Romanova, and A.V. Koldoba, 2013, "Advection of matter and B-fields in alpha-discs," MNRAS, 432, 127-137
[72] X. Guan and C.F. Gammie, 2009,"The Turbulent Magnetic Prandtl Number of MHD Turbulence in Disks," ApJ, 607, 1901-1906
[73] K. G. Powell, P.L. Roe, T.J. Linde, T.I. Gombosi and D.L. De Zeeuw, 1999, "A Solution-Adaptive Upwind Scheme for Ideal Magnetohydrodynamics,"J. Comput. Phys., 154, 284-309
[75] P.C. Schneider, H.M. Günther and H.M.M. Schmitt, 2011,"The X-ray puzzle of the L1551 IRS 5 jet,"A&A, 530, id.A123, 14 pp.
[76] R.V.E. Lovelace, M.M. Romanova, and G.S. Bisnovatyi-Kogan, 1995, "Spin-up/spin-down of magnetized stars with accretion discs and outflows," MNRAS, 275, 244-254
[77] J.J. Aly and J. Kuijpers, 1990, "Flaring interactions between accretion disk and neutron star magnetosphere, "A&A, 227, 473-482
[78] A.P. Goodson, K.-H. Bohm, and R.M. Winglee, 1999,"Jets from Accreting Magnetic Young Stellar Objects. I. Comparison of Observations and High-Resolution Simulation Results,"ApJ, 524, 142-158
[79] R. Kurosawa, M. M. Romanova and Harries, T., 2011,"Multidimensional models of hydrogen and helium emission line profiles for classical T-Tauri stars: method, tests and examples,"MNRAS, 416, 2623-2639
[80] R. Kurosawa and M. M. Romanova, 2012,"Line formation in the inner winds of classical T Tauri stars: testing the conical-shell wind solution,"MNRAS, 426, 2901-2916
[81] S. H. P. Alencar, J. Bouvier, F.M. Walter, C. Dougados, J.-F. Donati, R. Kurosawa, M. Romanova, X. Bonfils, G. H. R. A. Lima, S. Massaro, M. Ibrahimov and E. Poretti, 2012, "Accretion dynamics in the classical T Tauri star V2129 Ophiuchi," A&A, 541, id.A116, 14 pp.
[82] F. Bacciotti, J. Eislöffel, T.P. Ray, 1999, "The physical properties of the HH 30 jet from HST and ground-based data,"A&A, 350, 917-927
[83] J. Woitas, T.P. Ray, F. Bacciotti, C.J. Davis, J. Eislöffel, 2002,"Hubble Space Telescope Space Telescope Imaging Spectrograph Observations of the Bipolar Jet from RW Aurigae: Tracing Outflow Asymmetries Close to the Source," ApJ, 580, 336-342
[84] D. Coffey, F. Bacciotti, J. Woitas, T.P. Ray, and J. Eislöffel, 2004,"Rotation of Jets from Young Stars: New Clues from the Hubble Space Telescope Imaging Spectrograph," ApJ, 604, 758-765
[85] M.D. Perrin and J.R. Graham, 2007,"Laser Guide Star Adaptive Optics Integral Field Spectroscopy of a Tightly Collimated Bipolar Jet from the Herbig Ae Star LkHα," 233; ApJ, 670, 499-508
[86] M. Jardine, A.C. Cameron and J.-F. Donati, 2002,"The global magnetic topology of AB Doradus,"MNRAS, 333, 339-346
[87] J.-F. Donati, M.M. Jardine, S.G. Gregory, P. Petit, F. Paletou, J. Bouvier, C. Dougados, F. Mènard, A.C. Cameron, T.J. Harries, G. A. J. Hussain, Y. Unruh, J. Morin, S.C. Marsden, N. Manset, M. Aurière, C.

Catala and E. Alecian, 2008,“Magnetospheric accretion on the T Tauri star BP Tauri;” MNRAS, 386, 1234-1251
[88] S.G. Gregory, M. Jardine, I. Simpson and J.-F. Donati, 2006,“Mass accretion on to T Tauri stars,” MNRAS, 371, 999-1013
[89] R. V. E. Lovelace, M.M. Romanova, G.V. Ustyugova and A.V. Koldoba, 2010,“One-sided outflows/jets from rotating stars with complex magnetic fields,” MNRAS, 408, 2083-2091
[90] J.C.L. Wang, M.E. Sulkanen and R.V.E. Lovelace, 1992,“Intrinsically asymmetric astrophysical jets,” ApJ, 390, 46-65
[91] C. Fendt and S. Sheikhnezami, 2013, “ Bipolar Jets Launched from Accretion Disks. II. The Formation of Asymmetric Jets and Counter Jets;,” ApJ, 774, id 12, 15 pp.
[92] S. Dyda, R.V.E. Lovelace, G.V. Ustyugova, P.S. Lii, M.M. Romanova and A.V. Koldoba, 2015, “Asymmetric MHD outflows/jets from accreting T Tauri stars,” MNRAS, 450, 481-493
[93] C. Zanni, A. Ferrari, R. Rosner, G. Bodo and S. Massaglia, 2007,“MHD simulations of jet acceleration from Keplerian accretion disks. The effects of disk resistivity,”A&A, 469, 811-828

The unexpected confluence of plasma physics and climate science: On the lives and legacies of Norman Rostoker and Sherry Rowland

Katherine RM Mackey

Clare Boothe Luce Assistant Professor
Department of Earth System Science
University of California Irvine
Irvine 3204 Croul Hall Irvine, CA 92697

kmackey@uci.edu

The Norman Rostoker Memorial Symposium brought together approximately 150 attendees to share their recent work and to reflect on the contributions of Norman Rostoker to the field of plasma physics and the advancement of fusion as a source of renewable clean energy. The field has changed considerably in a few short decades, with theoretical advances and technological innovations evolving in lock step. Over those same decades, our understanding of human induced climate change has also evolved; measurable changes in Earth's physical, chemical, and biological processes have already been observed, and these will likely intensify in the coming decades. Never before has the need for clean energy been more pronounced, or the need for transformative solutions more pressing. As scientists work with legislators, journalists, and the public to take actions to address the threat of climate change, there is much to be learned from the legacies of innovators like Norman Rostoker, who have tackled complex problems with scientific insight and determination even when the odds were stacked against them. I write this from the perspective on an Earth system scientist who studies photosynthesis and the biogeochemistry of the oceans, and my statements about plasma physics and Norman Rostoker are based on information I gathered from the colloquium and from many enjoyable conversations with his friends and colleagues.

ENDURING LEGACIES OF GROUNDBREAKING SCIENCE AND PERSEVERANCE

Revolutionizing a field is not easy. The journey toward success is often met at first with questions and even cynicism from one's peers, and then with technological hurdles and opposition from outside interests. A common thread among many great leaders is the combination of scientific insight and the ability to stick with a problem until it is solved; a grittiness by which they stay the course despite challenges and objections. Successful perseverance, however, requires not only living with setbacks and keeping focused on the journey, but also on maintaining a level of objectivity by constantly testing and reevaluating the path forward.

Norman Rostoker's vision that fusion technology could provide the world with abundant, clean energy challenged many long standing paradigms in the field. Initial theoretical discussions about fusion pointed toward the use of deuterium/tritium fuels, which require less energy input but utilize neutron producing reactions that require complex engineering controls to make safe and operable[1]. Rostoker saw an opportunity to reduce engineering complexity by developing technology that would utilize aneutronic proton/boron fusion reactions, essentially putting

the challenge in the hands and minds of physicists. His vision was to see the physics community rise to the challenge of developing and realizing a new technology that many believed was not feasible.

Norman Rostoker. Courtesy of AIP Emilio Segre Visual Archives, Physics Today Collection

Like plasma physics, the field of Earth system science has also had its share of maverick researchers who challenge the status quo. Earth system science considers the Earth holistically as a coupled system in which human activity plays a significant role. Although now an accepted idea, many researchers and the public alike initially doubted that humans could affect the Earth on a global scale. One of the early discoveries of Earth system science was made by F. Sherwood (Sherry) Rowland and his post-doc Mario Molina, who in 1974 discovered that human-made chlorofluorocarbons (CFC's) would accumulate globally and contribute to the depletion of stratospheric ozone[2], an atmospheric trace gas that protects Earth from damaging ultraviolet radiation. At the time, ozone depletion had not been observed, and the work was initially met with skepticism from some of the science community and by outright hostility from CFC industry[3]. But like Rostoker, Rowland persevered, and more than a decade later his findings were verified when the science behind the Antarctic ozone hole, first reported in 1985, clearly identified CFCs as the culprit. His work ultimately led to the Montreal Protocol in 1987, an international agreement in which to date 196 countries have pledged to phase out CFC's. Rowland's story is one of the greatest success stories in the environmental movement, but it is worth noting that it took a decade or more for the tide of public opinion to change about his work.

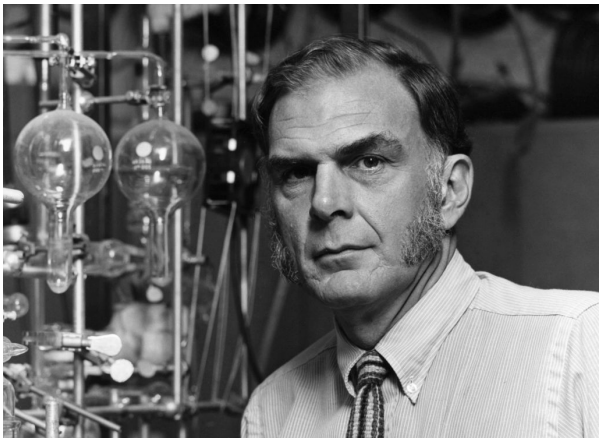

Frank Sherwood Rowland. Courtesy of UCI Libraries' Special Collections & Archives

Rostoker and Rowland exemplify how scientific insight combines with gritty perseverance to create real change both in science and society for the benefit of humanity. Yet their similarities don't end there. Rostoker and Rowland's careers overlapped extensively at UC Irvine. Both were early members of the faculty and played pivotal roles in shaping their departments. Rostoker joined the Physics faculty in 1972 and served as Chair from 1973-1976[4], laying the groundwork for the department to become a leading institution for research in plasma physics. UCI's current Dean of Physical Sciences Ken Janda noted, "At UC Irvine, [Rostoker] positioned the Department of Physics & Astronomy at the forefront of fusion research and was an inspiration and mentor to many dozens of students who are today's leaders in applied physics and technology.[4]" Rowland was the founding Chair of UCI's Chemistry Department in 1964, and in 1995 was a founding member of UCI's Earth System Science department, now recognized as one of the most influential academic departments in the nation devoted to studying Earth as a system.

Ultimately the vision and perseverance of Rostoker and Rowland were recognized broadly in their respective disciplines, with both researchers receiving high academic honors. In 1995 Sherry Rowland received the Nobel Prize in Chemistry for his work with CFCs, and in 1988 Rostoker received the American Physical Society's James Clerk Maxwell Prize for Plasma Physics. In 1998, Rostoker founded the fusion power company Tri Alpha Energy to bring his ideas about clean energy to fruition. In both cases, Rostoker and Rowland understood their journeys would be long and hard fought, but in both cases their dedication paid out. Chief Technology Officer of Tri Alpha Michl Binderbauer observed, "[Rostoker] excelled at the 'never surrender' notion. Without his steadfastness and strength of conviction, our vision would have remained on paper, and we would not have been able to conclusively demonstrate the merits of some of Norman's groundbreaking ideas in fusion research."[4]

The remarkable stories of Rostoker and Rowland reached confluence in 2005, when Rowland joined the scientific advisory board for Tri Alpha Energy, along with Nobel winning physicists Burton Richter and Arno Allan Penzias. Rowland brought his expertise in environmental science and his early training as a nuclear chemist to bear as a Tri Alpha adviser, while Rostoker got down to the nitty-gritty of making his brand of fusion energy a reality. Having persevered in their research and pioneered their respective groundbreaking fields, the two became friends and collaborators through Tri Alpha.

Through it all Rostoker and Rowland never lost their sense of humor about life and science. "Sherry was a story teller who laughed and smiled easily," recalls Don Blake, UCI Chemistry Professor and a former postdoc in the Rowland lab, and who lived across the street from Rostoker in University Hills. "Norman's sense of humor was more playful; a pinch of mischievousness with plenty of goodness. Norman would play with my children in the front yard - he had this toy bird that he would wind up and throw that would flap its wings - Norman and the kids both loved it." Rowland was also great with children, and at 6'5" was a gentle giant. "I remember when my son Tim was two years old Sherry took him on a walk to the chemistry mail room...he had to lean way down so the little guy could reach up and grab one of his enormous fingers." A final similarity is that Rostoker and Rowland were both devoted husbands of roughly six decades. Blake tells the story of how Rostoker's wife, Corinne, held the family's ownership of Tri Alpha. "When they sold their first set of shares Norman quipped, 'My father would be proud, he always wanted me to be married to a rich woman.'"

Rostoker and Rowland were two remarkable, revolutionary scientists who shared more in common than would be expected based on their seemingly disparate backgrounds. But perhaps the main thread in their stories is that they both possessed a sense of tenacity and critical scientific evaluation that enabled them to see their paradigm shifting ideas through to fruition. Now, as the world faces the challenge of climate change, both as scientists and as members of society, we have much to learn from the bold brand of science and innovation embodied by Rostoker and Rowland.

GLOBAL CHANGE AND THE NEED FOR CLEAN ENERGY SOLUTIONS

Much like the careers of Rostoker and Rowland, the fields of plasma physics and Earth system science have shared parallels during their histories. These fields are now reaching an unexpected nexus with the mandate for clean energy coming from the need to constrain global mean warming to 2°C above pre-industrial levels. Climate change has upped the ante in the quest for clean energy, making technologies like fusion, and others, all the more necessary to achieve sustainability on Earth. Below is an overview of modern climate science that highlights why the need for clean energy is so pressing.

Earth's climate system is strongly influenced by greenhouse gases in the atmosphere. These gases modulate how much the Earth must warm to radiate the amount of solar energy it absorbs. Greenhouse gases that are directly altered by human activities include carbon dioxide (CO_2), methane, nitrous oxide, as well as the CFCs and ozone studied by Sherry Rowland. The natural abundance of greenhouse gases has kept the Earth's average surface

temperature at about 14°C as opposed to approximately -16 °C that the planet would be if an atmosphere was not present[5]. Indeed, without an atmosphere containing water vapor and other gases like CO_2, Earth's surface would be frozen and uninhabitable by humans.

Earth's climate has experienced changes in the past, and scientists are able to measure these changes using an array of paleontological data. One example of direct paleo-atmosphere data is from the gas bubbles trapped in Antarctic ice. By analyzing the isotopic and chemical composition of gases trapped in the ice long ago, it is possible to reconstruct Earth's climate[6]. The longest ice-core record we have, and that seems possible, goes back about 1 million years. During this long time period the Earth's climate has cycled through glacial (usually long) and interglacial periods (usually short, about 20,000 years). Analyses of ice core bubbles have revealed a tight coupling between atmospheric CO_2 levels and temperature over these transitions, where the highest temperatures coincide with the highest CO_2 levels[6]. In terms of causation, warmer temperatures usually precede the rise in CO_2, but the CO_2 increases amplify the subsequent warming. Remarkably, throughout this long record the concentration of CO_2 in the atmosphere has remained below 300 ppm until very recently.

Modern atmospheric CO_2 levels are increasing rapidly due to human activities like the burning of fossil fuels and deforestation[5]. The trend has been recorded for nearly six decades at the Mauna Loa Observatory in Hawaii, beginning in the 1957 International Geophysical Year by C. David Keeling. The data set overlaps with and matches the ice core record, and has revealed an increase from about 315 ppm in 1958 to almost 400 ppm in 2014. The annual average for the year 2015 is on track to exceed 400 ppm for the first time in at least the last 800,000 years.

The Intergovernmental Panel on Climate Change (IPCC) was formed in 1988 in order to deliver unbiased, internationally accepted, scientific assessments of climate change for the anticipated 1990 United Nations Framework Convention on Climate Change (UNFCCC). The UNFCCC remains the international body addressing climate change to this day, and recently held its 21st meeting in December 2015 (COP-21, the Paris Climate Conference[7]). The IPCC generates assessment reports that synthesize scientific data and utilize climate models to present future climate change scenarios. The latest report indicates that under baseline scenarios where greenhouse gas emissions remain unchecked and no additional mitigation is introduced, global mean surface temperature will increase 3.7 - 4.8 °C by the year 2100[5]. The effects of past increases in CO_2 on temperature are already coming to bear: the ten hottest years on record have all occurred since 1998; and our most recent year 2015 is the hottest[8].

One particular reason for concern as we head into our unexplored 21st century climate is the uncertain positive feedbacks between global warming and the carbon cycle. Over the past ice ages we have seen a self- reinforcing cycle in that an initial warming caused by the Earth's orbital changes appears to cause increases in CO_2 that in turn amplify the warming. We have identified several mechanisms that might increase CO_2 in the coming century above and beyond that expected from our emissions alone. For example, as the Arctic warms, permafrost soils thaw, become biologically active, and their large stock of carbon may be released to the atmosphere. Additionally, the ocean absorbs much of the CO_2 we produce, but with warming the upper layers become more stable and less CO_2 can be stored.

Other examples of climate feedbacks could also occur. For example, as warming temperatures cause snow and ice to decline, these reflective substances melt to reveal land and liquid water, which are darker and absorb more heat. The greater heat absorption by land and water further warms the planet, intensifying the warming cycle. Evaporation also increases with climate warming, contributing more heat-trapping water vapor to the atmosphere, and in turn causing more water to evaporate and more warming to occur.

Climate change has already begun to manifest in observable ways. The pattern and type of rainfall has changed in many places with fewer days having light rain and the days with greatest rain becoming not more frequent but more intense. The frequency and intensity of certain types of storms is shifting. There is some evidence that the floods and droughts are becoming more common or extensive. These regional changes and shifting temperature patterns cause plants and animals to move poleward and toward higher elevations to track the changing conditions on land and sea. The timing with which organisms become active over seasonal cycles can also be adversely affected, as when interdependent species that rely on each other for food or pollination have their cycles pushed out of sync.

Sea levels rise is climate change's elephant in the room. It threatens coastal and low-lying settlements, fresh water supplies, and the current coastal ecosystems that supply us with goods and services. The effects are particularly pressing in certain low elevation island nations, where entire nations of people could be displaced as climate refugees within this century. Over the last century the global mean sea level rose by approximately 0.2 meters [5], but projections indicate that the rate of sea level rise is accelerating. Even if we control greenhouse gases and limit warming to 2°C, the seal level will continue to rise by as much as several meters over the next few centuries. Further, sea level rise is not uniform and depends regionally on ocean warming, currents, and atmospheric winds. Sea level rise occurs via two mechanisms. First, the ocean has absorbed most of the additional

heat from global warming, and this causes the water to thermally expand[5]. Second, melting glaciers and ice sheets on land add additional water to the ocean, further exacerbating sea level rise.

Aside from the thermal effects of global change, the ocean is affected by chemical changes that result from increased atmospheric CO_2 levels. The ocean absorbs the excess CO_2 from fossil fuel burning, which reacts with water to form carbonic acid, contributing to a phenomenon called ocean acidification. The pH of the ocean has already declined 0.1 pH units, and will continue to decline by an additional 0.2-0.3 pH units by the end of the century[5]. Like sea level rise, the increased acidity will depend on regional conditions. Ocean acidification affects the fitness of certain organisms like corals and shellfish that form shells of calcium carbonate, because this material is more soluble as pH declines. The growth of marine phytoplankton may also be affected as rates of photosynthesis and respiration adjust to the new CO_2 levels[9]. Together these effects on sea life have the potential to threaten industries that rely on marine organisms, as well as how the ocean contributes to Earth's biogeochemical cycles.

TOWARD A CLEAN ENERGY REVOLUTION

Climate change is a problem that is different from other threats humanity has faced before. The global scale and accelerating pace of climate change sets it apart from other problems that can be solved at a slower pace over the course of generations as new technologies develop and public understanding evolves. Additionally, there is no single technological or social solution for climate change, because many factors contribute to it. Climate change is a pressing, existential threat that requires rapid responses and bold solutions to be implemented now if the worst of the potential outcomes are to be averted. The extent to which we curb our emissions now will determine how much adaptation we will be required to do in the future.

Limiting climate change risks requires policies that bring about reductions in emissions and incentivize the development and use of low carbon technologies. Reducing emissions could be achieved by policies that would allow emissions to be priced according to their true cost to the environment. While there are concerns about how such costs would affect the economy, it is important to note that left unchecked, climate change will certainly affect the economy in adverse ways via the natural disasters described above. Making changes now toward a clean energy economy could open the path forward to create new jobs and open new markets in the energy sector. In addition to providing incentives to lessen emissions, carbon emission abatement relies on ingenuity and technological innovation, hence supporting research and development of clean energy technologies is critical[10]. Indeed, great strides have already been made in solar, wind, and geothermal energy technologies in a few short decades. The recent Paris Agreement negotiated during the 2015 United Nations Framework Convention on Climate Change in Paris[7] also signifies a breakthrough, with an international agreement across all countries to reduce effective carbon emissions.

Developing these new technologies will require scientific vision and perseverance, traits that were exemplified by Norman Rostoker and Sherry Rowland decades ago when their ideas were first put forward. Though the technology is still undergoing refinement, the example of Rostoker's willingness to challenge accepted paradigms captures the type of bold innovation that will challenge existing assumptions about how energy is produced and help humanity take steps toward clean energy and a sustainable future. The climate crisis needs disruptive, transformational solutions to be developed through the type of technological innovation and perseverance exemplified in Rowland's and Rostoker’s research.

ACKNOWLEDGEMENTS

Thanks to Toshi Tajima, Don Blake, and Michael Prather for inspiring discussions about Rostoker and Rowland, and to Randy Olsen for thoughtful suggestions about the manuscript.

REFERENCES

1. Lidsky, L. M. End product economics and fusion research program priorities. *J. Fusion Energy* **2,** 269–292 (1982).
2. Molina, M. & Rowland, F. S. Stratospheric sink for chlorofluoromethanes: chlorine atom-catalysed destruction of ozone. *Nature* **249,** 810–812 (1974).
3. Shapiro, T. R. F. Sherwood Rowland, Nobel Prize winner, dies at 84. *The Washington Post* (2012). at <https://www.washingtonpost.com/national/health-science/f-sherwood-rowland-nobel-prize-winner-dies-at-84/2012/03/12/gIQAIQhF8R_story.html>
4. UC Irvine Strategic Communications. UCI News - UCI nuclear fusion pioneer Norman Rostoker dies at 89. *UCI News* at <http://news.uci.edu/press-releases/uci-nuclear-fusion-pioneer-norman-rostoker-dies-at-89/>
5. Pachauri, R. K. *et al.* Climate Change 2014: Synthesis Report. Contribution of Working Groups I, II and III to the Fifth Assessment Report of the Intergovernmental Panel on Climate Change. (2014). at <http://epic.awi.de/37530/>
6. Petit, J. R. *et al.* Climate and atmospheric history of the past 420,000 years from the Vostok ice core, Antarctica. *Nature* **399,** 429–436 (1999).
7. UNFCCC. COP 21. at <http://newsroom.unfccc.int/paris/>
8. Northon, K. NASA, NOAA Analyses Reveal Record-Shattering Global Temperatures. *NASA* (2016). at <http://www.nasa.gov/press-release/nasa-noaa-analyses-reveal-record-shattering-global-warm-temperatures-in-2015>
9. Mackey, K., University of California, Irvine, Morris, J. J., Morel, F. & Kranz, S. Response of Photosynthesis to Ocean Acidification. *Oceanography* **25,** 74–91 (2015).
10. Cusack, D. F. *et al.* An interdisciplinary assessment of climate engineering strategies. *Front. Ecol. Environ.* **12,** 280–287 (2014).

Fusion in a Staged Z-pinch*

F. J. Wessel[1], H. U. Rahman[1], P. Ney[1],
J. Valenzuela[2], F. Beg[2], E. McKee[3] and T. Darling[3]

[1]*Magneto-Inertial Fusion Technologies, Inc., Tustin, CA*
[2]*University of California, San Diego, CA*
[3]*University of Nevada, Reno, NV*

*presented at the Norman Rostoker Memorial Symposium, Irvine, CA August 25, 2015

Abstract. This paper is dedicated to Norman Rostoker, our (FJW and HUR) mentor and long-term collaborator, who will always be remembered for the incredible inspiration that he has provided us. Norman's illustrious career dealt with a broad range of fundamental-physics problems and we were fortunate to have worked with him on many important topics: intense-charged-particle beams, field-reversed configurations, and Z-pinches. Rostoker 's group at the University of CA, Irvine was well known for having implemented many refinements to the Z-pinch, that make it more stable, scalable, and efficient, including the development of: the gas-puff Z-pinch [1], which provides for the use of an expanded range of pinch-load materials; the gas-mixture Z-pinch [2], which enhances the pinch stability and increases its radiation efficiency; e-beam pre-ionization [3], which enhances the uniformity of the initial-breakdown process in a gas pinch; magnetic-flux-compression [4, 5], which allows for the amplification of an axial-magnetic field B_z; the Z-θ pinch [6], which predicts fusion in a pinch-on-fiber configuration; the Staged Z-pinch (SZP) [7], which allows for the amplification of the pinch self-magnetic field, B_θ, in addition to a B_z, and leads to a stable implosion and high-gain fusion [8, 9, 10].

This paper describes the physical basis for a magneto-inertial compression in a liner-on-target SZP [11]. Initially a high-atomic-number liner implodes under the action of the $\vec{J}\times\vec{B}$, Lorentz Force. As the implosion becomes super Alfvénic, magnetosonic waves form, transporting current and magnetic field through the liner toward the interface of the low-atomic-number target. The target implosion remains subsonic with its surface bounded by a stable-shock front. Shock waves that pass into the target provide a source of target plasma pre-heat. At peak compression the assembly is compressed by liner inertia, with flux compression producing an intense-magnetic field near the target. Instability develops at the interface, as the plasma decelerates, which promotes the formation of target-hot spots. Early experiments provide evidence for the magneto-inertial implosion [8, 9, 10]. Studies underway are designed to verify these predictions on the National Terawatt Facility, Zebra Generator, located at the University of Nevada, Reno. Simulations for an unmagnetized, silver-plasma liner imploding onto a deuterium-tritium plasma target, driven by a 200 TW generator, predict fusion beyond break-even, with a 200 MJ yield in an ignited plasma, with an engineering gain factor of, $G = E_{fusion}/E_{stored} \sim 20$.

INTRODUCTION

Over the past 6 decades interest in the Z-pinch continues to remain high, since it is simple to implement and it can be used to produce extreme plasma-energy-densities in the laboratory, currently of order, $\xi \simeq 0.2$ GJ/cm^3 [12]. As a science platform, Z-pinches are used frequently in the study of fundamental problems dealing with: astrophysics, material equation of state, atomic radiation, shocks, and of course fusion [13, 14, 15, 16, 17, 18, 19, 20, 21, 22, 23, 24, 25].

In a Z-pinch investigators one deal with the Magneto-Rayleigh-Taylor Instability [26, 27], which grows on the outer surface of the pinch, disrupting its axial uniformity and limiting the energy density, at peak compression. The MRTI growth rate in a Z-pinch is typically of order, $\lesssim (10\ ns)^{-1}$, and is given by [28],

$$\gamma_{MRTI} = \sqrt{kg - (\mathbf{k}\cdot\mathbf{B})^2/\mu_0\rho}\,, \tag{1}$$

where k is the wavenumber, g is the acceleration, B is the magnetic-field, and ρ is the mass density. Pre-magnetizing the pinch with an axial-magnetic field, B_z, is found to reduce the MRTI growth rate.

In the limit, $\mathbf{k}\cdot\mathbf{B} \rightarrow 0$, the growth rate may be approximated as, $\gamma_{MRTI} \simeq \sqrt{2r_0k}$, using $r_0 = \frac{1}{2}gt_i^2$ in Equation (1). Hence, it is also beneficial to initiate the pinch from a small-initial radius, r_0, although too small a radius compromises the final-implosion energy, which to first order, scales roughly as the work done on the pinch,

$$W = \int \vec{F}\cdot\vec{dr} = \frac{I_{max}^2 h}{c^2}\ln(\frac{r}{r_0}), \tag{2}$$

where I_{max} is the maximum-load current and h is the pinch length.

The intensity of a compressed, axial-magnetic field in a liner Z-pinch has been measured by Faraday rotation in a coaxial, 100-μm diameter optical fiber [4]. Transverse-laser interferometry measured the location of the liner's inner surface, indicating that the coaxial fiber was destroyed, even as the liner did not contact fully the fiber. The effect was found to be due to surface current, induced on the fiber, that suppressed field penetration, while at the same time coupling a high-pressure impulse on a timescale much shorter than the rise time of the current pulse [29, 6]. The implications for a staged-energy transfer and fusion were evident, with experiments directed toward the study of a liner-on-target (LOT) Staged Z-pinch [30, 7, 9, 10], shown in Figure 1a.

The original description for the Staged Z-pinch included flux compression and amplification of both the B_θ and B_z fields [7]. Amplification of the axial-magnetic field varies quadratically with the compression ratio,

$$B_{zf} = B_{z0}\times[r_{i0}/r_{if}]^2, \tag{3}$$

where the i & f subscripts refer to the initial and final quantities, and r_{i0} and r_{if} are the "inner" radii of the liner, respectively [4, 5]. Amplification of the azimuthal-magnetic field varies as,

$$B_{\theta f} = B_{\theta 0}\ln[r_{i0}/a_i]/\ln[r_{if}/a_f] \tag{4}$$

where a_i is the target's initial-outer radius, c.f. Figure 2. At peak compression, $r_{if}/a_f \rightarrow 1$, from Equation (4). Hence, $1/\ln[r_{if}/a_f] \rightarrow \infty$, and the compressed $B_{\theta f}$ field intensity could be potentially much greater than B_{zf}.

The description for the energy-transfer process in a SZP now includes shocks [11, 31]. The origin, timing, and dispersion of shock waves in the plasma involves many non-linear, coupled parameters [32, 33, 34, 35], which can be influenced in an experiment by adjusting: the liner and target mass distributions, their material-atomic numbers, the degree of plasma ionization, the liner and target accelerations, the local magnetic-field intensity, etc.

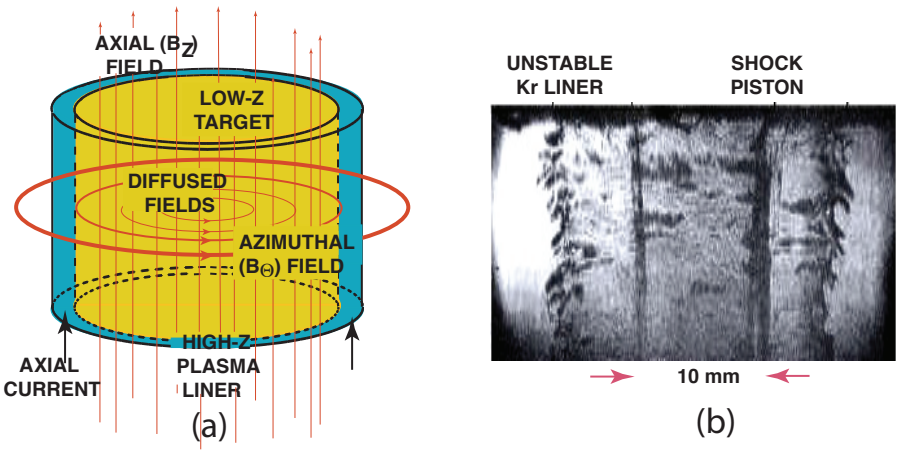

FIGURE 1. (a) Staged Z-pinch and (b) 5 ns laser schlieren image, at t = -75 ns, Kr $\rightarrow D^+$ target, with $B_{z0} = 10^{-2}$ T, $r_0 = 20$ mm.

High-intensity, compressional-sound waves arise in a Z-pinch during implosion. As the wave intensity steepens, there eventually develops a balance between dissipation and dispersion, with thin-shock fronts developing that separate

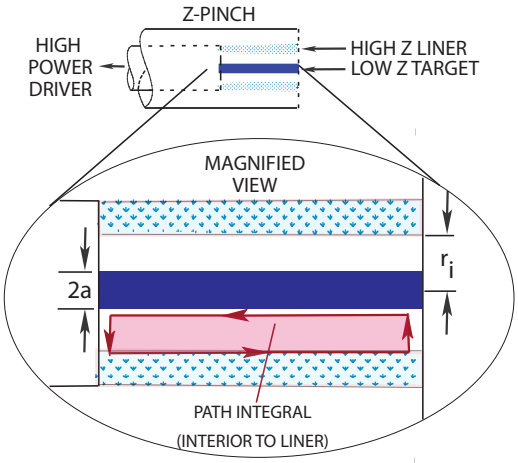

FIGURE 2. Amplification of a B_θ magnetic field in a SZP.

regimes of widely different density and temperature. The dispersion relation for magnetosonic waves propagating $\perp$ to a magnetic field is,

$$\frac{\omega^2}{k^2} = c^2 \, \frac{C_s^2 + V_A^2}{c^2 + V_A^2} \ , \tag{5}$$

(6)

with a wave speed,

$$V_{ms} \simeq \sqrt{C_s^2 + V_A^2}, \tag{7}$$

where B is the magnetic field, $C_s = \sqrt{ZT_e/M_i}$ is the sound speed, $V_A = B/(\mu_0\rho)^{1/2}$ is the Alfvén speed, c is the speed of light, and ρ is the plasma-mass density. MS waves transport current in plasma [36]. Figure 1b displays a R-Z, laser-image profile for the SZP, obtained during implosion, illustrating that an implosion shock front develops which is stable and distinctly separated from the unstable, outer surface of the liner.

As a B_z field can help stabilize the Z-pinch, confine fusion products, and suppress thermal conduction and material mixing [37], its use in Z-pinches still remains a topic of considerable debate. As the total-system energy partitions between the plasma-target thermal energy and the compressed-magnetic field energy, it is desirable that the high-field region for B_z be restricted to locations outside the target plasma, otherwise, the plasma-thermal energy at final compression will be reduced, compared to a pinch without a B_z.

Shock-driven implosions have been produced in an initially unmagnetized, high-atomic number, Z-pinch plasma [38, 39]. Simulations, provided below, suggest that the pinch can be designed to remain stable, until the moment of peak compression. The small amount of instability that does arise actually promotes the formation of target hot spots, at the most opportune time. The result is fusion ignition and an energy yield than is far greater than for a similar pinch that is initially magnetized [31].

High-Z plasmas are typically avoided in a Z-pinch liner, since they are highly radiative, which competes with the desire for a high final temperature. The cooler temperature also makes the plasma more resistive, promoting field penetration into the liner, which reduces the pinch-compressional force. In the SZP, the azimuthal-magnetic field is transported by MS waves, ahead of the slower-moving "liner-piston", stagnating near the target interface, and providing a means to pre-heat and pre-compress the target, prior to the peak pinch compression by liner inertia [11], elevating its adiabatic trajectory, and providing a stable, high-final-energy density.

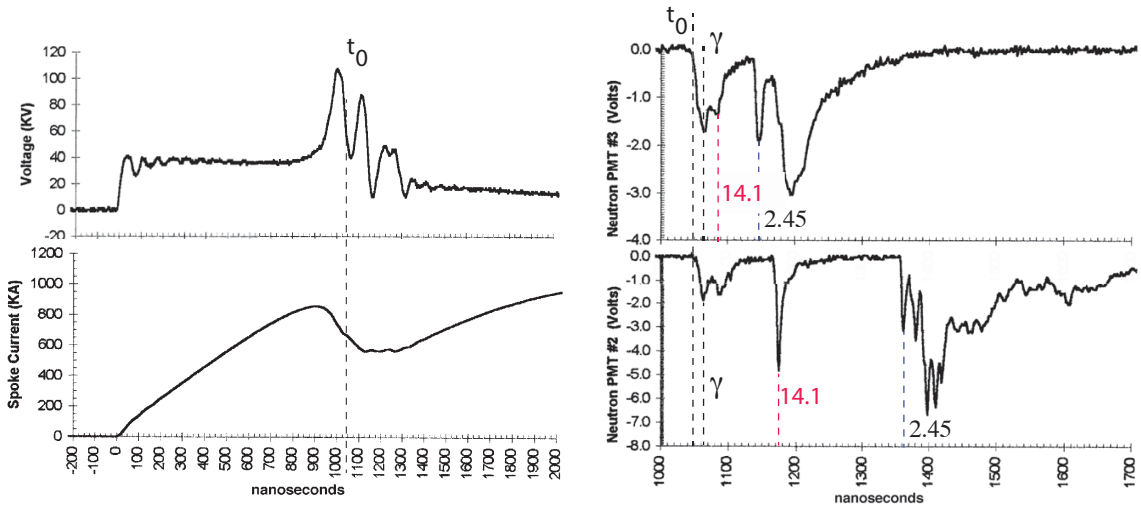

FIGURE 3. UCI SZP data: voltage, current, and neutron TOF signals for shot 697: $B_0 = 10^{-2}$ T, $r_0 = 20$ mm, Kr $\rightarrow$ D^+.

UC IRVINE SZP EXPERIMENTS

Shock fronts were first observed in an unmagnetized, gas-mixture (90% D_2 and 10% Ar, by mass) Z-pinch [38], as a uniform axial structure located within the liner, as illustrated in Figure 1b. This structure was initially postulated to be due to a charge-to-mass-ratio separation in the imploding plasma [40, 39, 41]. LOT Z-pinch implosions on the Magpie Z-pinch, at the Imperial College, London, also provide solid evidence for radially-converging shocks, using a fast, high-resolution, axial-imaging system [42].

It is well established that shocked surfaces may be used to accelerate plasmas to high velocities, without instability [33, 43, 44]. And in the particular case of the SZP, the high-Z, heavy mass liner accelerates a low-Z, low mass target, which is stable. SZP experiments at the UC Irvine, in the mid- to late 90's, configured the Z-pinch as a magnetized, Kr liner imploding onto a D^+ plasma target ($I_{peak} = 1.5$ MA, $\tau_{1/4} \sim 1$ μs, $E_{stored} = 50$ kJ). The pulsed, laser Schlieren image of the imploding pinch, shown in Figure 1(b), was recorded approximately 75 ns before peak compression [45], demonstrating that the liner and shock front have different implosion speeds, with instability present on the outer surface of the liner and a stable-shock front present inside the liner.

The UCI SZP experiments also used neutron-bubble detectors to estimate the total-neutron-yield per shot, finding it to be in the range, $Y_{neutrons} \sim 0.5 - 1 \times 10^{10}$, consistent with total-yield measurements obtained using a calibrated, silver-foil-activation detector and the predictions of simulations using the MACH2 MHD code [9]. Time-of-flight (TOF) measurements indicate that secondary neutrons were also produced [8]. Secondaries require triton confinement in a high-magnetic field. Recent reports for the (LOT) MagLIF Z-pinch experiments, where an axial field was pre-injected, also measure a significant secondary yield [46].

Figure 3 displays a panel for the UCI data: a) load voltage, b) discharge current, c) TOF neutron detector, located at 2.0-m, and d) TOF neutron detector, located 6.8-m. The pinch occurs at, $t = 1054$ ns, as indicated by the vertical-dotted lines on the voltage and current traces. The TOF data indicate the times for the prompt γ rays, 14.1 MeV, and 2.45 MeV neutron signals, dispersed based on their distance from the source. For $B_{z0} = 10^{-2}$ T, the compressed-axial field is of order, $B_{zf} \sim 5$ T, which is insufficient to confine tritons, gyro-radius, $\rho_T \sim 200$ mm. However, estimates suggest, $B_{\theta f} \sim 200$ T, with $\rho_T \sim 1$ mm, which may be sufficient to confine tritons. Alternately, axial-flux compression may lead to inductive-ion acceleration, effects that have yet to be understood and quantified.

Figure 4 compares streak images obtained on the UCI experiments (top) with simulated, radiation-intensity profiles (bottom), for two different Z-pinch configurations: 1) a Kr liner $\rightarrow$ D^+ target, $B_z(0) = 0$, and 2) a SZP, with a Kr liner $\rightarrow$ D^+ target and $B_z(0) = 10^{-2}$ T. The simulated images display the total-radiation intensity calculated from free-free, free-bound, and bremstrahlung radiation. Images from the experiment display a bright-converging, shock surface, located inside the pinch, that arrives on-axis prior to the liner [45]. The top right-side image, where an axial field is used, indicates that the central region of the pinch appears to be hollow, which is due to the lower-radiative

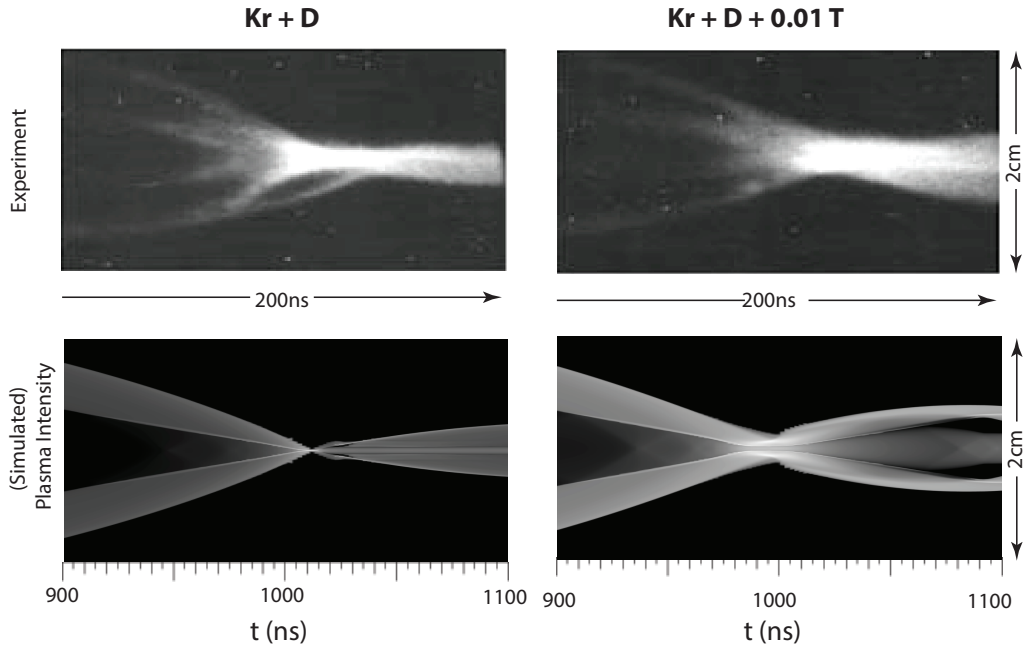

FIGURE 4. SZP streak images (top) and simulated radiation intensity (bottom), for 200 ns centered on the peak implosion.

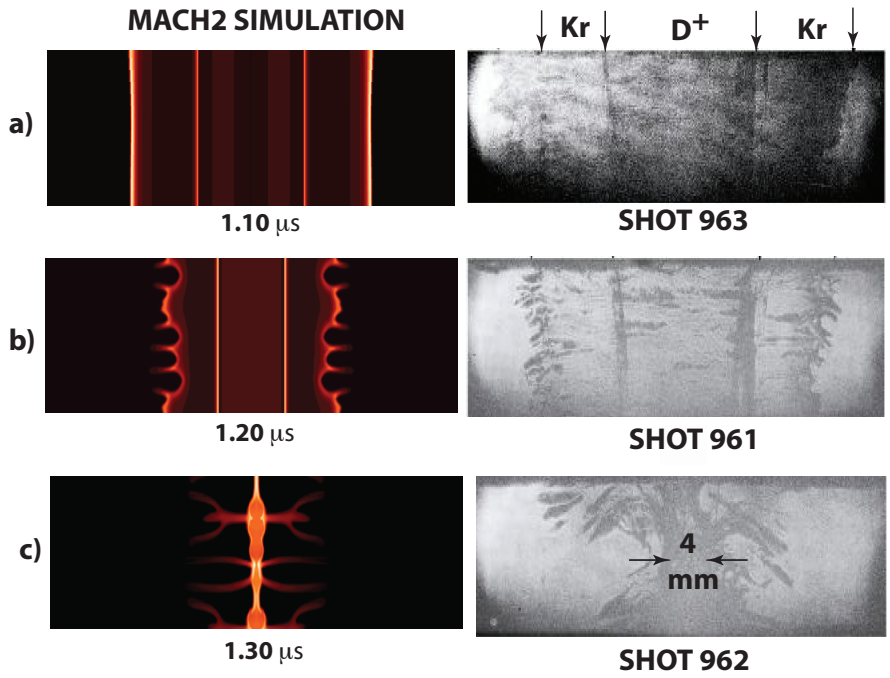

FIGURE 5. SZP schlieren images (right) vs. simulated contours for n_{ion} (left): $B_0 = 10^{-2}$ T, $r_0 = 20$ mm, Kr $\rightarrow$ D^+.

emission of the magnetically-confined, hydrogenic plasma-target.

Figure 5 compares Schlieren images obtained on the experiments (right side) for an imploding Staged Z-pinch

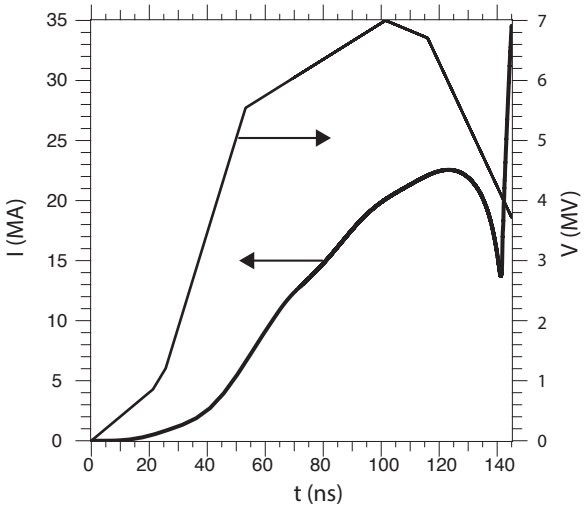

FIGURE 6. Voltage and current profiles for the 200 TW generator simulation.

(shots 963, 961, and 962) with simulations (left side) for the ion density iso-countours in the RZ-plane, obtained from MACH2. The Schlieren and simulation images agree that as the implosion proceeds the outer boundary of liner plasma becomes more unstable due to the MRTI, whereas the shock piston is stable until peak compression.

SZP SIMULATIONS FOR A 200 TW GENERATOR

We have prepared simulations for an unmagnetized, 3-mm initial radius, solid liner imploding onto a 2.9-mm radius, DT target plasma, and Table 1 summarizes the design parameters and simulation results for this study. The driver parameters used are typical of a 200 TW pulsed-power generator, similar to the Sandia National Laboratories, Z Facility, currently in operation. The circuit voltage and pinch current time profiles are illustrated in Figure 6. Previously published simulations considered a $r \sim 5$ - 20 mm, Xe plasma liner $\rightarrow$ DT target plasma pinch [47], however the present configuration provides a far greater fusion-energy yield.

TABLE 1. Simulations for a SZP driven by a 200 TW generator.

Liner Material & Initial Temperature, T_{liner_0} [meV]	Ag, 20
Target Material & Initial Temperature, T_{target_0} [eV]	DT, 10
Initial Liner Radius & Thickness, r_0 [mm], Δr [μm]	3, 100
Liner & Target Density, ρ_L [kg/m$^3 \times 10^3$], ρ_T [kg/m^3]	10, 8
Peak Load Current & Implosion Time, I_z [MA], τ_i [ns]	23, 141
Minimum Pinch Radius & Dwell Time, r_f [μm], τ_d [ns]	150, 0.6
Peak Ion Density & Temperature, $\hat{n}_i$ [10^{18} m^{-3}], $\hat{T}_i$ [keV]	7, 40
Peak Kinetic- & Ion-Thermal Energy, $\hat{E}_k$, $\hat{E}_i$ [MJ]	1.1, 0.8
Peak Azimuthal Magnetic Field, $\hat{B}_\theta$ [kT]	35
Fusion Energy, $E_{fusion} = E_n + E_\alpha$ [MJ]	400
Energy Gain, G = $E_{fusion}/\hat{E}_i$	200
Neutron Yield, Y [10^{20}/shot]	1

MACH2 is a 2-1/2D MHD code, which contains the essential-physics for the SZP [48, 49]. MACH2 was also modified to include an inductive-electric field, produced when the magnetic fields are compressed. The code solves

the continuity, momentum, energy, and magnetic-field equations, using a finite-volume-differencing technique on a R-Z grid of quadrilateral cells and computes three components of the ($\vec{v}$ and $\vec{B}$) vector fields, outputting the results as two-dimensional profiles. The circuit package uses a specified voltage profile as an input, with the load current calculated for the time-changing pinch parameters.

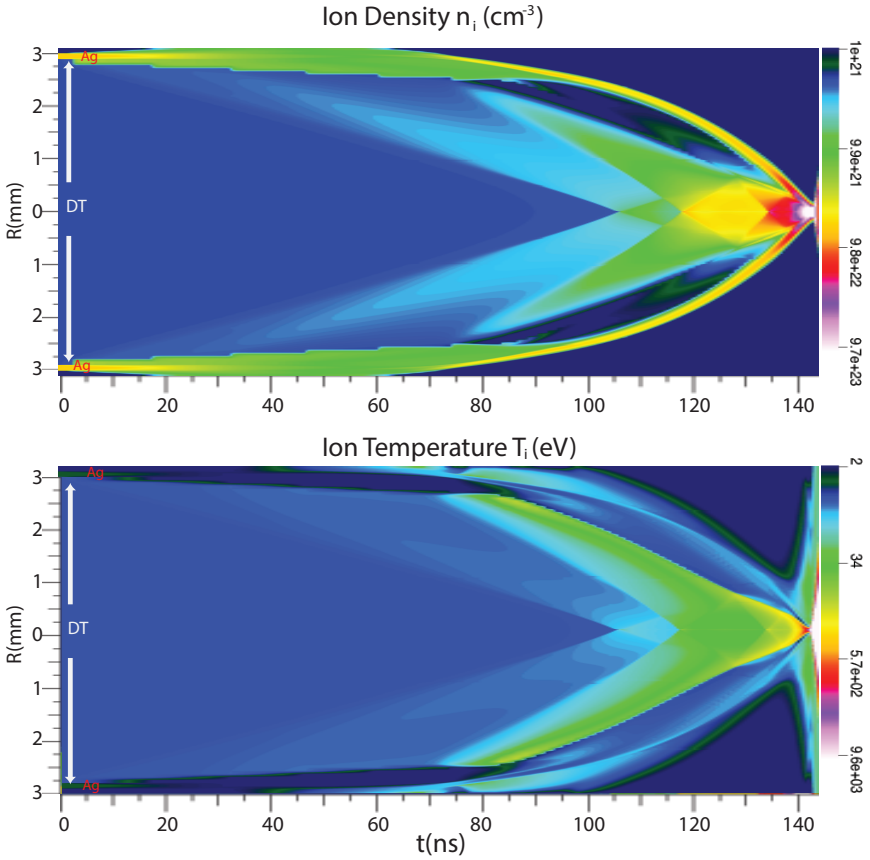

FIGURE 7. Ion density, n_i, and ion temperature, T_i, as a function of radius, r, and time, t, for Table 1 parameters.

Simulations are run in Eulerian mode axially, and ALE radially. The plasma equations-of-state and transport variables (radiation opacities, thermal and electrical conductivity, etc.) are obtained from semi-empirical (LANL SESAME) tables. Radiation is calculated using the built-in, non-equilibrium, flux-limited diffusion package, with Planck- and Rosseland-mean opacities. A 5% initial, density-perturbation is applied randomly, on a cell-by-cell basis, throughout the computational grid, to seed the MRTI growth; higher perturbation levels reduce the quality of the compression, but do not affect significantly the relative results. Before simulating 2D profiles, the code is run in 1D to determine appropriate load masses that optimize the output yield. For the same parameters, the 2D yields are typically 1/2 as large as the 1D yield.

The axially-averaged, ion densities and ion temperatures are displayed in Figure 7, as a function of r and t. Shortly after the load current builds, the Ag liner expands inward, producing reflections in the target densities and temperatures, as the target plasma compresses to the axis. Around 75 ns an inner surface, shock front separates from the Ag liner, converging to the axis more rapidly than does the liner, stagnating at the target interface. The use of the thin, high-Z liner promotes penetration of the axial current toward the axis that continues to build, during implosion, on the shock-front boundary. Shock waves that pass inside the target reflect off the liner-target interface, causing the plasma target to heat continuously during implosion. Peak compression occurs at roughly, $t_i \sim 141$ ns, when the liner stagnates, compressing the target plasma inertially and adiabatically to 7 keV, with hot spot temperatures in excess of 10 keV. Thus, distinct stages of energy delivery are correlated with the full compression cycle: initially the

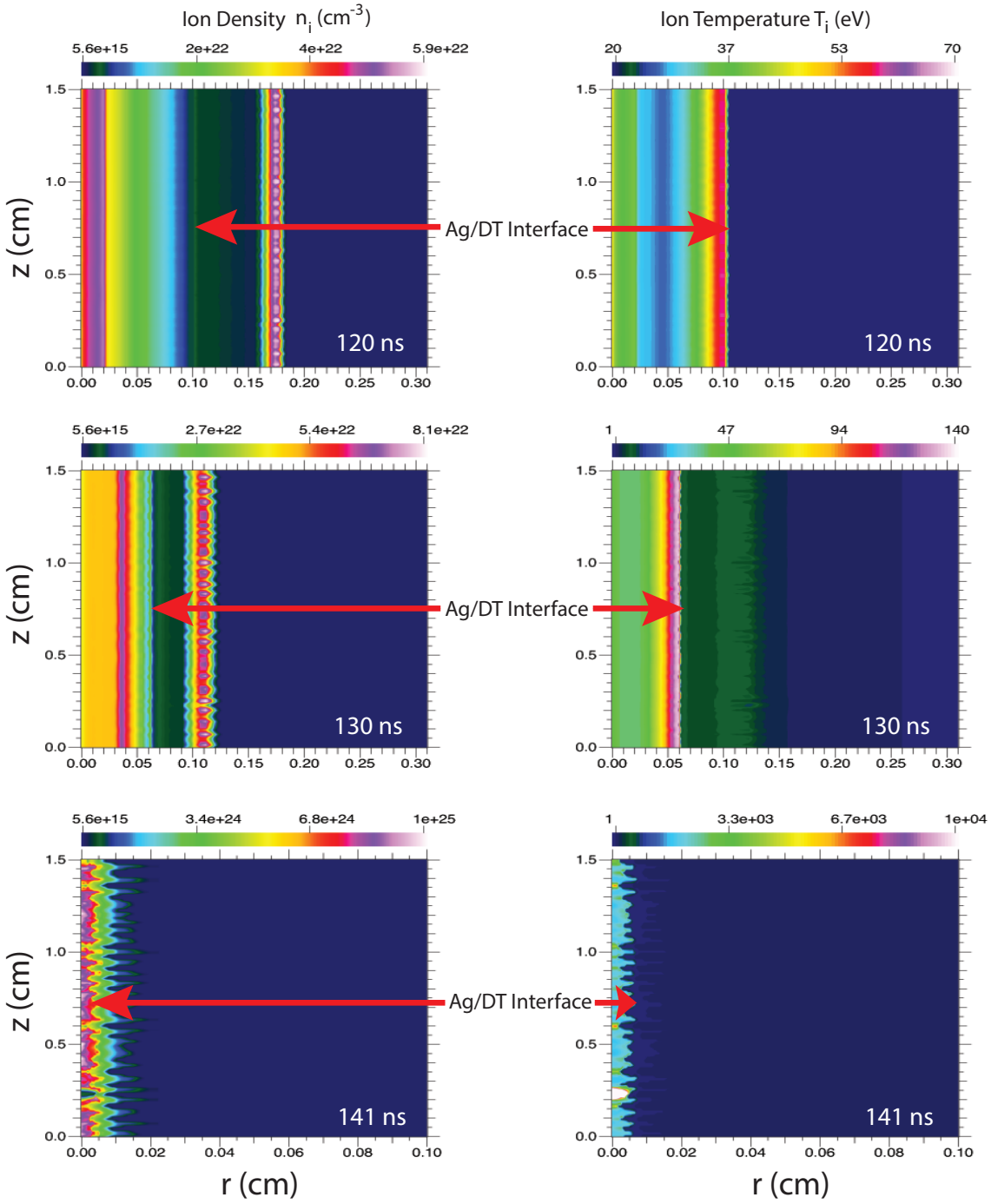

FIGURE 8. R-Z contours for ion density, n_i (left), and ion temperature, T_i (right), at 130, and 140 ns (top to bottom).

liner is heated ohmically, followed by shock heating of the target, and finally adiabatic heating of the target, as the magnetically accelerated liner compresses the entire system inertially.

2D contours are shown in Figure 8 for the ion density, n_i (left), and ion temperature, T_i (right), at 120, 130, and

141 ns; note the expanded radial scale used on the 141 ns panel. Secondary shocks are observed to propagate back and forth, within the liner and target. At 120 ns the liner's outer surface has moved from 3 mm to 0.18 cm and the shock front is located at 0.12 cm. At 130 ns the outer surface of the liner plasma implodes to 0.112 cm and begins to show evidence for the growth of the MRTI, wavelength, $\lambda_{RT} \sim 400\ \mu$m, while the interface is located at 0.062 cm and remains axially uniform and stable. At this time the target-ion temperature is 50 to 140 eV and its density is above solid, even as the liner-plasma temperature is less than 10 eV.

At 141 ns the liner radius is 0.01 cm, with noticeably more MRTI, even as the target achieves a final radius of 0.005 cm, ion density, $n_i \sim 1.0 \times 10^{25}$ cm^{-3}, and ion temperature, $T_i \sim 3$ -10 keV. Although instability penetrates into the target, it is not sufficient to disrupt the uniformity of the target, and in fact, it helps by forming hot spots that promote ignition. Hot-spots that are present are characterized by a temperature that is several times higher than the bulk plasma. The liner-convergence ratio is, $C_L = r_{L0}/r_{Lf} \sim 30$, whereas for the target it is, $C_T = r_{T0}/r_{Tf} \sim 50$.

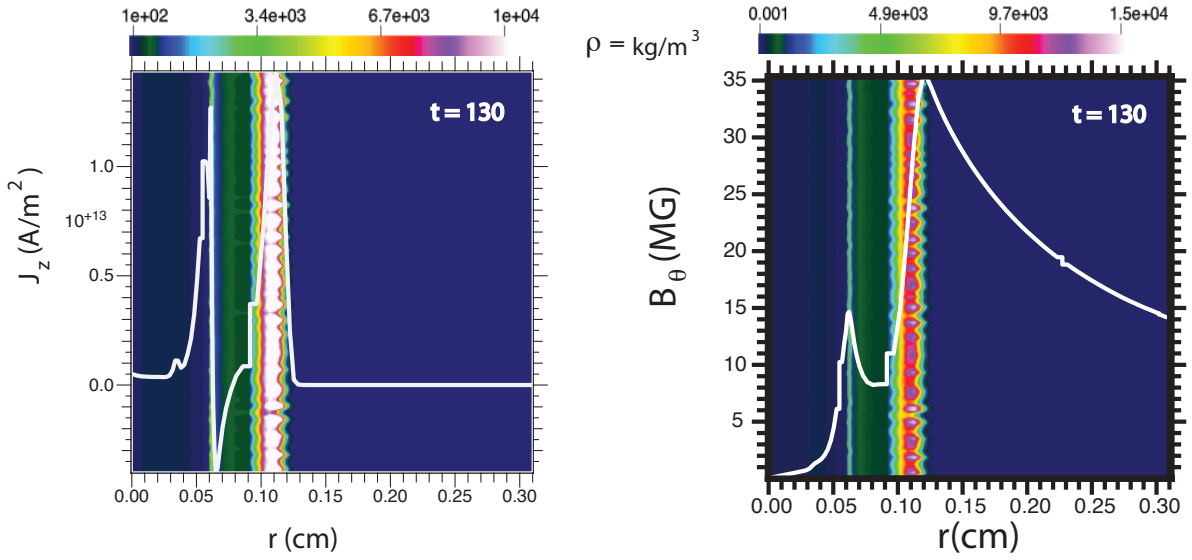

FIGURE 9. Current density, J_z (left), and azimuthal-magnetic field, B_Θ (right) at 130 ns. The color contours are mass density, ρ.

Figures 9 and 10 plot the mass density, ρ (as 2D surface-color contours), overlaid with line-plots for the axial-current density, J_z (left side) and azimuthal field, B_Θ (right side), at 130 ns and 141 ns, respectively. At 130 ns the current density in the liner and the target are similar in magnitude, in the range of, $J = 1.0 \times 10^{13}$ A/m^2. Note how the current density reverses sign at the interface, characteristic of current-density profiles that trap magnetic flux between the shocked layer and the liner plasma. The reversal of the interface-current density is due to a closed-current loop that exists between the target and liner and trapping of the azimuthal-magnetic-flux in close proximity to the target. At this time the peak-azimuthal-magnetic field rises to, $\hat{B}_\theta = 15$ MG near the target interface, and $\hat{B}_\theta = 35$ MG at the liner's outer surface.

At 141 ns (peak implosion, c.f., Figure 10) the current density near the target is, $J = 1.3 \times 10^{15}$ A/m^2, producing a peak-azimuthal-magnetic field of, $\hat{B}_\theta = 175$ MG. At the liner the current density is, $J = 5.0 \times 10^{14}$ A/m^2, with $\hat{B}_\theta = 375$ MG. This field intensity is clearly sufficient to confine fusion-produced alpha particles, with a gyro-radius, $\rho_\alpha \lesssim 0.1\ \mu$m.

The shock behavior in the SZP is clarified by examining the radial-velocity profiles for the plasma-implosion velocity, V_r, the Alfvén velocity V_A, the sound velocity C_s, and the magnetosonic velocity, V_{ms}. Figure 11 plots these profiles at 130 ns (right) and 140 ns (left). For both time steps the liner implodes super-Alfvénically, and the target implodes subsonically. Magnetosonic shocks are responsible for transporting axial current (and azimuthal-magnetic field) inward to the target interface, producing a shock front and a secondary-current channel, the intensity of which increases during the implosion, according to Equation (2), as the entire assembly is compressed by liner inertia.

Figure 12(a) displays the simulated, axially-averaged, plasma-thermal and magnetic pressures vs. time and Figure 12b displays the energie-time profiles, for the fusion energy, E_f, kinetic energy, E_k, ion-thermal energy, E_i, and

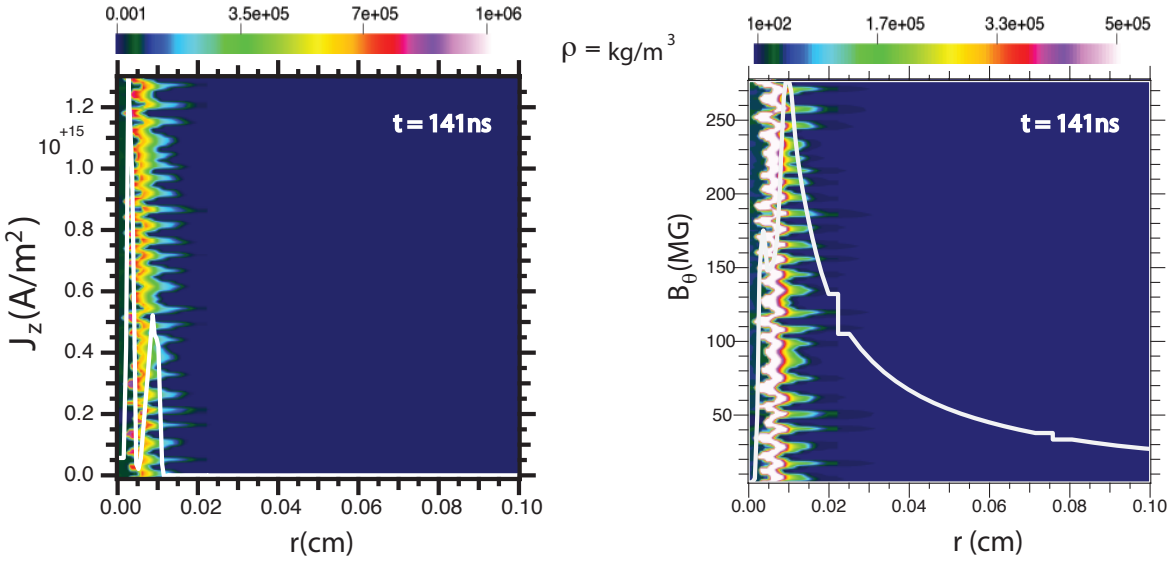

FIGURE 10. Current density, J_z (left), and azimuthal-magnetic field, B_Θ (right) at 141 ns. The color contours are mass density, ρ.

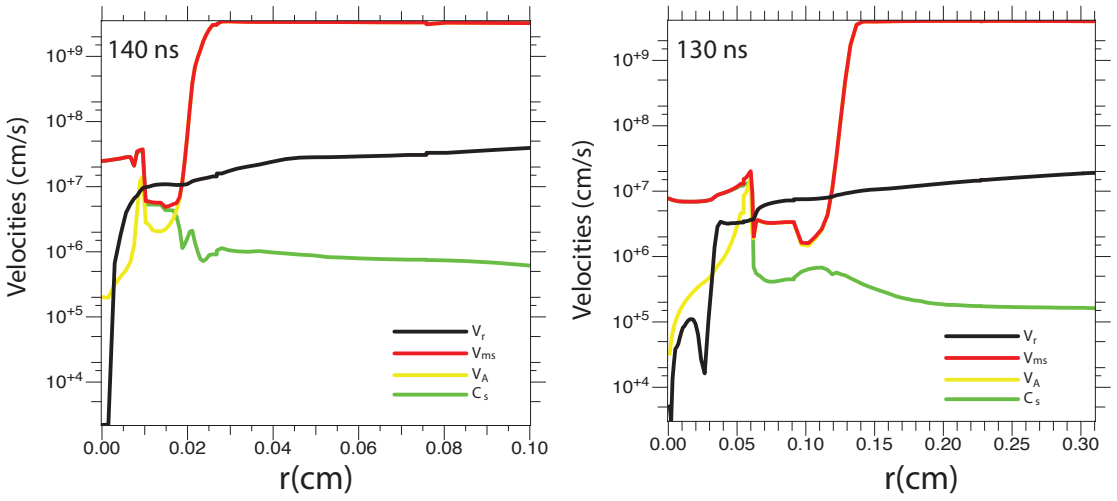

FIGURE 11. Radial profiles for the plasma-implosion speed, v_r, the Alfvén velocity V_A, the sound velocity C_s, and the magnetosonic velocity, v_{ms}, at 130ns and 140 ns.

radiation energy, E_r, over the expanded-time period, from 130 → 145 ns.

At peak compression the plasma pressure approaches a peak value of 10^3 Gbar, exceeding the B_θ magnetic-field pressure. Shock convergence to the axis produces spikes in the plasma pressure, observed in Figure 12 at roughly 125 ns, 135 ns and 141 ns. These spikes are not evident in the magnetic-pressure profile, since it is averaged over a larger plasma volume, and is more reflective of the liner inertia. If the pinch was pre-magnetized with an applied B_z field, there would be a close coupling of the compressed-axial field and plasma pressures, with the two pressures being nominally comparable, as well as much closer to the peak pressure recorded for the azimuthal-magnetic field.

In Figure 12(b) the plasma-thermal energy increases significantly at roughly at 137 ns, continuing through the fusion burn cycle to approximately 142 ns. Over this period the liner-kinetic energy reaches a local maximum of,

E_k = 1 MJ, at roughly 139 ns, decreasing as the plasma stagnates, with a dwell time of roughly, τ_d ~0.6ns, followed abruptly by an order of magnitude increase in E_k, as the fusion burn transitions to full ignition at roughly 141 ns. During this period the radiation energy output remains relatively flat in time, reaching a peak value of, $E_r \sim 0.6$ MJ, which is fully consistent with simple estimates for the plasma density, temperature, and atomic number characterizing this plasma (using the NRL Plasma Formulary).

α-particle production increases rapidly at roughly 140 ns, providing an additional source of heat energy to the ions and ignition, as the ion energy increases rapidly to 20 MJ, at 141.5 ns. The total fusion-energy yield, including α-particles and neutrons, is almost 400 MJ at 141.5 ns. The fusion-energy gain produced is, $Q = E_{fusion}/E_{ion} > 200$, and the total-energy gain, $G = E_{fusion}/E_{stored} \sim 20$.

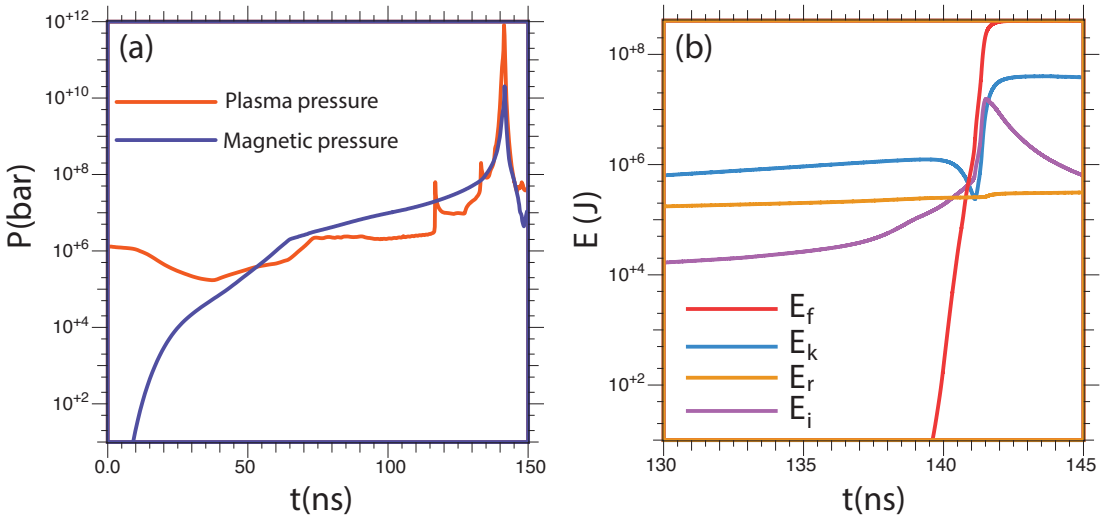

FIGURE 12. (a) Plasma & magnetic pressures vs. t. (b) Energies vs. t: fusion, E_f, kinetic, E_k, ion thermal, E_i, and radiation, E_r.

DISCUSSION

The above simulations are for an idealized, Z-pinch load configuration. There are legitimate concerns pertaining to the choice of the small-initial diameter for the load, the liner and target initial temperatures, and the specific choice of the radiation model used. For example, the present simulation considers a uniform, and thin, distribution of the load masses, which may be difficult to achieve in a real experiment, especially with prescribed initial temperatures. The small-initial radius for the pinch also presents a higher-load inductance than does one with a larger-initial radius, which may also contribute to current loss in the generator's power feeds, providing less compressional force and inertia than calculated. Material mixing and end-losses may also reduce the target's final temperature. For our simulations the built-in radiation model and SESAME data tables are what's presently available in the code: and there may be better alternatives [50, 51]. Since the target plasma is low-atomic-number, A = 1, treatment of its radiation is greatly simplified, relative to that for the high-atomic-number liner. Toward this end we have also recently simulated a magnetized, Beryllium liner → Deuterium target implosion, representative of the MagLIF experiments [37, 52], as real data exists for this LOT Z-pinch configuration. The results of those simulations are with close agreement with observations.

Notable differences between the SZP and the simulated parameters for the MagLIF configuration are: the liner-atomic number, Ag (A = 47) vs. Be (A = 4); the liner thickness, 100 μm vs. 500 μm; the initial-target temperature, 2 vs. 10 eV; and the pinch length, 1.5 cm vs. 0.75 cm, respectively. The 10 eV initial-target temperature used in the above simulation compensates for the fact that the 100 eV temperature assumed in the experiment is applied at a later time during the implosion, when the plasma liner begins to accelerate. As shown, the predictions from the simulation agree well with the measured data for the final-pinch radius, final-target temperature, compressed-axial-magnetic field, and

total-neutron yield [53, 46]. Nevertheless, the present simulations provide a fair basis to predict the outcome for a real experiment and to compare competing Z-pinch load designs.

CONCLUSIONS

We present an experimental and computational case for the Staged Z-pinch. Early experiments at low pinch current and stored energy, ~ 1.2 MA, 50 kJ, demonstrate that a high-Z liner on low-Z target compression will provide a stable-shock front compression of the target, even in the presence of liner instability, and prior to inertial compression by the liner. Shocks arise due to the large difference between the liner and target atomic numbers, their atomic masses, and dynamic temperature profiles. Magnetosonic shocks beneficially alter the implosion dynamics, allowing for axial-current transport, magnetic-field compression, enhanced-energy coupling, and pinch stabilization. Simulations for pulsed-power parameters that may be realistically attained on an advanced-implosion generator, configured with a Ag liner → DT target, are predicted to achieve a radial convergence ratio for the liner of, $C_{liner} \sim 30$, and for the target of, $C_{target} \sim 50$. At peak compression the azimuthal-magnetic field is flux-compressed to, $B_\theta > 30$ kT, sufficient to trap fusion-alpha particles and to allowing them to deposit their energy in the target plasma, which leads to fusion ignition. The simulated neutron-output yield for these conditions is, $Y > 1.0 \times 10^{20}$, the fusion-energy output is, $E_{fusion} > 400$ MJ, and the fusion-energy gain factor is, $Q = E_{fusion}/E_{ion} > 200$, with a total-energy gain of, $G = E_{fusion}/E_{stored} \sim 20$, where E_{stored} is the capacitor-bank energy.

ACKNOWLEDGEMENTS

The authors (FJW and HUR) would like to express their special gratitude to Amnon Fisher, Technion, Israel, for first introducing us to the technology of Z-pinches and for his continuing support and guidance over the past 4 decades. Alan Van Drie, Tri Alpha Energy, is also acknowledged as one of the key participants in the early development of the SZP and its experimental implementation at UCI. Our participation in this symposium and the preparation of this paper is supported by the Advanced Research Projects Agency-Energy, US Department of Energy, DE-AR0000569.

REFERENCES

[1] J. Shiloh, A. Fisher, and N. Rostoker. Z pinch of a gas jet. *Physical Review Letters*, volume 40:p. 515 (1978).

[2] J. Bailey, Y. Ettinger, A. Fisher, and N. Rostoker. Gas-puff Z-pinches with D2 and D2-Ar mixtures. *Applied Physics Letters*, volume 40(6):pp. 460–462 (1982).

[3] E. Ruden, H. U. Rahman, A. Fisher, and N. Rostoker. Stability enhancement of low initial density hollow gas puff Z-pinch by e-beam preionization. *Journal of Applied Physics*, volume 61:p. 1311 (1987).

[4] F. J. Wessel, F. S. Felber, N. C. Wild, and H. U. Rahman. Generation of high magnetic fields using a gas-puff Z-pinch. *Applied Physics Letters*, volume 48(48):p. 1119 (1986).

[5] F. S. Felber, M. M. Malley, F. J. Wessel, M. K. Matzen, M. A. Palmer, R. B. Spielman, M. A. Liberman, and A. L. Velikovich. Compression of ultrahigh magnetic fields in a gaspuff z pinch. *Physics of Fluids*, volume 31(7):pp. 2053–2056 (1988).

[6] H. U. Rahman, P. Ney, F. J. Wessel, A. Fisher, and N. Rostoker. *Thermonuclear fusion by Z-Θ pinch*, volume 195 of *AIP Conference Series*. American Institute of Physics (1989).

[7] H. U. Rahman, F. J. Wessel, and N. Rostoker. Staged Z-pinch. *Physical Review Letters*, volume 74:p. 714 (1995).

[8] F. J. Wessel. Staged Z-pinch. *Final Report*, volume DoE FG03-93ER544220 (2000).

[9] P. Ney, H. U. Rahman, N. Rostoker, and F. J. Wessel. Staged z-pinch for controlled fusion. *Physics of Plasmas*, volume 8:p. 616 (2001).

[10] H. U. Rahman, F. J. Wessel, N. Rostoker, and P. Ney. High Yield Fusion in a Staged Z-pinch. *Journal of Plasma Physics* (2009).

[11] H. U. Rahman, F. J. Wessel, P. Ney, R. Presura, R. Ellahi, and P. K. Shukla. Shock waves in a Z-pinch and the formation of high energy density plasma. *Physics of Plasmas*, volume 19:pp. 122701:1–13 (2012).

[12] M. R. Gomez, S. A. Slutz, A. B. Sefkow, K. D. Hahn, S. B. Hansen, P. F. Knapp, P. F. Schmit, C. L. Ruiz, D. B. Sinars, E. C. Harding, C. A. Jennings, T. J. Awe, M. Geissel, D. C. Rovang, I. C. Smith, G. A. Chandler, G. W. Cooper, M. E. Cuneo, A. J. Harvey-Thompson, M. C. Herrmann, M. H. Hess, D. C. Lamppa, M. R. Martin, R. D. McBride, K. J. Peterson, J. L. Porter, G. A. Rochau, M. E. Savage, D. G. Schroen, W. A. Stygar, and R. A. Vesey. Demonstration of thermonuclear conditions in magnetized liner inertial fusion experimentsa). *Physics of Plasmas*, volume 22(5):056306 (2015).

[13] W. H. Bennett. Magnetically self-focussing streams. *Physical Review*, volume 45:p. 890 (1934).

[14] T. G Paget and B. Moses. Improvements in, or relating to, gas discharge apparatus for producing thermonuclear reactions. U.K. Patent GB817681 (1947).

[15] O. A. Anderson, W. R. Baker, S. A. Colgate, J. Ise, and R. V. Pyle. Neutron production in linear deuterium pinches. *Phys. Rev.*, volume 110:p. 1375 (1958).

[16] D. C. Hagerman and J. W. Mather. Neutron production in a high-power pinch apparatus. *Nature*, volume 181:p. 226 (1958).

[17] S. Glasstone and R. H. Lovberg. *Controlled Thermonuclear Reactions*. Van Nostrand-Reinhold, Princeton, NJ (1960).

[18] J. D. Sethian. The quest for a z-pinch based fusion energy source – a historical perspective. *AIP Conf. Proceedings, Dense Z Pinches*, volume 1(3):p. 409 (1997).

[19] M. K. Matzen. Z-pinches as intense x-ray sources for inertial confinement fusion applications. *Fusion and Engineering Design*, volume 44:pp. 287–294 (1999).

[20] R. B. Spielman and J. S. De Groot. Z-pinches—a historical view. *Laser and Particle Beams*, volume 19:pp. 509–525 (2001).

[21] J. E. Bailey, G. A. Chandler, D. Cohen, M. E. Cuneo, M. E. Foord, R. F. Heeter, D. Jobe, P. W. Lake, J. J. MacFarlane, T. J. Nash, D. S. Nielson, R. Smelser, and J. Torres. Radiation science using z-pinch x rays. *Physics of Plasmas*, volume 9(5):pp. 2186–2194 (2002).

[22] A. L. Velikovich, R. W. Clark, J. Davis, Y. K. Chono, C. Deeney, C. A. Coverdale, C. Ruiz, G. Cooper, J. Franklin, L. I. Rudakov, and Albuquerque NM. Sandia National Laboratories. Z-pinch plasma neutron sources (2006).

[23] G. A. Rochau, J. E. Bailey, Y. Maron, G. A. Chandler, G. S. Dunham, D. V. Fisher, V. I. Fisher, R. W. Lemke, J. J. MacFarlane, K. J. Peterson, D. G. Schroen, S. A. Slutz, and E. Stambulchik. Radiating shock measurements in the z-pinch dynamic hohlraum. *Phys. Rev. Lett.*, volume 100:p. 125004 (2008).

[24] M. G. Haines. A review of the dense z-pinch. *Plasma Physics and Controlled Fusion*, volume 53:pp. 093001:1–168 (2011).

[25] J. L. Giuliani and R. J. Commisso. A review of the gas-puff z-pinch as an x-ray and neutron source. *IEEE Transactions on Plasma Science*, volume 43(8):pp. 2385–2453 (2015).

[26] S. Chandrasekar. *Hydrodynamic and Hydromagnetic Instability*. Dover, NY (1981).

[27] E. Teller. *Fusion*. Academic Press, NY (1981).

[28] A. B. Budko, A. L. Velikovich, M. A. Liberman, and F. S. Felber. Development of rayleigh-taylor and bulk convective instabilities in the dynamics of plasma liners and pinches. *Sov. Phys. JETP*, volume 69(1):pp. 76–88 (1989).

[29] H. U. Rahman, F. S. Felber, F. J. Wessel, N. Rostoker, M. A. Lieberman, and A. L. Velikovich. *Megagauss Technologies and Pulsed Power Applications*, volume 1, p. 191. Plenum, C. M. Fowler, R. S. Caird, and D. J. Erickson (1987).

[30] F. J. Wessel, B. Etlicher, and P. Choi. Implosion of an aluminum plasma jet onto a coaxial wire: enhanced stability and energy transfer. *Physical Review Letters*, volume 69(22):p. 3181 (1992).

[31] F. J. Wessel, H. U. Rahman, P. Ney, and R. Presura. Fusion in a staged z-pinch. *IEEE Transactions on Plasma Science*, volume 43(8):pp. 2463 – 2468 (2015).

[32] C. F. Kennel and R. Z. Sagdeev. Collisionless shock waves in high beta plasmas. Technical report, International Atomic Energy Agency (1966).

[33] IA. B. Zeldovich, IU. P. Raizer, Wallace D. Hayes, and Probstein R. F. *Physics of shock waves and high-temperature hydrodynamic phenomena*. Academic Press, NY (1966).

[34] P. K. Shukla, M. Y. Yu, H. U. Rahman, and K. H. Spatschek. Nonlinear convective motion in plasmas. *Physics Reports*, volume 105:pp. 227–228 (1984).

[35] R.C. Sagdeev and C.F. Kennel. Collisionless shock waves. *Scientific American*, volume 264(4):p. 106 (1991).

[36] Hannes Alfven. Existence of electromagnetic-hydrodynamic waves. *Nature*, volume 150(3805):pp. 405–406 (1942).

[37] S. A. Slutz, M. C. Herrmann, R. A. Vesey, A. B. Sefkow, D. B. Sinars, D. C. Rovang, K. J. Peterson, and M. E. Cuneo. Pulsed-power-driven cylindrical liner implosions of laser preheated fuel magnetized with an axial field. *Physics of Plasmas*, volume 17(5):056303 (2010).

[38] J. E. Bailey. Effect of radiation cooling and plasma atomic number on z-pinch dynamics. *ProQuest Dissertations and Theses*, (303337178):pp. 1–270 (1984).

[39] P. Amendt, H. U. Rahman, and M. Strauss. Magnetic instabilities in accelerating plasma surfaces. *Physical Review Letters*, volume 53(13):pp. 1226–1228 (1984).

[40] G. Barak and N. Rostoker. Semi-hydrodynamic model for ion separation in a fast pinch. *Applied Physics Letters*, volume 41:p. 918 (1982).

[41] H. U. Rahman, P. A. Amendt, and N. Rostoker. Z pinches with multi-ion species: Ion separation and stability. *Physics of Fluids*, volume 28(5):pp. 1528–1531 (1985).

[42] G.C. Burdiak, S.V. Lebedev, R.P. Drake, and et.al. The production and evolution of multiple converging radiative shock waves in gas-filled cylindrical liner z-pinch experiments. *HED Physics*, volume 9:pp. 52–62 (2013).

[43] N. Rostoker and H. Tahsiri. *A Perspective of Physics*. Rayleigh Taylor Instability for Impulsively Accelerated Shells. Gordon and Breech, NY, Sir Rudolph Peierls, Ed. (1978).

[44] M. A. Liberman, J. S. DeGroot, A. Toor, and R. B. Spielman. *Physics of high-density Z-pinch plasmas*. Springer, New York, New York (1999).

[45] H. U. Rahman, P. Ney, A. Van Drie, N. Rostoker, and F. J. Wessel. Control of the Rayleigh-Taylor Instability in a Staged Z-Pinch. *Physics of Plasmas*, volume 11:p. 5595 (2004).

[46] P. F. Schmit, P. F. Knapp, S. B. Hansen, M. R. Gomez, K. D. Hahn, D. B. Sinars, K. J. Peterson, S. A. Slutz, A. B. Sefkow, T. J. Awe, E. Harding, C. A. Jennings, G. A. Chandler, G. W. Cooper, M. E. Cuneo, M. Geissel, A. J. Harvey-Thompson, M. C. Herrmann, M. H. Hess, O. Johns, D. C. Lamppa, M. R. Martin, R. D. McBride, J. L. Porter, G. K. Robertson, G. A. Rochau, D. C. Rovang, C. L. Ruiz, M. E. Savage, I. C. Smith, W. A. Stygar, and R. A. Vesey. Understanding fuel magnetization and mix using secondary nuclear reactions in magneto-inertial fusion. *Phys. Rev. Lett.*, volume 113:p. 155004 (2014).

[47] H. U. Rahman, P. Ney, N. Rostoker, and F. J. Wessel. Fusion in a Staged Z-pinch. *Astrophysics and Space Science* (2009).

[48] R. E. Peterkin, M. H. Frese, and C. R. Sovinec. Transport of magnetic flux in an arbitrary coordinate ALE code. *Journal of Computational Physics*, volume 140(1):pp. 148–171 (1998).

[49] S.D. Frese and M.H. Frese. Recent improvements to mach2 and mach3 for fast z-pinch modeling. In J. Davis, editor, *Proceedings of the 5th International Conference on Dense Z-Pinches*, p. 156 (2002).

[50] J. W. Thornhill, Y. K. Chong, J. P. Apruzese, J. Davis, R. W. Clark, J. L. Giuliani Jr., R. E. Terry, A. L. Velikovich, R. J. Commisso, K. G. Whitney, M. H. Frese, S. D. Frese, J. S. Levine, N. Qi, H. Sze, B. H. Failor, J. W. Banister, P. L. Coleman, C. A. Coverdale, B. Jones, and C. Deeney. One- and two-dimensional modeling of argon k-shell emission from gas-puff Z-pinch plasmas. *Physics of Plasmas*, volume 14:p. 063301 (2007).

[51] D. J. Ampleford, S. B. Hansen, C. A. Jennings, B. Jones, C. A. Coverdale, A. J. Harvey-Thompson, G. A. Rochau, G. Dunham, N. W. Moore, E. C. Harding, M. E. Cuneo, Y.-K. Chong, R. W. Clark, N. Ouart, J. W. Thornhill, J. Giuliani, and J. P. Apruzese. Opacity and gradients in aluminum wire array z-pinch implosions on the z pulsed power facility. *Physics of Plasmas*, volume 21(3):031201 (2014).

[52] S. A. Slutz and R. A. Vesey. High-gain magnetized inertial fusion. *Phys. Rev. Lett.*, volume 108:p. 025003 (2012).

[53] M. R. Gomez, S. A. Slutz, A. B. Sefkow, D. B. Sinars, K. D. Hahn, S. B. Hansen, E. C. Harding, P. F. Knapp, P. F. Schmit, C. A. Jennings, T. J. Awe, M. Geissel, D. C. Rovang, G. A. Chandler, G. W. Cooper, M. E. Cuneo, A. J. Harvey-Thompson, M. C. Herrmann, M. H. Hess, O. Johns, D. C. Lamppa, M. R. Martin, R. D. McBride, K. J. Peterson, J. L. Porter, G. K. Robertson, G. A. Rochau, C. L. Ruiz, M. E. Savage, I. C. Smith, W. A. Stygar, and R. A. Vesey. Experimental demonstration of fusion-relevant conditions in magnetized liner inertial fusion. *Phys. Rev. Lett.*, volume 113:p. 155003 (2014).

Divertor for a linear fusion device

D.D. Ryutov[1], P.N. Yushmanov[2], D.C. Barnes[2], S.V. Putvinski[2]

[1] *Lawrence Livermore National laboratory, Livermore, CA, 94550,*
[2] *Tri Alpha Energy, Inc., P.O. Box 7010, Rancho Santa Margarita, CA 92688, USA*

Abstract. Linear fusion devices can use large magnetic flux flaring in the end tanks to reduce the heat load on the end structures. In order to reduce parallel electron heat loss, one has to create conditions where the neutral gas density in the end tanks is low, as otherwise cold electrons produced by the ionization of the neutrals would cool down the core plasma electrons. The processes determining the neutral gas formation and spatial distribution are analysed for the case where neutrals are formed by the surface recombination of the outflowing plasma. The conditions under which the cooling of the core plasma is negligible are formulated.

1. INTRODUCTION

An approach to aneutronic fusion suggested by Professor N. Rostoker in 1990's is based on the use of a field-reversed configuration embedded into a mirror-like magnetic field. Very promising results obtained in the studies of this approach in the Tri Alpha Energy, Inc. were recently reported in an invited talk by M. Binderbauer at the 2014 APS Division of Plasma Physics Annual Meeting [1].

The issues of the plasma behaviour on the open field lines of such device (i.e., on the field lines in the area beyond the FRC separatrix [2]) are similar to those studied in the mirror machines. In those, the magnetic field lines connect the core plasma with the material surfaces at both ends of the vacuum vessel. A concern then is that the electron heat loss to the end surfaces would be inadmissibly high. This concern often is phrased as a "proof" of the impossibility of reaching high electron temperatures in linear facilities. A closer look, however, shows that there is no any intrinsic difficulty for a good electron confinement on the open field lines: a real problem is eliminating any potential sources of the cold electrons on the end walls. In the situations where such sources are absent, the quasineutrality constraint leads to the formation of an electrostatic potential barrier that confines the majority of electrons and adjusts itself so that electron and ion fluxes to the wall become equal; the electron energy loss would then be, roughly, comparable to the ion heat loss.

In the case of a plasma column of a constant end-to-end radius (like in the gas discharge experiments), and the plasma density roughly uniform along the column (not varying by more than a factor of 2), the main part of this repelling potential is concentrated in the narrow Debye sheaths immediately adjacent to the end walls and has an amplitude of a several T_e/e [3].

In large linear devices, with a large power exhaust through each end, one has to use significant flaring of the magnetic field beyond the mirror throat, Fig. 1a, in order to reduce the power load to the wall to the level compatible with a long life-time of the plasma-facing components. In this case the potential distribution becomes different from the aforementioned gas-discharge example in that a substantial fraction of the electron-repelling potential is now spread over the whole expansion section, to maintain the plasma neutrality in the whole expansion tank ("divertor"), whose length is much greater than the Debye radius. In this case, only a fraction of the total potential drop occurs in the Debye sheath (Fig. 1b.) For large expansion, this fraction may become significantly smaller than the overall potential drop. This situation is thought to occur in the GDT facility at Novosibirsk [4], although it is still desirable to make dedicated

experiments to quantify this effect. The regime where the potential drop occurs predominantly in the bulk of the expander (divertor) is highly desirable, as the drop in the Debye sheath becomes small, thereby reducing the electric field strength on the absorbing surface (high electric fields may lead to enhanced emission from the surface imperfections and thereby cause faster energy loss).

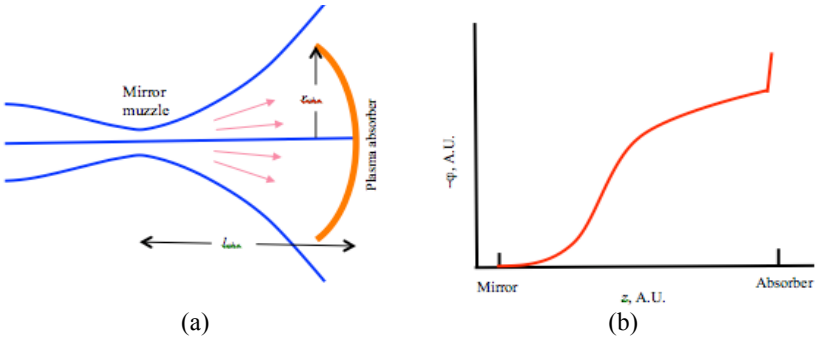

FIGURE 1. (a) Schematic of the end section of a linear device; the confinement zone is to the left; magnetic field lines are shown in blue; arrows show the outflowing plasma; (b) potential distribution along the axis of the end tank; the potential in the mirror is set to zero; note a steep potential variation in the Debye sheath near the wall; Note also that the plotted quantity is $-\varphi$.

In a large expansion tank one more source of cold electrons is present: a neutral gas whose ionization would cause formation of low-energy electrons that would lead to enhanced cooling of the core plasma. A ubiquitous source of the neutrals is surface recombination of the outflowing plasmas at the end wall. As the neutrals formed at the wall are very slow compared to the outflowing plasma ions, the particle balance consideration shows that the neutral density may become substantial [5]. It is this effect that is the prime focus of our study. We assess various factors affecting the neutral formation and formulate conditions under which the effects of cold particles are negligible (a desirable mode of operation). If the background gas is present in non-negligible amounts, it has to be included into analysis, and we do that in Sec. 3.4.

We present a broad-brush characterization of the properties of the plasma flow in the expansion tanks (divertors), focusing on the effects introduced by the neutrals formed as a result of the plasma recombination at the end plates. This analysis creates a background needed for the further studies of such effects as electron heat loss, plasma rotation, and plasma stability. For the numerical examples we choose parameters typical to the current experiments and near-future upgrades of the C2 facility [1]. Sec. 2 contains description of the plasma flow in the flaring magnetic field. Sec. 3 addresses the formation of the neutral gas on the end plates and its further redistribution. Sec. 4 contains discussion and a brief summary of the results.

2. PLASMA PARAMETERS IN A FLARING MAGNETIC FIELD

The operation of the divertor shown in Fig. 1 is intimately related to the processes in the confinement volume between the mirrors. Among others, the plasma composition and the plasma collisionality play significant role. Here we consider a deuterium plasma, as it is used in the current experiments [1]. We also assume that the electron-electron collision time is shorter than the plasma confinement time, as is the case for the current and near-future experiments. This means that the electrons in the mirror throat have a near-Maxwellian distribution.

The aforementioned ansatz of equal number of electrons and ions escaping to the non-emitting wall is based on the implicit assumption that there is no significant non-ambipolar transport across the magnetic field. If such transport channel is non-negligible, then the electron loss current along the flux tube may be different from the ion loss current from the same flux-tube. This would affect the ratio of the ambipolar (smooth) part of the plasma potential variation in the expander region and Debye sheath potential jump at the wall. In this note we consider the situation where main loss channel is along the field lines.

We will evaluate the sound speed in the mirror, assuming that the ions are adiabatic whereas the electrons are isothermal:

$$u_{mir} = \sqrt{\frac{1}{m_i}\left(\frac{5}{3}T_i + T_e\right)} \tag{1}$$

We also assume for a while that there is no significant ionization of the gas in the end tank and interaction of the outflowing plasma with neutrals can be ignored (we return to this issue later).

In such a setting, one electron is lost per one ion. As the electron thermal velocity is much higher than the ion thermal velocity, a high potential that repels the electrons is formed in the expansion tank. Part of this potential drop is distributed over the length and determined by the quasineutrality constraint; the second part is localized in the near-wall sheath. The distribution between the two is determined by the magnitude of the expansion coefficient K. For modest values of K, essentially the entire potential drop occurs within the sheath, whereas for $K > (2-3)\sqrt{m_i/m_e}$ most of the potential drop occurs in the expander volume.

In the absence of the volumetric energy loss in the expander, the energy flowing through a mirror muzzle is equal to the energy flowing through the absorber (we mean here the energy flow through the whole cross-section). However, the distribution of the energy flux between the species changes on the way to the wall. At the mirror muzzle it is carried predominantly by the electrons (unless their temperature is excessively low), whereas at the wall essentially all the energy is carried by the ions.

Indeed, if we look at the electrons at the mirror throat, only those that have enough energy to overcome a high potential barrier are lost. To maintain an equal particle loss (one electron per one ion), one has to have a potential barrier for the electrons at the level of

$$e\left(\varphi_{mir} - \varphi_{wall}\right) = T_e \ln\frac{v_{te}}{2\sqrt{\pi}u_{mir}} \tag{2}$$

where we use a definition $\mathrm{v}_{e,i,n} = \sqrt{2T_{e,i,n}/m_{e,i,n}}$ for the particle thermal velocity. In other words, each electron lost per one ion carries away an energy that is significantly higher than an energy carried away by the ion (if the temperatures are comparable).

This circumstance is often expressed in the form of the following expression for the power lost per a mirror [5, 6]:

$$P = S_{\mathrm{mir}} n_{\mathrm{mir}} u_{\mathrm{mir}} \left(A_{\mathrm{e}} T_{\mathrm{e}} + A_{\mathrm{i}} T_{\mathrm{i}}\right) \tag{3}$$

where the kinetic energy of the ions in the mirror $m_i u_{mir}^2/2$ is absorbed by the coefficients A_e and A_i. Specific numbers for A_e and A_i depend on the plasma collisionality inside the confinement system. The usual "rule of thumb" is that A_e~5-6, whereas A_i~2 [6].

For $K > \sqrt{m_i/m_e}$, the energy at the wall is carried (almost) entirely by the ion flow (contrary to what takes place in the mirror). For $K < \sqrt{m_i/m_e}$ some non-negligible part can be carried by the electrons. The particle flux at the wall is, obviously, $n_{mir}u_{mir}/K$. Using Eq. (3), one can express it as

$$\frac{n_{\mathrm{mir}} u_{\mathrm{mir}}}{K} = \frac{P}{S_{\mathrm{abs}}\left(A_{\mathrm{e}} T_{\mathrm{e}} + A_{\mathrm{i}} T_{\mathrm{i}}\right)} \tag{4}$$

The flow velocity v_{wall} at the absorbing end-wall will be higher than u_{mir} due to the flow acceleration. The specific value of v_{wall} is not particularly sensitive to the model of the potential distribution; we will simply assume that

$$v_{wall} = 2u_{mir}. \tag{5}$$

The value of v_{wall} is needed for the evaluation of the plasma density near the wall, which is:

$$n_{\text{wall}} = \frac{P}{2S_{\text{abs}}\sqrt{\frac{1}{m_i}\left(\frac{5}{3}T_i + T_e\right)}(A_{\text{e}}T_{\text{e}} + A_{\text{i}}T_{\text{i}})} \tag{6}$$

This equation shows that the plasma density near the wall depends only on the power flux at the wall and the particle temperatures. The plasma density at the wall (on the plasma side of the sheath) is shown in Fig. 2 for various assumptions regarding T_e/T_i. The previous analysis was based on the assumption that the system is in a steady state. In particular, it was assumed that the ion transit time through the end tank is shorter than the time within which P and $T_{e,i}$ vary.

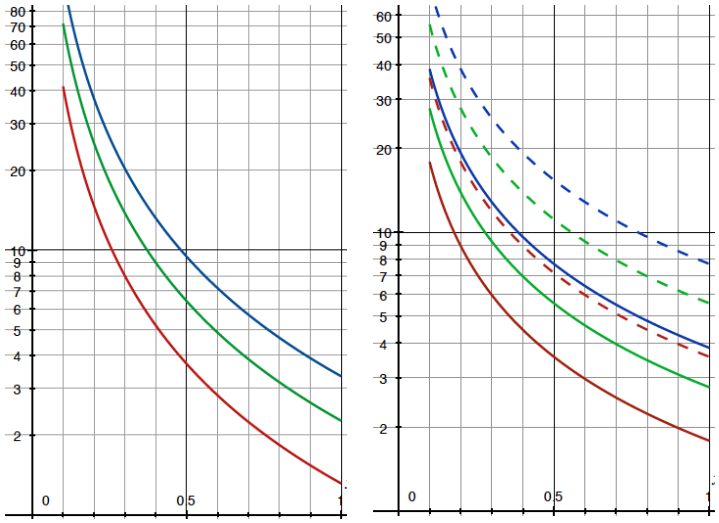

(a) (b)

FIGURE 2. (a) Plasma density near the absorbing wall in the units of 10^9 cm^{-3} vs the ion temperature in keV. Red, green and blue curves correspond to T_e/T_i=1.0, 0.5 and 0.25, respectively. The coefficients A_e and A_i are 5 and 2. The power loss is P=3 MW per end, S_{abs}=3 m^2. (b) Density of the first-generation neutrals near the end wall in the units of 10^{11} cm^{-3} vs. the ion temperature in keV. Red, green and blue curves correspond to T_e/T_i=1.0, 0.5 and 0.25, respectively. The coefficients A_e and A_i are 5 and 2. The power loss is P=3 MW per end (solid curves) or 6 MW per end (dashed curves), S_{abs}=3 m^2, R=1.

3. NEUTRALS IN THE END TANK

In this section we consider the formation and further redistribution of the neutrals appearing because of the plasma recombination at the absorbing wall. In any real device, there will be some amount of neutrals of different origin in the end tank (residual gas, gas appearing during the start-up phase, etc.). This source is scenario-specific and is thought to be subdominant in the upgraded facilities. We will therefore focus on the ubiquitous source related to the surface recombination of the outflowing plasma.

3.1. First-generation neutrals

By the first generation we mean neutrals formed by a surface recombination on the end plate. If they are not ionized during their transit through the plasma, they strike the walls of the expansion tank and produce much slower neutrals of the second generation. The role of the latter will be considered in Sec. 3.2, while now we discuss parameter of the first-generation neutrals. The density of the first-generation neutrals near the wall, n_{n1}, can be evaluated if their characteristic velocity, v_{n1}, is known. Assuming that the neutrals

emerge from the wall with an isotropic angular distribution, one would have the following expression for their flux:

$$q_l = \frac{v_{nl} n_{nl}}{3} \tag{7}$$

where the coefficient 1/3 qualitatively accounts for the isotropic distribution of their velocities (into the 2π solid angle). In a more detailed analysis, for a perfectly isotropic distribution of the emerging particles, the flux is equal to $v_{nl} n_{nl}/\ln(1/\varepsilon)$, where ε is the smallest angle that the particles form with the surface. The latter may be determined by the surface waviness, as well as by the physics of the processes occurring at the surface. We assumed that it is ~3 degrees (~1/20 of the radian). The dependence on ε is logarithmic, so that an exact value of the limiting angle is not particularly important. Below, we use a coefficient of 1/3.

The number of neutrals born per unit area of the end wall per unit time is given by expression (4), multiplied by the recycling coefficient R. We then get:

$$n_{nl} = \frac{3PR}{S_{\text{abs}}(A_{\text{e}} T_{\text{e}} + A_{\text{i}} T_{\text{i}}) v_{nl}} \tag{8}$$

For saturated surfaces, a significant fraction of the recycled particles will have an energy of ~ 1 eV (Franck-Condon neutrals); see e.g. Ref.7, Fig.5). In the further analysis, we would have to account for the presence of not only atomic, but also molecular hydrogen among the recycled neutrals. This may be important, as for the proton energies below a few keV the charge-exchange cross-section on the molecules is smaller than that on the atomic hydrogen. A first-generation neutral density near the wall is shown in Fig. 3, assuming that $v_{n1}=1.5\cdot10^6$ cm/s. This result may change if there is a significant contribution of slower, room temperature neutrals. The composition (atomic vs. molecular) and velocity distribution of the recycled neutrals may depend on the substrate material and the level of saturation.

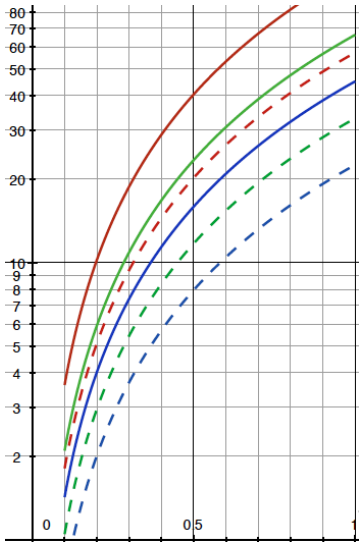

FIGURE 3. Mean-free path (in meters) for the first generation neutrals vs. the ion temperature in keV. Red, green and blue curve correspond to T_e/T_i=1.0, 0.5 and 0.25, respectively. The coefficients A_e and A_i are 5 and 2. The power loss is P=3 MW per end (solid curves) or 6 MW per end (dashed curves), S_{wall}=3 m^2.

Moving away from the wall, these neutrals interact with the incoming plasma via the processes of ionization and charge exchange. The relative role of these processes is determined by the ratio of the corresponding reactivities: $\langle \sigma v_e \rangle_i$ and $\langle \sigma v_i \rangle_{cx}$. In these expressions v_e and v_i correspond to the electrons and ions of the incoming plasma flow. For the anticipated electron temperatures, the ionization reactivity is close to its maximum value,

$$< \sigma v_e >_i \approx 3 \cdot 10^{-8}\, cm^3/s \tag{9}$$

In the range of the ion energies of 0.5 keV – 2 keV the charge-exchange reactivity for hydrogen also varies insignificantly

$$< \sigma v_i >_{cx} \approx 8 \cdot 10^{-8}\, cm^3/s \tag{10}$$

So, the charge-exchange process dominates by roughly a factor of 3.

The mean-free path for the first-generation neutrals near the absorbing wall is

$$\lambda_{nl} = \frac{v_{nl}}{n_{wall}\left(< \sigma v_e >_i + < \sigma v_i >_{cx}\right)} \tag{11}$$

The plot of this quantity for various assumptions on the ion temperature in the outflow is shown in Fig. 3 for various assumptions regarding T_e/T_i. For T_i exceeding 0.2 keV the mean-free path is larger than the plasma size near the absorber. In this case, the majority of the first-generation neutrals reach the side walls.

Charge-exchange mean-free path for the incoming plasma ions on the neutrals of the first generation is larger than the size of the outflowing plasma (~ 1m) for the ion temperatures beyond ~ 0.2 keV. For smaller temperatures, the CX process may lead to substitution of a significant fraction of the incoming ions by slow charge-exchange ions.

3.2. Second-generation neutrals for the case of the ion temperatures T_i>0.2 keV (plasma transparent for the first-generation neutrals)

The particle balance for the second-generation neutrals can be written as:

$$\left(1-\alpha_S\right) S_S n_{n2} v_{n2} \approx \frac{P}{A_e T_e + A_i T_i} \tag{12}$$

where subscript "S" stands for the absorbing side walls (cryopumps), with S_S being their surface area and α_S being their albedo. The total number of the second-generation neutrals hitting the plasma surface in unit time is, roughly, $S_p n_{n2} v_{n2}$. In other words, the total number of slow neutrals hitting the plasma surface per unit time is:

$$\dot{N} \approx \frac{S_P}{S_S\left(1-\alpha_S\right)} \frac{P}{\left(A_e T_e + A_i T_i\right)} \tag{13}$$

If this number is small compared to the total number of ions escaping from the trap, the effect of the plasma interaction with the neutral gas will be minimal. The figure of merit is then

$$Q \equiv \frac{S_S\left(1-\alpha_S\right)}{S_P} \tag{14}$$

If this "quality factor" is greater than 10, then, energy-wise, the effect of the neutrals will be small, even if they all are ionized in the plasma. Note that Q here has an entirely different meaning from the fusion enhancement factor Q also used in the literature.

Interaction of these particles with the plasma will be dominated by charge exchange, as the charge-exchange reactivity (Eq. 10) is higher than the ionization reactivity. Each charge-exchange event will lead to a loss of full ion energy. However, for Q>10 this will not be too important.

3.3. Neutrals of the second generation; electron and ion "quality factors"

As the neutrals of both the first and second generation move very slowly compared to plasma ions and electrons, their mean-free path in a plasma has to be evaluated as

$$\lambda = \frac{v_n}{< \sigma v > n_i} \tag{15}$$

where $\langle \sigma v \rangle$ is a reactivity for the corresponding process, v_n is the velocity of the neutral particle and n_i is the plasma density. For the reactivity data we use Fig.1.25 of Ref. 7. Table 1 summarizes the information for several most important processes. Serendipitously, the reactivities in the range of electron and ion temperatures of interest to us are weak functions of temperature, this makes the estimates quite robust (albeit somewhat crude): the numbers presented in Table 1 can vary by about 50% for the plasma temperatures varying from 50 to 500 eV.

TABLE 1. Most important atomic processes for deuterium[a)]

#	Process	$\langle \sigma v \rangle$, 10^{-8} cm^3/s	λ, m for W_n=0.025 eV	λ, m for W_n=1 eV
1	$D+e \rightarrow D^+ +2e$	3	0.5/ n_{i11}	3.2/ n_{i11}
2	$D_2+e \rightarrow D_2^+ +2e$	5	0.2/ n_{i11}	1.3/ n_{i11}
3	$D+D^+_{fast} \rightarrow D^+ + D_{fast}$	7	0.2/ n_{i11}	1.3/ n_{i11}
4[b)]	$D_2^+ +e \rightarrow D+D^+ +e$	9	0.1/ n_{i11}	0.7/ n_{i11}
5[b)]	$D_2^+ +e \rightarrow 2D^+ +2e$	1	1.5/ n_{i11}	6.5/ n_{i11}

a) The density in this table, n_{i11}, is measured in the units of 10^{11} cm^{-3}. b) Processes 4 and 5 involve not the neutral particles but molecular ions that are formed in a plasma by the process #2. The λ for these cases means the mean-free path along the field lines.

The two last columns correspond to the energies of the thermal particles (1/40 eV) and Franck-Condon particles with the energy of 1 eV. The data on reactivities presented in Ref. 8 correspond to hydrogen, but should be the same for deuterium as well. The velocities v_n are evaluated for the atomic and molecular deuterium. A lot of information on the cross-sections can also be found in Ref. 9.

The surface area of the plasma cone S_p is:

$$S_p = \pi r_{abs} \sqrt{l^2 + r_{abs}^2} \approx 7m^2 \tag{16}$$

where the dimensions are specified in a caption to Fig. 4. The surface area of the side walls of the expansion tank and its end walls is S_S~25-30 m^2 and is roughly by a factor of 4 larger than the plasma surface area. The neutrals produced at or reflected from the walls of the vessel would probably have quasi-isotropic distribution and, due to a relatively small surface of the plasma, will bounce between the side-walls until they hit the plasma (see schematic in Fig. 4). There are two possibilities here: A) the plasma is "optically thin" for them and their density would then be almost uniform inside the plasma; B) the plasma is "optically thick" and they are all "digested" by the plasma in a thin surface layer.

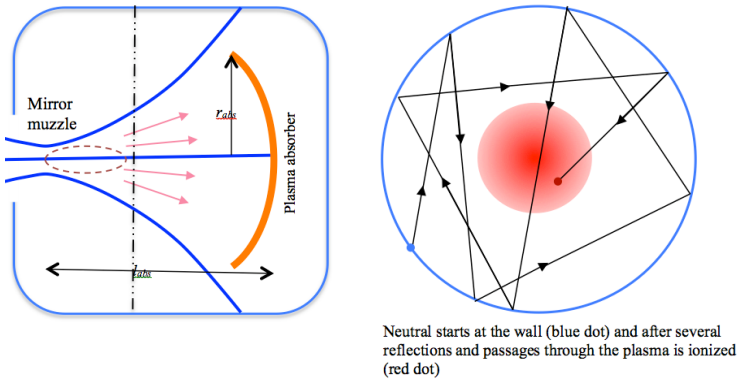

(a) (b)

FIGURE 4. The geometry of the problem: (a) The outer blue contour is a boundary of the end tank; the dashed oval circumscribes an area impermeable to the neutrals; vertical dash-dotted line shows a cross-section illustrated in the right panel; b) a cross-section of the end tank The dimensions assumed in the numerical estimates: l=2 m, a_w=1 m.

The penetration length of the neutrals to the plasma is inversely proportional to the plasma density. As the plasma radius a at a given distance z from the mirror is

$$a = a_{mir} + \frac{(a_W - a_{mir})z}{l}, \tag{17}$$

the plasma density for a conical flow scales as

$$n \approx n_{mir} \frac{a_{mir}^2}{\left(a_{mir} + \frac{(a_W - a_{mir})z}{l}\right)}, \tag{18}$$

where a_{mir} and a_W are the plasma radii at the mirror and at the absorbing wall, and l is the distance between the mirror and absorber.

Using the results of Sec.2, one can evaluate the plasma density in the mirror throat. We use Eq. 1 for the plasma velocity and Eq. 18 for plasma density. The results are shown in Fig. 5. The horizontal lines correspond to the condition $\lambda/a_{mir}=1$ for $a_{mir}=15$ cm for the processes 1 – 3. One sees that for the outflowing plasma temperatures of interest in our problem the plasma in the mirror is impermeable to the thermal neutrals. With regard to the Franck-Condon neutrals it may or may not be permeable, depending on the specific process and plasma temperature.

In a more sophisticated analysis, the length-scale for the neutrals penetration to the plasma will be smaller than their mean-free path (Eq. 15) by, probably, a factor of 2. The reason is that they hit the plasma surface in a quasi-isotropic fashion. The decay profile will be non-exponential, so that it is somewhat tricky to characterize it by a single length-scale.

Reaction 4 involves molecular ions produced by reaction 2. As soon as the molecular ion is formed, it is split to an atom and atomic ion by reaction 4. Reaction 4 has a very high reactivity and one can roughly think of this process as a single-step one, with the slower process determining the rate at which the neutral atoms are formed from the molecules. The slow atoms then exchange charge with the fast ions (with a high cross-section). This is why the processes 2 and 4 are important in an overall dynamics of the system.

Even if the plasma is opaque with respect to some process near the mirror, it may become transparent further downstream due to a rapid plasma density decrease ($\sim 1/z^2$). The plot characterizing the plasma opacities near the absorber is shown in Fig. 6. When making this plot, we assumed that the plasma density near the absorber is determined by Eq. 6 and that the plasma radius is 1 m; dashed lines correspond to Table 1 parameters. For the green curve and ion temperatures exceeding ~ 250 eV the area near the wall is transparent for the processes 1-3. On the other hand, at the initial part of the conical flow, until approximately z=l/2, the plasma is shielded from the penetration of thermal particles and, in some cases, even from the Franck-Condon particles.

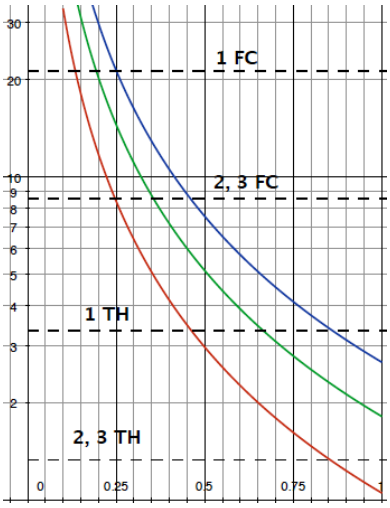

FIGURE 5. Plasma density at the mirror in the units of 10^{11} cm^{-3} vs. the ion temperature in keV. Red, green and blue curves correspond to T_e/T_i=1.0, 0.5 and 0.25, respectively. The coefficients A_e and A_i are 5 and 2. The power loss is P=3 MW per end, S_{wall}=3 m^2. The horizontal dashed lines correspond to the condition where the plasma radius at the mirror (a_{mir}=15 cm) is equal to the mean-free paths for the processes 1 and 2, 3 (the reactivities for the latter two are very close to each other, see Table 1). The letters TH and FC correspond to THermal and Franck-Condon particles, respectively. In the area above these lines the penetration length of the neutrals with respect to the corresponding processes is smaller than a_{mir}.

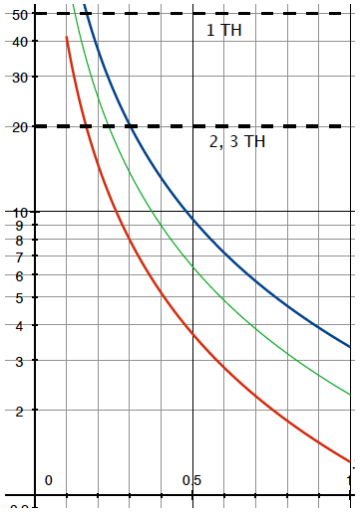

FIGURE 6. Plasma density at the absorber in the units of 10^9 cm^{-3} vs. the ion temperature in keV. Red, green and blue curves correspond to T_e/T_i=1.0, 0.5 and 0.25, respectively. The coefficients A_e and A_i are 5 and 2. The power loss is P=3 MW per end, S_{wall}=3 m^2. The horizontal dashed lines correspond to the condition where the plasma radius at the absorbing wall (a_{wall}=1 m) is equal to the mean-free paths for the processes 1-3 for thermal particles (TH=thermal). In the area above these lines the penetration length of the thermal neutrals with respect to the corresponding processes is smaller than a_{wall}. For Franck-Condon particles the plasma near the absorbing wall is transparent in all cases covered by this figure.

In what follows, we focus on the area where plasma is transparent for the neutrals, i.e., roughly the last half of the conical flow. As was mentioned above, the neutrals bouncing between the walls of the absorber have essentially isotropic and uniform spatial distribution (except for the shaded zones near the mirrors in Fig. 4). The neutral particle balance can then be written in the following rough way:

$$\frac{P}{A_e T_e + A_i T_i} = (1-\alpha_S) S_S \left(\frac{n_{2TH} v_{TH}}{2} + \frac{n_{2FC} v_{2FC}}{2} \right) \quad (19)$$

This is indeed a rather crude description, as we do not distinguish between the atomic and molecular species and characterize the surface by some compound albedo. On the other hand, it allows one to identify basic trends and make rough estimates.

We will use an assumption that the fluxes of the two types of neutrals are approximately equal. Then, the neutral density is dominated by the thermal particles. In this note we consider the case where the plasma is transparent to the neutrals, as is the case for sufficiently high temperature of the outflowing plasma. In terms of the energy loss, the "worst" process is charge exchange, due to its high reactivity. In each such event the ion loses all its energy, and the fast neutral leaves the plasma without being re-ionized. The fraction of the energy lost by the plasma stream on its way to the absorber will then be approximately $\frac{S_P}{S_S(1-\alpha_S)}$. We assume here that this fraction is significantly less than 1.

So, we will consider interaction of the transparent plasma with the neutral population in some more detail. The density of the neutrals in a transparent plasma is uniform and, with our earlier assumption of equal fluxes of thermal and F-C particles, is predominantly thermal. The number of ionizations per unit time in the whole plasma volume is $\sim n_{2TH} \langle \sigma v \rangle_i N_i$, where N_i is the total inventory of plasma ions (and electrons) in the whole volume of the conical flow (we neglect here a small part of the volume impermeable for the neutrals). This number can be compared with the number of the electrons leaving the plasma confinement zone in the ideal case where there are no neutrals in the plasma. The latter is simply

$$\frac{P}{A_e T_e + A_i T_i} \quad (20)$$

One can characterize a fraction of additional electrons (formed in the conical flow) by an electron quality factor Q_e:

$$Q_e = \frac{P}{A_e T_e + A_i T_i} \times \frac{1}{n_{2TH} < \sigma v >_i N_i} \quad (21)$$

The aforementioned fraction is equal to $1/Q_e$ and is small if Q_e is large. Its significance is related to possible increase of the electron heat loss if too many cold electrons are formed in the conical flow. Using Eq. 19 for the first multiplier, we get:

$$Q_e = \frac{(1-\alpha_S) v_{TH} S_S}{< \sigma v >_i N_i} \quad (22)$$

On the other hand, the total particle inventory in the conical flow is approximately

$$N_i \approx \pi l r_w^2 n_w \approx S_P r_w n_w \quad (23)$$

In other words,

$$Q_e \approx \frac{(1-\alpha_S) v_{TH} S_S}{< \sigma v >_i n_{iw} S_P r_w} = Q \frac{\lambda_{iTH}}{r_w} \quad (24)$$

where λ_{iTH} is ionization length of thermal neutrals near the absorbing surface and Q is defined by Eq. 14. It is roughly determined by some compound reactivity of the processes 1 and 2 in Table 1.

We now switch to the processes that determine the loss of fast ions and the processes that "load" the flow by slow ions formed as a result of ionization. The charge exchange process creates a slow ion in place of a fast ion and causes an effective friction force for the ion flow. The ionization of thermal neutrals creates slow ions that "load" the flow. We are not particularly concerned by the energy loss of the outflowing ions, as they are lost, anyway. On the other hand, the appearance of slow ions (formed by both processes) may change the dynamics of the flow and also affect the control of plasma rotation by a segmented end wall. One can think that, if the number of the slow ions formed in the outflow per unit time is less than the ion exhaust from the device, the effect of the slow ions will be small. We therefore introduce an ion "quality factor", Q_i, analogously to Q_e. One has:

$$Q_i \approx \frac{(1-\alpha_S)\nu_{TH} S_S}{(<\sigma v>_i + <\sigma v>_{cx}) n_{iw} S_P r_w} = Q\left(\frac{r_w}{\lambda_{iTH}} + \frac{r_w}{\lambda_{cxTH}}\right)^{-1} \tag{25}$$

The ion quality factor is by a factor of 3 or 4 lower than the electron quality factor, due to the large charge-exchange reactivity.

3.4. The limiting neutral density

When operating the facility at the finite background pressure, the contribution of this pre-existing gas to the quality factors may be significant. In this section we relate Q_e and Q_i to the certain value to the neutral density, not finding it from a self-consistent analysis based on the book-keeping for the neutrals formed by the surface neutralization. The corresponding expression comes out of Eqs. 3, 6, 21 and 23 and geometrical relations:

$$n_{n2} = \frac{2}{Q_e <\sigma v>_i l} \sqrt{\frac{T_e + (5/3)T_i}{m_D}} \tag{26}$$

where l is the length of the expander. This equation provides a value of the neutral density corresponding to a certain value of Q_e. There is no assumption that the neutral density has reached a steady state. (We assumed that the flow velocity at the wall is twice the sound speed in the mirror throat, Eq. 5.) The ionization reactivity is an aggregate reactivity that accounts for both atomic and molecular density. We take for it the value 4×10^{-8} cm^3/s (see Table 1). The plot of the neutral density vs the ion temperature is shown in Fig. 7.

An analogous result for the neutral density corresponding to a certain level of "loading" of the ion flow is (Cf. Eq. 25):

$$n_{n2} = \frac{2}{Q_i (<\sigma v>_i + <\sigma v>_{CX}) l} \sqrt{\frac{T_e + (5/3)T_i}{m_D}} \tag{27}$$

This quantity is also shown in Fig. 7 under the assumption that $\left(\langle\sigma v\rangle_i + \langle\sigma v\rangle_{cx}\right) = 10^{-7} cm^3/s$ (see Table 1.)

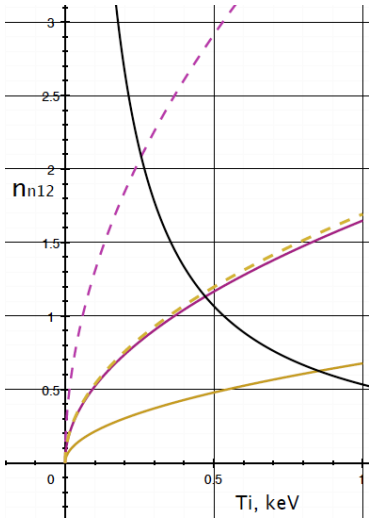

FIGURE 7. The critical density for the electron loading, Eq. 26, magenta curves and for the ion loading, Eq. 27, orange curves. Solid lines correspond to $Q_{e,i}$=5, dashed lines, to $Q_{e,i}$=2. The density is in the units of 10^{12} cm^{-3}. The length l=2 m, T_e/T_i=0.5. The black curve shows the neutral density accumulated during one transit time (see explanations in the text after Eq. 28).

The neutral transit time across the expansion tank is different for thermal neutrals and Franck-Condon neutrals. We will assume that thermal neutrals are dominating. Then, the transit time of the neutrals between two successive collisions with the walls will be, roughly, $\tau_{trans} \sim 2r_{exp}/v_{nTH} \sim 4$ ms. At the times shorter than that, the neutrals of the second generation will not reach the plasma cone. In other words, the plasma behaviour will be determined essentially by the neutrals of the first generation and, possibly, with the FC neutrals of the second generation. The steady state will form after multiple transits, at the time $\tau_{steady} \sim \tau_{trans}/(1-\alpha)$. For $\alpha=0.9$ this would be ~ 40 ms. At the times, $\tau_{transit} < t < \tau_{steady}$ the neutral density (at a constant plasma outflow) will grow linearly with time, gradually tapering-off when approaching the steady state. (If the much faster Franck-Condon neutrals dominate the process, the steady state will establish faster by a factor of roughly 6, but we focus on the case where the thermal neutrals are dominant.)

The density of the thermal neutrals accumulated during one transit time will be

$$n_{n.tr} = \frac{P\tau_{transit}}{\left(A_e T_e + A_i T_i\right) V_{exp}} \tag{28}$$

This quantity is plotted as a black line in Fig. 7.We assume that the background density of the neutrals is small (which may not necessarily be the case).

When discussing the evolution of the neutral density, we assume that the background level of the neutral density determined by the pump rate and leaks is at least a few times below the level that we are interested in. If this assumption is correct, then the time-scale for the pump-out of possible initial gas (produced, e.g. by the transiting plasmoid) will be about the time-scale for establishing a steady state.

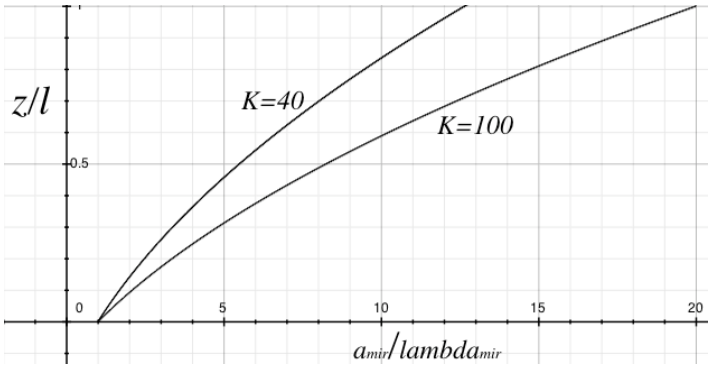

FIGURE 8. The distance from the mirror at which the plasma becomes transparent if it was opaque in the mirror; *K* is an expansion coefficient. The curves reach the unity if the opacity in the mirror is so high that the plasma remains opaque even at the maximum expansion.

3.5 The length of the opaque zone

Now we evaluate the length of the zone impermeable for the neutrals near the mirror (Fig. 4). Consider an atomic process with respect to which the plasma is impermeable in the vicinity of the mirror, i.e.

$$\lambda_{mir} < a_{mir} \tag{29}$$

where λ_{mir} is defined by Eq. 15. The reactivity for the process of interest should be taken from Table 1. The condition that the plasma becomes transparent with respect to this process at some distance z down the stream is

$$\frac{a^2(z)v(z)}{a_{mir}^2 v_{mir}} = \frac{n_{mir}}{n(z)} = \frac{\lambda}{\lambda_{mir}} = \frac{a(z)}{\lambda_{mir}} \tag{30}$$

or

$$\frac{a(z)v(z)}{a_{mir}v_{mir}} = \frac{a_{mir}}{\lambda_{mir}} \tag{31}$$

For the function *a(z)* we use Eq. 17; the modest acceleration of the flow velocity between the mirror and the absorber we describe by $v=v_{mir}\left(1+\frac{z}{l}\right)$. Equation 31 then yields the distance z where the plasma becomes transparent (Fig. 8).

4. DISCUSSION

The term "divertor" is widely used in the physics and technology of toroidal fusion devices, where it is normally related to a special magnetic configuration containing a singular, self-intersecting magnetic flux surface [10]. In this divertor the magnetic field at the location of the plasma-absorbing plates is about the same as in the core plasma, this creating a lot of difficulties with the handling of the accompanying heat loads. Conversely, in the linear device like that of Ref. 1, one can reduce the heat flux at the end walls by as much as one wants, simply by flaring the magnetic field in the end tanks. This provides significant advantage for the systems of the type [1] in a number of engineering issues.

The presence of the direct electric contact of the plasma surrounding the FRC with the end walls allows one to control the potential distribution in these plasmas and thereby improve the stability of the whole confinement system. This is a second large advantage of the linear facility.

Behaviour of the material surfaces exposed to the streaming exhaust plasmas depends on a number of hard-to-control processes, like formation of thin films and modification of the surface structure subjected to ion bombardment. A long exposure to the hydrogen-containing plasma may cause formation of sponge-like surfaces. This area involves significant fraction of empiricisms and is not quite amenable to strict cause-and-effect analyses. If these problems prove to be serious, they can be handled by scheduled replacement of the critical surfaces – a luxury that becomes available due to the absence of strong neutron activation of the plasma-facing components in the $p^{11}B$ facilities (in a canonical DT fusion this would be a big hurdle).

The efficiency of the thermal insulation of the confined plasma by the use of large expansion tanks depends on the vacuum conditions in these tanks: if the amount of gas exceeds certain limit, the ionization and charge exchange processes in the tank may lead to a cooling of the core plasma. The electric contact between the end walls and the core may also be compromised. Our paper addresses these issues and allows one to circumscribe the desirable regimes of operation in the facilities of the current generation and their upgrades with the deuterium plasma. The transition to the facilities that will use the $p^{11}B$ fuel would require the reassessment of the processes occurring in the divertor. The trends found in our study indicate that operation at higher temperatures and better plasma confinement will reduce the amount of neutral gas and make the corresponding problems more easily manageable if present at all.

ACKNOWLEDGMENTS

Work at LLNL was funded by Tri Alpha Energy, Inc and performed under DoE contract DE-AC52-7NA27344

REFERENCES

1. M. W. Binderbauer, T. Tajima, L. C. Steinhauer, E. Garate, M. Tuszewski, L. Schmitz, H. Y. Guo, A. Smirnov, H. Gota, D. Barnes, B. H. Deng, M. C. Thompson, E. Trask, X. Yang, S. Putvinski, N. Rostoker, R. Andow, S. Aefsky, N. Bolte, D. Q. Bui, F. Ceccherini, R. Clary, A. H. Cheung, K. D. Conroy, S. A. Dettrick, J. D. Douglass, P. Feng, L. Galeotti, F. Giammanco, E. Granstedt, D. Gupta, S. Gupta, A. A. Ivanov, J. S. Kinley, K. Knapp, S. Korepanov, M. Hollins, R. Magee, R. Mendoza, Y. Mok, A. Necas, S. Primavera, M. Onofri, D. Osin, N. Rath, T. Roche, J. Romero, J. H. Schroeder, L.

Sevier, A. Sibley, Y. Song, A. D. Van Drie, J. K. Walters, W. Waggoner, P. Yushmanov, K. Zhai, and TAE Team. “A high performance field-reversed configuration.” Phys. Plasmas **22**, 056110 (2015).
2. L. C. Steinhauer. “Review of field-reversed configurations.” Phys. Plasmas, **18**, 070501 (2011).
3. G. D. Hobbs, J. A. Wesson, “Heat flow through a Langmuir sheath in the presence of electron emission [from the wall].” Journal of Nuclear Energy. C. Plasma Physics, Accelerators, Thermonuclear Research, **9**, 85-87 (1967).
4. P. A. Bagryansky, A. G. Shalashov, E. D. Gospodchikov, A. A. Lizunov, V. V. Maximov, V. V. Prikhodko, E. I. Soldatkina, A. L. Solomakhin, and D. V. Yakovlev. “Threefold Increase of the Bulk Electron Temperature of Plasma Discharges” in a Magnetic Mirror Device.” Phys. Rev. Lett., **114**, 205001 (2015).
5. D. D. Ryutov. "Axial electron heat loss from mirror devices revisited", Fusion Sci. Technol., **47,** 148-154, (2005).
6. D.D. Ryutov "Open-ended traps". Soviet Physics Uspekhi, v.31, p.300 (1988).
7. Z. Guvenc, D. Guvenc. “Hydrogen recombination on a mixed adsorption layer at saturation on a metal surface: H ->(D+H)(sat)+Ni(100)” Surface Science, **529**, 11 (2003).
8. P. Stangeby. “The Plasma Boundary of Magnetic Fusion Devices.” Taylor & Francis, 2000.
9. R. Tawahara et al. J. Chem. Phys. Ref. Data, **19**, 617 (1990)
10. ITER Physics Expert Group on Divertor, ITER Physics Expert Group on Divertor Modelling, and Database and ITER Physics Basis Editors. “Chapter 4: Power and particle control.” Nucl.Fusion 39, 2391 (1999).

CONCLUSIONS

T. Tajima and M. Binderbauer

The proceedings of the Norman Rostoker Memorial Symposium was attended by some 150 people, Norman's professional colleagues, friends, and family members as well as some press around the world. As we now know, an Editor from SCIENCE has reported from NRMS.

We remain very grateful to the participation by all the participants in a variety of ways in this memorable occasion, which now made up a equally memorable collection of expertise review of author's achievements as related to Professor Rostoker's reach in this book. Nearly all speakers turn their talks into a paper in this book to commemorate Norman's legacy and contributions to the science. Some of the papers go back long in history and reveal a deep philosophy behind the old and famous works that had become classical. Some show new establishments and pioneering achievements of late, which arose from years of collaboration and belaboring efforts with Norman, only now brilliantly blossomed. For example, Professor Penzias gave a moving banquet speech reviewing his perspective of Norman's fusion efforts is here. Even a person who could not attend the Symposium kindly sent his tribute to Norman, which was by Professor Walter Kohn, who collaborated with Norman in his celebrated work on the KKR theory in solid state physics.

I was so wiped out during the week of Symposium, but when I finally coming to recover to a bit of normalcy, words buoyed in my mind, which I jotted down in the form of the Waka poem (5-7-5-7-7 syllables).

「恩師の霊
　　会場に降下し
　　遺志の畏怖
　　旧友結び
　　新たな誓ひ」
　　田島　俊樹 (8/29/15)

"The mentor's spirit
Descends in the corridor
Our aspiration
To follow his legacy
Renews old friends' bonds and vows"

Toshiki Tajima (8/29/15)